

Journal of ASTM International
Selected Technical Papers



STP 1513

A photograph of a nuclear power plant at night, with a large cooling tower emitting steam, illuminated against a dark sky. The plant is reflected in a body of water in the foreground.

Effects of Radiation on Nuclear Materials and the Nuclear Fuel Cycle

24th Volume

Guest Editors

Jeremy T. Busby
Brady Hanson

Journal of ASTM International
Selected Technical Papers STP1513
**Effects of Radiation on Nuclear Materials
and the Nuclear Fuel Cycle:
24th Volume**

JAI Guest Editors:

Jeremy T. Busby
Brady D. Hanson



INTERNATIONAL
Standards Worldwide

ASTM International
100 Barr Harbor Drive
PO Box C700
West Conshohocken, PA 19428-2959

Printed in the U.S.A.

ASTM Stock #: STP1513

Library of Congress Cataloging-in-Publication Data

ISBN: 978-0-8031-3425-6

ISSN: 1050 7515

Copyright © 2010 ASTM INTERNATIONAL, West Conshohocken, PA. All rights reserved. This material may not be reproduced or copied, in whole or in part, in any printed, mechanical, electronic, film, or other distribution and storage media, without the written consent of the publisher.

Journal of ASTM International (JAI) Scope

The JAI is a multi-disciplinary forum to serve the international scientific and engineering community through the timely publication of the results of original research and critical review articles in the physical and life sciences and engineering technologies. These peer-reviewed papers cover diverse topics relevant to the science and research that establish the foundation for standards development within ASTM International.

Photocopy Rights

Authorization to photocopy items for internal, personal, or educational classroom use, or the internal, personal, or educational classroom use of specific clients, is granted by ASTM International provided that the appropriate fee is paid to ASTM International, 100 Barr Harbor Drive, P.O. Box C700, West Conshohocken, PA 19428-2959, Tel: 610-832-9634; online: <http://www.astm.org/copyright>.

The Society is not responsible, as a body, for the statements and opinions expressed in this publication. ASTM International does not endorse any products represented in this publication.

Peer Review Policy

Each paper published in this volume was evaluated by two peer reviewers and at least one editor. The authors addressed all of the reviewers' comments to the satisfaction of both the technical editor(s) and the ASTM International Committee on Publications.

The quality of the papers in this publication reflects not only the obvious efforts of the authors and the technical editor(s), but also the work of the peer reviewers. In keeping with long-standing publication practices, ASTM International maintains the anonymity of the peer reviewers. The ASTM International Committee on Publications acknowledges with appreciation their dedication and contribution of time and effort on behalf of ASTM International.

Citation of Papers

When citing papers from this publication, the appropriate citation includes the paper authors, "paper title", J. ASTM Intl., volume and number, Paper doi, ASTM International, West Conshohocken, PA, Paper, year listed in the footnote of the paper. A citation is provided as a footnote on page one of each paper.

Foreword

THIS COMPILATION OF THE *JOURNAL OF ASTM INTERNATIONAL* (JAI), STP1513, on *Effects of Radiation on Nuclear Materials and the Nuclear Fuel Cycle: 24th Volume*, contains only the papers published in JAI that were presented at a symposium in Denver, CO from June 24–26, 2008 and sponsored by ASTM Committees E10 on Nuclear Technology and its Applications and C26 on the Nuclear Fuel Cycle.

The JAI Guest Editors are Jeremy T. Busby, Materials Science and Technology, Oak Ridge National Laboratory, Oak Ridge, TN, and Brady D. Hanson, Radiochemical Science and Engineering, Pacific Northwest National Laboratory, Richland, WA.

Contents

Overview	vii
International Atomic Energy Agency Coordinated Research Projects on Structural Integrity of Reactor Pressure Vessels	
W. L. Server and R. K. Nanstad	1
Analysis of the Belgian Surveillance Fracture Toughness Database Using Conventional and Advanced Master Curve Approaches	
E. Lucon, M. Scibetta, and R. Gérard	26
Final Results from the Crack Initiation and Arrest of Irradiated Steel Materials Project on Fracture Mechanical Assessments of Pre-Irradiated RPV Steels Used in German PWR	
H. Hein, E. Keim, H. Schnabel, T. Seibert, and A. Gundermann	40
Embrittlement Correlation Method for the Japanese Reactor Pressure Vessel Materials	
N. Soneda, K. Dohi, A. Nomoto, K. Nishida, and S. Ishino	64
Magnox Steel Reactor Pressure Vessel Monitoring Schemes—An Overview	
M. R. Wootton, R. Moskvic, C. J. Bolton, and P. E. J. Flewitt	93
Investigation of Beltline Welding Seam of the Greifswald WWER-440 Unit 1 Reactor Pressure Vessel	
H. W. Viehrig, J. Schuhknecht, U. Rindelhardt, and F. P. Weiss	114
Microstructural Characterization of RPV Materials Irradiated to High Fluences at High Flux	
N. Soneda, K. Dohi, K. Nishida, A. Nomoto, M. Tomimatsu, and H. Matsuzawa	128
Irradiation-Induced Grain-Boundary Solute Segregation and Its Effect on Ductile-to-Brittle Transition Temperature in Reactor Pressure Vessel Steels	
Y. Nishiyama, M. Yamaguchi, K. Onizawa, A. Iwase, and H. Matsuzawa	152
Irradiation-Induced Hardening and Embrittlement of High-Cr ODS Ferritic Steels	
J. H. Lee, R. Kasada, H. S. Cho, and A. Kimura	163
Kinetic Monte Carlo Simulation of Helium-Bubble Evolution in ODS Steels	
A. Takahashi, S. Sharafat, K. Nagasawa, and N. Ghoniem	175
Study of Microstructure and Property Changes in Irradiated SS316 Wrapper of Fast Breeder Test Reactor	
C. N. Venkiteswaran, V. Karthik, P. Parameswaran, N. G. Muralidharan, V. A. Raj, S. Saroja, V. Venugopal, M. Vijayalakshmi, K. V. K. Viswanathan, and B. Raj	195
Unusual Enhancement of Ductility Observed During Evolution of a “Deformation Wave” in 12Cr18Ni10Ti Stainless Steel Irradiated in BN-350	
M. N. Gusev, O. P. Maksimkin, I. S. Osipov, N. S. Silniagina, and F. A. Garner	209
Interrelationship between True Stress–True Strain Behavior and Deformation Microstructure in the Plastic Deformation of Neutron-Irradiated or Work-Hardened Austenitic Stainless Steel	
K. Kondo, Y. Miwa, T. Tsukada, S. Yamashita, and K. Nishinoiri	219
Influence of Neutron Irradiation on Energy Accumulation and Dissipation during Plastic Flow and Hardening of Metallic Polycrystals	
D. A. Toktogulova, M. N. Gusev, O. P. Maksimkin, and F. A. Garner	237

Comparison of CANDU Fuel Bundle Finite Element Model with Unirradiated Mechanical Load Experiments

T. J. Lampman, A. Popescu, and J. Freire-Canosa	251
Author Index	275
Subject Index	277

Overview

The Effects of Radiation on Materials series began in 1956 with a meeting jointly sponsored by the E-10 Committee (called the Committee on Radioisotopes and Radiation Effects at the time) and the Atomic Industrial Forum. In 1960, this symposium transitioned to its current format under the E-10 Committee and, for the past 44 years, this symposium has been an international forum. In this most recent meeting, over half of the presentations originated outside the United States with lead authors from eleven different countries. These proceedings reflect that international scope.

The 24th Symposium on the Effects of Radiation on Materials marked the first joint sponsorship between the E-10 and C-26 Committees. The expanded meeting scope was well received as the broader view provided an opportunity to examine radiation damage for the entire fuel cycle.

These proceedings continue the long-established strength and depth of the Effects of Radiation on Materials series. Papers on radiation effects in reactor pressure vessel steels are again an integral component with specific topics ranging from surveillance programs around the world to detailed characterization of irradiated microstructures. Radiation effects in oxide-dispersion strengthened alloys and austenitic stainless steels are also included with several papers highlighting renewed interest in non-uniform deformation in these steels. The balance of the papers covers a diverse set of radiation-effects topics, ranging from modeling helium bubbles to finite-element modeling of fuel bundles.

The editors wish to express our gratitude to all of the reviewers, who are a vital component in a publication of this quality. The ASTM staff also played a key role in the production of these proceedings. Finally, and most importantly, we would like to thank the symposium presenters and authors for their participation and dedication to this series.

Jeremy T. Busby
Oak Ridge National Laboratory

Brady D. Hanson
Pacific Northwest National Laboratory

William L. Server¹ and Randy K. Nanstad²

International Atomic Energy Agency Coordinated Research Projects on Structural Integrity of Reactor Pressure Vessels

ABSTRACT: The International Atomic Energy Agency (IAEA) has conducted a series of coordinated research projects (CRPs) that have focused on irradiated reactor pressure vessel (RPV) steel fracture toughness properties and approaches for assuring structural integrity of RPVs throughout operating life. A series of nine CRPs has been sponsored by the IAEA, starting in the early 1970s, focused on neutron radiation effects on RPV steels. The purpose of the CRPs was to develop comparisons and correlations to test the uniformity of irradiated results through coordinated international research studies and data sharing. Consideration of dose rate effects, effects of alloying (nickel, manganese, silicon, etc.) and residual elements (e.g., copper and phosphorus), and drop in upper shelf toughness is also important for assessing neutron embrittlement effects. The ultimate use of embrittlement understanding is assuring structural integrity of the RPV under current and future operation and accident conditions. Material fracture toughness is the key ingredient needed for this assessment, and many of the CRPs have focused on measurement and application of irradiated fracture toughness. This paper presents an overview of the progress made since the inception of the CRPs in the early 1970s. The chronology and importance of each CRP have been reviewed and put into context for continued and long-term safe operation of RPVs.

KEYWORDS: reactor pressure vessels, fracture toughness, master curve, radiation embrittlement, Charpy impact, nickel, copper, PWR, WWER

Manuscript received August 25, 2008; accepted for publication June 2, 2009; published online August 2009.

¹ ATI Consulting, Pinehurst, NC 28374.

² Oak Ridge National Laboratory, Oak Ridge, TN 37831.

Cite as: Server, W. L. and Nanstad, R. K., "International Atomic Energy Agency Coordinated Research Projects on Structural Integrity of Reactor Pressure Vessels," *J. ASTM Intl.*, Vol. 6, No. 7. doi:10.1520/JAI102096.

Copyright © 2009 by ASTM International, 100 Barr Harbor Drive, PO Box C700, West Conshohocken, PA 19428-2959.

Introduction

A series of nine coordinated research projects (CRPs) has been sponsored by the International Atomic Energy Agency (IAEA), starting in the early 1970s, and was focused on neutron radiation effects on reactor pressure vessel (RPV) steels. In conjunction with the CRPs, information exchanges have included many consultants' meetings, specialists' meetings, and international conferences dating back to the mid-1960s. In 1972, 25 countries operated water cooled type reactors. Individual studies on the basic phenomena of radiation hardening and embrittlement were performed in these countries to better understand increases in tensile strength and shifts to higher temperatures for the ductile-brittle transition temperature. The purpose of the CRPs was to develop correlative comparisons to test the uniformity of results through coordinated international research studies and data sharing.

Two basic mechanisms of irradiation embrittlement, which result in radiation hardening and shifts in transition temperature, have been identified: (1) matrix damage (MD) due to irradiation-produced point defect clusters and dislocation loops and (2) irradiation-enhanced formation of copper-enriched clusters in RPV steels containing residual amounts of copper. The understanding and modeling of these mechanisms have evolved over the past 40 years, and sophisticated embrittlement correlations have been developed that incorporate the knowledge of these mechanisms. Non-hardening embrittlement, such as segregation of phosphorus to grain boundaries leading to intergranular-type fracture, is another mechanism important for a few steels but generally is not considered a significant mechanism for most RPV steels. Considerations of dose rate effects, effects of alloying elements (nickel, manganese, silicon, etc.) and residual elements (copper and phosphorus), and drop in upper shelf toughness are also important for assessing neutron embrittlement effects.

The ultimate use of embrittlement understanding is application to assure structural integrity of the RPV under current and future operation and accident conditions. Material fracture toughness is the key ingredient needed for this assessment, and many of the CRPs have focused on measurement and application of irradiated fracture toughness.

IAEA CRPs

A summary of the knowledge gained and key accomplishments from each of the nine CRPs is presented next. Emphasis has been centered on the most recent CRPs since they provide the most current understanding of embrittlement and utilize direct measurements of irradiated fracture toughness when possible.

IAEA CRP-1, Irradiation Embrittlement of Reactor Pressure Vessel Steels

The first two CRPs had ten organizations from nine different IAEA Member States participating and were devoted to the measurement and understanding of neutron radiation embrittlement of RPV steels. In the 1970s and 1980s, the determination of the degree of embrittlement involved an indirect approach

using Charpy V-notch impact tests to measure transition temperature shifts. The first CRP was initiated in 1971 based on the recommendation from the IAEA Working Group on Engineering Aspects of Irradiation Embrittlement of Reactor Pressure Vessel Steels. This initiating CRP focused on standardization of methods for measuring embrittlement in terms of both mechanical properties and the neutron irradiation environment. A reference steel plate was chosen, which was ASTM A533 Grade B Class 1 [Heavy Steel Section Technology (HSST) 03 Plate] from the HSST Program and provided to the IAEA by Union Carbide Corporation (contractor for Oak Ridge National Laboratory at that time), USA, and this material was irradiated in different reactors.

The main goals were (1) to establish if the basis for describing embrittlement and for performing the measurement of neutron spectrum, fluence, and mechanical properties was sufficiently standardized to permit direct intercomparison between international programs without major adjustment of the data and (2) to compare the embrittlement sensitivity of national steels with that of the reference steel.

Comparisons were made using irradiation embrittlement and hardening results from different reactors. Also, investigations of the benefits of post-irradiation annealing for restoration of initial properties, especially the hardness and strength, of irradiated samples were conducted, and advancements in fracture toughness methodology were integrated into the program.

No major discrepancies were observed in the results in spite of the use of unique irradiation rig assemblies in nine different reactors with individual evaluations of neutron fluence and neutron spectra. Differences in mechanical test procedures and data interpretation might also have produced complications in the comparison and analysis of data. In fact, this proved not to be true, and the variations in the results were more likely due to neutron environmental measurement differences, some partly due to differences related to irradiation temperature and type of moderator (light water or heavy water). It was believed that further adjustments of experimental data for neutron spectrum variations or flux determination may reduce the scatter.

Several investigators irradiated steel specimens derived from other sources in addition to the standard steel used for the program. These additional tests were found to be particularly useful since the relative uniformity of the results on the standard material could be used as a basis for direct comparison. It was recommended that such comparison should be encouraged so as to increase the database on irradiation embrittlement of RPV steels.

One of the outcomes from CRP-1 was the confirmation that specific residual elements, namely, copper and phosphorus, enhance the irradiated embrittlement of RPV steels. Details of the breadth of CRP-1 are contained in a special IAEA report, IAEA-176 [1].

IAEA CRP-2, Analysis of the Behavior of Advanced Reactor Pressure Vessel Steels under Neutron Irradiation

After a detailed review of CRP-1, it was decided to initiate a new CRP. The general goal was to demonstrate that knowledge had advanced to the point that steel manufacture and welding for nuclear technology could routinely produce

steels for RPVs of high radiation damage resistance. CRP-2 involved testing and evaluation, by various countries, of RPV steels that had reduced residual elements of copper and phosphorus. Irradiations were conducted to fluence levels beyond expected end-of-life. In addition to Charpy transition temperature testing, some emphasis was placed on using tensile and early-design fracture toughness test specimens and applying elastic-plastic fracture mechanics. Progress was achieved in reducing scatter in neutron dosimetry methods.

Many organizations and countries provided steels for CRP-2, and during 1977–1979, the participants received test materials from advanced steels and welds typical for current practice in France, the Federal Republic of Germany, and Japan. These included

- (1) plate ASTM A533-B, Cl.1 from Nippon Steel Corporation, Japan, and Marrel-Creusot-Loire, France (HSST Plate 03 was also available from CRP-1);
- (2) forging ASTM A508 Cl.3 from Japan Steel Works, Japan, and Framatome, France; and
- (3) submerged-arc welds from Mitsubishi Heavy Industries, Ltd., Japan, Framatome, France, and Thyssen AG, Federal Republic of Germany.

The main goal was to undertake a comparative study of the irradiation embrittlement behavior of improved (advanced) steels produced in various countries. It was intended to demonstrate that careful specification of pressure vessel steel could eliminate or vastly reduce the issue of neutron irradiation embrittlement, and to show that knowledge had advanced to the point where steel manufacture and welding technology could routinely produce steel RPVs of high radiation damage resistance. The program was also designed to study effects of neutron irradiation to neutron fluences well beyond normal operating life for reactors currently in operation, and to allow comparison of the mechanical properties after irradiation of improved plates, welds, and forging steels of RPV grades produced from various sources.

Within this program, which lasted from 1977 to 1983, the following key conclusions were obtained.

- (1) These modern pressure vessel materials (plates, forgings, and welds) possess relatively high resistance to neutron irradiation damage.
- (2) Reducing the copper content (together with low phosphorus content) of steels leads to an improvement in their irradiation resistance. The copper content of these modern steels is usually less than 0.1 wt %, while phosphorus content is usually lower than 0.012 wt %. Charpy transition temperature shifts of the modern steels were generally lower than those steels represented by the HSST 03 Plate.
- (3) Changes in tensile yield strength and hardness followed the Charpy transition temperature changes, and the results support the recommendation to include tensile tests in any scheme to measure irradiation damage sensitivity; hardness testing also could be utilized with adequate validation.
- (4) There was no systematic variation in Charpy upper shelf energy change (decrease) with neutron fluence. The actual levels of upper shelf energy for the modern steels were higher than those typified by the HSST 03 Plate.

- (5) The results of fracture toughness tests showed that modern steels are more resistant to neutron irradiation than the older pressure vessel steels. A good correlation was observed between the Charpy 41 J transition temperature increase on irradiation and the shift in transition temperature, defined at the 100 MPa·m^{1/2} level (the same as used in the master curve methodology described later), from dynamic and static fracture toughness tests. No reasonable correlation was found between Charpy upper shelf energy decrease after irradiation and that determined from dynamic or static upper shelf fracture toughness determination.

Further progress in the application of the fracture mechanics approach to radiation damage assessment was achieved in this program. Improvements and unification of neutron dosimetry methods provided better data with reduced scatter. All results, analyses, and raw data were summarized in IAEA Technical Report Series (TRS) No. 265 [2]. A summary paper by Steele et al. documented the results for both CRP-1 and CRP-2 [3].

IAEA CRP-3, Optimizing Reactor Pressure Vessel Surveillance Programs and Their Analyses

The third CRP involved 24 organizations from 18 IAEA Member States and was initiated in June 1983. This CRP included direct measurement of fracture toughness using irradiated surveillance specimens. The principal goal of CRP-3 was to optimize RPV surveillance programs and related methods of analysis for international application. One key objective was to consolidate the now increasing body of knowledge on neutron radiation embrittlement and the technique used to determine its significance. It was intended to establish guidelines for surveillance testing, which could then be used internationally. There was a focus on advancing quantitative fracture mechanics methodologies and assuring the extrapolation of qualitative ductile-to-brittle transition temperature methods, which were predominately used in reactor vessel surveillance.

More than 20 steels were chosen for the irradiation and fracture toughness study. Primary interest was centered upon a group of Japanese laboratory melts to assess composition effects and on a “radiation sensitive” correlation monitor heat from Japan. A crucial recommendation was to provide the latter steel to serve as a reference material for this program and for future research and surveillance programs throughout the world. This reference material involved the procurement of a 20–25 ton heat of steel, designated as JRQ, produced as a special heat by Kawasaki Steel Corporation in Japan. The baseline properties and fabrication details for the JRQ heat were documented in IAEA TECDOC-1230 [4]. This heat has proven to be a good reference steel for irradiation studies.

More than 60 irradiated Charpy curves were tested as a part of this program on three groups of materials: (1) materials of “advanced quality” characterized by a low quantity of detrimental elements like copper and phosphorus; these materials have been used in RPVs fabricated in the 1980s; (2) materials of “poor quality” prepared only for this program; these materials represented RPVs of so-called “first generation” with high contents of copper and phos-

phorus; and (3) experimental steels prepared for this program to study the effects of detrimental elements and their synergistic interaction (copper, phosphorus, and nickel).

The following are the main conclusions from CRP-3.

- (1) Results from this CRP show that there are comparable knowledge, experience, irradiation, and testing facilities in the Member States to create a world-wide evaluation of the behavior of RPV steels under neutron irradiation exposure.
- (2) In general, mechanical test results are quite reproducible, and the data are suitable for a reliable assessment of RPV life.
- (3) Creation of a database of all experimental results obtained within the program has proven to be essential for a detailed analysis of all the data.
- (4) Testing of “old” and “advanced” types of materials illustrated a decreasing material susceptibility to radiation damage by decreasing phosphorus and copper contents in the advanced materials. Study of the embrittling effects of phosphorus, copper, and nickel contents on specially prepared experimental heats has provided further insight and validation of some models on radiation damage.
- (5) Transition temperature shifts from Charpy impact testing showed practically identical results independent of the indexing parameter (i.e., 41 J shift, 68 J shift, and 0.89 mm lateral expansion shift), while static fracture toughness transition temperature shifts (at 100 MPa·m^{1/2}) produce, in general, larger shifts than from Charpy impact testing.
- (6) The JRQ steel (with high copper and phosphorus contents) was tested by all participants, and this material has been validated for use as a “reference steel” for future surveillance, as well as research irradiation programs. JRQ has been found to be fairly homogenous with reproducible results.
- (7) Progress in neutron dosimetry resulted in better instrumentation and characterization of irradiation experiments; however, the uncertainty in neutron fluence determination can still be greater than about 30 %. Note that even with this high degree of uncertainty and data scatter, some transition temperature results appear to be anomalous.
- (8) Progress in the application of the fracture mechanics approach to radiation damage assessment was achieved. Further improvement and unification of the test and analysis method can provide an efficient way for improving precision and reliability of RPV life evaluation based on surveillance specimen programs. Improvement and unification of neutron dosimetry methods have provided better data with reduced scatter of data, but further steps still seem to be necessary.

IAEA CRP-4, Assuring Structural Integrity of Reactor Pressure Vessels

The main emphasis during CRP-4, which began in 1995, was the experimental verification of the Master Curve approach for surveillance size specimens. This CRP involved 24 organizations from 19 Member States and was directed at confirmation of the measurement and interpretation of fracture toughness

using the Master Curve method with structural integrity assessment of irradiated RPVs as the ultimate goal. The Master Curve approach using small size specimens, such as precracked Charpy (PCC), was shown to be adequate for producing valid values of fracture toughness in the transition temperature region. The main material tested was JRQ reference steel, but additional testing was conducted on other “national” materials.

The main aim of the extensive testing was to verify the application of the Master Curve using small fatigue PCC specimens suitable for RPV surveillance programs. The key conclusions from CRP-4 are the following.

- (1) In general, the JRQ steel was found to be relatively homogeneous and suitable for experimental programs as a reference material if strict requirements to specimens' location and orientation are satisfied.
- (2) No difference in the scatter of resulting T_0 values has been found between different laboratories; also, investigations of a test temperature dependence did not show any deviations in the results, thus supporting use of a multi-temperature methodology.
- (3) The guidance for a test temperature for fracture toughness testing based on Charpy impact results was investigated relative to the correlation in the Draft ASTM E1921 test method: $T_{28 J} - 50^\circ\text{C}$. The measured data for the JRQ steel show a difference between $T_{28 J}$ and T_0 equal to -35°C .
- (4) The “Master Curve” approach can be applied to a wide set of national light water reactor RPV materials, as well as steels used in the Russian design water-water energetic reactor (WWER).
- (5) The Master Curve approach also can be applied for dynamic fracture toughness testing, resulting in significant differences in static and dynamic T_0 values. Transition temperature shifts derived from static fracture toughness tests seem to be higher than impact notch toughness tests.
- (6) Transition temperatures from impact tests ($T_{28 J}$, $T_{41 J}$, and $T_{68 J}$) correlate well with transition temperatures T_0 in the whole range of tested materials.
- (7) It was demonstrated that small specimens (Charpy size and even smaller) can be used for determination of valid values of fracture toughness of materials in the transition temperature region. It also was demonstrated that the Master Curve approach is fully applicable for these RPV materials, test specimens, and material conditions using either single or multiple temperature methods.

IAEA CRP-5, Surveillance Program Results Application to Reactor Pressure Vessel Integrity Assessment

The fifth CRP was titled “Surveillance Program Results Application to Reactor Pressure Vessel Integrity Assessment,” and 24 organizations from 15 Member States participated. This CRP had a first objective to develop a large database of fracture toughness data using the Master Curve methodology for both PCC (10 mm² square cross section three-point bend test specimens) and 25.4 mm (1 in.) thickness compact tension fracture specimens (1T-CT). Second, CRP-5 was

chartered to develop international guidelines for measuring and applying Master Curve fracture toughness results for RPV integrity assessment.

The results from CRP-5 show clear evidence that lower values of unirradiated T_0 are obtained using PCC specimens as compared to results from 1T-CT specimens. This bias in test results is very important when considering use of PCC specimens in evaluating RPV integrity. International guidelines also were written and provide a framework for using small surveillance fracture toughness specimens to assess the integrity of RPVs.

This CRP created two deliverables: (1) a large database of Master Curve fracture toughness data generated by many laboratories, primarily focused on one RPV material, heat JRQ (see IAEA TECDOC 1435 [5]) and (2) the development of international guidelines for applying Master Curve fracture toughness results for RPV integrity assessment (see IAEA TRS 429 [6]). A flow chart from TRS 429 delineating the various paths needed to utilize Master Curve fracture toughness results for assessing RPV integrity is shown in Fig. 1. Also indicated are the various text sections of TRS 429 [6].

Figure 2 illustrates the results generated for the PCC and 1T-CT specimens. The obvious difference in the value of the Master Curve transition temperature T_0 is an issue that has been mentioned in the ASTM Standard E1921 for the determination of T_0 . This bias remains an issue that still needs further characterization and understanding and will be assessed in more detail in topic area 1 in CRP-8.

Another topic area that was identified (and pursued further in CRP-8 to a broader range of loading rates) was that of loading rate effects on T_0 even in the range of acceptable values specified in ASTM E1921. Changes were made in ASTM E1921, restricting the range of loading rates allowed for determining valid quasi-static T_0 values (stress intensity rate of 0.1–2 MPa·m^{1/2}/s), in response to recommendations from the participants in this CRP.

IAEA CRP-6, Mechanism of Ni Effect on Radiation Embrittlement of RPV Materials

CRP-6 was focused on WWER-1000 and pressurized water reactor (PWR) RPV steels with high Ni contents. Eleven institutes from ten Member States participated in this CRP, with irradiation experiments of the CRP WWER-1000 RPV materials being conducted by six of the institutes. In addition to the irradiation and testing of those materials, irradiation experiments of various national steels also were conducted. Moreover, some institutes performed microstructural investigations of both the CRP materials and national steels. It has been known that high levels of nickel can have a synergistic effect with copper and phosphorus increasing the radiation sensitivity of RPV steels. Some Russian WWER-1000 RPV steels have higher levels of nickel than used in typical western steels. The radiation sensitivity of the higher nickel WWER steels was evaluated through a small round robin exercise and collection of data. Two major observations from this CRP were (1) analyzed results clearly show significantly higher radiation sensitivity of high nickel weld metal (1.7 wt %) compared with lower nickel base metal (1.2 wt %) and (2) for a given high level of nickel in the steel and all other factors being equal, high manganese content

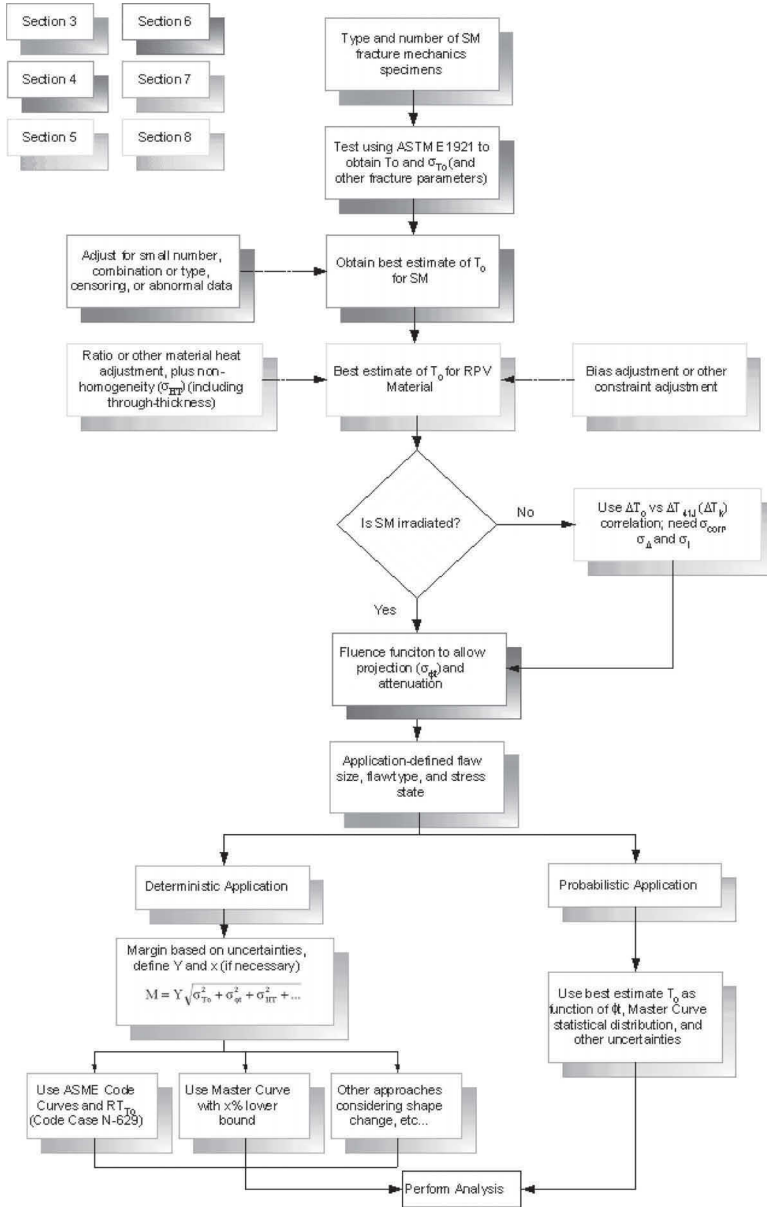


FIG. 1—IAEA guidelines for implementation of master curve [6].

leads to much greater irradiation-induced embrittlement than low manganese content for both WWER-1000 and PWR materials. The results from CRP-6 were published in IAEA-TECDOC-1441 [7].

To conduct the experimental investigations regarding nickel influence on

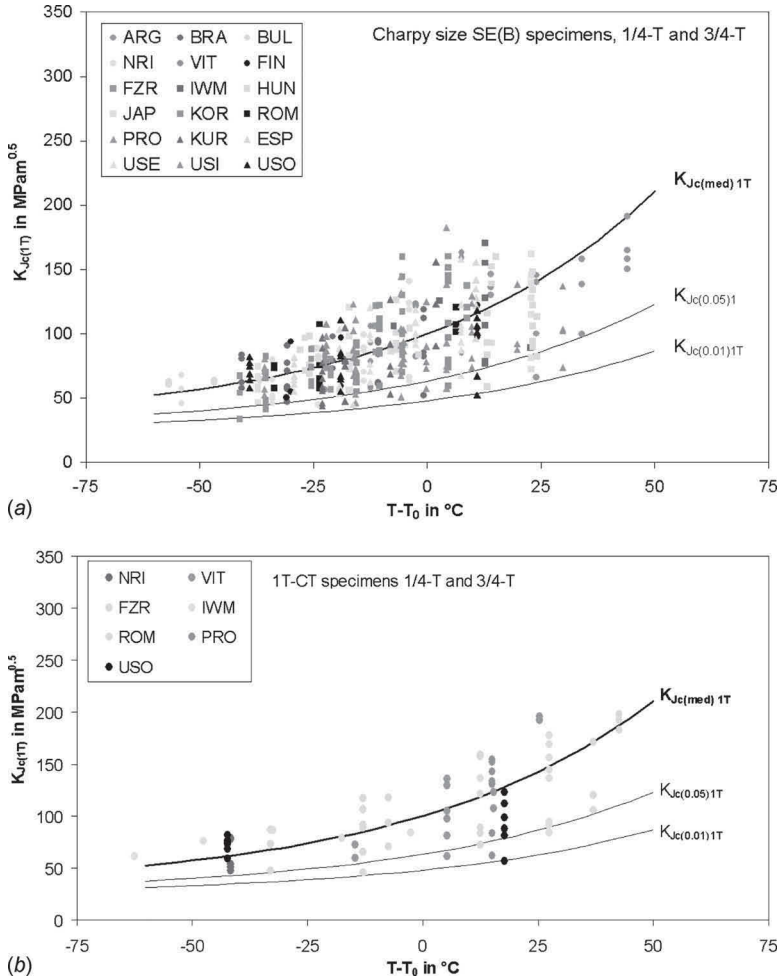


FIG. 2—Fracture toughness (K_{Jc}) values and master curve for: (a) PCC specimens and (b) 1T-CT specimens from the 1/4-T and 3/4-T locations of the JRQ plate tested by different laboratories [5].

radiation embrittlement of WWER-1000 RPV metals, the Russian Research Centre “Kurchatov Institute” (RRC KI) offered two materials with different nickel content, one base metal (1.2 wt %) and one weld metal (1.7 wt %). Standard Charpy V-notch (CVN) impact specimens were prepared and distributed by RRC KI to participants of the project. Participants in the irradiation phase of the CRP were requested to irradiate the specimens to a neutron fluence not less than the neutron fluence on the inside wall of the WWER-1000 RPV at the end of its design lifetime [$\sim 6 \times 10^{23} n \cdot m^{-2}$ ($E > 0.5$ MeV)] and at the temperature that corresponds to the beltline region of the WWER-1000 RPV (290°C). A

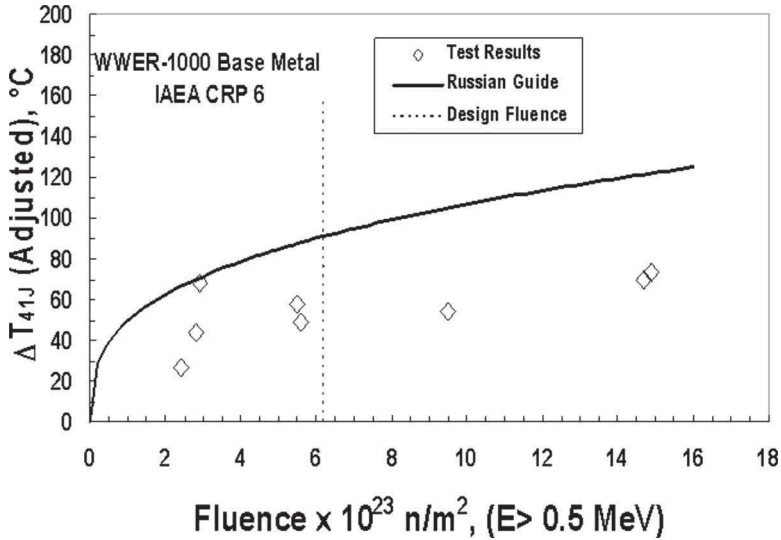


FIG. 3—Fluence dependence of ΔT_{41J} for WWER-1000 base metal (using $T_{41J-ADJ} = -83^{\circ}\text{C}$) [7].

total of 48 CVN specimens, 12 for testing of each material in both unirradiated and irradiated conditions, were provided to each participant.

By choice of the individual participants, some of the irradiations were conducted in power reactors and some in research reactors, with fast neutron fluxes varying from 5.1×10^{15} to $5.0 \times 10^{17} \text{ n} \cdot \text{m}^{-2} \cdot \text{s}$ ($E > 0.5 \text{ MeV}$). Moreover, the total exposures varied from 2.4×10^{23} to $14.9 \times 10^{23} \text{ n} \cdot \text{m}^{-2}$ ($E > 0.5 \text{ MeV}$), providing the opportunity to evaluate the embrittlement as a function of fluence (no attempt was made to evaluate effects of flux with the limited data available). In the unirradiated condition, considerable scatter was observed from the participants' results for the base metal, but much less scatter was obtained for the weld metal. To investigate the potential effect of scatter in the Charpy 41-J energy temperature (T_{41J-UN}) values, the mean T_{41J-UN} of the individual values obtained in the different laboratories was used to calculate an adjusted value, ($T_{41J-ADJ}$), of the irradiation-induced shift $\Delta T_{41J-ADJ}$. Figures 3 and 4 show the $\Delta T_{41J-ADJ}$ versus fluence for the base metal and weld metal, respectively, compared with the predictive curves from the Russian Guide. The following equation represents the predicted upper bound for irradiated RPV steels in the Russian Guide PNAE-86 [8]:

$$T_{41J} = A_F(F/F_0)^{1/3}, \quad (1)$$

where:

- $A_F = 23$ for base metal and 20 for weld metal,
- $F =$ neutron fluence ($\text{n} \cdot \text{cm}^{-2}$; $E > 0.5 \text{ MeV}$), and
- $F_0 = 10^{18} \text{ n} \cdot \text{cm}^{-2}$ ($E > 0.5 \text{ MeV}$).

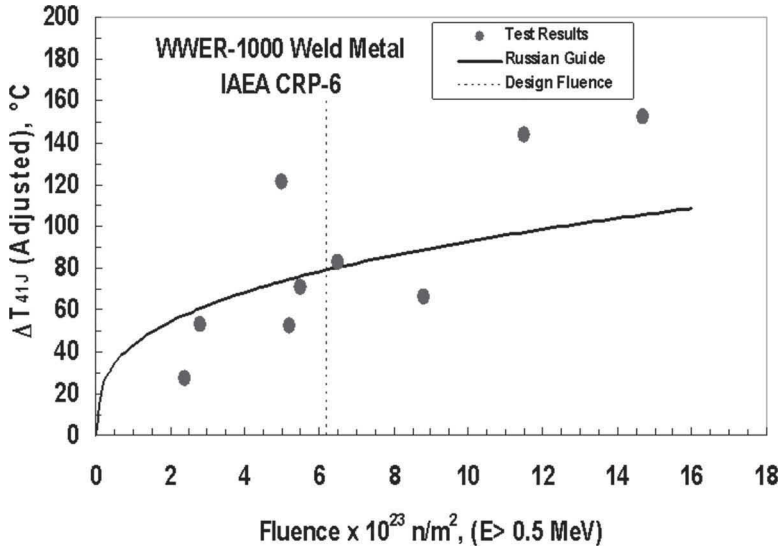


FIG. 4—Fluence dependence of ΔT_{41J} for WWER-1000 weld metal (using $T_{41J-ADJ} = -55^{\circ}\text{C}$) [7].

As shown in Fig. 3, all the irradiation-induced shifts are less than the Russian Guide predictive curve for base metal, but Fig. 4 shows that some results for the weld metal at relatively high fluence are greater than the curve predicted by the Russian Guide. However, regardless of the increased sensitivity of the CRP WWER-1000 high nickel weld metal (1.7 wt %), all but one of the transition temperature shifts at fluences lower than the WWER-1000 RPV design (40 years) fluence; $\sim 6 \times 10^{23} \text{ n} \cdot \text{m}^{-2}$ ($E > 0.5 \text{ MeV}$)³ are still below the predicted curve from the Russian Guide.

Figure 5 shows that there is a clear effect of nickel and a clear difference in embrittlement versus fluence between the base metal and the weld metal. Since the contents of copper and phosphorus are very low and practically identical in the two materials, the higher irradiation-induced embrittlement exhibited by the weld metal is attributed to its much higher nickel content, 1.7 wt % versus 1.2 wt %. As with transition temperature shifts, the higher nickel weld metal shows the greatest irradiation-induced decreases in upper shelf energies, although the lowest energy measured was a respectable 79 J at the very high fluence of $14.7 \times 10^{23} \text{ n} \cdot \text{m}^{-2}$ ($E > 0.5 \text{ MeV}$).

Other results provided in the CRP [7] for model alloys and other high nickel steels, including those for western type PWRs, corroborate the observations of the effects of nickel observed for the WWER-1000 materials discussed above. Thus, the results validate the predictive formulas for the PWR type steels,

³Personal correspondence from Dr. A. A. Chermobaeva. Fluence for core welds (three and four) is 5.6×10^{23} and for core shell fluence is $6.4 \times 10^{23} \text{ n} \cdot \text{m}^{-2}$ ($E > 0.5 \text{ MeV}$).

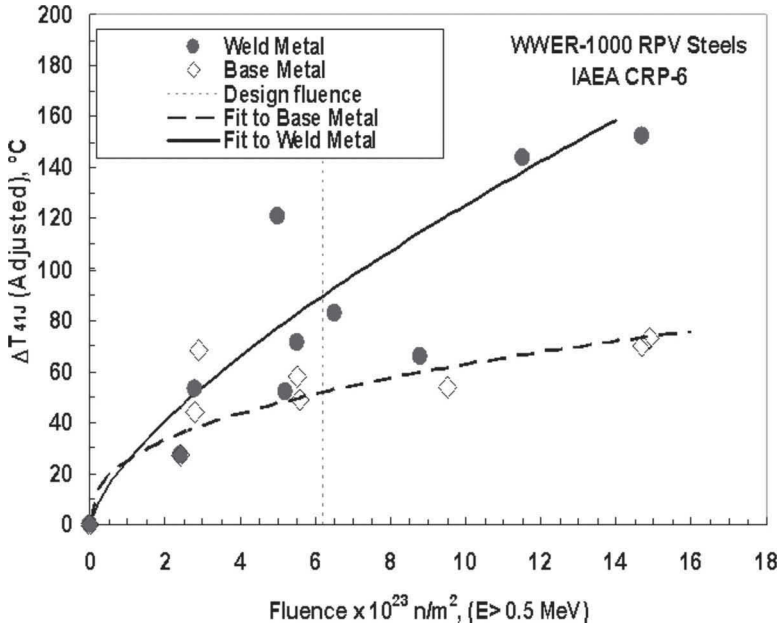


FIG. 5—Fluence dependencies of $\Delta T_{41 \text{ J-ADJ}}$ for WWER-1000 base and weld metals (using adjusted $T_{41 \text{ J-ADJ}}$ values) [7].

which contain nickel content as a primary variable. However, the predictive formula for WWER-1000 RPV materials does not include nickel content as a variable.

Another very significant observation from this CRP regards the synergistic effects of manganese. Data from various participants demonstrated that for a given high level of nickel in the material, and all other factors being equal, high manganese content leads to much greater embrittlement than low manganese content [7]. In addition to the effect of manganese on the WWER-1000 steels, results for steels with nickel content as high as 3.5 wt %, about two times higher than the WWER-1000 weld metal used for this CRP, showed that a super-clean steel with high nickel, but with only 0.02 wt % manganese and 0.03 wt % copper, demonstrated quite low radiation sensitivity [7,9].

In addition to mechanical property results, various microstructural investigations of high nickel steels were conducted, and the results were included in the CRP. The microstructural methods used were atom probe tomography (APT), positron annihilation, and small-angle neutron scattering. Examples of APT results for a high nickel WWER-1000 weld metal and a high nickel PWR steel are shown in Fig. 6(a) and 6(b), respectively [7]. Note that the WWER-1000 microstructure shown is from a specimen at a relatively low fluence of $2.4 \times 10^{23} \text{ n} \cdot \text{m}^{-2}$ ($>0.5 \text{ MeV}$).

From this and other such results, the role of nickel appears to be synergistic with copper in producing copper-enriched precipitates that evolve first as non-random fluctuations to embryos to clusters and then to precipitates. How-

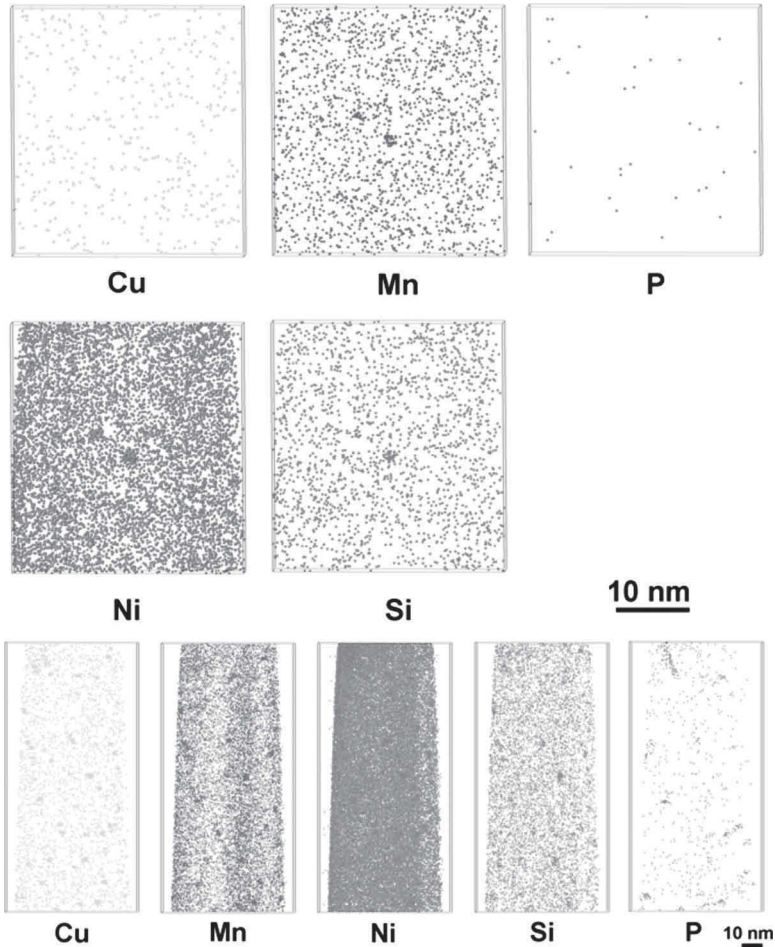


FIG. 6—Atom maps from APT analysis of (a) WWER-1000 weld metal irradiated to $2.4 \times 10^{23} \text{ nm}^{-2}$ ($>0.5 \text{ MeV}$) showing Mn, Ni, and Si in nanoclusters, and (b) high Cu content A533B weld metal irradiated to $\sim 3 \times 10^{23} \text{ nm}^{-2}$ ($>1 \text{ MeV}$) showing a high number density of Cu-, Mn-, Ni-, Si-, and P-enriched nanoprecipitates [10].

ever, the situation is very complex, and there is also an important effect of Mn (and possibly Si) coupled with Ni, even for low Cu steels. When there is very little Mn, even for very high Ni content steels, the available data indicate that very little embrittlement occurs. Thus, high Ni, when not combined with Cu and moderate Mn, does not appear to be a serious embrittling agent.

The main conclusions from CRP-6 and described in IAEA-TECDOC-1441 [7] are as follows.

- (1) The analyzed results are clear in showing the significantly higher radiation sensitivity of the high nickel weld metal (1.7 wt %) compared with the lower nickel base metal (1.2 wt %). These results are supported by

other similar results in the literature for WWER-1000 RPV materials, PWR-type materials, and model alloys.

- (2) Regardless of the increased sensitivity of the CRP WWER-1000 high nickel weld metal (1.7 wt %), the transition temperature shifts at fluences lower than the WWER-1000 RPV design fluence are still below the predicted curve from the Russian Guide.
- (3) Although manganese content was not incorporated directly in this CRP, results from tests of national steels demonstrated that for a given high level of nickel in the material and all other factors being equal, high manganese content leads to much greater irradiation-induced embrittlement than low manganese content for both WWER-1000 and PWR materials.
- (4) Microstructural investigations have shown, for both WWER-1000 and PWR materials, that nickel associates with copper in the irradiation-induced copper-enriched precipitates and that manganese (and sometimes silicon) is similarly associated.
- (5) Experimental results and microstructural investigations for a very high nickel steel (~ 3.5 wt %) have indicated that when there is very little manganese and low copper, the radiation sensitivity is very low even for such a high nickel steel.

Following the conclusion of CRP-6 and publication of the final report [7], additional APT experiments of the WWER-1000 base and weld metals irradiated at the higher fluences were conducted by Oak Ridge National Laboratory in collaboration with researchers from RRC KI. That study observed high number densities of ~ 2 -nm-diameter Ni-, Si-, and Mn-enriched nanoclusters in both materials, and no copper enrichment of the nanoclusters or copper-enriched precipitates was observed. The number density of the nanoclusters increased with increasing fluence, but the average size of the nanoclusters did not change significantly. The nanoclusters were present following a post-irradiation anneal of 2 h at 450°C, but not after 24 h at 450°C, indicating that the nickel, silicon, and manganese had all dissolved into the matrix. Moreover, phosphorus, nickel, silicon, and to a lesser extent manganese, were observed segregated to dislocations [10].

IAEA CRP-7, Prediction of Irradiation Embrittlement of Operating WWER-440 RPVs

The seventh CRP was focused on WWER-440 steels and the need for an improved predictive embrittlement correlation. In this study, a group of eight representatives from seven Member States developed new correlations for WWER-440 RPVs that provide better predictive capabilities based on chemical content and neutron exposure. These new correlations were developed in a framework that better simulates the known embrittlement mechanisms for these steels and was published in IAEA-TECDOC-1442 [11]. The CRP was accomplished through the completion of four tasks: (1) collection of WWER-440 surveillance and other relevant data and input into the IAEA International Database on RPV Materials (IDRPVM), (2) analysis of radiation embrittlement data of WWER-440 RPV materials using the IDRPVM database, (3) evaluation

of predictive formulae depending on material chemical composition, neutron flux and fluence, and (4) guidelines for prediction of radiation embrittlement of operating RPVs of WWER-440 including methodology for evaluation of surveillance data of a specific operating unit.

The CRP reviewed and compared three different procedures for evaluation of reactor surveillance data: (1) the Russian Code PNAE-86 [8], (2) U.S. Nuclear Regulatory Guide 1.99, Revision 2 [12], and (3) the VERLIFE procedure [13] developed within the European Union Fifth Framework program. All three procedures for predictions of RPV irradiation embrittlement are based on Charpy impact tests. However, only the VERLIFE procedure also allows the use of direct fracture toughness measurements to determine the properties of the aged RPV materials. In that regard, the Master Curve method specified in ASTM E1921-02 or the method developed by Prometey Institute in St. Petersburg, Russia, are cited [14].

For the irradiation embrittlement modeling part of the CRP activity, a relatively large Charpy impact surveillance data set for WWER-440 pressure vessel materials was collected. For fracture toughness data, however, only a limited number of data were collected; thus, the developed trend curve fitting performed in the CRP was based only on the Charpy impact data (also limited to data obtained with the ISO 2 mm radius striker). The weld data set consisted of a total of 121 data points, with 34 from low flux and 87 from high flux irradiations. The base metal data set consisted of 100 data points, with 24 from low flux and 76 from high flux irradiations. For the fitting investigations, three basic functions were used: (1) power law, (2) exponential, and (3) hyperbolic tangent (tanh). The data sets used for the fitting were characterized by the phosphorus and copper contents, neutron fluence, and neutron flux, where the neutron parameters are for $E > 0.5$ MeV. Five types of trial functions were used in fitting, one of which had the same form as the Russian Code formula for weld metal, and one was a function where a MD term was added to the form of the Russian Code formula.

Figure 7 shows all the experimental data plotted with the predicted ΔT_k versus the measured ΔT_k , showing very good agreement between the predicted shifts and the measured shifts. However, because a phosphorus threshold term equal to 0.015 mass % was considered rather high and not validated by independent methods, the CRP proposed, for practical purposes, a Russian Code type function in revised form. The formulae are given in Table 1.

The CRP-7 also evaluated WWER-440 fracture toughness data with the Master Curve. The evaluations demonstrated the applicability of the Master Curve shape for the WWER-440 RPV materials in both the unirradiated and irradiated conditions. Both the Charpy and fracture toughness results were used to develop guidelines for assessment of irradiation embrittlement of ferritic materials for operating WWER-440 RPVs. These guidelines incorporate two cases, one in which there are sufficient surveillance data and the other in which there are insufficient data. For the former case, the shift in brittle fracture transition temperature is determined with the equations shown in Table 1. If there are insufficient fracture toughness data available, then the Master Curve reference temperature T_0 of base and weld metals for the applicable fluence ($T_0^{\text{operation}}$) may be conservatively determined as

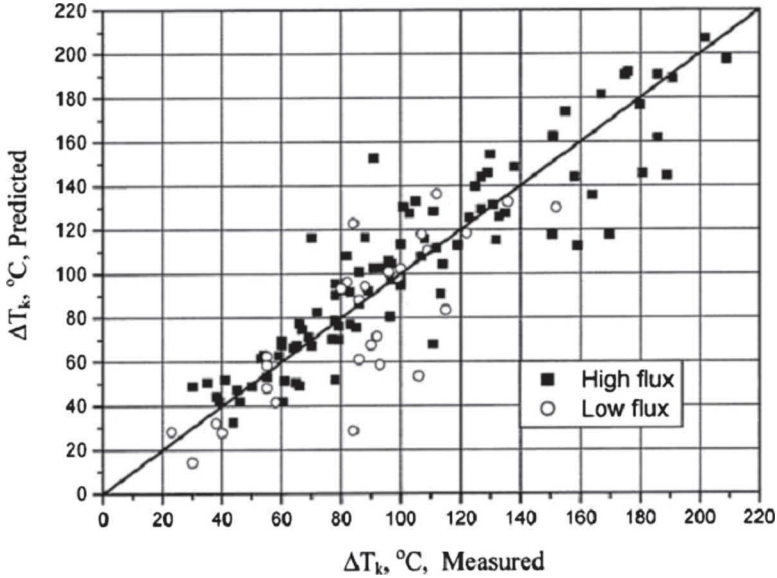


FIG. 7—Comparison of all experimental data from CRP-7 with predictions [11].

$$T_0^{operation} = T_0^{initial} + 1.1\Delta T_F, \tag{2}$$

where:

ΔT_F = determined Charpy impact 41 J temperature shift and

$T_0^{initial}$ = initial non-irradiated value of T_0 .

In all cases, a margin term based on the determined standard deviation for each case is applied to the calculated shift.

IAEA CRP-8, Master Curve Approach to Monitor the Fracture Toughness of Reactor Pressure Vessels in Nuclear Power Plants

CRP-8 is an extension of CRP-5 to address some of the outstanding issues associated with use of the Master Curve fracture toughness methodology. Fifteen organizations from 11 Member States have been involved in this CRP. The overall objectives of CRP-8 include (1) better quantification of fracture toughness issues relative to testing surveillance specimens for application to RPV

TABLE 1—Proposed formulae for WWER-440 steels for engineering use, valid for neutron fluences (Φ) in the range of $10^{22} < \Phi < 4 \times 10^{24}$ n·m⁻² ($E > 0.5$ MeV).

Metal	Formula	Standard Deviation (°C)
Weld metal	$\Delta T = [884 \times P + 51.3 \times Cu] \Phi^{0.29}$	22.6
	$= 800 \times (1.11 \times P + 0.064 \times Cu) \Phi^{0.29}$	
Base metal	$\Delta T = 8.37 \times \Phi^{0.43}$	21.7

integrity assessment and (2) development of approaches for addressing MC technical issues in integrity evaluation of operating RPVs. Since the Master Curve approach is applicable to all nuclear power plant ferritic steel components, including the RPV, the scope of materials addressed includes both RPV and non-RPV materials. The three topic areas investigated are described next; more detailed descriptions of the topic areas are available in Refs 15–17.

Test Specimen Bias, Constraint, and Geometry—A key consideration for RPV integrity is the understanding of constraint and bias between the sample specimen(s) being tested (generally of one geometry) and the flaw assumed to exist in the RPV. CRP-5 showed that lower values of unirradiated T_0 are obtained using PCC specimens as compared to results from 1T-CT specimens. For IAEA CRP-5, more than 300 PCC and 1T-CT specimens of A533B-1 steel (heat JRQ) were tested by different organizations; the T_0 based on the PCC specimens was 12°C lower than from the 1T-CT specimens. Moreover, many other RPV steels were tested and showed differences from 12 to 45°C (average of 22°C), with the three-point bend specimens giving the lower T_0 value in every case. There are many other examples in the literature that show similar results. Tests of one specific plate of A533 Grade B Class 1 steel showed the PCC specimens gave a T_0 value 37°C lower than that from 1T-CT specimens (i.e., bias of -37°C) [18]. The Wasiluk, Petti, and Dodds constraint correction [19] reduced the bias to -13°C for that material [18]. A more fundamental stress-strain analysis, which is dependent on the use of a finite element analysis of the specimen geometry, was also used to perform a constraint adjustment of the PCC results for Plate 13B and resulted in a bias of about -11°C. Thus, this more complicated procedure results in a bias for the PCC specimens of Plate 13B similar to the Wasiluk, Petti, and Dodds result of -13°C. Figure 8 shows a plot comparing T_0 results from PCC specimens and various sizes of CT specimens for the IAEA reference steel JRQ; all data shown were supplied by CRP-8 participants. Except for an apparent outlier indicated by the circle, this material shows an average bias of -11°C, similar to the result from testing of JRQ steel during CRP-5.

This bias in test results is very important when considering use of PCC specimens in evaluating RPV integrity. Questions regarding constraint limits for the MC method in general and the PCC specimen in particular, especially as a consequence of irradiation, must be resolved. The potential use of even smaller specimens highlights the significance of this issue, as evaluation of specimen size effects are needed to fully understand limits of applicability and associated uncertainties. A series of finite element round robin exercises was conducted to better quantify the differences in fracture toughness specimens relative to the RPV and their significance. For part one of the round robin, it was found that the ANSYS code produced systematically higher forces, but remaining differences for the other finite element codes were less than 3%. The second part of the round robin was used to evaluate the loss of constraint of each specimen and to compare the shallow and deep crack configuration. It was found that shallow crack specimens are more sensitive to loss of constraint than those with deep cracks for a given specimen size. The difference in terms of reference temperature was evaluated to be about 40°C, with the shallow

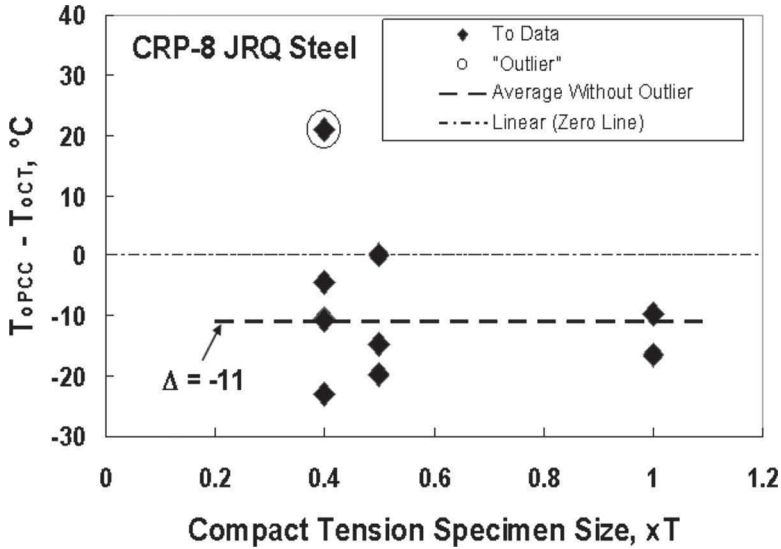


FIG. 8—Results from CRP-8 showing bias in T_0 between PCC and CT specimens of IAEA reference steel JRQ.

crack case giving the lower T_0 . For deep crack specimens, loss of constraint was identified to appear at M values around 200 [15]. These results are consistent with others reported in the literature.

Effect of Loading Rate—ASTM Standard Test Method E1921-02 was the basis for the fracture toughness testing and determination of T_0 for the surveillance test samples in CRP-5. Test results from different loading rates showed a difference in the measured T_0 values even within the allowable range in ASTM E1921-02, which was stated as the time to reach the elastic load P_M in the range from 0.1 and 10 min. These results were reported to the appropriate ASTM Committee for consideration in tightening the ASTM E1921 loading rate requirements, and ASTM E1921-05 has revised loading rate requirements for quasi-static loading to be within the range of stress intensity rates from 0.1 to 2 MPa·m^{1/2}/s.

In follow-up to these findings from CRP-5, CRP-8 further investigated the issue of loading rate effects. The effect of loading rate *within* the loading rate range specified in ASTM E1921-05 for quasi-static loading and the effect of loading rate for higher loading rates including impact conditions using PCC specimens tested with an instrumented pendulum were examined. A major focus was on dynamic instrumented impact loading, which includes a round robin exercise using the JRQ steel. Figure 9 shows the results from all the participants, with the Master Curve and tolerance bounds included. The T_0 determined from this data set is -4.2°C . The three data points from Laboratory 7 (plotted at -20 and -10°C above the 95 % curve) were considered to be outliers and a reanalysis of the data without those data resulted in a T_0 of -0.8°C . Similarly, a reanalysis of all the raw data by one laboratory resulted in

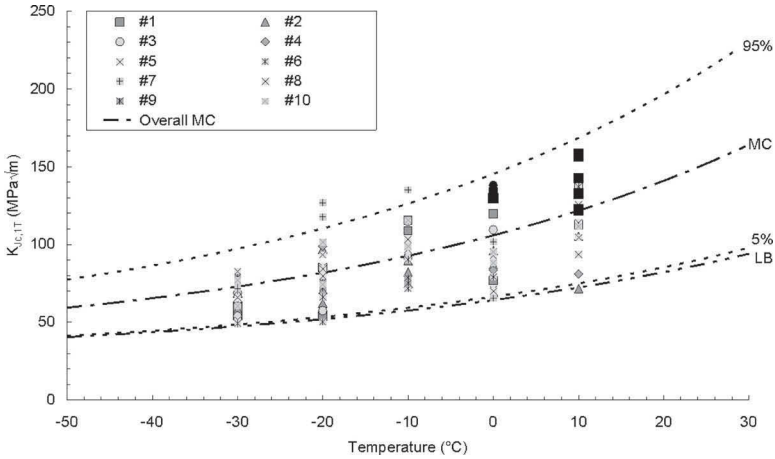


FIG. 9—Overall Master Curve analysis of the PCC impact round-robin data set (with 5–95 % tolerance bounds and margin-adjusted 5 % tolerance bound). Black symbols represent invalid (censored) data.

a T_0 of -2.3°C . This latter value of -2.3°C indicates a temperature shift of 69.1°C from the quasi-static value for JRQ steel from the same laboratory. Except for one laboratory (which appeared to have force calibration problems), the results supplied by the participants are very consistent and show reasonable scatter. Based on the results from this round robin exercise, the Master Curve approach has proven to be fully applicable to impact fracture toughness measurements obtained in the ductile-to-brittle transition region, but it is clear that the quality of impact fracture toughness measurements strongly depends on the quality of instrumented force values. Hence, a reliable calibration of the instrumented striker is of primary importance.

Additionally, supplemental investigations were performed to evaluate the effects of the type of loading (partial unloading vs. monotonic), side-grooving (with and without), and strain rate effect on irradiation-induced ΔT_0 . The results from these studies will be summarized in an IAEA TECDOC to be published in 2009.

Changes in Master Curve Shape—The third topic addressed possible changes in the Master Curve shape for highly irradiated materials and/or materials showing an intergranular fracture (IGF) mode. This task is crucial since the general shape of the Master Curve is considered to be invariant for most realistic irradiation conditions. For properly heat-treated, as-received ferritic structural steels, the standard Master Curve approach can normally be applied without consideration of validity constraints, provided the testing requirements specified in ASTM E1921 are fulfilled. A deviation from the standard K_{IC} versus temperature dependence (which defines the Master Curve shape) is anticipated if IGF due to thermal aging or irradiation begins to dominate or significantly affects the fracture behavior [20]. The existence of fracture modes other than pure cleavage usually, but not necessarily, means that one of the basic premises

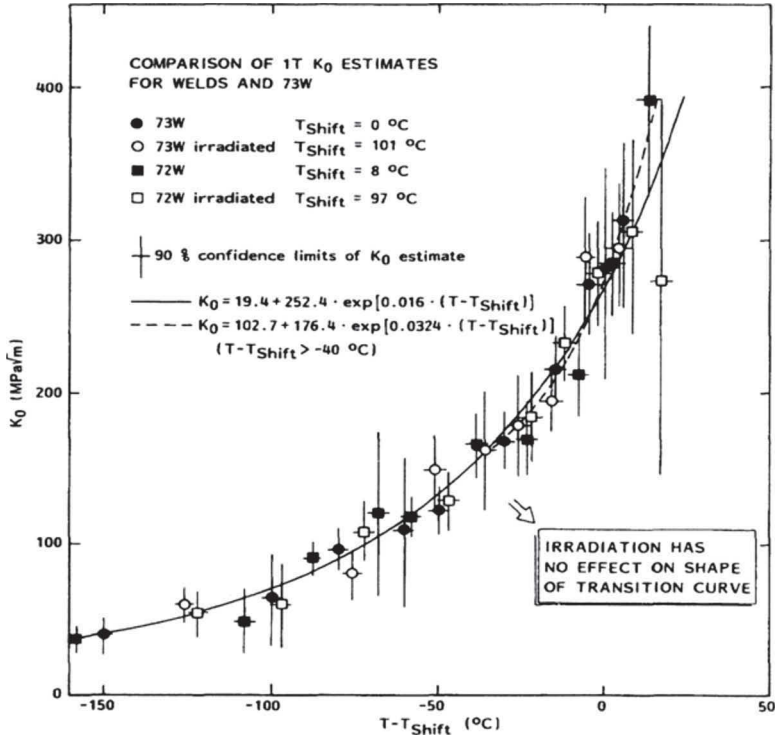


FIG. 10—Effect of irradiation on the temperature dependence of parameter K_0 (scale factor of the Weibull distribution) for welds 72 W and 73 W [19,20].

for applicability of the Master Curve methodology is not fulfilled. If the Master Curve does change shape, the conditions and extent of deviation need to be defined.

Therefore, the overall scope of this topic area was to (1) assess limits of applicability for Master Curve application at the upper range of the transition region in the standard Master Curve form, (2) determine the effects of heterogeneity (material and environment conditions), and (3) evaluate the importance of fracture mode change on the Master Curve shape (i.e., upper shelf ductile fracture or IGF modes). One major conclusion from this task is that irradiation may slightly lower the fracture toughness in the upper transition region in relation to that predicted by the standard curve shape, but the effect after T_0 shift values up to about 100°C seems to be negligible. One example leading to this conclusion is shown in Fig. 10, indicating that a large body of data from two high-copper welds, unirradiated and irradiated [21], follows the Master Curve shape both in the unirradiated condition and after irradiation with shifts up to about 100°C [22]. Based on these observations and others discussed in [17], the CRP recommended that very brittle materials (with T_0 above $\approx 100^\circ\text{C}$)

should be analyzed case-specifically, using a procedure to evaluate data for heterogeneity, e.g., the SINTAP procedure [23], for conservatively addressing the true fracture toughness.

IAEA CRP-9, Review and Benchmark of Calculation Methods for Structural Integrity Assessment of Reactor Pressure Vessels during PTS

CRP-9 was implemented by ten organizations from ten Member States to develop a critical review of and benchmark calculation methods for structural integrity assessment of RPVs during pressurized thermal shock (PTS) events. The overall objective was to perform various deterministic PTS benchmark calculations in order to identify the effects of individual parameters on RPV integrity. The final product will be an IAEA TECDOC to be published in 2009, which will have recommendations for best practices to be used in PTS evaluations.

A series of deterministic benchmark vessel integrity calculations for a typical PTS regime was performed by varying critical parameters in order to quantify their effects on RPV integrity during PTS. Both WWER and PWR three-loop vessels were investigated. Based on the sensitivity of the outcome of the vessel integrity assessments to the various parameters studied, an IAEA technical report will be written to provide a "Good Practice Handbook for RPV Deterministic Integrity Evaluations During PTS." This handbook will substantially contribute to better technical support of operational safety and life management. The deterministic calculations will have broader application even for probabilistic evaluations of RPV failure frequency through characterization of the fracture mechanics sub-routine.

Another phase for CRP-9 is underway and is devoted to preparation of an IAEA TRS report on Review of Pressurized Thermal Shock. The resulting TRS report will present a broad international survey of the PTS issue. A substantial enhancement will result from incorporating the recommended good practices and integrity criteria of the Good Practice Handbook into the draft TRS on PTS.

Summary

From 1971 until the present time, the IAEA has contributed significantly to the dissemination of knowledge regarding issues related to the structural integrity of nuclear RPVs. Through the establishment of nine CRPs that have brought together experts from a variety of organizations in many of the world's nuclear power producing countries, advances in the engineering materials field have been evaluated and published in the forms of special CRP IAEA TECDOC reports, Technical Reports Series, and technical journal papers. With the advancements in materials science and engineering over the past 36 years, the IAEA CRPs have taken advantage of those advancements by incorporating them in the evaluations of the specific issues and objectives of each particular CRP, for example, (1) advances in elastic-plastic fracture mechanics that allow for determination of fracture toughness of RPV steels with a relatively few number of relatively small specimens (i.e., the Master Curve), (2) the assembly

of larger databases of surveillance data from various types of reactors that allow for reductions in the uncertainties associated with development of predictive embrittlement correlations/models, (3) tremendous advances in the tools, such as APT, for examination of the steel microstructure following irradiation that allow for greater understanding of radiation damage mechanisms, and (4) significant advances in the computational sciences that provide the ability to rapidly perform modeling studies such as molecular dynamics. Such a combination of experimental, modeling, and microstructural studies leads to advances in predictive capability, and the IAEA CRPs have adapted these concepts in the pursuit of application to safety in operating RPVs.

Acknowledgments

At the risk of excluding many people who have contributed significantly to the CRPs since 1971, the authors especially wish to acknowledge Len Steele for his leadership and technical contributions in the 1970s and 1980s. Likewise, Milan Brumovsky has been a constant and significant contributor since CRP-1 through the present time with CRP-9. We also acknowledge the various IAEA Scientific Secretaries for the responsible International Working Group on Nuclear Power Plants who have guided the CRPs to successful conclusions; in particular we acknowledge the help and guidance of Ki-Sig Kang, the current Scientific Secretary.

References

- [1] International Atomic Energy Agency, 1975, "Coordinated Research Program on Irradiation Embrittlement of Pressure Vessel Steels," *IAEA-176*, Vienna.
- [2] International Atomic Energy Agency, 1986, "Analysis of the Behavior of Advanced Pressure Vessel Steels Under Neutron Irradiation," *Technical Report Series No. 265*, International Atomic Energy Agency, Vienna.
- [3] Steele, L. E., Davies, L. M., Ingham, T., and Brumovsky, M., "Results of the International Atomic Energy Agency (IAEA) Coordinated Research Programs on Irradiation Effects on Advanced Pressure Vessel Steels," *Effects of Radiation on Materials: Twelfth International Symposium, ASTM STP 870*, 1985, F. A. Garner and J. S. Perrin, Eds., ASTM International, West Conshohocken, PA, pp. 863-899.
- [4] International Atomic Energy Agency (IAEA), 2001, "Reference Manual on the IAEA JRQ Correlation Monitor Steel for Irradiation Damage Studies," *IAEA-TECDOC 1230*, Vienna.
- [5] International Atomic Energy Agency (IAEA), 2005, "Application of Surveillance Program Results to Reactor Pressure Vessel Integrity Assessment," *IAEA-TECDOC 1435*, Vienna.
- [6] International Atomic Energy Agency (IAEA), "Guidelines for Application of the Master Curve Approach to Reactor Pressure Vessel Integrity," *Technical Reports Series No. 429*, IAEA, Vienna, 2005.
- [7] International Atomic Energy Agency, 2005, "Effects of Nickel on Irradiation Embrittlement of Light Water Reactor Pressure Vessel Steels," *IAEA-TECDOC-1441*, Vienna.

- [8] PNAE-G-7-002-86, 1989, "Calculation Standards for Strength of Equipment and Pipes of Nuclear Power Units," Energoatomizdat, Moscow.
- [9] Burke, M. G., Stofanak, R. J., Hyde, J. M., English, C. A., and Server, W. L., "Microstructural Aspects of Irradiation Damage in A508 Gr 4N Forging Steel: Composition and Flux Effects," *Effects of Radiation on Materials, ASTM STP 1447*, M. L. Grossbeck and R. G. Lott, Eds., ASTM International, West Conshohocken, PA, 2002.
- [10] Miller, M. K., Chernobaeva, A. A., Shtrombakh, Y. I., Russel, K. F., Nanstad, R. K., Erak, D. Y., and Zabusov, O. O., "Evolution of the Nanostructure of VVER-1000 RPV Materials Under Neutron Irradiation and Post Irradiation Annealing," *J. Nucl. Mater.*, Vol. 285, 2009, pp. 615–622.
- [11] International Atomic Energy Agency, 2005, "Guidelines for Prediction of Irradiation Embrittlement of Operating WWER-440 Reactor Pressure Vessels," *IAEA-TECDOC-1442*, Vienna.
- [12] U.S. Nuclear Regulatory Commission, 1988, "Radiation Embrittlement of Reactor Vessel Materials," *Regulatory Guide 1.99, Revision 2*, U.S. Nuclear Regulatory Commission, Washington, D.C.
- [13] "Unified Procedure for Lifetime Assessment of Components and Piping in WWER Nuclear Power Plants (VERLIFE)," Final Report, M. Brumovsky (CZ), Ed., Contract No: FIKS-CT-2001-20198, European Commission, 2003.
- [14] Margolin, B. Z., Gulenko, A. G., Nikolaev, V. A., and Ryadkov, L. N., "A New Engineering Method for Prediction of the Fracture Toughness Temperature Dependence for RPV Steels," *Int. J. Pressure Vessels Piping*, Vol. 80(12), 2003, pp. 817–829.
- [15] Nanstad, R. K. and Scibetta, M., "IAEA Coordinated Research Project on Master Curve Approach to Monitor Fracture Toughness of RPV Steels: Effects of Bias, Constraint, and Geometry," *Proceedings of the ASME Pressure Vessel and Piping Conference*, San Antonio, TX, 2007, ASME, Paper No. PVP2007-26231 (on CD).
- [16] Viehrig, H.-W. and Lucon, E., "IAEA Coordinated Research Project on Master Curve Approach to Monitor Fracture Toughness of RPV Steels: Effect of Loading Rate," *Proceedings of the ASME Pressure Vessel and Piping Conference*, San Antonio, TX, 2007, ASME, Paper No. PVP2007-26087 (on CD).
- [17] Planman, T., Onizawa, K., Server, W., and Rosinski, S., "IAEA Coordinated Research Project on Master Curve Approach to Monitor Fracture Toughness of RPV Steels: Applicability for Highly Embrittled Materials," *Proceedings of the ASME Pressure Vessel and Piping Conference*, San Antonio, TX, 2007, ASME, Paper No. PVP2007-26257 (on CD).
- [18] Nanstad, R. K., McCabe, D. E., Sokolov, M. A., and Merkle, J. G., "Experimental Evaluation of Deformation and Constraint Characteristics in Pre-cracked Charpy and Other Three-Point Bend Specimens," *Proceedings of PVP 2007 ASME Pressure Vessels and Piping Division*, San Antonio, TX, July 22–26, 2007, ASME, Paper No. PVP2007-26651 (on CD).
- [19] Wasiluk, B., Petti, J., and Dodds, R. H., Jr., "Constraint Differences Between C(T) and SE(B) for the Euro-Material," Presentation at ASTM E08.08.03 Meeting, Salt Lake City, UT, May 2004.
- [20] Nanstad, R. K., Sokolov, M. A., and McCabe, D. E., "Applicability of the Fracture Toughness Master Curve to Irradiated Highly Embrittled Steel and Intergranular Fracture," *J. ASTM Int.*, Vol. 5 (3), 2008, Paper ID JAI101346.
- [21] Nanstad, R. K., McCabe, D. E., Haggag, F. M., Bowman, K. O., and Downing, D. J., "Statistical Analyses of Fracture Toughness Results for Two Irradiated High-Copper Welds," *Effects of Radiation on Materials: 15th International Symposium*,

ASTM STP 1125, 1992, R. E. Stoller, A. S. Kumar, and D. S. Gelles, Eds., ASTM International, West Conshohocken, PA, pp. 270–291.

- [22] Wallin, K., “Irradiation Damage Effects on the Fracture Toughness Transition Curve Shape for Reactor Pressure Vessel Steels,” *Int. J. Pressure Vessels Piping*, Vol. 55, 1993, pp. 61–79.
- [23] Nevasmaa, P., Bannister, A., and Wallin, K., “Fracture Toughness Estimation Methodology in the SINTAP Procedure,” *Proceedings of the 17th International Conference on Offshore Mechanics and Arctic Engineering*, 1998, ASME, Reston, VA; Also in British Steel “SINTAP–Structural Integrity Assessment Procedures for European Industry,” Project BE95–1426, Final Procedure, Internal Report, British Steel, Rotherham, 1999.

Enrico Lucon,¹ Marc Scibetta,¹ and Robert Gérard²

Analysis of the Belgian Surveillance Fracture Toughness Database Using Conventional and Advanced Master Curve Approaches

ABSTRACT: The “classical” regulatory approach to the analysis of surveillance capsules in nuclear power plants entails an indirect estimate of the fracture toughness of the beltline materials, by inferring rather than measuring their toughness properties. Indeed, the irradiation-induced shift of the fracture toughness curve is assumed to be equal to the shift of the Charpy absorbed energy transition curve at a predefined level (41 J). An alternative surveillance approach, primarily based on direct fracture toughness measurements in the ductile-to-brittle transition region using the Master Curve procedure, has been applied to surveillance materials from several Belgian nuclear power plants in the past 15 years. This has led to the establishment of a significant database, consisting of 292 fracture toughness data points for 23 material conditions (unirradiated materials and surveillance capsules). In this study, different temperature normalization approaches are applied to the available data. The analyses show that data clearly follow the Master Curve formalism. Moreover, it is confirmed that both the static (K_{Ic}) and the dynamic (K_{IR}) curves of the ASME Code Section XI provide an effective lower bound to the measured results, although more conservatism is evident when using RT_{NDT} as the normalization parameter. Both the conventional (ASTM E1921-08, “Standard Test Method for Determination of Reference Temperature, T_0 , for Ferritic Steels in the Transition Range”) and advanced (Multi-Modal) Master Curve analyses of the database clearly demonstrate that normalizing data by $(T - RT_{T0})$ provides the best rationalization of the available information and the most effective representation of the experimental scatter.

Manuscript received May 20, 2008; accepted for publication January 17, 2009; published online February 2009.

¹ SCK-CEN, Institute for Nuclear Material Science, Boeretang 200, B-2400 Mol, Belgium.

² Tractebel Engineering-Suez, Arianelaan 7, B-1200 Brussel, Belgium.

Cite as: Lucon, E., Scibetta, M. and Gérard, R., “Analysis of the Belgian Surveillance Fracture Toughness Database Using Conventional and Advanced Master Curve Approaches,” *J. ASTM Intl.*, Vol. 6, No. 3. doi:10.1520/JAI101897.

Copyright © 2009 by ASTM International, 100 Barr Harbor Drive, PO Box C700, West Conshohocken, PA 19428-2959.

KEYWORDS: surveillance capsules, fracture toughness, ductile-to-brittle transition region, Master Curve, Multi-Modal Master Curve

Introduction

Nuclear reactor pressure vessels are subjected to intense neutron irradiation in the core region, causing embrittlement of base and weld materials. Such embrittlement is quantified by post-irradiation mechanical examinations of specimens contained in surveillance capsules periodically retrieved from the reactor.

Surveillance specimens are mostly of Charpy-V type and are used within the classical regulatory framework to indirectly estimate the fracture toughness of the irradiated materials. Toughness properties are inferred rather than measured, since:

- fracture toughness is represented by lower bound curves, obtained by conservatively fitting arrest/dynamic (K_{IR}) or initiation (K_{Ic}) experimental results;
- the irradiation-induced shift of these lower bound curves is defined equal to the shift of the Charpy absorbed energy transition curve at a predefined level (41 J).

This approach entails several weaknesses and does not allow an accurate prediction of the evolution of the actual material properties with neutron irradiation, often leading to over conservatism and in few cases to nonconservatism.

An advanced surveillance approach, primarily based on direct fracture toughness measurements in the ductile-to-brittle transition region using the Master Curve procedure, has been applied to the surveillance materials from several Belgian nuclear power plants in the past 15 years. This has led to the establishment of a significant fracture toughness database, which currently consists of 292 data points for 23 material conditions (unirradiated materials and surveillance capsules). For the irradiated materials, the large majority of test results were obtained on precracked Charpy (PCC) specimens, obtained by reconstitution from previously tested surveillance impact specimens. Previous investigations [1] have demonstrated that, due to the limited size of the plastic zone when testing in the ductile-to-brittle transition region, specimen reconstitution does not affect Master Curve fracture toughness test results, even when relatively short inserts (10–12 mm length) are used.

In this study, different temperature normalization approaches have been applied to the available data, namely using $(T - T_0)$, $(T - RT_{NDT})$, and $(T - RT_{T0})$, where:

- T is the test temperature;
- T_0 is the Master Curve reference temperature, corresponding to a median toughness of 100 MPa \sqrt{m} for compact specimens with a thickness of 1 in. = 25.4 mm;
- RT_{NDT} is the reference temperature, calculated according to the U.S. legislation (ASME Section III) from a combination of drop weight and Charpy test results;
- RT_{T0} is an alternative definition of the reference temperature, based on T_0 and included in two recent ASME Code Cases (N-629 and N-631).

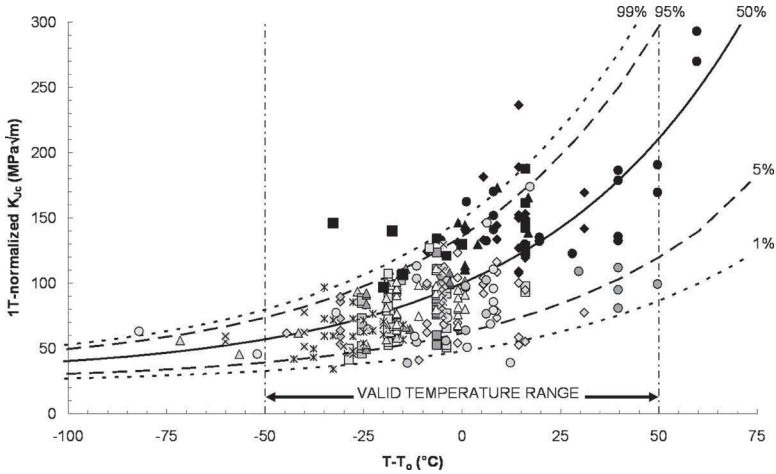


FIG. 1—Normalized Master Curve representation of the Belgian surveillance fracture toughness database. Different materials are indicated by different symbols and black symbols represent invalid data (above the censoring limit).

One of the aims of this study is to identify which one of the normalization approaches can provide a better rationalization of the existing database and a more effective representation of the experimental scatter.

The existing information has also been analyzed using the advanced Multi-Modal Master Curve (MMMC) extension [2], which has been recently proposed for the analysis of datasets consisting of multiple populations, each characterized by a random variable T_0 that is assumed to follow a Gaussian distribution.

Normalized Master Curve Representation of the Data Base

As previously mentioned, the current Belgian surveillance fracture toughness database consists, as far as the ductile-to-brittle transition region is concerned, of 292 data points and 23 Master Curve datasets [3].

According to the Master Curve approach, K_{Jc} data are normalized to the reference thickness (1 in.). In order to represent data points from different material conditions on the same Master Curve plot, it is customary to normalize the abscissae by using the difference between each test temperature and the corresponding T_0 . This representation allows assessing the general applicability of the Master Curve methodology to a population constituted by several individual datasets, each one characterized by its own reference temperature T_0 . Moreover, it allows plotting results from different specimen configurations (i.e., $C(T)$ versus bend samples) on the same diagram, since the use of $(T - T_0)$ takes care of possible T_0 bias.

For the Belgian surveillance database, this normalized Master Curve representation is shown in Fig. 1. The valid test temperature range according to ASTM E1921-08 is given by $T_0 \pm 50^\circ\text{C}$.

TABLE 2—Number and percentage of data points falling below various MC failure probabilities.

MC Failure Probability	Number of Data Points	% Data Points
1 %	6	2
5 %	20	7
50 %	158	54
95 %	272	93
99 %	282	97

The results of an overall Master Curve (MC) analysis performed on the normalized database are given in Table 1; as expected, $T_0=0^\circ\text{C}$ is obtained. In the table, N is the number of data points, r the number of valid tests, K_0 the Weibull fitting parameter (a scale parameter located at the 63.2 % cumulative failure probability level), $K_{Jc(\text{med})}$ the median K_{Jc} value for the dataset corresponding to 50 % failure probability, $\sum n_i$ the sum of the specimen weighting factors (T_0 is valid if $\sum n_i \geq 1$) and σ_{T_0} the standard deviation of the reference temperature calculated according to Annex X4 of ASTM E1921-08.

In Table 2, we report the percentage of data points falling below the Master Curves corresponding to various levels of failure probability (1, 5, 50, 95, and 99 %), in order to assess the capability of the method to effectively model the materials' variability.

We note that the actual percentages are slightly higher than the nominal values for low and median failure probabilities and slightly lower for high failure probabilities. However, in general the Belgian surveillance database follows quite satisfactorily the Master Curve formalism.

Nevertheless, an analysis according to the Multi-Modal Master Curve approach was also performed. More details about this method are given in the following section.

Multi-Modal Master Curve (MMMC)

Based on the maximum likelihood (MML) principle, this method was developed for the analysis of datasets consisting of multiple populations, each characterized by a random variable T_0 that is assumed to follow a Gaussian distribution [2]. It is especially suited to datasets including several heats of a single material or inherently macroscopically inhomogeneous materials. The required minimum size of the dataset for a reliable analysis is around 20.

A simple criterion to judge the likelihood that the data represent an inhomogeneous material is given by the parameter MLNH (*Measure of the Likelihood of a dataset to be Non Homogeneous*):

$$MLNH = \frac{\sigma_{T_0,MMMC}}{\sigma_{T_0,E1921-08}} > 2 \quad (1)$$

i.e., the steel is likely to be inhomogeneous if the standard deviation from the MML estimate ($\sigma_{T_0,MMMC}$) is larger than twice the theoretical uncertainty for a homogeneous steel ($\sigma_{T_0,E1921-08}$).

TABLE 1—Results of the Master Curve analysis on the database normalized by $(T - T_0)$.

$T - T_0$ (°C)	N	r	K_0 (MPa \sqrt{m})	$K_{Jc(med)}$ (MPa \sqrt{m})	$\sum n_i$	T_0 (°C)	σ_{T_0} (°C)	T_0 VALID
-82 to +59.6	292	226	103.5	96.2	34.07	0	4.2	YES

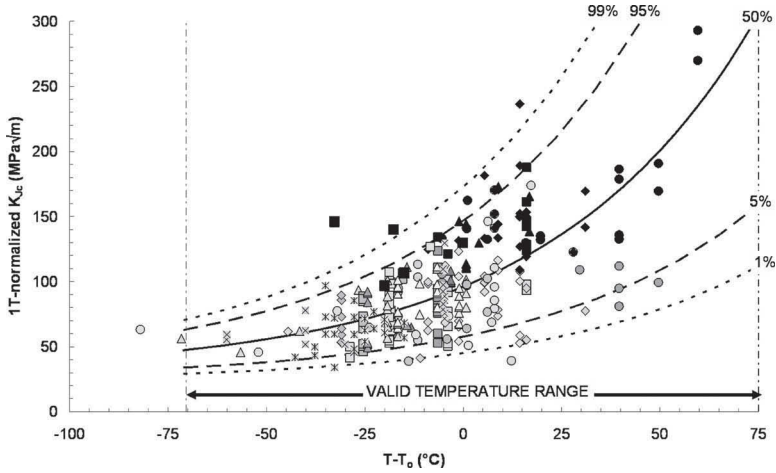


FIG. 2—Normalized Belgian surveillance database analyzed using the MMMC approach.

The results of the MMMC analysis of the database normalized by $(T - T_0)$, see Fig. 2, deliver a reference temperature of 2.4°C (very close to the value of the standardized analysis) with a standard deviation $\sigma_{T_0,MMMC} = 11.7^\circ\text{C}$. The MLNH parameter has a value of 2.8, therefore the dataset is suspected to be inhomogeneous. This circumstance is believed to be related to the intrinsic heterogeneity of several Belgian surveillance materials, particularly weld metals and materials from older power plants [3].

Test Temperature Normalization Using RT_{NDT}

RT_{NDT} is a reference temperature which is defined in the ASME Code, Paragraph NB-2300 [4] and is used to index both the static (K_{Ic}) and dynamic (K_{IR}) lower bound fracture toughness curves according to 10 CFR Pt. 50, Appendix G. These lower bound curves are used in Appendix G of ASME Code Section XI for calculating pressure-temperature ($P-T$) limit curves which control the heatup and cooldown processes for an operating nuclear power plant.

In the unirradiated condition, RT_{NDT} is defined as the highest between:

- the nil-ductility transition temperature NDT measured by drop weight (Pellini) tests;
- the index temperatures from Charpy impact tests corresponding to 68 J absorbed energy (T_{68J}) and 0.89 mm lateral expansion ($T_{0.89mm}$).

Upon irradiation, RT_{NDT} is increased by an amount which corresponds to the shift of the Charpy energy curve at the 41 J level (ΔT_{41J}).

The entire Belgian surveillance database has been normalized using the difference between individual test temperatures and RT_{NDT} for the relevant material condition. The comparison with the static and dynamic lower bound curves is shown in Fig. 3. Note that toughness values have not been normalized,

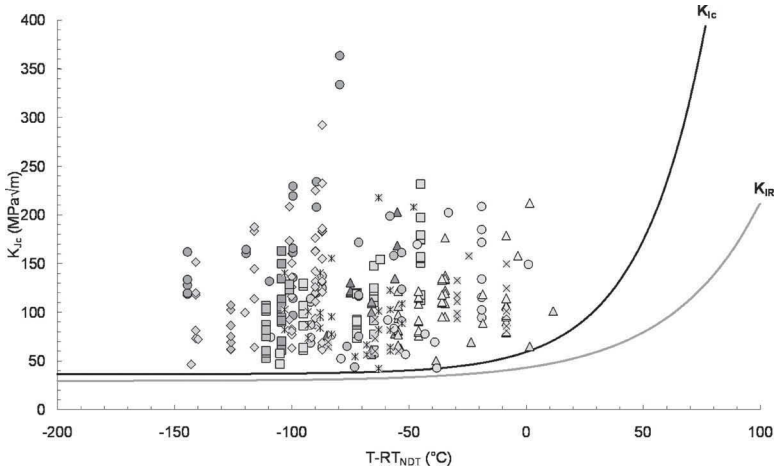


FIG. 3—Comparison between Belgian surveillance database, normalized using ($T - RT_{NDT}$), and ASME K_{Ic} and K_{IR} lower bound curves.

since the ASME curves were obtained by fitting a lower bound to an existing database collected from specimen of different sizes [5].

It is observed that both ASME curves appropriately bound the whole database, thus confirming their definition of lower bound curves, although a few data points are lying on top or very close to the K_{Ic} curve (which has been assessed to be an approximate 2σ lower bound to initiation data available in the early 70s [6]).

Test Temperature Normalization Using RT_{T_0}

An alternative definition of RT_{NDT} , RT_{T_0} , has been implemented into two recent ASME Code Cases, N-629 and N-631 [7,8]. This avoids the use of Charpy-based information and relies on direct fracture toughness measurements of the reference temperature T_0 , either in the unirradiated or irradiated condition:

$$RT_{T_0} = T_0 + 19.4^\circ \text{C} \quad (2)$$

RT_{T_0} has been used for an alternative temperature normalization of the Belgian surveillance database, as shown in Fig. 4, where data are again compared to the ASME static and dynamic lower bound fracture toughness curves K_{Ic} and K_{IR} .

We again remark that both ASME curves represent an effective lower bound to the database; a single data point, corresponding to a pop-in event which was recorded on a 0.5 T Compact specimen, lies below the K_{Ic} curve but is bounded by the K_{IR} curve. Qualitatively, the comparison between Figs. 3 and 4 shows that the data population lies closer to the ASME curves in the horizontal direction (i.e., temperature-wise) when RT_{T_0} is used for normalization, thus indicating that the use of RT_{NDT} generally introduces additional conservatism.

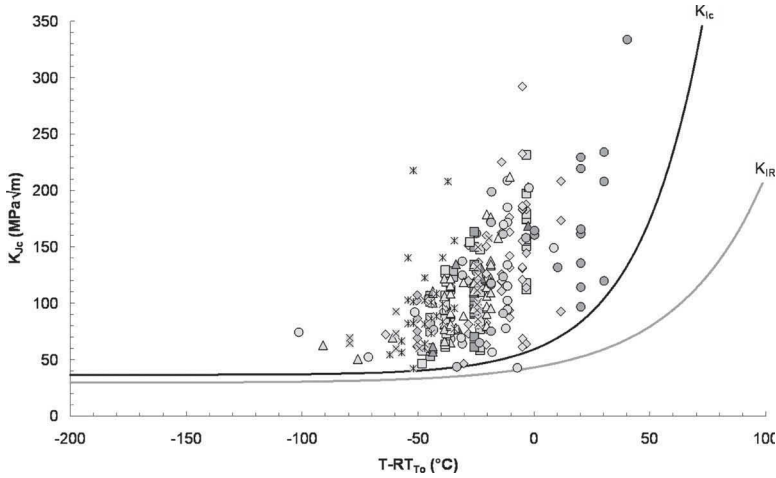


FIG. 4—Comparison between Belgian surveillance database, normalized using $(T - RT_{T_0})$, and ASME K_{Ic} and K_{IR} lower bound curves.

Master Curve Analyses on the Normalized Databases

Conventional (E1921-08) and Multi-Modal Master Curve analyses have been performed on the database, after normalization of test temperatures using RT_{NDT} and RT_{T_0} . The aim of this exercise was to assess which of the two normalizing approaches provides a better rationalization of the available information and a more effective representation of the experimental scatter.

Results of the conventional MC analyses in accordance with ASTM E1921-08 are provided in Table 3, Fig. 5 (RT_{NDT}) and Fig. 6 (RT_{T_0}). In both figures, invalid (censored) data, which correspond to results exceeding the specimen measurement capacity $K_{Ic(limit)}$ and are replaced in the analysis by the corresponding limit values, are highlighted in red. Note also that, when RT_{T_0} is used, $T_0 = -19.5^\circ\text{C}$ is obtained, which corresponds approximately to the value of the constant in Eq 2.

It is clear that the data represented as a function of $(T - RT_{NDT})$ in Fig. 5 do not really follow the Master Curve approach. This can be easily explained if one considers that:

- in the unirradiated condition, RT_{NDT} has no direct relationship with the actual fracture toughness of the material;
- in the irradiated condition, a weak relationship exists since RT_{NDT} is obtained by coupling the unirradiated value (see above) to the increase of the Charpy T_{41J} temperature, which has been shown to be roughly equivalent to ΔT_0 [9].

On the other hand, data normalized by $(T - RT_{T_0})$ are effectively represented by the Master Curve formalism (Fig. 6). Six data points (corresponding to 2 % of the population) fall below the 1 % failure probability curve.

After applying the MMMC approach, the results shown in Table 4 and Figs. 7 and 8 have been obtained.

TABLE 3—Results of the Master Curve analyses on the database after normalization of the test temperatures.

Norm. Parameter	$T - RT_x$ (°C)	N	r	K_0 (MPa \sqrt{m})	$K_{Jc(med)}$ (MPa \sqrt{m})	Σn_i	T_0 (°C)	σ_{T_0} (°C)	T_0 VALID
RT_{NDT}	-144.5 to +11.5	292	173	139.4	129.0	28.18	-103	4.2	YES
RT_{T_0}	-101.4 to +40.2	292	224	103.5	96.2	33.62	-19.5	4.2	YES

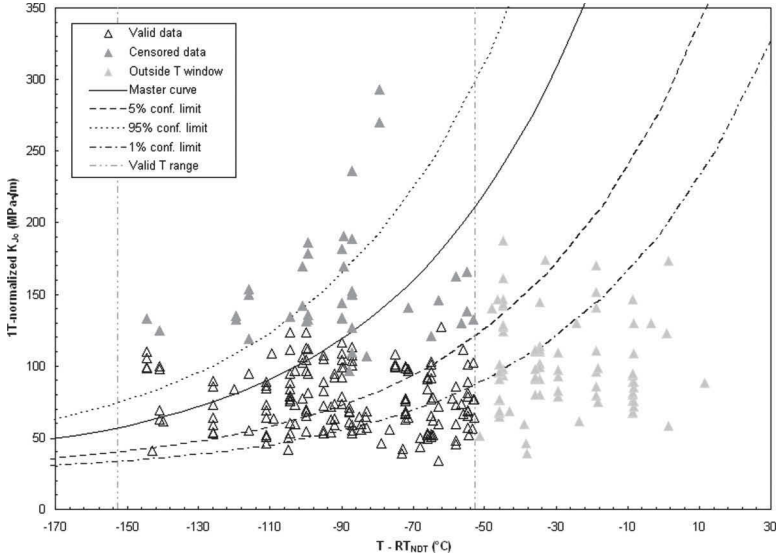


FIG. 5—Conventional Master Curve analysis of the database after normalization by $(T - RT_{NDT})$.

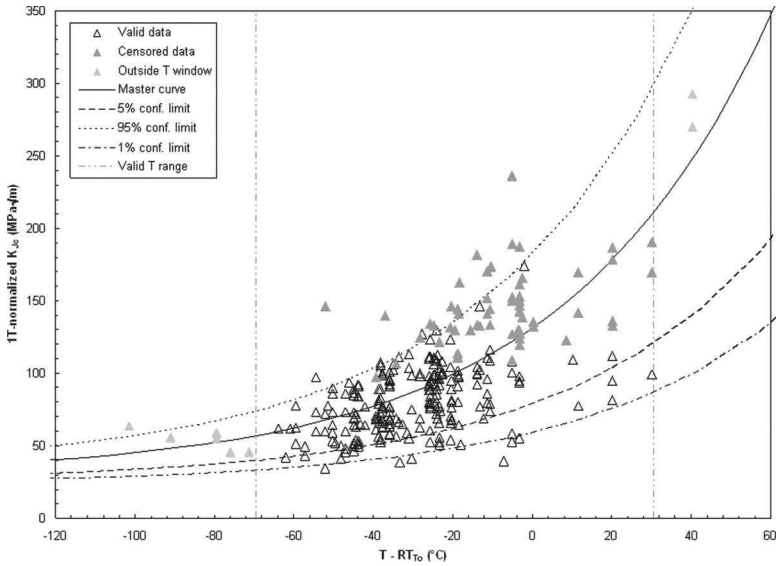


FIG. 6—Conventional Master Curve analysis of the database after normalization by $(T - RT_{T_0})$.

TABLE 4—Results of the Multi Modal Master Curve analyses on the Belgian surveillance database after normalization of the test temperatures.

Norm. Parameter	$T - RT_x$ (°C)	N	r	T_0 (°C)	σ_{T_0} (°C)	Likely Not Homogeneous
RT_{NDT}	-144.5 to 11.5	292	232	-65.8	45.2	YES
RT_{T_0}	-101.4 to 40.2	292	230	-17.0	11.7	YES

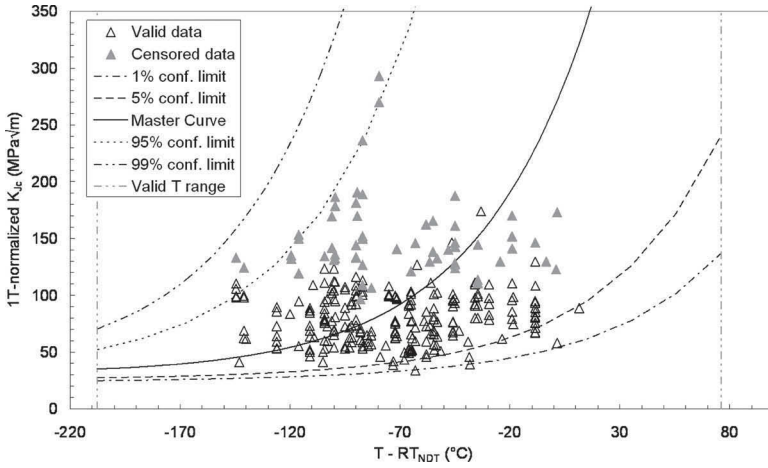


FIG. 7—Multi-Modal Master Curve analysis of the Belgian surveillance database after normalization by $T - RT_{NDT}$.

Although in both cases the MMMC analysis identifies the database as “likely not homogeneous,” the standard deviation of the reference temperature for the RT_{NDT} normalization is four times larger than when using RT_{T_0} . Moreover, for the latter normalization the difference between reference temperatures calculated by the conventional and the Multi-Modal MC approaches is only 2.5°C.

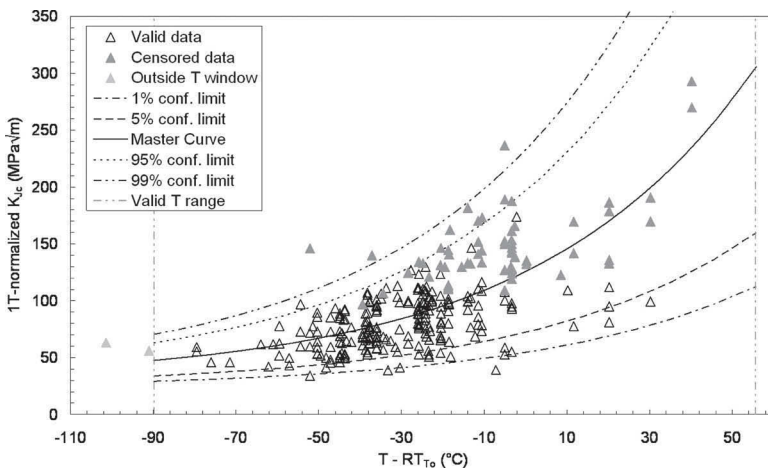


FIG. 8—Multi-Modal Master Curve analysis of the Belgian surveillance database after normalization by $T - RT_{T_0}$.

Conclusions

- (a) An overall Master Curve analysis of the Belgian surveillance materials' database, normalized by $(T-T_0)$, shows that it follows the MC trend, as confirmed by the fact that the percentage of data points falling below various failure probability limits are within a few % of the nominal figures.
- (b) When data are normalized by $(T-RT_{NDT})$ or $(T-RT_{T_0})$, both ASME lower bound curves (static K_{Ic} and dynamic K_{IR}) provide an effective lower bound to the database; however, an additional margin of conservatism can be observed when the Charpy-based RT_{NDT} is used.
- (b) Both the conventional (E1921-08) and Multi-Modal Master Curve (MMMC) analyses of the normalized databases show that the normalization using RT_{T_0} provides a better rationalization of the available results and a more effective representation of the experimental scatter. In particular, the MMMC analysis returns a much larger standard deviation for RT_{NDT} (45.2°C) than for RT_{T_0} (11.7°C), and for the latter normalization also yields a value of T_0 which is almost identical to the conventional approach.

Acknowledgments

This work was partially sponsored by Electrabel/Tractebel Engineering, whose support is kindly appreciated.

References

- [1] Keim, E., et al., "RESQUE: Determination of the Lowest Acceptable Insert Length for Reconstituted C_v -impact and Precracked C_v Specimens," in *Small Specimen Test Techniques: Fourth Volume, ASTM STP 1418*, M. A. Sokolov, Ed., ASTM International, West Conshohocken, PA, 2002.
- [2] Wallin, K., Nevasmaa, P., Laukkanen, A., and Planman, T., "Master Curve Analysis of Inhomogeneous Ferritic Steels," *Eng. Fract. Mech.*, Vol. 71, 2004, pp. 2329–2346.
- [3] Lucon, E., Scibetta, M., Chaouadi, R., van Walle, E., and Gérard, R., "Improved Safety Margins for Belgian Nuclear Power Plants by the Application of the Master Curve Approach to RPV Surveillance Materials," *Int. J. Pressure Vessels Piping*, Vol. 84, 2007, pp. 536–544.
- [4] American Society of Mechanical Engineers, "Rules for Construction of Nuclear Power Plants, ASME Boiler and Pressure Vessel Code," Section III, Rep. ASME NB-2300, ASME, New York, 2002.
- [5] PVRC Ad Hoc Group on Toughness Requirements, "PVRC Recommendations on

- Toughness Requirements for Ferritic Materials," *WRC Bulletin*, Vol. 175, Aug. 1972.
- [6] Jouris, G. M. and Shaffer, D. H., "Methodology for Obtaining Lower Bound Fracture Toughness Data," *Proceedings of the 5th International Conference on Structural Mechanics in Reactor Technology*, Berlin, Aug. 1979.
- [7] ASME Boiler and Pressure Vessel Code: An American National Standard, Code Case N-629, "Use of Fracture Toughness Test Data to Establish Reference Temperature for Pressure Retaining Materials," Section XI, Division 1, American Society of Mechanical Engineers, New York, May 7, 1999.
- [8] ASME Boiler and Pressure Vessel Code: An American National Standard, Code Case N-631, "Use of Fracture Toughness Test Data to Establish Reference Temperature for Pressure Retaining Materials Other than Bolting for Class 1 Vessels," Section III, Division 1, American Society of Mechanical Engineers, New York, Sept. 24, 1999.
- [9] Sokolov, M. A. and Nanstad, R. K., "Comparison of Irradiation-Induced Shifts of K_{Jc} and Charpy Impact Toughness for Reactor Pressure Vessel Steels," *Effects of Radiation on Materials: 18th International Symposium, ASTM STP 1325*, R. K. Nanstad, M. L. Hamilton, F. A. Garner, and A. S. Kumar, Eds., ASTM International, West Conshohocken, PA, 1999.

H. Hein,¹ E. Keim,¹ H. Schnabel,¹ T. Seibert,¹ and
A. Gundermann¹

Final Results from the Crack Initiation and Arrest of Irradiated Steel Materials Project on Fracture Mechanical Assessments of Pre-Irradiated RPV Steels Used in German PWR

ABSTRACT: Pre-irradiated original reactor pressure vessel (RPV) materials covering all four German pressurized water reactors (PWR) construction lines were tested in the Crack Initiation and Arrest of Irradiated Steel Materials program to create a database of fracture toughness and arrest values for neutron fluences beyond the end of life range. The new database comprises data from both unirradiated and irradiated RPV base and weld materials generated by tensile, Charpy-V impact, fracture toughness K_{Jc} , and crack arrest K_{Ia} tests. The test matrix consists of materials with optimized chemical composition and with high Copper or high Nickel content, respectively. Based on the generated and already existing data the RT_{NDT} and the RT_{70} (Master Curve) concepts are applied with specific view on reference temperatures, transition temperature shifts, and on possible correlations between the criteria used in both concepts. In this context the consequences of some influencing factors like type and chemical composition of the RPV steel, its manufacturing conditions, and the specimen type and size on the reference temperatures are discussed. Moreover, the test results are assessed with respect to the American Society of Mechanical Engineers (ASME) code and German Nuclear Safety Standards Commission safety standards. The crack arrest characteristics for these typical RPV materials are also determined in a twofold way by testing Compact Crack Arrest specimens and by evaluation of instrumented Charpy-V impact test data. The

Manuscript received June 20, 2008; accepted for publication June 2, 2009; published online July 2009.

¹ AREVA NP GmbH, Paul-Gossen-Straße 100, D-91052 Erlangen, Germany.

Cite as: Hein, H., Keim, E., Schnabel, H., Seibert, T. and Gundermann, A., "Final Results from the Crack Initiation and Arrest of Irradiated Steel Materials Project on Fracture Mechanical Assessments of Pre-Irradiated RPV Steels Used in German PWR," *J. ASTM Intl.*, Vol. 6, No. 7. doi:10.1520/JAI101962.

Copyright © 2009 by ASTM International, 100 Barr Harbor Drive, PO Box C700, West Conshohocken, PA 19428-2959.

available results made a good point that crack arrest is a reliable phenomenon that doubtless exists. It is also shown that the obtained K_{Ia} data can be enveloped by applying the ASME K_{Ic} lower bound curve indexed by different reference temperatures. Finally, the results show that the used RPV materials are well designed in terms of material behavior under irradiated conditions and that optimized manufacture specifications are of great benefit particularly after long operation times.

KEYWORDS: reactor pressure vessel steel, neutron irradiation, irradiation embrittlement, fracture toughness, crack arrest, master curve, RT_{NDT} , RT_{T_0}

Introduction

The proof of a sufficient safety margin against brittle fracture of the reactor pressure vessel (RPV) is an essential part of the safety of a nuclear power plant. In Germany the procedure usually applied for the safety assessment of the RPV is based on the RT_{NDT} concept according to the current set of rules of the German Nuclear Safety Standards Commission (KTA). In this procedure a lower bound fracture toughness—temperature curve that was determined deterministically by measured data—is adjusted for the concerned material by the specific adjusted reference nil-ductility temperature $RT_{NDT(f)}$ for the brittle fracture transition.

At present the new RT_{T_0} procedure for the RPV safety assessment, which is based on the Master Curve concept, is under development world wide. Unlike the RT_{NDT} concept, fracture toughness data are used by statistical assessment in the Master Curve concept instead of Charpy impact and drop-weight test data. An essential advantage of the RT_{T_0} procedure is the direct determination of the reference temperature RT_{T_0} for the brittle fracture transition and therefore a more realistic application to the behavior of the component concerned.

In this context there is a strong interest to assess the consequences by using the Master Curve based RT_{T_0} procedure compared to the RT_{NDT} concept that requires a careful comparison of both methods by using representative RPV materials. Obviously, such an assessment can be succeeded only if appropriate data can be made available, which cover both unirradiated and irradiated material conditions. Apart from the crack initiation issue crack arrest can be used as a further approach in RPV safety assessment if the arrest of a global or local unstable crack can be proven. The verification of crack arrest curves defined in ASME code and the KTA standard by experimental results of representative materials is therefore another point of interest.

The project Crack Initiation and Arrest of Irradiated Steel Materials (CAR-ISMA) gave an unique chance to create a representative database by extensive testing of unirradiated and irradiated specimens manufactured from original RPV base and weld materials being representative for all four German PWR construction lines and to assess the new data by the two most common procedures. In this way the project contributes to the further update and improvement of the RPV safety assessment in particular for German plants.

Objectives

The main objective of the CARISMA project [1–3] is to create an experimental database for unirradiated and irradiated specimens made of original RPV base and weld materials being representative for all four German PWR construction lines by tensile, Charpy-V impact, fracture toughness K_{Jc} , and crack arrest K_{Ia} testing, and to assess these data with the aim to determine reference temperatures for the ductile brittle transition region.

The project allows

- (a) to determine fracture toughness properties for both crack initiation and arrest,
- (b) to compare the safety assessment by the RT_{NDT} concept and the Master Curve concept in the context with the present status in the German KTA safety standard,
- (c) to determine material and manufacture specific influences on fracture toughness properties,
- (d) to clarify some open issues like the identification of appropriate specimen shapes and sizes, and the proof of suitability of pre-fatigued C_v -specimens for T_0 determination, and
- (e) to assess the feasibility of getting crack arrest values for irradiated materials and how to integrate the crack arrest into the new safety concept.

The nuclear power plants of the concerned PWR generations built by former Siemens/KWU Company in Germany are Obrigheim, Stade (first generation, both shut down), Biblis A, Biblis B, Unterweser, Neckarwestheim 1 (second generation), Grafenrheinfeld, Grohnde, Phillipsburg 2, Brokdorf (third generation), and Emsland, Isar 2, Neckarwestheim 2 (fourth generation).

Materials and Specimens

Three base materials (BM) of forgings and four weld metals (WM) were selected from the materials available at AREVA NP GmbH laboratories in Erlangen for the examinations in the CARISMA project. The selected seven materials are characterized by following project names and material specifications:

- (a) P7 BM: 22 NiMoCr 3-7 (similar to ASME SA-508 Grade 2 Class 1, manufactured by Klöckner) covering first and second generations,
- (b) P147 BM: 22 NiMoCr 3-7 (similar to ASME SA-508 Grade 2 Class 1, manufactured by JSW) covering third and fourth generations,
- (c) P141 BM: 20 MnMoNi 5-5 (similar to ASME SA-508 Grade 3 Class 1, manufactured by JSW) covering fourth generation,
- (d) P141 WM: S3NiMo1/OP41 TT UP, 1 % Ni (manufactured by GHH Company) covering fourth generation,
- (e) P16 WM: S3NiMo3/OP41 TT UP, 1.7 % Ni (manufactured by Udcomb) covering third generation,
- (f) KS05 WM: NiCrMo1 UP/LW320 (manufactured by GHH) covering from second to fourth generations, and
- (g) P370 WM: NiCrMo1 UP (modified)/LW320, LW340 (manufactured by Klöckner) covering first generation.

TABLE 1—*Chemical composition of the specimen materials.*

PWR Generation	Material	Project	Type	Cu (wt %)	P (wt %)	Ni (wt %)
4 (Konvoi)	20 MnMoNi 5-5 JSW	P141	BM	0.05	0.007	0.79
1-2	22 NiMoCr 3-7 Klöckner	P7	BM	0.12	0.015	0.97
3	22 NiMoCr 3-7 JSW	P147	BM	0.05	0.006	0.84
4 (Konvoi)	S3NiMo1/OP 41 TT UP, GHH	P141	WM	0.03	0.019	1.01
3	S3NiMo3/OP 41 TT UP, Uddcomb	P16	WM	0.08	0.012	1.69
2-4	NiCrMo1 UP/LW320, GHH	KS05	WM	0.05	0.009	0.91
1	NiCrMo1 UP (modified)/LW320, LW340	P370	WM	0.22	0.015	1.11

The specimen materials were taken from original RPV materials and welds, respectively, and are representative for all four German PWR generations. Tensile specimens, Charpy-V specimens, Wedge Opening Load X (WOL-X), Pre-Cracked-Charpy-V (PCCV, manufactured from Charpy-V specimens), Single-Edge notched Bend SE(B), and Compact Crack Arrest (CCA) specimens were tested both in the unirradiated and irradiated states.

The chemical composition of the specimen materials in terms of the most important chemical elements is described in Table 1.

Irradiation of the Specimen Materials

All CARISMA materials except the KS05 WM were irradiated in the German test reactor VAK (Versuchsatomkraftwerk Kahl) in the 1980s. The specimen materials P16 WM, P141 WM, P141 BM, and P7 BM were irradiated in the frame of a dedicated research program for ensuring the RPV integrity considering possible changes in future concept designs and plant life extension measures. In the frame of this research program six large irradiation capsules have been irradiated in the VAK reactor in the years 1983 and 1985.

The VAK reactor (Fig. 1), an experimental boiling water reactor (BWR) with an electrical output of about 15 MW, was in operation until 1985 and was used between 1975 and 1985 by the former Siemens/KWU Company as additional irradiation facility for various research and RPV irradiation surveillance programs. The neutron spectrum of the VAK was similar to the neutron spectrum of other Siemens/KWU PWR, and the neutron flux density at the capsule positions was approximately 2×10^{12} n/cm²/s ($E > 1$ MeV), which was higher than at the surveillance position in the RPV of power reactors. The irradiation temperature in all VAK irradiation programs was in a range between 265 and 316°C.

Originally the VAK RPV had 12 mounting positions for the irradiation capsules, which were extended later by three inner irradiation positions at 90°, 180°, and 270° (Fig. 2).

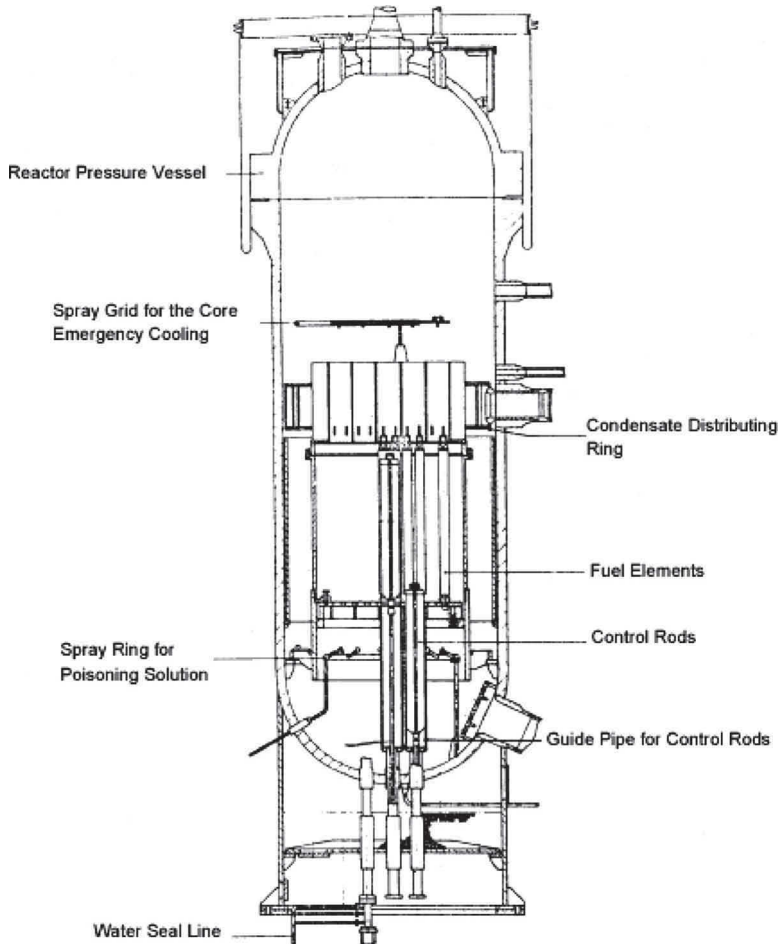


FIG. 1—The VAK reactor.

These additional irradiation positions made it possible to irradiate also large capsules with a length of 965 mm and a cross section of $100 \times 146.5 \text{ mm}^2$ (Fig. 3). The six large capsules were equipped with 39 WOL-100X, 60 drop weight, 48 tensile, and 765 Charpy-V specimens and have been irradiated to neutron fluences between 6×10^{18} and $5 \times 10^{19} \text{ n/cm}^2$ ($E > 1 \text{ MeV}$).

The specimen materials P147 WM and P370 WM were also irradiated in the VAK reactor but in other capsules.

The specimen material KS05 was irradiated in the GKSS FRG-2 reactor in the frame of the FKS-Program [4]. The WOL-25X specimens of the material P16 SG and the Charpy-V compound specimens of the P370 WM were part of RPV irradiation surveillance programs.

After the irradiation the capsules and specimens were transported to the

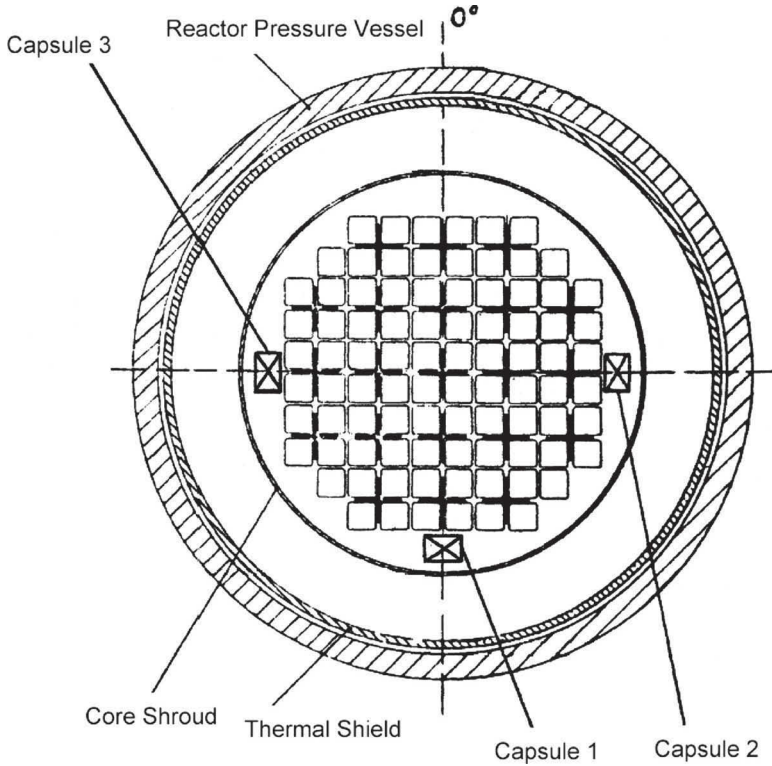


FIG. 2—VAK irradiation positions.

hot cell laboratory of AREVA NP GmbH in Erlangen, Germany, where they were stored until the test program started.

Irradiation Temperatures and Neutron Fluences

In order to make the specimens and temperature monitors and neutron detectors available for testing, inspection and measurements the VAK irradiation

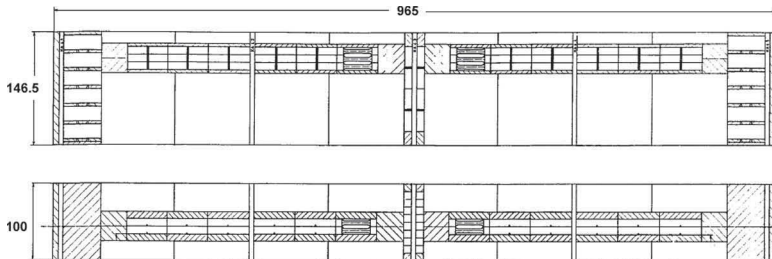


FIG. 3—Large VAK irradiation capsule of $100 \times 146.5 \times 965$ mm³ size.

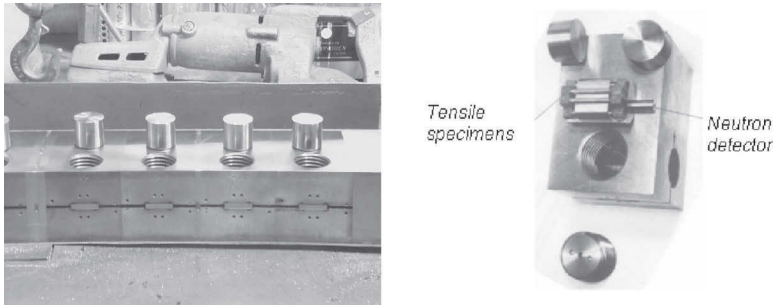


FIG. 4—Dismantled VAK capsule.

capsules RT2, RT3, KWO 01, KA1, KA2, KA3, and KA6 were opened in the hot cells laboratory of AREVA NP GmbH in Erlangen.

Figure 4 shows a VAK capsule after opening and dismantling the capsule walls.

The evaluation of the temperature monitors led to maximum temperatures during the irradiation in the ranges of 284–288°C for the VAK capsules KWO 01, 277–281°C for the capsule KA1, and 282–286°C for the remaining VAK capsules. For the capsules K7 and K8 irradiated in a PWR, maximum temperatures of 288–289°C were determined.

The averaged irradiation temperature of the specimens in the capsule CK100-6 amounted to $290 \pm 5^\circ\text{C}$, whereas the fracture mechanics specimens of the specimen material P16 WM were irradiated in a PWR at a irradiation temperature between 300 and 302°C.

Table 2 contains a summary of the irradiation facilities and the irradiation

TABLE 2—Irradiation temperatures of the specimen materials.

Material	Project	Type	Irradiation Facility	Capsule	Irradiation Temperature (°C)
20 MnMoNi 5-5 JSW	P141	BM	VAK	KA3	282–286
22 NiMoCr 3-7, Klöckner	P7	BM	VAK	KA6	282–286
22 NiMoCr 3-7, JSW	P147	BM	VAK	RT2	282–286
				RT3	280–286
S3NiMo1/OP 41 TT, SAW, GHH	P141	WM	VAK	KA2	282–286
S3NiMo3/OP 41 TT, SAW, Uddcomb	P16	WM	VAK	KA1	277–281
			PWR	RPV capsule	300–302
NiCrMo1 UP/LW320, GHH	KS05	WM	GKSS	CK100-6	285–295
NiCrMo1 UP (modified)/LW320, LW340	P370	WM	VAK	KWO 01	284–288
			PWR	K7, K8	288–289

temperatures of the specimen materials tested within the project.

The precise and reliable determination of the neutron fluences accumulated by the specimen sets during the irradiation is of high importance for the assessment of the results from the material testing.

The neutron fluences applied by the specimens irradiated in the capsules RT2, KA1, KA2, KA3, and KA6 were calculated by well established neutron transport codes such as the three-dimensional transport code TORT [5] and by using the cross section library BUGLE 96 [6]. The neutron fluences for the specimens irradiated in the capsules RT3, KWO 01, K7, K8, and CK100-6 were taken from existing calculations already performed. The neutron fluences accumulated by the irradiated material specimen sets are given in Table 3.

Experimental Test Program

The experimental test program includes comprehensive material tests both on unirradiated and irradiated specimens in order to determine the material behavior in terms of strength and toughness by a two step approach:

Step 1. Basic characterization of the specimen materials by application of the RT_{NDT} and Master Curve concepts and determination of the most important quantities such as ultimate tensile and yield strength, Charpy V-notch energy transition temperatures (41 J), adjusted reference temperature $RT_{NDT(j)}$, $T_{Fa=4}$ kN (from instrumented Charpy test), fracture toughness K_{Jc} , and reference temperature RT_{T_0} . In this first step a basic characterization of the materials concerned is carried out by regular tensile and Charpy impact tests and by fracture mechanics test according to Ref. 7. The fracture mechanics tests are also used for the determination of a reference temperature RT_{T_0} according to Ref. 8. Besides the changes in mechanical strength this step allows conclusions to the lower bound curve for crack initiation in the brittle to ductile regime.

Step 2. Crack arrest behavior of the specimen materials and determination of the most important quantities such as crack arrest toughness K_{Ia} and reference temperature $T_{K_{Ia}}$.

In the second step the crack arrest behavior of the material after brittle initiation is investigated. The crack arrest acts as a further barrier in the integrity assessment against brittle failure. One of the main objectives to perform the crack arrest tests is to confirm the lower bound curves given in the ASME and KTA standards for irradiated materials being representative for RPV steels. For this purpose CCA specimens are tested according to the ASTM E1221 standard [9]. In Fig. 5 a schematic view of the crack arrest test procedure is shown. The CCA specimens are loaded cyclically by the wedge and split-pin assembly to certain crack mouth opening displacements until crack initiation occurs.

Depending on the amount of available material compact specimens and reconstituted (compound) specimens using original material inserts (taken from WOL-X specimens or broken Charpy-V halves) and dummy material for the studs have been used for testing, as shown in Fig. 6.

Table 4 shows the test matrix for all the specimen materials concerned. It can be seen that some test data could be taken from previous examinations, but

TABLE 3—Neutron fluences of the material specimen sets.

Project	Type	Cu (wt %)	P (wt %)	Ni (wt %)	Specimen Type	Neutron Fluence ($E > 1$ MeV) [n/cm^2]
P141	BM	0.06	0.008	0.8	Tensile	6.81×10^{18}
					Charpy-V	1.05×10^{19}
					PCCV	7.59×10^{18}
					CCA	6.87×10^{18}
P7	BM	0.12	0.015	0.98	Tensile	3.81×10^{19}
					Charpy-V	4.11×10^{19}
					PCCV	4.45×10^{19}
					CCA	3.89×10^{19}
P147	BM	0.06	0.007	0.9	Tensile	1.09×10^{19}
					Charpy-V	1.03×10^{19}
					SE(B) ^a	1.06×10^{19}
					SE(B)24 × 50 ^a	7.78×10^{18}
					CCA	1.17×10^{19}
P141	WM	0.03	0.019	1	Tensile	8.84×10^{18}
					Charpy-V	1.35×10^{19}
					PCCV	9.79×10^{18}
					CCA	8.39×10^{18}
P16	WM	0.08	0.012	1.7	Tensile	7.27×10^{18}
					Charpy-V	$4.14 \times 10^{18}/1.16 \times 10^{18}$
					PCCV	8.36×10^{18}
					WOL-25X	6.21×10^{18}
					CCA	7.25×10^{18}
KS05	WM	0.05	0.009	0.91	Tensile	$2.10 \times 10^{19}/5.32 \times 10^{19}$
					Charpy-V	$2.18 \times 10^{19}/4.96 \times 10^{19}$
					SE(B)	2.54×10^{19}
					CCA	5.25×10^{19}
P370	WM	0.22	0.015	1.11	Tensile	2.16×10^{19}
					Charpy-V/ ^a	$2.25 \times 10^{19}/2.22 \times 10^{19}$
					PCCV	2.25×10^{19}
					WOL 100X	2.25×10^{19}

^aCompound specimens.

most of the specimen materials had to be tested within the project. The fracture mechanics tests have been performed for both unirradiated and irradiated conditions mainly with three-point-bending (3PB) specimens.

Concerning the database generated by the experimental test program, the application of reference temperatures ($RT_{NDT(j)}$ versus RT_{T0} and $T_{K_{Ia}}$ versus $T_{Fa=4 \text{ kN}}$) is common in both steps for the assessment of the material behavior.

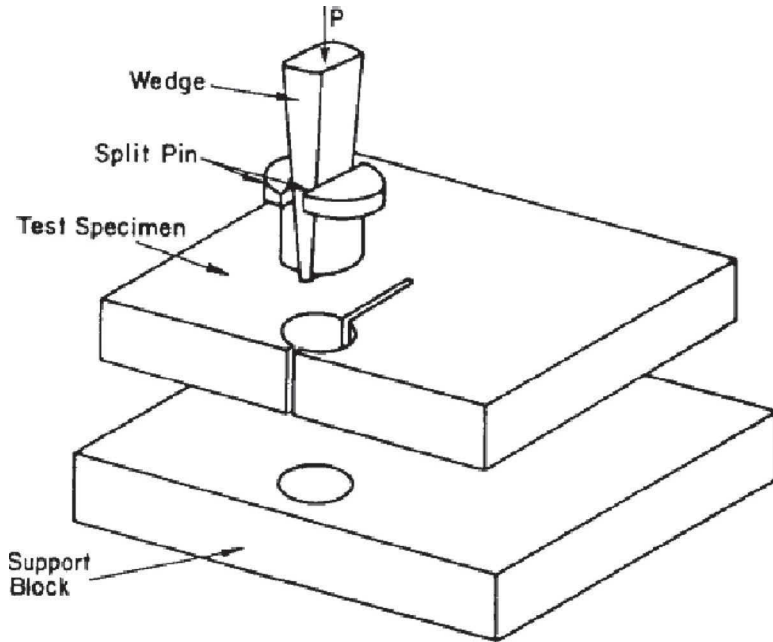


FIG. 5—Schematic view of the crack arrest test procedure.

Results and Discussion

Tensile Tests

For each of the irradiated specimen materials P141 BM, P7 BM, and P141 WM indicated in Table 4, three specimens were tested at temperatures of -50 , -100 , and 25°C . The three specimens of the P16 WM were tested at temperatures of 23 , 150 , and 275°C . The chosen test temperatures are representative for the temperature range required for the subsequent determination of the transition temperature T_0 according to ASTM E1921.

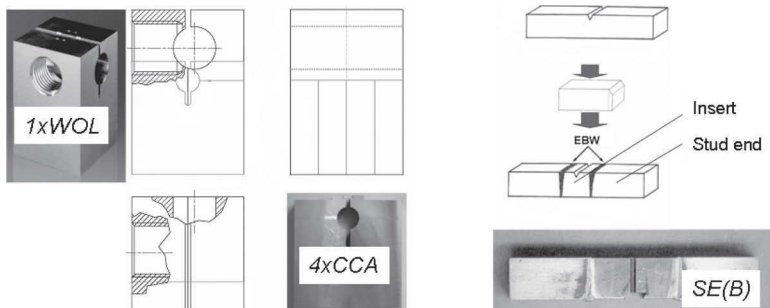


FIG. 6—Manufacturing of reconstituted specimens.

TABLE 4—*Experimental test matrix.*

Project	Type	Tensile	Charpy-V	Irradiated 3PB	WOL-X	Crack	
						Arrest	Unirradiated 3PB
P141	BM	T	Cv	PCCV	...	CCA	SE(B)
P7	BM	T	Cv	PCCV	...	CCA	SE(B)
				SE(B) ^a ,			
P147	BM	Existing	Existing	SE(B) 24 × 50 ^a	...	CCA	SE(B)
P141	WM	T	Cv	PCCV	...	CCA	SE(B)
P16	WM	T	Cv	PCCV	25X	CCA	Existing (CT (1T))
				SE(B)			
KS05	WM	Existing	Existing	(from WOL-00X)	...	CCA	Existing (WOL-X)
P370	WM	Existing	Existing	PCCV	100X	...	SE(B)

^aCompound specimens.

The tensile testing was performed according to the DIN EN 10002 Standard for Metallic Materials, Tensile Testing, Part 1: Method of Test at Ambient Temperature; Part 5: Method of Test at Elevated Temperature. The testing was also according to the international standard ISO 15579: 2000, "Metallic Materials—Tensile Testing at Low Temperature." The obtained yield and ultimate tensile strength values for each specimen material are summarized in Tables 5 and 6 for base and WMs and for both unirradiated and irradiated conditions, respectively.

The well known hardening effect due to irradiation is obviously shown at high neutron fluences and more emphasized for the specimen materials with higher Cu (P370 WM) and Ni (P16 WM) contents.

Charpy-V Impact Tests

The Charpy-V impact tests have been performed according to the DIN EN 10045-1 standard Charpy Impact Test on Metallic Materials. Charpy-V specimens were used with a cross section of 10 × 10 mm², 55 mm length, and a 2 mm deep 45° V-notch. A testing machine of PW 300 type (Wolpert Company) was operated in the hot cells laboratory to perform the tests at temperatures in the range between -50 and 275°C.

The testing machine was equipped with a digital monitor for the energy absorbed during fracture. The 300 J striker was operated with a semiconductor strain-gauge instrumentation in order to record the force-time diagrams during the fracture process according to DIN EN ISO 14556 Steel—Charpy V-notch Pendulum Impact Test—Instrumented Test Method.

The most essential Charpy-V test results including the reference temperatures RT_{NDT(j)} for both the unirradiated and irradiated state are summarized in Table 7, and the T₄₁ transition temperature shifts are shown in Fig. 7.

With respect to the irradiation induced material behavior two trends can be observed. The first one indicates low or moderate ΔT₄₁ values over the neutron fluence within usual scattering for the main part of the irradiated specimen materials. The second trend is related to the two WMs, P370 WM (0.22 % Cu)

TABLE 5—Yield and ultimate tensile strength for BMs.

$\Phi > 1$ MeV [n/cm ²]	Specimen Orientation	<i>T</i> (°C)	Yield (MPa)	Ultimate (MPa)
P141 BM				
0	T	RT	434	583
		−50	489	670
		−100	564	732
6.81×10^{18}	T	RT	471	602
		−50	541	664
		−100	620	731
P7 BM				
0	T	RT	450	610
		−50	501	687
		−100	593	762
3.81×10^{19}	T	RT	598	718
		−50	670	782
		−100	730	845
P147 BM				
0	L	275	417	594
		RT	488	626
		−100	626	760
1.09×10^{19}	L	275	457	625
		RT	543	660
		−80	626	761

and P16 WM (1.7 %Ni), which show a strong increase in ΔT_{41} over the fluence range concerned. This confirms the well known effect of high contents of copper and nickel, respectively, on the irradiation embrittlement of ferritic RPV steels.

Fracture Mechanical Tests

As indicated in Table 4 fracture mechanical tests have been performed for both unirradiated and irradiated conditions mainly with 3PB specimens of PCCV (manufactured from Charpy-V specimens) and of SE(B) type of dimension $10 \times 10 \times 55$ mm³. Some testing was also performed with SE(B) specimens of dimension $24 \times 50 \times 225$ mm³ and with WOL-100X and WOL-25X specimens.

The pre-fatigued specimens provided with side notches were tested according to ASTM E1921 standard [7] as well as the verification of the validity criteria, the test analysis, and the calculation of the characteristic values. According to the applied standard all test results were recalculated to the specimen thickness 1 T(=25.4 mm) in order to facilitate an evaluation, which is independent on the specimen thickness. Besides the suitability of WOL and conventional SE(B) specimens, the use of PCCV specimens for the fracture mechanics tests delivered good results.

TABLE 6—Yield and ultimate strength for WMs.

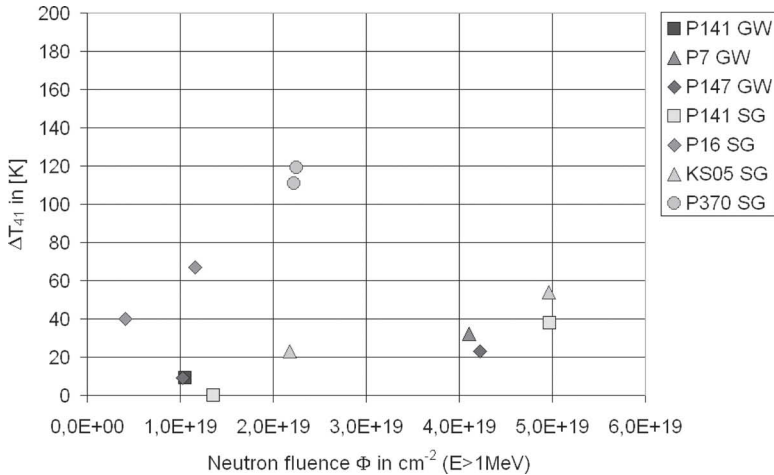
$\Phi > 1$ MeV [n/cm ²]	Specimen Orientation	T (°C)	Yield (MPa)	Ultimate (MPa)
P141 SG				
0	T	RT	516	604
		-50	552	648
		-100	619	706
8.84×10^{18}	T	RT	577	643
		-50	642	705
		-100	718	765
P16 WM				
0	T	200	476	550
		100	527	583
		RT	555	632
7.27×10^{18}	T	275	535	633
		150	571	622
		RT	659	713
KS05 WM				
0	T	275	527	612
		80	597	679
		RT	612	704
2.1×10^{19}	T	275	564	634
		80	619	687
		RT	654	719
5.32×10^{19}	T	275	605	669
		80	672	729
		RT	684	749
P370 WM				
0	T	280	534	616
		150	546	623
		RT	604	696
2.16×10^{19}	T	275	669	757
		75	772	823
		RT	821	860

In Fig. 8 a typical fracture toughness test evaluation in a K_{Jc} - T diagram with Master Curve application is shown where the fracture toughness is measured with PCCV specimens for the irradiated BM P7 BM. The diagram contains the 1, 5, 95, and 99 % percentiles, the Master Curve (50 % median) and the $T_0 \pm 50$ K intervals. The T_0 transition temperature at $100 \text{ MPa} \cdot \text{m}^{0.5}$ is used for the determination of the reference temperature $RT_{T_0} = T_0 + 19.4 \text{ K}$ according to Ref. 8 in order to compare the reference temperatures RT_{T_0} and $RT_{NDT(j)}$ with each other.

In Fig. 9 the reference temperatures RT_{T_0} are given for all specimen mate-

TABLE 7—Charpy-V test results.

Project	Type	Specimen Orientation	$\Phi > 1$ MeV [n/cm ²]	T_{41} (°C)	ΔT_{41} (K)	T_{68} (°C)	$T_{0.9}$ (°C)	T_{NDT} (°C)	$\text{RT}_{\text{NDT}(f)}$ (°C)
P141	BM	T-L	0	-18	0	-4	-14	-17	-17
P141	BM	T-L	1.05×10^{19}	-9	9	5	-2	...	-8
P7	BM	T-L	0	-7	0	13	2	-5	-5
P7	BM	T-L	4.11×10^{19}	25	32	59	41	...	27
P147	BM	T-L	0	-51	0	-36	-38	-17	-17
P147	BM	T-L	1.03×10^{19}	-42	9	-24	-29	-7	-8
P147	BM	T-L	4.22×10^{19} ^a	-28	23	-9	-17	...	6
P141	WM	T-L	0	-7	0	4	-3	-27	-12
P141	WM	T-L	1.36×10^{19}	-7	0	8	-1	...	-12
P141	WM	T-L	4.97×10^{19}	31	38	44	49	...	26
P16	WM	T-L	0	-55	0	-37	-47	-60	-58
P16	WM	T-L	4.14×10^{18}	-15	40	10	10	...	-18
P16	WM	T-L	1.16×10^{19}	12	67	42	61	...	9
P16	WM	T-L	5.22×10^{19} ^a	123	178	183	225	...	120
KS05	WM	T-L	0	-28	0	-7	-8	-35	-18
KS05	WM	T-L	2.18×10^{19}	-5	23	22	20	-5	5
KS05	WM	T-L	4.96×10^{19}	26	54	46	35	5	36
P370	WM	T-L	0	-12	0	-1	-10	-35	-28
P370	WM	T-L	2.22×10^{19}	99	111	142	122	...	83
P370	WM	T-L	2.25×10^{19}	107	119	124	124	80	91

^aData from another project.FIG. 7— T_{41} transition temperature shifts.

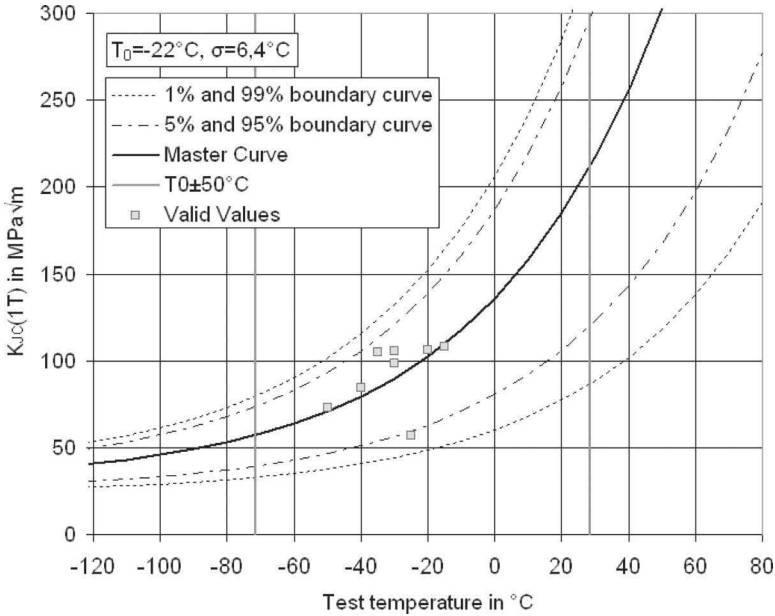


FIG. 8—Measured $K_{Jc}(1 T)$ values and Master Curve for T_0 determination for P7 BM ($\Phi = 4.45 \times 10^{19}$ n/cm², $E > 1$ MeV).

rials investigated. In order to confirm the apparent trends of increasing RT_{T_0} values with increasing neutron fluences some additional data from other research programs are also shown. Beside the obvious effect of high fluences (P7 BM) the well known effect of high copper (P370 WM) and high nickel (P16 WM)

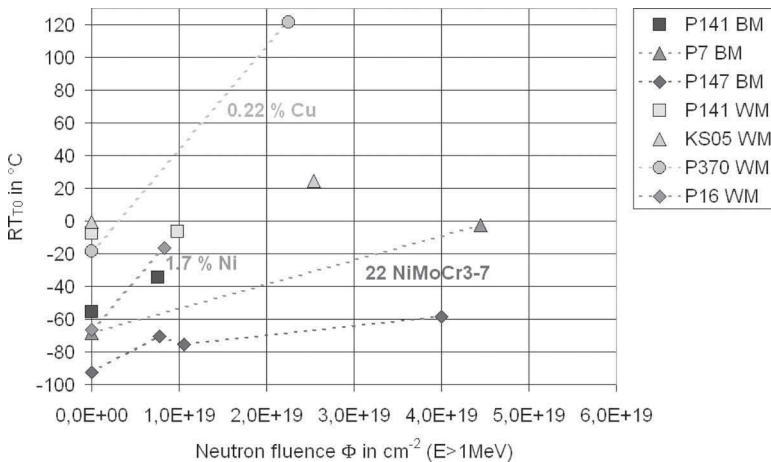


FIG. 9—Measured reference temperatures RT_{T_0} .

TABLE 8—Fracture mechanics test results.

Project	Type	Specimen Type	Specimen Orientation	$\Phi > 1$ MeV [n/cm ²]	T_0 (°C)	ΔT_0 (K)	RT_{T_0} (°C)
P141	BM	SE(B) 10×10	T-L	0	-75	0	-56
P141	BM	PCCV	T-L	7.59×10^{18}	-54	21	-35
P7	BM	SE(B) 10×10	T-L	0	-88	0	-69
P7	BM	PCCV	T-L	4.45×10^{19}	-22	66	-3
P147	BM	SE(B) 10×10	L-S/T-L	0	-112	0	-93
P147	BM	SE(B) 24×50 ^a	L-S	7.78×10^{18}	-90	22	-71
P147	BM	SE(B) 10×10 ^a	T-L	1.06×10^{19}	-95	17	-76
P147	BM	PCCV	T-L	4.00×10^{19} ^b	-78	34	-59
P141	WM	SE(B) 10×10	T-L	0	-27	0	-8
P141	WM	PCCV	T-L	9.79×10^{18}	-26	1	-7
P16	WM	CT(1T)	T-L	0	-86	0	-67
P16	WM	WOL-25X	T-L	6.21×10^{18} ^c	-10	16	9
P16	WM	PCCV	T-L	8.36×10^{18}	-36	50	-17
KS05	WM	WOL-25/50/100X	T-L	0 ^c	-20	0	-1
KS05	WM	SE(B) 10×10	T-L	2.54×10^{19}	5	25	24
P370	WM	SE(B) 10×10	T-L	0	-38	0	-19
P370	WM	WOL-100X	T-L	2.12×10^{19} ^c	103	141	122
P370	WM	PCCV	T-L	2.25×10^{19}	102	140	121

^aCompound specimens.

^bData from other project.

^cInvalid.

content and the impact of the manufacturing conditions (P7 BM versus P147 BM) for the 22 NiMoCr 3-7 on the reference temperature shift is clearly seen.

In Table 8 the values for the T_0 temperature at 100 MPa·m^{0.5}, its shift, and the reference temperature $RT_{T_0} = T_0 + 19.4$ K according to Ref. 8 are summarized for all specimen materials investigated.

The measured RT_{T_0} values indicate some influence of the specimen type and size on the reference temperature. For the P147 BM testing of the large SE(B) 24×50 mm² specimens resulted in a somewhat higher RT_{T_0} compared to the smaller SE(B) 10×10 mm² specimens irradiated to 1.06×10^{19} n/cm² in spite of the fact that the irradiation was lower (7.78×10^{18} n/cm²) and the orientation L-S for the large SE(B) specimens. However, the impact of the residual stresses caused by the manufacturing weld is unclear and still under investigation.

Unfortunately the few WOL-X data allowed no valid determination of T_0 according to the ASTM E1921 standard. Thus, the results of the irradiated P16 WM seem to confirm the known trend that testing PCCV specimens gives lower RT_{T_0} values than testing of WOL specimens however the T_0 based on only a few WOL-25X data is invalid. On the other hand the P370 WM data show almost no effect of specimen size, but the T_0 based on WOL-100X testing is not valid.

Another point of interest is whether the measured fracture toughness data

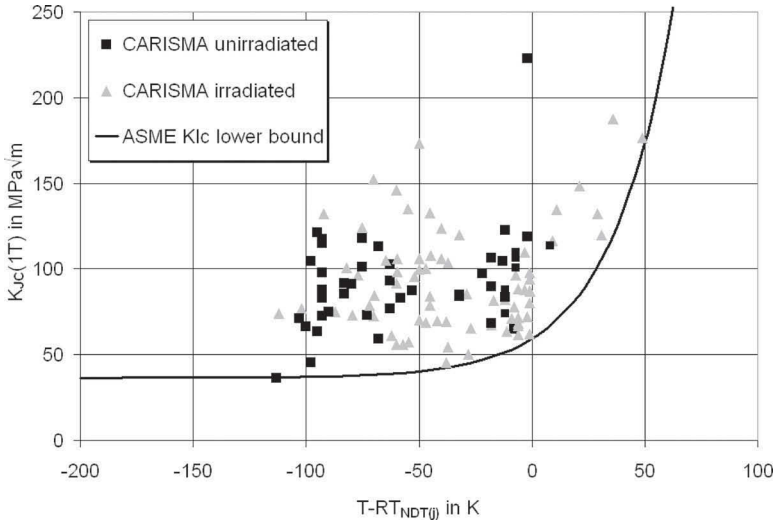


FIG. 10—Fracture mechanics test results normalized by $(T - RT_{NDT(j)})$.

are enveloped by the lower bound curve of the ASME Boiler and Pressure Vessel Code [10] representing conservative values based on measured static initiation K_I values. The measured fracture toughness data for static initiation are shown in Figs. 10 and 11 together with the ASME K_{Ic} lower bound curve. The data measured at test temperature T are normalized with $T - RT_{NDT(j)}$ and $T - RT_{T_0}$, respectively. Obviously, the measured data are enveloped by the ASME lower bound curve for both unirradiated and irradiated conditions and for both

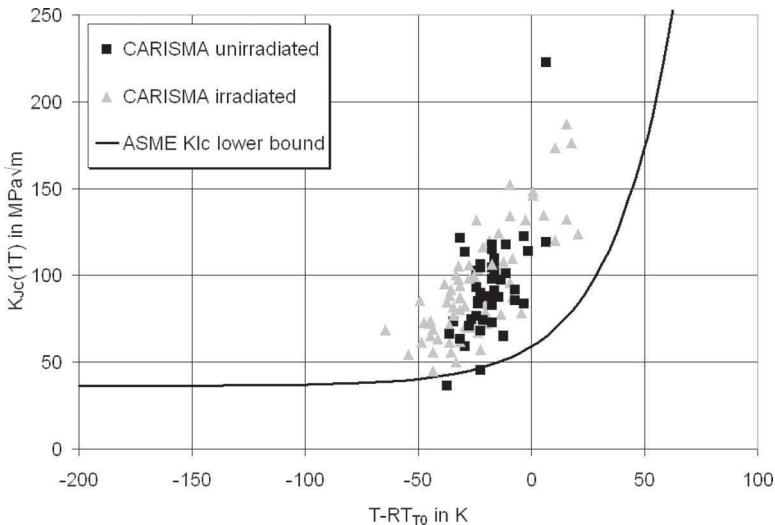


FIG. 11—Fracture mechanics test results normalized by $(T - RT_{T_0})$.

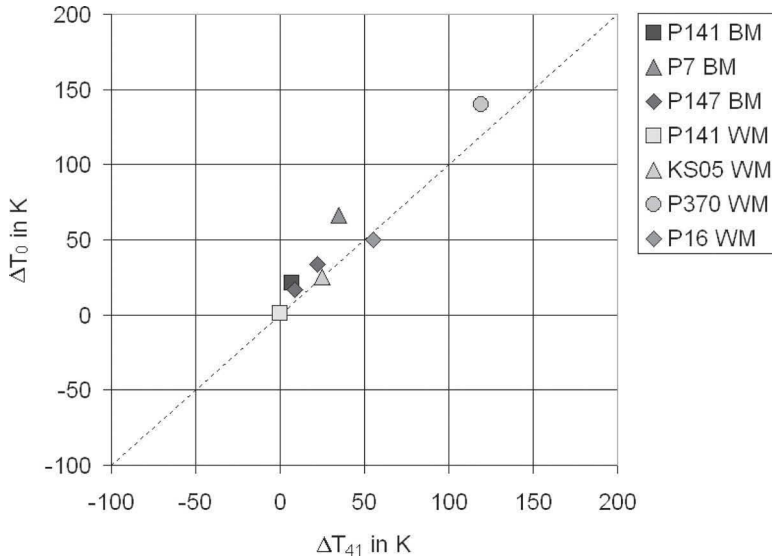


FIG. 12—Measured ΔT_0 versus ΔT_{41} adjusted to fluence.

reference temperatures $RT_{NDT(j)}$ and RT_{T_0} with the exception of one and two data points, respectively, lying on or slightly below the lower bound curve. These exceptions originate from testing the unirradiated P147 BM with a very low $T_0 = -112^\circ\text{C}$ at very low temperatures at -130 and -115°C . Besides possible inhomogeneous material areas the scattering of testing small SE(B) specimens and the missing of any significant plasticization at such low test temperatures might be an explanation for these few exceptions.

For the irradiated condition the data confirm the conservative layout of the ASME K_{IC} lower bound curve and thus indicate that the toughness properties of the tested specimen materials are representative for RPV steels. Moreover, the validity of the RT_{T_0} concept for German RPV steels as reported in Ref. 11 can be confirmed with the obtained test results.

With regard to the comparison between both concepts RT_{NDT} and RT_{T_0} (Master Curve), the existence of any correlations between ΔT_0 versus ΔT_{41} and $RT_{NDT(j)}$ versus RT_{T_0} is also of importance.

In Fig. 12 the measured ΔT_0 data are plotted against the measured ΔT_{41} data. The correlation between ΔT_0 and ΔT_{41} is relatively good and apparently linear for both base and weld materials.

In Fig. 13 the measured $RT_{NDT(j)}$ values (fluence adjusted) versus the measured RT_{T_0} values (valid T_0 data for irradiated condition) are shown. The measured data indicate a general trend of $RT_{NDT(j)} > RT_{T_0}$ for BMs. For the WMs $RT_{NDT(j)}$ is in some cases lower than RT_{T_0} .

A possible explanation might for this different behavior be the condition of the acceptance drop-weight tests for the WMs and the manufacturing process itself at that time. This may result in T -NDT data for WMs from the acceptance tests being not always such conservative as for the BMs. Thus, the trend for the

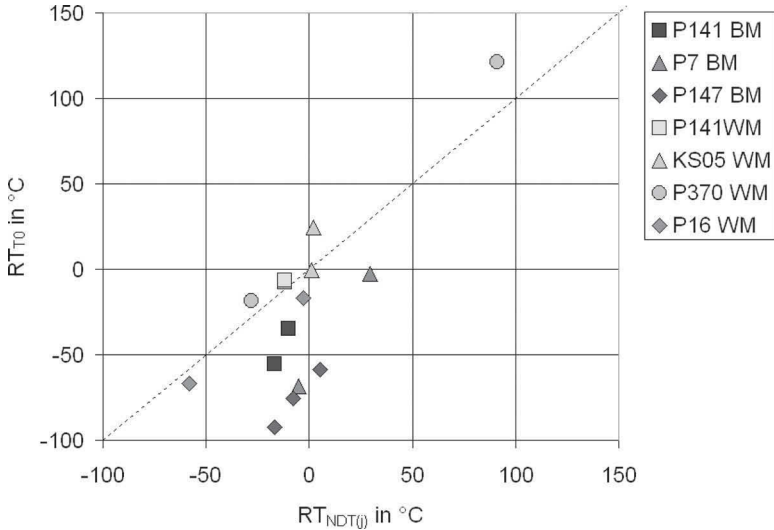


FIG. 13—Measured RT_{T_0} versus $RT_{NDT(j)}$ adjusted to fluence.

BMs with $RT_{NDT(j)}$, which is significantly higher than RT_{T_0} , is apparently originated from the very conservative determination of RT_{NDT} in the unirradiated condition where the T -NDT is the leading temperature, whereas for the WMs the $T_{AV}(68 \text{ J})$ from Charpy-V testing is the leading temperature. Moreover, the acceptance drop-weight tests were performed for very tough unirradiated materials. In this context base and WMs seem to deliver different results in that test. For WMs it seems to be a crack initiation test. Therefore, the correlation with RT_{T_0} is very well. But for base metals the test seems to be more like a crack arrest test, which leads to higher $RT_{NDT(j)}$ values compared to RT_{T_0} .

In the German Safety Standard KTA 3203 [12], a so-called RT_{limit} curve was introduced, which defines an upper bound for the reference temperature as a function of the neutron fluence ($E > 1 \text{ MeV}$). The RT_{limit} curve is based on measured German RPV surveillance data and is valid for all German pressure vessel materials of PWRs and BWRs, forgings and plates, 22 NiMoCr 3-7 and 20 MnMoNi 5-5 BMs, and weld materials with $\text{Cu} \leq 0.15 \%$ and $\text{Ni} \leq 1.1 \%$. This RT_{limit} curve was also confirmed by U.S. and French irradiation surveillance results of appropriate materials under comparable irradiation conditions [13].

Both measured $RT_{NDT(j)}$ and RT_{T_0} values indicate a comparatively low irradiation embrittlement and are enveloped with a comfortable safety margin by the upper bound curve RT_{limit} of KTA 3203 for all specimen materials where the Cu and Ni contents are in the valid range (maximum of 0.15 % Cu and 1.1 % Ni) according to the standard as shown in Fig. 14. Even the reference temperatures of the specimen materials with higher contents of Cu and Ni (P370 WM and P16 WM, respectively) are still below the RT_{limit} curve for fluences of around $1 \times 10^{19} \text{ n/cm}^2$ ($E > 1 \text{ MeV}$), and the safe operation of the RPVs concerned was ensured in the past according to the safety standards.

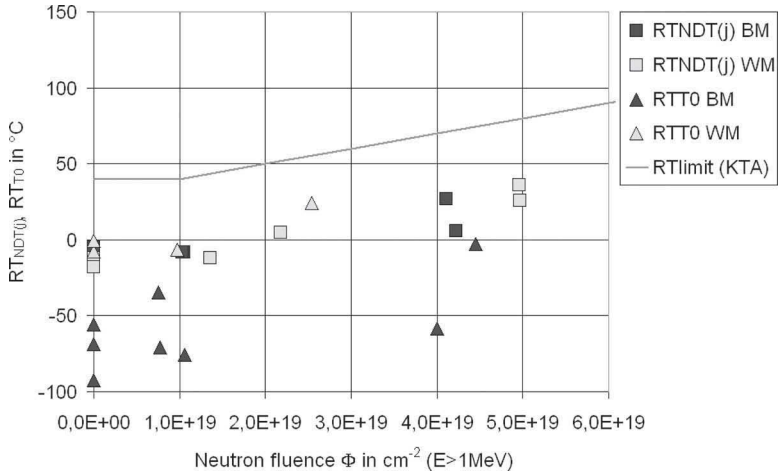


FIG. 14—Measured RT_{T_0} and $RT_{NDT(j)}$ data with $Cu \leq 0.15\%$ and $Ni \leq 1.1\%$ versus RT_{limit}

Crack Arrest Tests

The crack arrest tests have been performed according to ASTM E1221 [9] using CCA specimens. The irradiated specimens were manufactured from irradiated WOL-100X specimens using the compound technique. In the CCA specimens a brittle weld seam was produced in the starter notch by electron beam welding without any filler metal. Knife edges, starter hole, starter notch, and side grooves were produced by wire-electro discharge machining.

In Fig. 15 the K_{Ia} values measured for the BMs are plotted against $T - RT_{NDT(j)}$ at which the $RT_{NDT(j)}$ was interpolated to the neutron fluence of the fracture mechanic specimens. The results confirm the lower bound K_{Ia} curve according to ASME [10] and the real existence of the crack arrest phenomenon for irradiated RPV steels.

For the WMs that exhibit mainly a higher irradiation embrittlement, the manufacturing of CCA specimens from irradiated material is pretty difficult. The reason is related to annealing effects caused by the manufacturing process. The welding procedure needed to create a brittle zone at the tip of the starter notch in the CCA specimen leads to annealing effects in the irradiated material. These annealing effects cause a recovery process at the crack tip and lead to a crack arrest in the HAZ without further instable crack growth. Moreover, WMs have a lower carbon content, which makes it more difficult to achieve the required hardening in the tip of the starter notch.

Figure 16 shows the broken crack surfaces of two irradiated CCA specimen materials, the P7 BM and the P16 WM.

For the irradiated P7 BM the first crack arrest occurs in the HAZ (pop in) without any influence on the determined crack arrest value because the crack did arrest finally in the middle of the specimen. A completely different behavior

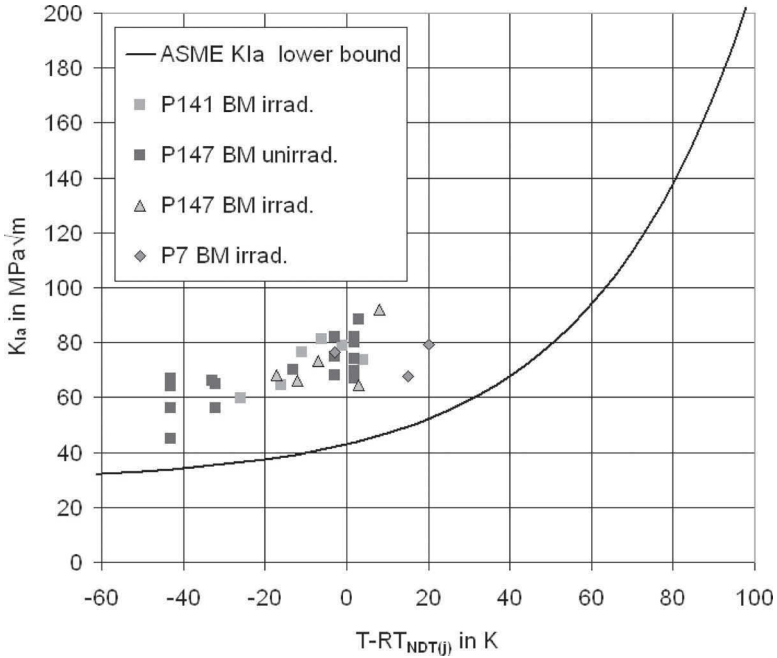


FIG. 15—Crack arrest test results normalized by $(T - RT_{NDT(j)})$ for BMs.

was observed for the irradiated P16 WM where the crack did arrest in the HAZ (pop in), but then no further unstable crack initiation occurred.

As a remedy action for this problem so-called Duplex specimens with a pre-hardened specimen part are to be used instead of CCA specimens. The qualification tests for the Duplex specimens are still ongoing.

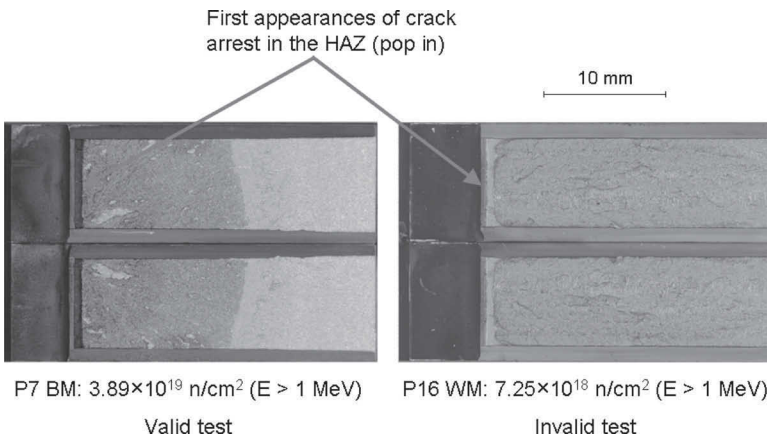


FIG. 16—Broken surfaces of CCA specimens P7 BM and P16 WM.

TABLE 9—Reference temperature $T_{K_{Ia}}$ and T_{Fa4} kN for BMs.

Project	Type	$T_{K_{Ia}}$ (°C)	T_{Fa4} kN (°C)
P141	BM	14 (6.87×10^{18} cm ⁻²)	14 (1.05×10^{19} cm ⁻²)
P7	BM	62 (3.89×10^{19} cm ⁻²)	51 (4.11×10^{19} cm ⁻²)
P147	BM	18 (1.17×10^{19} cm ⁻²)	17 (1.03×10^{19} cm ⁻²)

In order to adjust the K_{Ia} lower bound curve for the specimen materials tested two types of reference temperatures have been applied, a reference temperature $T_{K_{Ia}}$ defined by the Master Curve concept at $K_{Ia}=100$ MPa \sqrt{m} from CCA tests and a reference temperature T_{Fa4} kN defined at a crack arrest load of $F_a=4$ kN received from the load-displacement curves of instrumented Charpy-V tests.

Taking into account the different neutron fluences accumulated by the CCA and the Charpy-V specimens, the data obtained indicate a linear correlation in the form $T_{K_{Ia}}=T_{Fa4}$ kN + ΔT as described by other studies reported in Ref. 14, where ΔT was given as 12 K. This is an encouraging result, although the few data obtained allow only a general trend.

It is pointed out that the use of $T_{K_{Ia}}$ instead of $RT_{NDT(j)}$ for normalizing the K_{Ia} data in Fig. 15 would result in an even increased safety margin to the ASME K_{Ia} lower bound curve since the $T_{K_{Ia}}$ values in Table 9 are essentially higher than the $RT_{NDT(j)}$ values in Table 7 for the specimen materials concerned.

Summary and Conclusions

The CARISMA program has produced a new database to characterize the fracture toughness of pre-irradiated original RPV materials being representative for all four German PWR construction lines. For this purpose tensile, Charpy-V impact, fracture toughness, and crack arrest tests have been performed for neutron fluences beyond the end of life range. RPV steels with optimized chemical composition and with high copper or high nickel contents were examined in this study. Both the RT_{NDT} and the Master Curve concepts were applied to the assessment of the generated data in order to compare both approaches. The most essential results of the project are the following.

- (1) The ASME K_{Ic} lower bound curve was confirmed by the measured fracture toughness data for the irradiated condition with only a very few exceptions for the unirradiated condition.
- (2) The measured data indicate a good correlation between ΔT_0 and ΔT_{41} .
- (3) A general trend of $RT_{NDT(j)} > RT_{T_0}$ was found for the tested BMs but not for the tested WMs. This behavior is apparently originated from the too conservative determination of RT_{NDT} for the BM in the unirradiated condition.
- (4) The measured $RT_{NDT(j)}$ and RT_{T_0} values are both enveloped with a comfortable safety margin by the upper bound curve RT_{limit} of the German safety standard KTA 3203 for all specimen materials where the Cu and

Ni contents are in the valid range (max. 0.15 % Cu and 1.1 % Ni) underpinning that both concepts are applicable.

- (5) The already known effects of high contents of Cu and Ni on irradiation embrittlement could be confirmed.
- (6) Some indications were found for the influence of specimen type and size and manufacture on the reference temperature.
- (7) The measured crack arrest toughness data for irradiated BMs are enveloped by the ASME K_{Ia} lower bound curve.
- (8) A still limited suitability of irradiated CCA specimens manufactured from irradiated specimens was found for WMs. Therefore, so-called Duplex specimens with a pre-hardened specimen part are intended to be used instead of the CCA specimens. The qualification tests for the Duplex specimens are still ongoing.
- (9) As a trend a reasonable correlation was found between $T_{Fa4\ kN}$ (Charpy-V) and $T_{K_{Ia}}$ (Master Curve) for the BMs.

The available results made a good point that crack arrest is a reliable phenomenon that exists with no doubt for irradiated RPV steels; however some issues such as the manufacturing of suitable crack arrest specimens are still remaining.

Furthermore, the results show that optimized manufacture specifications are of big benefit even after long operation times compared to less designed material with lower fracture toughness.

In the future the generated database will be extended by additional specimen materials irradiated to higher neutron fluences. Therefore, a follow up project was already launched with a specific focus on long term effects. In this context the so far available results from microstructural examinations for some of the CARISMA materials [15] are intended to complement by additional studies using small angle neutron scattering, atom probe tomography, and other techniques.

Acknowledgments

The project was supported financially by the VGB (German utilities, NPP Gös-gen), the German Ministry of Economics and Technology (sponsorship number 1501284), NPP Borselle (The Netherlands), and NPP Trillo (Spain). For that the authors are very grateful.

References

- [1] Keim, E., Langer, R., and Hein, H., "Crack Initiation and Arrest of Irradiated RPV-Steels: A National Project on German RPV Weld and Base Materials," *Proceedings of 2004 ASME/JSME Pressure Vessels and Piping Conference*, The Pressure Vessels and Piping Division, ASME, PVP2004-2552, San Diego, CA, July 25-29, 2004, pp. 121-124.
- [2] Keim, E., Langer, R., Schnabel, H., and Hein, H., "Crack Initiation and Arrest of Irradiated RPV-Steels: A National Project on German RPV Weld and Base Materi-

- als," *Proceedings of Fontevraud 6, Contribution of Materials Investigations to Improve the Safety and Performance of LWRs*, SFEN (French Nuclear Energy Society), France, September 18–22, 2006, pp. 793–803.
- [3] Hein, H., Keim, E., and Schnabel, H., "Das Projekt CARISMA zur Ermittlung von Bruchmechanikkennwerten an vorbestrahlten Proben für die deutschen DWR-Baulinien-Status und Zwischenbericht," *Proceedings of the 32nd MPA-Seminar, Werkstoff & Bauteilverhalten in der Energie & Anlagentechnik*, October 5–6, 2006, Stuttgart, Germany, pp. 12.1–12.20.
 - [4] Forschungsprogramm Komponentensicherheit (FKS), "Einfluß der Neutronenbestrahlung auf die Eigenschaftsänderungen der Werkstoffe von Reaktordruckbehältern für Leichtwasserreaktoren," *Final Report (in German)*, Staatliche Materialprüfungsanstalt (MPA), University of Stuttgart, October 1996.
 - [5] Rhoades, W. A. and Childs, R. L., *TORT-DORT Two- and Three-Dimensional Discrete Ordinates Transport, Version 2.7.3, RSICC Code Package CCC-543*, 1993, Oak Ridge National Laboratory, Oak Ridge, Tennessee.
 - [6] "RSICC Data Library Collection BUGLE 96, Contributed by Oak Ridge National Laboratory, Oak Ridge, TN, 1996, Coupled 47 Neutron, 20 Gamma-Ray Group Cross Section Library Derived from ENDF/B-VI for LWR Shielding and Pressure Vessel Dosimetry Applications," NEA Data Bank Package-ID: DLC-0185/01, Program-Name: ZZ-BUGLE-96.
 - [7] ASTM E1921–05, 2005, "Standard Test Method for Determination of Reference Temperature, T_0 , for Ferritic Steels in the Transition Range," *Annual Book of ASTM Standards*, Vol. 03.01, ASTM International, West Conshohocken, PA.
 - [8] ASME Boiler and Pressure Vessel Code: An American National Standard, Code Case N-629, "Use of Fracture Toughness Data to Establish Reference Temperature for Pressure Retaining Materials," Section XI, Division 1, ASME, New York, May 7, 1999.
 - [9] ASTM E1221-96, re-approved 2002, "Standard Test Method for Determining Plane-Strain Crack-Arrest Fracture Toughness K_{Ia} of Ferritic Steels," *Annual Book of ASTM Standards*, Vol. 03.01, ASTM International, West Conshohocken, PA.
 - [10] 2007 ASME Boiler and Pressure Vessel Code, Section XI, Division 1, Appendix A, A-4200, "Fracture Toughness," ASME, 2007 Edition, July 1, 2007.
 - [11] Keim, E., Siegele, D., and Nagel, G., "Validation of RT_{T0} for German Reactor Pressure Vessel Steels," *Proceedings of the ASME Pressure Vessels and Piping Division Conference*, The Pressure Vessels and Piping Division, ASME, PVP2005–71197, July 17–21, 2005, Denver, CO, pp. 1–3.
 - [12] KTA 3203 (6/01), 2001, "Surveillance of the Irradiation Behavior of Reactor Pressure Vessel Materials of LWR Facilities," Safety Standards of the Nuclear Safety Standards Commission (KTA), Salzgitter, Germany.
 - [13] Bartsch, R., Langer, R., and Nagel, G., "New German KTA Rule 3203 for Irradiation Surveillance Evaluation and Application in the Safety Analysis of RPV," *Proceedings of Fontevraud 5, Contribution of Materials Investigations to the Resolution of Problems Encountered in Pressurized Water Reactors*, SFEN (French Nuclear Energy Society), France, September 23–27, 2002.
 - [14] Müller, K. and Pusch, G., "Use of Charpy Impact Testing to Evaluate Crack Arrest Fracture Toughness," from *Charpy to Present Impact Testing*, D. Francois and A. Pineau, Eds., Elsevier Science Ltd. and ESIS, 2002, pp. 263–270.
 - [15] Bergner, F., Ulbricht, A., Hein, H., and Kammel, M., "Flux Dependence of Cluster Formation in Neutron Irradiated Weld Material," *J. Phys.: Condens. Matter*, Vol. 20, 2008, pp. 104262.

Naoki Soneda,¹ Kenji Dohi,² Akiyoshi Nomoto,² Kenji Nishida,²
and Shiori Ishino³

Embrittlement Correlation Method for the Japanese Reactor Pressure Vessel Materials

ABSTRACT: A new embrittlement correlation method developed for the Japanese reactor pressure vessel (RPV) steels is presented. The Central Research Institute of Electric Power Industry and the Japanese electric utilities conducted a project to develop a new embrittlement correlation method for the Japanese RPV steels based on the understandings on the mechanisms of the RPV embrittlement. In addition to the information from the literatures, we generated new information by characterizing the microstructural changes in the surveillance materials of the Japanese commercial reactors. We found that in low Cu materials, solute atom clusters containing little or no Cu atoms are formed at relatively low fluence of 3×10^{19} n/cm², E > 1 MeV. The volume fraction of the solute atom clusters has a good correlation with the Charpy transition temperature shift regardless of the Cu content. We also found that the microstructure of the boiling water reactor surveillance material is different from that of the archive material irradiated in material testing reactor. The understandings on the RPV embrittlement mechanisms were formulated using a set of rate equations, and the coefficients of the equations were optimized using the ΔRT_{NDT} values of the Japanese surveillance database. This method considers the effect of neutron flux. Only one set of coefficients was developed, and they are independent of the product form. Predictions of the new embrittlement correlation method were compared with

Manuscript received September 19, 2008; accepted for publication January 2, 2010; published online February 2010.

¹ Central Research Institute of Electric Power Industry, 2-11-1 Iwado-kita, Komae, Tokyo 201-8511, Japan (Corresponding author), e-mail: soneda@criepi.denken.or.jp

² Central Research Institute of Electric Power Industry, 2-11-1 Iwado-kita, Komae, Tokyo 201-8511, Japan.

³ Professor Emeritus, Univ. of Tokyo, 13-4 Iwado-minami 3-chome, Komae-shi, Tokyo 201-0005, Japan.

Cite as: Soneda, N., Dohi, K., Nomoto, A., Nishida, K. and Ishino, S., "Embrittlement Correlation Method for the Japanese Reactor Pressure Vessel Materials," *J. ASTM Intl.*, Vol. 7, No. 3. doi:10.1520/JAI102127.

Copyright © 2010 by ASTM International, 100 Barr Harbor Drive, PO Box C700, West Conshohocken, PA 19428-2959.

those of the recent U.S. correlation method as well as the U.S. surveillance data. The comparison shows the characteristics of the present method.

KEYWORDS: reactor pressure vessel, neutron irradiation embrittlement, microstructural characterization, embrittlement correlation, surveillance data

Introduction

The accurate understanding and prediction of the neutron irradiation embrittlement of reactor pressure vessel (RPV) materials are very important to ensure the structural integrity of nuclear power plants. The embrittlement of Japanese RPV materials of commercial reactors is monitored following the embrittlement surveillance program specified in the Japan Electric Association Code, JEAC4201-2004 [1], and the amount of embrittlement during the plant life is predicted using the embrittlement correlation equation that is also specified in JEAC4201-2004. The embrittlement correlation equation of JEAC4201-2004 was developed and issued in 1991 based on the understanding of embrittlement in the 1980s using surveillance data available at that time together with surveillance data from the United States and test reactor irradiation data. Since then, a large amount of surveillance data has been compiled, enabling us to develop a new embrittlement correlation method primarily based on domestic surveillance data.

On the other hand, activities to develop a new embrittlement correlation method have been conducted worldwide. The U.S. Nuclear Regulatory Commission (NRC) developed a new embrittlement equation in 1996 [2], and ASTM issued a modified version of the embrittlement equation in ASTM E900-02 in 2002 [3]. More recently, another embrittlement correlation equation was developed by Oak Ridge National Laboratory (ORNL) under the sponsorship of U.S. NRC [4]. A very important characteristic of these approaches is that they have been developed on the basis of the understanding of embrittlement mechanisms, and thus the equations are called “mechanism-guided” embrittlement correlations.

Under these circumstances, the Central Research Institute of Electric Power Industry (CRIEPI) and the Japanese electric power companies have decided to develop a new embrittlement correlation method for RPV materials in Japan. The first version of the embrittlement correlation method was developed in 2004. The method adopted a new approach to predict the microstructural changes in materials during irradiation using a set of rate equations, and the predicted microstructural changes were correlated with the embrittlement, i.e., transition temperature shifts. Since this first development, a new project to perform detailed microstructural analyses of various Japanese surveillance materials has been conducted to verify and improve the correlation method. Some new findings have been obtained through this project, especially on the embrittlement mechanism of low-copper materials and the effect of flux on the microstructural evolution and embrittlement.

In this paper, the development of a new revised embrittlement correlation method for Japanese RPV materials is described. The microstructural charac-

teristics of some of the Japanese RPV materials are summarized focusing on the effect of the solute atoms and the flux effect. The correlation between the microstructures and the mechanical properties of the materials is also presented. We then describe a new embrittlement correlation method that consists of a set of rate equations to model the microstructural changes and the resulting changes in mechanical properties. The application of the new method to Japanese surveillance data is demonstrated, followed by the comparison with the U.S. surveillance data.

Microstructural Changes in RPV Materials during Irradiation

General Consensus on Embrittlement Mechanisms

Extensive efforts through experiments and theoretical simulations have led to a general consensus on the embrittlement mechanisms [5]. The three-dimensional atom probe (3DAP) technique, positron annihilation (PA) measurement, small angle neutron scattering, and field-emission gun-scanning transmission electron microscopy (TEM) combined with mechanical tests have been used as powerful techniques in experiments in the 1990s and 2000s, while molecular dynamics and kinetic Monte Carlo simulation techniques have played an important role in simulations. Embrittlement is primarily caused by the formation of copper-enriched clusters (CEC)/copper-rich precipitates (CRP) and by (stable) matrix damage (S)MD. CECs, or CRPs, are solute atom clusters in which the content of impurity copper atoms is greatly enriched. For example, the bulk copper content in high copper material is 0.2 wt %, while the copper content in a cluster can be more than 10 wt %. The clusters also contain other solute atoms such as nickel, manganese, silicon, and sometimes phosphorus [6–8]. Bulk copper content is the most important parameter in describing the contribution of CEC to embrittlement, but the synergetic effect of nickel with copper is also well known [9]. The mean diameter of such clusters is typically 2–3 nm, and such nanoscale clusters act as obstacles to dislocation motion leading to the hardening of the material and thus embrittlement. MD is another type of hardening center that causes hardening and embrittlement. Point defect clusters such as dislocation loops and vacancy clusters and point defect-solute atom complexes are the candidates for the nature of MD. MD is the main contributor to embrittlement in low-copper materials, while both MD and CECs contribute to the embrittlement of copper-containing materials. The simple sum of the contributions of CEC and MD is the total amount of embrittlement [2,3].

An important concern is the effect of neutron flux. The contribution of CEC to embrittlement reaches a plateau, showing saturation of the contribution, but the time (or neutron fluence) required to reach the plateau is affected by the neutron flux (dose rate). In the flux levels of commercial reactors and their surveillance program conditions, lower flux irradiation of copper-containing materials, with Cu content > 0.1 wt %, results in larger embrittlement [10], while no flux effect has been identified in low-copper materials.

The other important concern is the so-called “late-blooming phase,” which

consists of nickel and manganese (and silicon), without copper [11,12]. This phase is expected to occur primarily in high-nickel RPV materials irradiated to high fluences.

Most of the above observations are for materials irradiated in test reactors, and limited information is available for surveillance materials irradiated in commercial reactors. Furthermore, the copper content of Japanese RPV steels is in general very low, and the microstructural information on such relatively low-copper material is also limited. Thus, we decided to investigate some of the Japanese RPV surveillance materials to see if the above general consensus is still valid for RPV materials irradiated in commercial reactors.

Summary of the Microstructural Analyses of Surveillance Materials

Materials from Pressurized Water Reactors

Summary of the Microstructures Microstructural analyses of several surveillance materials irradiated in the Japanese commercial pressurized water reactor (PWR) plants were performed. Materials having from medium Cu content to very low Cu content were investigated using such techniques as 3DAP analysis, PA spectroscopy of both lifetime and coincidence Doppler broadening measurements, TEM, and Vickers hardness tests. Of course, Charpy impact test results have already been obtained for these materials in the surveillance programs. The details of the microstructural analyses as well as the experimental details can be found elsewhere [13], and here we just describe the summary of the experimental results.

Table 1 shows the summary of the results obtained from the four surveillance materials. The highest copper content among the materials investigated is 0.12 wt %, which is relatively high for Japanese RPV materials. The lowest copper content is 0.03 wt %. The neutron fluence of the materials ranges from 3×10^{19} to 6×10^{19} n/cm², $E > 1$ MeV. Characteristics of the solute atom clusters such as number density, size, and volume fraction are obtained by 3DAP measurement. The cluster size is the Guinier diameter, which is defined as the radius of gyration multiplied by $2 \times (5/2)^{1/2}$, and the cluster volume fraction was calculated as the cluster number density multiplied by the average cluster volume divided by the total volume analyzed.

In material A, clusters contain nickel, manganese, and silicon atoms in addition to copper atoms. The average copper content in the clusters is relatively high compared with the other materials from B to D. The cluster number density is also the largest, although the neutron fluence is not necessarily the largest. These characteristics of the clusters in the material A are very consistent with the general consensus on CECs. Material B is a low-copper content material with 0.07 wt % copper irradiated to high fluence. In recent U.S. studies on embrittlement correlation [2,3], it is obtained from the analysis of surveillance data that there is no contribution of CEC (CRP) to the embrittlement in materials with copper content of less than 0.072 wt %. Our observation shows that even in such low-copper materials as material B, the well-developed solute atom clusters are formed with relatively high number density. As shown in Table 1, the average cluster diameter of the material B is as large as 3.5 nm,

TABLE 1—Summary of the microstructural analyses of the PWR surveillance materials.

ID	Fluence ($\times 10^{19}$ n/cm ² , $E > 1$ MeV)	Bulk Chemical Composition				Cluster Characteristics				Cluster Composition				Dislocation Loops	
		Cu (wt %)	Ni (wt %)	P (wt %)	Guinier Diameter (nm)	Number Density ($\times 10^{22}$ m ⁻³)	Volume Fraction	Cu (at. %)	Ni (at. %)	Mn (at. %)	Si (at. %)	Diameter (nm)	Number Density ($\times 10^{22}$ m ⁻³)		
A	4.4	0.12	0.58	0.014	3.1	23	0.0043	5.8	9.9	5.5	6.6	2.6	1.8		
B	5.8	0.07	0.59	0.009	3.5	12	0.003	1.8	10.8	5.0	8.9		
C	6.3	0.03	0.57	0.007	3.1	5.6	0.0011	0.3	11.7	5.7	11.8	2.3	1.9		
D	3.1	0.04	0.74	0.005	3.1	2.3	0.0005	0.3	12.8	6.2	11.5		

resulting in the mean volume of the clusters in material B being 30 % larger than that of material A. In spite of the low bulk copper content, most of the solute atom clusters in the material B include copper atoms. The average copper content of 1.8 at. % is much lower than that of the material A as expected. It is interesting to see that the chemical composition of the solute atom clusters in the material B is similar to that of the material A except for the copper content. It should be noted that some of the clusters were found to include no copper atoms, particularly when the clusters are relatively small in the material B.

Solute atom cluster formation was also observed even in the material C, which has a very low-copper content of 0.03 wt %. Although the number density is less than half of the material B, the important point regarding the material C is that solute atom clusters containing no copper atoms are clearly and uniformly formed. The average cluster diameter is 3.1 nm, which is almost the same size as those of other materials. The clusters basically consist of nickel, silicon, and manganese atoms. It is interesting to see that the silicon content is large. Material D has a similar copper content to the material C but irradiated to a lower fluence than that of the material C. In this material, solute atom clusters with no copper atom were again observed. The cluster number density is less than half of that of the material C, and this may be due to the fact that the fluence of material C is almost half of the material D. In spite of the very low number density, the cluster size of 3.1 nm is comparable with those of the other materials. The cluster composition of the material D is very similar to that of the material C. The formation of the solute atom clusters with less or no copper atom has already been reported elsewhere [14–16] for low-copper materials irradiated at high flux. However, the results of materials C and D show that such solute atom cluster formation occurs even in low-copper materials irradiated at low flux of the commercial reactors.

TEM observations were performed on materials A and C, and the formation of dislocation loops was observed. Most of the dislocation loops have a Burgers vector of $a_0\langle 100 \rangle$ in both materials. The mean diameters of the loops of materials A and C are 2.6 and 2.3 nm, respectively, and the loop number densities are 1.8×10^{22} and $1.9 \times 10^{22} \text{ m}^{-3}$, respectively. The number density of dislocation loops in material A is almost one-tenth of that of solute atom clusters, suggesting that the contribution of dislocation loops to embrittlement is very small in this material. On the other hand, in material C, the number density of dislocation loops is one-third of that of solute atom clusters. Thus, in this material, the dislocation loops should have some contribution to the embrittlement.

Correlation with the Mechanical Property Changes The above observations are not necessarily consistent with the general consensus on the embrittlement mechanism summarized in the General Consensus on Embrittlement Mechanisms section of this chapter. In the conventional understanding, solute atom clusters are CECs that are basically formed by the clustering of copper impurity atoms beyond the solubility limit. This mechanism is consistent with the microstructure of material A, which has a relatively high copper content of 0.12 wt %. On the other hand, in the other materials having lower copper contents,

it is clear that a mechanism other than the clustering of supersaturated copper atoms causes the formation of solute atom clusters because the clusters contain very little copper atoms. However it is interesting to see that the copper content of the solute atom clusters in these low-copper materials still depends on the bulk copper content, and the cluster number density of material B is larger than that of material C, which has a lower copper content than material B but a similar nickel content and neutron fluence to material B. This suggests that the copper atoms do not form CECs in low-copper materials, but they are still effective in the nucleation of solute atom clusters.

Since such elements as nickel, silicon, and manganese are alloying elements in RPV steels, it is highly probable that the formation of solute atom clusters with these elements without copper may not be explained only by a thermodynamics point of view. In the atom probe analyses of these materials, it is frequently observed that these elements are enriched at dislocations and grain boundaries, both of which are sinks of point defects. Therefore, one possible mechanism of such solute atom cluster formation is the heterogeneous nucleation by the segregation of such elements to point defects and the induction of their clusters by irradiation.

These considerations suggest a slightly different mechanism of embrittlement for the formation of solute atom clusters and MD. The formation of solute atom clusters is accelerated in the copper-containing materials due to the enhanced clustering of supersaturated copper atoms under irradiation (i.e., irradiation-enhanced clustering), but it is also caused by heterogeneous nucleation by the segregation of solute atoms to irradiation-induced point defects (i.e., irradiation-induced clustering). A small amount of Cu atoms help the irradiation-induced clustering process. The MD consists of interstitial dislocation loops, but the number density of the dislocation loops may not be very large to be a major contributor to the embrittlement in medium copper materials.

The correlation between the microstructural changes and the transition temperature shifts is the key to the development of the embrittlement correlation method. In Fig. 1, we plot the transition temperature shift at 41 J against the square root of the volume fraction of the solute atom clusters measured in the surveillance materials. The data of all the surveillance materials investigated in this project, including that for the boiling water reactor (BWR) material discussed in the next section, are shown. One can see that there is a linear correlation between the two parameters. This observation is very interesting from the following two points of view. First, the cluster volume fraction describes the embrittlement as a first-order approximation, and the contribution of the MD looks small even in the materials having small cluster volume fraction. Second, the correlation does not depend on the chemical composition of the clusters. In other words, the volume of a cluster determines the obstacle strength. Of course there is some scatter in the plot of Fig. 1, and the above discussions may need to be revised, but it works very well considering its simplicity.

Materials from Boiling Water Reactors—The second group of materials investigated includes high copper surveillance materials of Japanese BWR RPVs. The details are again reported elsewhere [13], and here we just summarize the

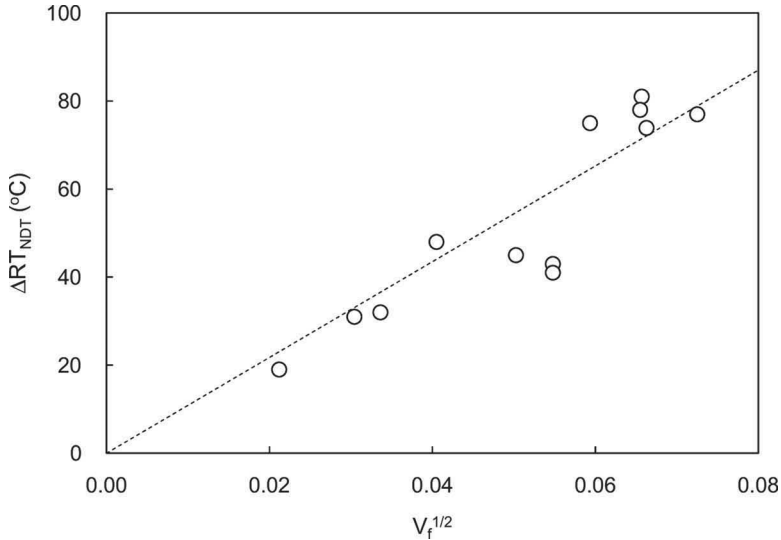


FIG. 1—Correlation between the Charpy transition temperature shift, ΔRT_{NDT} , and cluster volume fraction, V_f .

results. It is known that a flux (dose rate) effect exists in copper-containing RPV materials. During the EPRI-CRIEPI workshop on the dose rate effect, a consensus was reached among the participants that embrittlement is accelerated and appears at lower fluences in copper-containing materials irradiated at low fluxes [10]. This has also been seen in Japanese surveillance materials. RPV materials with a high copper content irradiated in a surveillance capsule located on the inner wall of a pressure vessel (hereafter, wall capsule) where the neutron flux, ϕ , is as low as $\sim 10^9$ n/cm²·s, $E > 1$ MeV, show greater embrittlement than the same materials irradiated in an accelerated irradiation capsule (accelerated capsule) located at a higher-flux position with $\phi \sim 10^{10}$ n/cm²·s [17]. In order to further clarify the flux effect, a new irradiation program was designed, in which the archive material of the commercial RPV was irradiated at a much higher flux in a material testing reactor (MTR) than that of the wall capsule to compare the mechanical property changes as well as the microstructural changes due to different irradiation conditions.

The archive RPV material was irradiated in a MTR at an irradiation temperature of 276°C and was compared with the material irradiated in the wall capsule in a Japanese commercial BWR. The material is SA302B modified plate with copper and nickel contents of 0.24 and 0.6 wt %, respectively. The irradiation was performed in the LVR-15 reactor of the Nuclear Research Institute, Rez, in the Czech Republic. The irradiation temperature was controlled at $276 \pm 10^\circ\text{C}$, and the neutron flux was 7×10^{11} n/cm²·s, $E > 1$ MeV. A comparison of the transition temperature shifts caused by irradiation under different conditions is shown in Fig. 2. The transition temperature shift of the material irradiated in the test reactor is similar in magnitude to that irradiated in the accelerated capsule with a flux of $\sim 10^{11}$ n/cm²·s, and both of these are

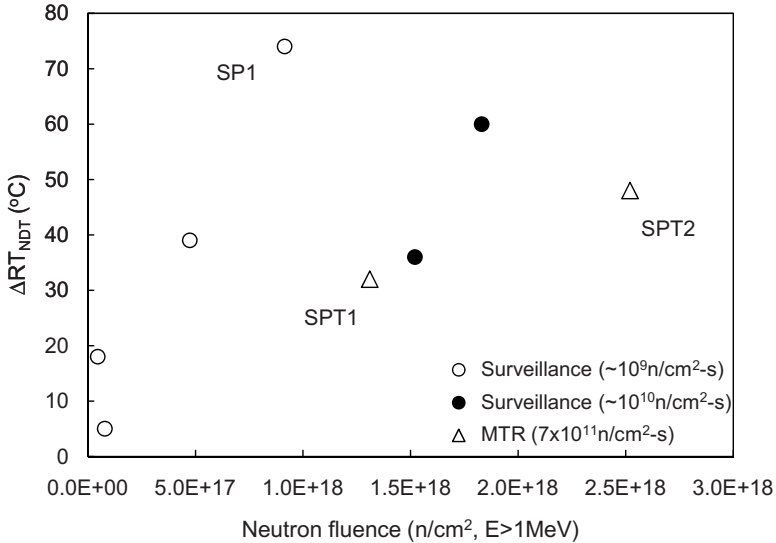


FIG. 2—Transition temperature shifts, ΔRT_{NDT} 's, of high copper (0.24 wt %) RPV material irradiated at three different fluxes: i.e., $\sim 1 \times 10^9$ n/cm²·s in open circle, $\sim 10^{10}$ n/cm²·s in solid circle, and 7×10^{11} n/cm²·s in open triangle.

lower than those of the material irradiated in the wall capsule.

In order to understand the reason for the difference in the transition temperature shift, we performed microstructural analyses of the materials irradiated in the wall capsule to a fluence of 9×10^{17} n/cm², $E > 1$ MeV (SP1), and in the MTR to fluences of 1.3×10^{18} and 2.5×10^{18} n/cm², $E > 1$ MeV (SPT1 and SPT2). The results are summarized in Table 2. In both materials, CECs are formed in spite of the very low fluences. The mean cluster diameter of the SP1 material is 2.6 nm, which is about 30 % larger than that of the SPT1 material (2.0 nm). The cluster number density of 4.3×10^{23} m⁻³ in the SP1 material is also larger than that of 2.9×10^{23} m⁻³ in the SPT1 material by about 30 % in spite of the lower neutron fluence of the SP1 material. These differences result in the cluster volume fraction of the SP1 material being three times larger than that of SPT1 material. It is highly probable that this large difference in the cluster volume fraction is the reason for the difference in the transition temperature shift. It is interesting to note that in the SPT2 material, the cluster number density is almost double that of the SPT1 material, showing a good correspondence with the difference of the neutron fluence, while the cluster mean diameters in SPT1 and SPT2 materials are almost the same. It is also interesting to note that the cluster chemical compositions do not change among SP1, SPT1, and SPT2 in spite of the large difference in the mean volume (diameter) of the clusters.

Flux has been thought to affect embrittlement through changing the amount of diffusion of impurity copper atoms [18,19]. Kinetic Monte Carlo simulation [20] shows that in a high-flux region, which we will refer to here as

TABLE 2—Summary of the microstructural analyses of the BWR surveillance materials.

ID	Fluence ($\times 10^{18}$ n/cm ² , $E > 1$ MeV)	Bulk Chemical Composition			Cluster Characteristics			Cluster Composition			
		Cu (wt %)	Ni (wt %)	P (wt %)	Guinier Diameter (nm)	Number Density ($\times 10^{22}$ m ⁻³)	Volume Fraction	Cu (at. %)	Ni (at. %)	Mn (at. %)	Si (at. %)
SPT1	0.9	0.24	0.6	0.018	2.6	43	0.0044	11.0	8.8	6.5	3.3
SPT1	1.3				2.0	29	0.0013	11.4	8.7	6.3	3.6
SPT2	2.5				2.0	45	0.0025	12.3	9.6	6.1	4.4

region I, the intercascade pair recombination of point defects becomes dominant, resulting in the reduction of the number of vacancy jumps, which can be a measure of the diffusivity of copper atoms, and a suppression of the copper clustering. If the flux is sufficiently low, *region II*, point defects may diffuse to sinks such as dislocations or grain boundaries before they find other point defects produced in other cascades. In other words, displacement cascades are isolated from each other below a certain flux level, and thus no flux effect will exist. In such a situation, a change in flux simply results in a change in the average vacancy concentration in the matrix. If we further decrease the flux, *region III*, the average vacancy concentration becomes comparable to the thermal equilibrium vacancy concentration at the temperature, and another type of flux effect, i.e., the contribution of thermal vacancies, will become effective.

In this context, the flux levels of the accelerated capsule and the MTR capsule are in region II, where the flux effect is weak, and the flux level of the wall capsule is in region III, where a relatively strong effect of thermal vacancies is expected. The above experimental results may be interpreted to mean that thermal vacancies may not have a strong effect on the nucleation of copper clusters in region III, but they have a strong effect on the cluster growth. As we saw in Fig. 1, the volume fraction of the clusters plays a very important role in determining the transition temperature shift, and the effect of very low-flux irradiation on accelerating the embrittlement in copper-containing materials works primarily through the increase in the number density of the clusters as well as an increase in their volume.

Development of an Embrittlement Correlation Method

Modeling of Microstructural Changes during Irradiation

The general consensus on the embrittlement mechanism may be modified considering the observations and discussion in the previous chapter as follows. In the RPV materials irradiated by fast neutrons, solute atom clusters are formed regardless of the amount of copper impurity, and this is the primary mechanism of embrittlement in Japanese RPV materials. In copper-containing RPV materials, copper atoms are highly enriched in the clusters with the agglomeration of other elements such as nickel, silicon, and manganese. The number of copper atoms in the clusters decreases with decreasing bulk copper content, but even in relatively low-copper materials of less than 0.072 wt %, clusters contain some copper atoms according to the bulk copper content, and this affects the number density of the clusters. In the materials with very low-copper content, no copper atoms can be found in the solute atom clusters formed in the matrix, and they consist of nickel, silicon, and manganese. Under a low-flux condition such as BWR irradiation, a change in flux alters the relative contributions of irradiation-produced and thermally induced vacancies to the diffusion of impurity copper atoms in copper-containing materials. The volume fraction of solute atom clusters becomes very large in a low-flux region due to this mechanism, and this enhances embrittlement. As a very simple

model, the amount of embrittlement has a very good linear correlation with the square root of the volume fraction of the solute atom clusters.

Based on the above new interpretation of the embrittlement mechanism, we modified our embrittlement correlation method that was developed in 2004 [21]. In this method, the microstructural changes due to irradiation are modeled by a set of rate equations, and then the microstructural characteristics are used to determine the total embrittlement.

The rate equations used to describe the microstructural changes are as follows:

$$\frac{\partial C_{SC}}{\partial t} = \frac{\partial C_{SC}^{ind}}{\partial t} + \frac{\partial C_{SC}^{enh}}{\partial t} = \xi_3 \cdot ((C_{Cu}^{mat} + \varepsilon_1) \cdot D_{Cu} + \varepsilon_2) \cdot C_{MD} + \xi_8 \cdot (C_{Cu}^{avail} \cdot D_{Cu} \cdot (1 + \xi_7 \cdot C_{Ni}^0))^2 \quad (1)$$

$$\frac{\partial C_{MD}}{\partial t} = \xi_4 \cdot F_t^2 \cdot (\xi_5 + \xi_6 \cdot C_{Ni}^0)^2 \cdot \phi - \frac{\partial C_{SC}^{ind}}{\partial t} \quad (2)$$

$$\frac{\partial C_{Cu}^{mat}}{\partial t} = -v_{SC} \cdot \frac{\partial C_{SC}}{\partial t} - v'_{SC} \cdot C_{SC} \quad (3)$$

$$v_{SC} = \xi_2 \cdot (C_{Cu}^{avail} \cdot D_{Cu})^2 \cdot t_r \quad (4)$$

$$v'_{SC} = \xi_1 \cdot C_{Cu}^{avail} \cdot D_{Cu} \quad (5)$$

$$C_{Cu}^{avail} = \begin{cases} 0 & C_{Cu}^{mat} \leq C_{Cu}^{sol} \\ C_{Cu}^{mat} - C_{Cu}^{sol} & C_{Cu}^{mat} > C_{Cu}^{sol} \end{cases} \quad (6)$$

$$D_{Cu} = D_{Cu}^{thermal} + D_{Cu}^{irrad} = D_{Cu}^{thermal} + \omega \cdot \phi^\eta \quad (7)$$

Equation 1 is to describe the time evolution of the number density of the solute atom clusters, C_{SC} . C_{SC} further consists of C_{SC}^{ind} and C_{SC}^{enh} , which correspond to the number densities of irradiation-induced and irradiation-enhanced solute atom clusters, respectively. C_{Cu}^{mat} is the matrix copper content, which is the number of copper atoms in solid solution, C_{Cu}^{avail} is an amount of copper in supersolution, whose definition can be found in Eq 6, C_{Ni}^0 is the bulk nickel content, and D_{Cu} is a parameter used to model the diffusivity of Cu atoms but does not precisely correspond to the actual diffusion coefficient. The irradiation-induced solute atom clusters are those formed regardless of impurity copper atoms, but their number density increases with bulk copper content. Since the physical process of irradiation-induced clustering is segregation, we assume that this can be written as a product of the diffusivity and the nucleation sites, which are MD features, C_{MD} , as modeled in Eq 2. It should be noted that this term does not become zero even if the copper content is zero. This is the modeling of the experimental observations of solute atom clusters with little or no copper atoms in low-copper surveillance materials.

The irradiation-enhanced solute atom clusters are CECs or CRPs formed by a thermodynamic precipitation mechanism enhanced by irradiation vacancies. Therefore, it is described as the square of the product of the concentration of copper atoms in supersolution and the diffusivity. Since the synergetic effect between copper and nickel is well known [9], the effect of nickel is also taken into consideration in irradiation-enhanced clustering term.

Equation 2 is used to describe the time evolution of the number density of MD features, C_{MD} . F_t is the Jones and Williams' temperature term, which has the form $F_t = 1.869 - 4.57 \times 10^{-3} T$ ($^{\circ}\text{C}$) [22], and ϕ is the neutron flux. It is known that the hardness of a Fe-Ni alloy irradiated by neutrons increases with nickel content, and this is due to the increase in the number density of dislocation loops [19]. Although the effect of nickel is not included in the U.S. model [2,3], a recent correlation method proposed in Europe [23] also considers the effect of nickel on MD. The second term in Eq 2 describes the amount of MD consumed as nuclei of irradiation-induced solute atom clusters. It should be noted that nickel has an effect on the formation of irradiation-induced solute atom clusters through its effect on the formation of MD features.

The matrix copper content decreases with the formation of copper-containing solute atom clusters. This process is described in Eq 3. This decrease may be due to (1) the formation of new clusters and (2) the growth of existing clusters, and the two terms in the right-hand side of Eq 3 correspond to these processes. Equations 4 and 5 describe the amount of copper atoms removed from the solid solution by these mechanisms. The formation of new copper clusters is basically due to clustering by the irradiation-enhanced clustering mechanism, and thus it is assumed that the amount of copper atoms removed is proportional to the square of the product of diffusivity and copper concentration, while the cluster growth due to segregation is proportional to the product of diffusivity and copper concentration. For the growth of irradiation-induced clustering, a time available for cluster formation is considered, and t_r , which we call "relaxation time," is multiplied. We assume that this is approximately proportional to $1/\phi$.

The parameter used to describe the diffusivity of copper atoms, D_{Cu} , is determined by Eq 7. We assume that the average vacancy concentration is determined by those of the irradiation-produced vacancies and thermal vacancies. As we discussed, since the diffusivity decreases at very high fluxes due to intercascade interaction, we assume that the contribution of the irradiation-induced vacancies is an exponent function of flux with an exponent of less than unity. On the other hand, the concentration of thermal vacancies is not affected by flux and is set to be a constant value.

Modeling of Transition Temperature Shift

The correlation between the microstructures and the Charpy transition temperature shifts at 41 J is modeled using the following equations:

$$\Delta T_{SC} = \xi_{16} \cdot \sqrt{V_f} = \xi_{16} \cdot \sqrt{\xi_{15} \cdot f(C_{Cu}^{mat}, C_{SC}) \cdot g(C_{Ni}^0) + h(\phi t)} \cdot \sqrt{C_{SC}} \quad (8)$$

$$f(C_{\text{Cu}}^{\text{mat}}, C_{\text{SC}}) = \xi_{11} \cdot \frac{C_{\text{Cu}}^0 - C_{\text{Cu}}^{\text{mat}}}{C_{\text{SC}}} + \xi_{12} \quad (9)$$

$$g(C_{\text{Ni}}^0) = (1 + \xi_{13} \cdot (C_{\text{Ni}}^0)^{\xi_{14}})^2 \quad (10)$$

$$h(\phi t) = \xi_9 \cdot (1 + \xi_{10} \cdot D_{\text{SC}}) \cdot \phi t, \quad D_{\text{SC}} \approx D_{\text{Cu}} \quad (11)$$

$$\Delta T_{\text{MD}} = \xi_{17} \cdot \sqrt{C_{\text{MD}}} \quad (12)$$

$$\Delta T = \sqrt{(\Delta T_{\text{SC}})^2 + (\Delta T_{\text{MD}})^2} \quad (13)$$

The contribution of the solute atom clusters to the embrittlement is calculated as the square root of the cluster volume fraction, V_f , which is modeled as the cluster number density C_{SC} multiplied by the average volume of clusters. C_{SC} can be obtained as the time-integrated value of Eq 1. The average volume of clusters is modeled using three functions f , g , and h , as shown in Eqs 9–11, respectively. Function f is the average amount of copper in a cluster, which can be calculated as the total amount of copper atoms in clusters divided by the cluster number density. Function f is multiplied by function g to consider the synergy effect between copper and nickel. Function h is used to describe cluster growth during irradiation. This is based on the microstructural analysis results of RPV materials irradiated in a material test reactor to high fluences of up to $\sim 10^{20}$ n/cm², showing that the average number of copper atoms in a cluster does not change at fluences beyond 3×10^{19} n/cm², $E > 1$ MeV, while the average cluster volume keeps increasing due to the continuous agglomeration of nickel, silicon, and manganese atoms at high fluences [16]. The increase in the volume fraction of clusters results in greater embrittlement at high fluences in the experiments. In order to take this effect into consideration, function h , which increases with fluence, is added to model the volume fraction of clusters. The effect of diffusivity is also considered in function h . It should be noted that the above observations, particularly no change in the average number of copper atoms in a cluster at high fluences, are from the results of material test reactor irradiation, and thus there may be an effect of high flux. Further verification is necessary by examining the high fluence surveillance materials that will come out in the near future.

The contribution of MD to the embrittlement is considered to be proportional to the square root of the number density of clusters. This is a conventional way to model the contribution of MD.

Once the contributions to the embrittlement of solute atom clusters, ΔT_{SC} , and MD, ΔT_{MD} , are obtained, the total amount of embrittlement is calculated using Eq 13. In the other embrittlement correlation models, the total temperature shift is a simple sum of the CEC and MD contributions. In general, however, the square root of the sum of the squares of the contributors is a more generic approximation. The linear-sum method can be a good approximation when the obstacle strengths of the two kinds of particle are very different and

the population of stronger particles is much less than that of the weaker particles. Equation 13 has the characteristic that the stronger contributor dominates the total shift.

Determination of Coefficients

The coefficients of Eqs 1–13 are determined using the Japanese surveillance data available as of the end of December 2006. In the surveillance database, the Charpy transition temperature shifts of base metals and weld metals in the heat-affected zone (HAZ) are included together with the data of standard reference materials irradiated in PWR plants. Note that HAZ data were not used to determine the coefficients. In addition, some base metals and weld metals irradiated in the Halden Reactor as part of the Plant Life Management Project of Japan Power Engineering and Inspection Corporation [24] in Japan are also used to optimize the coefficients at high fluences and high fluxes.

Our policies in the optimization of the coefficients are threefold: (1) Minimize the difference between the measured and predicted values, (2) reproduce the embrittlement “trend” for materials having more than two surveillance data points, and (3) check the consistency between the measured and predicted microstructural characteristics for those materials whose microstructures were investigated in this study. The consideration of the second and third points is very important for our approach because our model has many fitting parameters, which may be easily overfitted to the surveillance data without satisfying constraint conditions (2) and (3).

In the conventional correlation methods [1], it has been standard practice to determine different sets of parameters for different product forms such as plate, forging, and weld metals. However, no clear difference has been recognized in the microstructural changes due to irradiation among these product forms, and there is no mechanistic basis that implies the necessity of using a different set of coefficients depending on the product form. Therefore, in this project, we tried to find only one set of coefficients that can be commonly used for plate, forging, and weld metals. The final set of coefficients together with the computer code used to integrate the rate equations can be found elsewhere [13] as well as in the Appendix of this paper.

Plant Specific Offset Adjustment

In the application of the JEAC4201-2004 code, the so-called plant-specific adjustment may be used to adjust the embrittlement correlation predictions according to the actual measured values. The adjustment is done by optimizing the chemical factor of the prediction equation. This kind of adjustment is not applicable to the new embrittlement correlation method described here, and thus we have proposed another type of adjustment method called *offset adjustment* [25]. As is well known, the data from the Charpy impact test, especially the transition temperature at 41 J, have inherent scatter due to the scatter of measurements in the transition temperature region. Our estimation of the standard deviation of the scatter is about 5°C for the modern SA533B Cl.1 plate material. If we have this amount of scatter in the determination of the initial

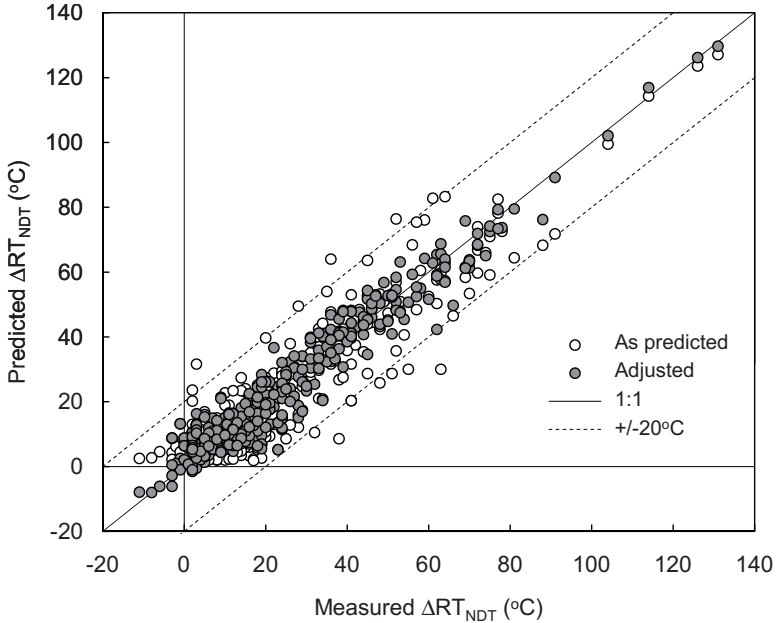


FIG. 3—Comparison of the predictions by new correlation method with the measurements of the surveillance program.

transition temperature, the scatter can be added to all the successive surveillance data as an offset value. The idea of the offset adjustment method is to calculate this offset value for each of the materials as the mean value of the difference between the surveillance values and predicted values when more than two values of surveillance data are available for the material.

Predictions of the New Embrittlement Correlation Method

A comparison of the predictions of the new embrittlement correlation method, hereafter called CRIEPI model, with all the Japanese surveillance data for the base metals and weld metals of both PWRs and BWRs is shown in Fig. 3. The vertical axis shows the predicted values and the horizontal axis shows the measured values. The 1:1 line with $\pm 20^\circ\text{C}$ lines is shown in the figure. Open symbols represent the predictions without offset adjustment, and solid symbols represent those with offset adjustment. The standard error of the predictions of the new embrittlement correlation is 9.4°C (less than 10°C), which is superior to the predictions with other correlation methods for this database. The average value of the prediction errors is 0.1°C , and a no bias of prediction toward a conservative or non-conservative side is observed. Note that only one set of coefficients is used in the CRIEPI model, while different sets of coefficients or different forms of correlation equations are used in the other predictions. If we apply the offset adjustment, the standard error of the predictions is further

improved to 5.5°C with an average prediction error of 0.05°C. The high accuracy of the adjusted predictions suggests that the new embrittlement correlation method captures the embrittlement trend of the materials, which have more than two surveillance data points, and this is an important characteristic for the predictive capability of the correlation method.

Predictions for a typical range of chemical compositions of RPV steels under typical irradiation conditions of a PWR surveillance capsule are shown in Fig. 4(a)–4(c). An irradiation temperature of 288°C and neutron flux of 1×10^{11} n/cm²·s, $E > 1$ MeV, are assumed. Predictions by U.S. NRC-ORNL model [4], hereafter called Eason-Odette-Nanstad-Yamamoto (EONY) model, are also plotted. The CRIEPI model gives slightly larger shifts than the EONY model for plates, while it gives much larger shifts for forgings. For weld metals with relatively high-nickel content, the predictions are similar for high copper materials but are larger for low-copper materials. More details of these CRIEPI model predictions will be studied in the next section. The effect of neutron flux is shown in Fig. 5, where predictions at three different fluxes of 10^9 , 10^{10} , and 10^{11} n/cm²·s, $E > 1$ MeV, are compared for a material with relatively high copper content. An irradiation temperature of 276°C is assumed. In the blue line showing the result for the lowest flux, the embrittlement at low fluences is enhanced due to the accelerated clustering of impurity copper atoms, but this slows down at higher fluences because of the shortage of available copper for clustering. Predictions of the CRIEPI model and the EONY model are similar for the flux levels of 10^{10} and 10^{11} n/cm²·s, $E > 1$ MeV, but the trends are different at very low flux of 10^9 n/cm²·s, $E > 1$ MeV.

Comparison with the U.S. Surveillance Data

The coefficients of the CRIEPI model were optimized for the latest Japanese surveillance database. Applying this method to such a database that was not used for the parameter optimization is very useful to understand the characteristics of the new correlation method. Therefore, in this section, we will compare the predictions of the CRIEPI model with the U.S. surveillance database. The sources of the U.S. surveillance database are the one used for the development of the EONY model [4], and the integrated surveillance program database [26] developed in EPRI BWR vessel and Internals Project. Since the range of the chemical composition of the U.S. database and the Japanese database is very different, we used the U.S. data points that meet the following conditions:

$$\text{Cu} \leq 0.25 \text{ wt } \%$$

$$0.5 \text{ wt } \% \leq \text{Ni} \leq 1.1 \text{ wt } \%$$

$$\text{P} \leq 0.025 \text{ wt } \% \tag{14}$$

In the recent U.S. embrittlement correlation equations [2–4], different coefficients are given for plates, forgings, and weld metals. Therefore we will also make comparisons here on a product form basis. The first comparison is given in Fig. 6, where the prediction errors defined as the prediction values sub-

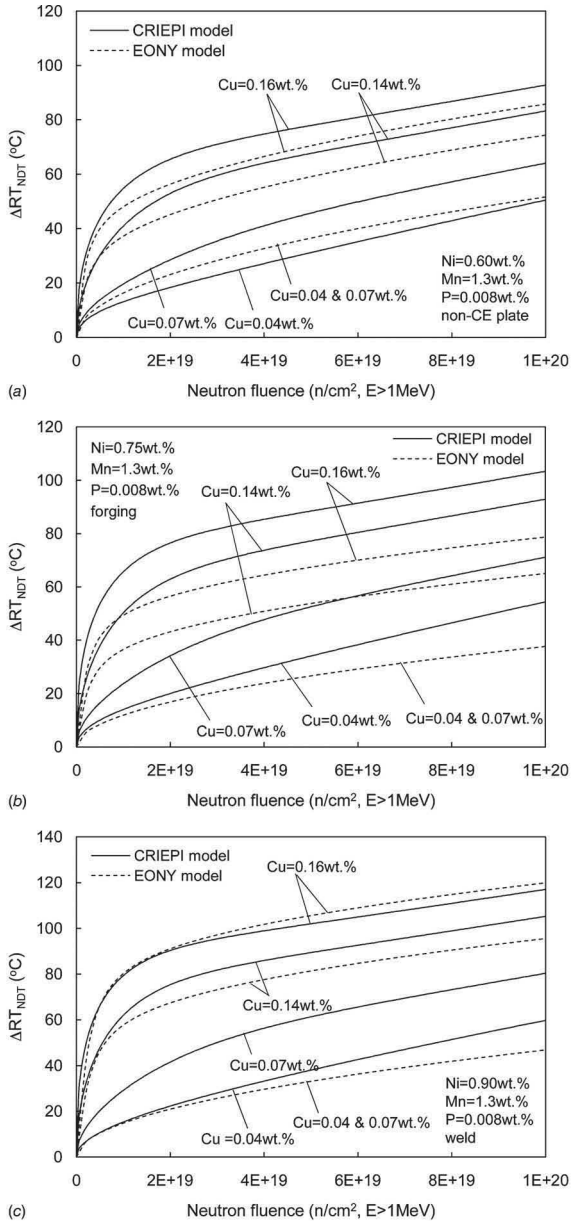


FIG. 4—Predictions of the CRIEPI model compared with the predictions of EONY TTS model under PWR conditions. (a) Predictions for non-CE plates with 0.60 wt % nickel, 1.3 wt % Mn, and 0.008 wt % P. (b) Predictions for forgings with 0.75 wt % nickel, 1.3 wt % Mn, and 0.008 wt % P. (c) Predictions for weld metals with 0.90 wt % nickel, 1.3 wt % Mn, and 0.008 wt % P.

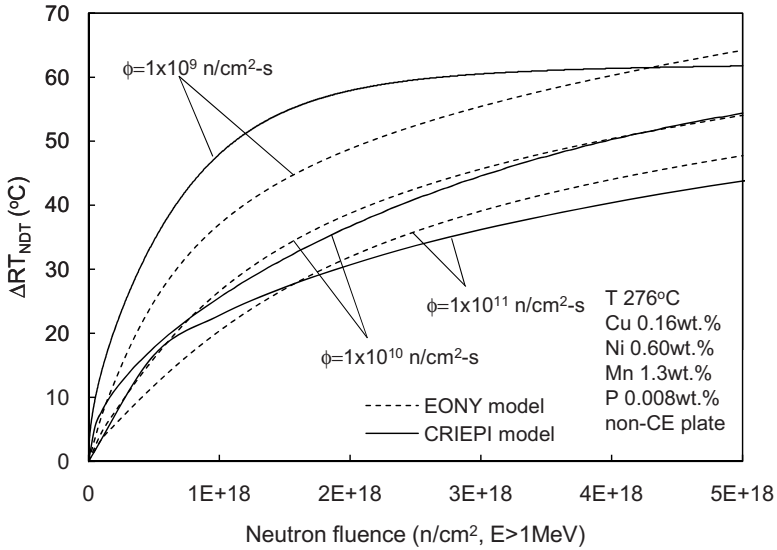


FIG. 5—Predictions of the CRIEPI model compared with the predictions of EONY TTS model under BWR conditions.

tracted by the measured values in the surveillance program are plotted as a function of fluence. The minus value of prediction means under-prediction. The data points that have Cu content greater than or equal to 0.19 wt % are plotted as solid symbols, and the other data points are plotted as open symbols. Fur-

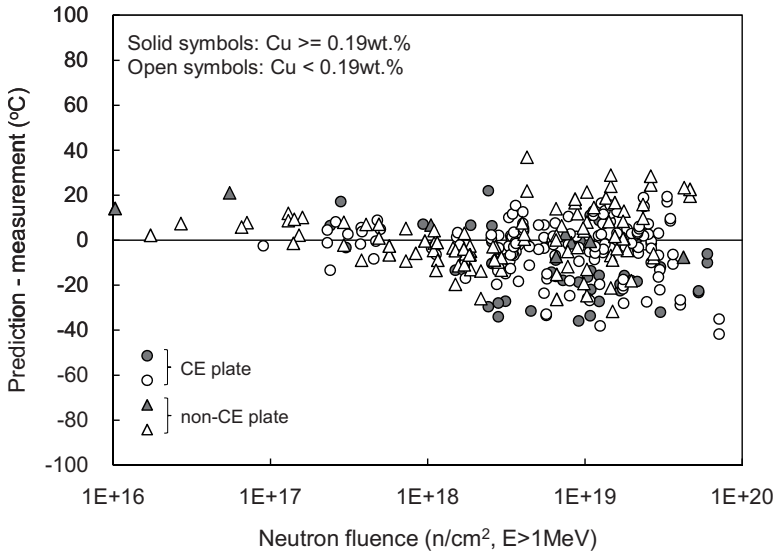


FIG. 6—Prediction error of the CRIEPI model for plates as a function of fluence.

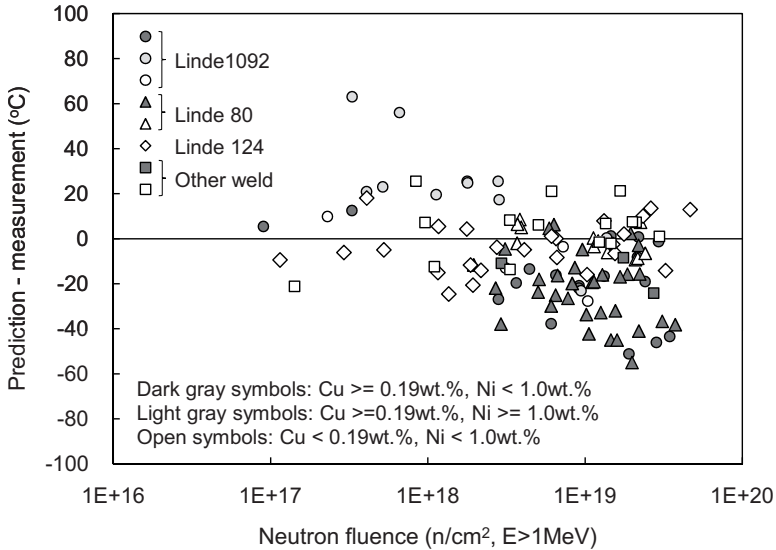


FIG. 7—Prediction error of the CRIEPI model for weld metals as a function of fluence.

thermore, since the recent U.S. equations [3,4] give different values to the coefficients for the CRP term of the combustion engineering (CE)-fabricated plates and other plates. We also use different colors: Red for CE and blue for non-CE fabricated plates.

The predictions by the CRIEPI model agree well with the measurements of the non-CE plates in blue. This is a reasonable result because the Japanese RPV plates are in general non-CE plates. On the other hand, however, the predictions of the CE plates have a tendency of under-prediction, and this is more enhanced for the high Cu CE plates. In the U.S. surveillance database, it is recognized that the embrittlement of CE plates is in general larger than that of non-CE plates, and this fabricator-effect is included in the recent correlation equations [3,4] by making the coefficient of the CRP term for the CE plate larger than that for the non-CE by about 30%. In this sense, the under-prediction tendency of the CRIEPI model for the CE plates is rational because no CE effect is taken into consideration because of the nature of the Japanese surveillance database. The CRIEPI model is consistent with the understandings of the U.S. correlations. It should be noted that the reason why CE plates give larger shifts has not been understood yet.

Figure 7 shows the prediction error for the weld metals as a function of fluence. Materials with Cu content greater than 0.19 wt % are shown in solid symbols, and the others are shown in open symbols. In addition, materials with Ni content of less than 1.0 wt % are shown in circles, and the others are shown in diamond symbols. A very large under-prediction tendency can be recognized for the Linde 80 weld metals. Four data points from Linde 1092 weld metals are also under-predicted by more than 25°C, but they are the data points for the same material at different fluences. Other welds are well predicted in general.

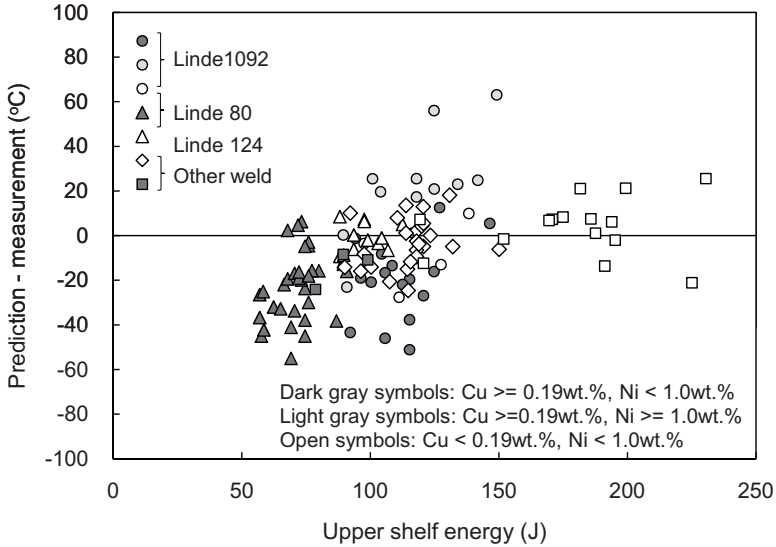


FIG. 8—Prediction error of the CRIEPI model for weld metals as a function of upper shelf energy.

For more detailed analysis, the prediction errors of weld metals are plotted against the upper shelf energy values in Fig. 8. It is clear that most of the materials that are largely under-predicted are the materials having low upper shelf energies, and the upper shelf energies of the Linde 80 weld metals are particularly low as expected.

Figure 9 would be a good example to illustrate the effect of upper shelf energy on RT_{NDT} value. Four hyperbolic tangent curves simulating the temperature effect on the Charpy absorption energy are plotted in Fig. 9. These curves have common lower shelf energy (LSE) of 0 J and different upper shelf energies of 50, 100, 200, and 300 J. The temperature, T_0 , at which the energy reaches the half of the upper shelf energy is the same among the four curves to be 0°C, indicating that the physical ductile-to-brittle transition temperatures are the same. However, the RT_{NDT} , defined as the temperature at which the absorption energy becomes 41 J, is affected very much by the values of the upper shelf energies. Figure 9 clearly demonstrates that the RT_{NDT} values become higher as the upper shelf energy becomes lower. This means that the shift in RT_{NDT} , ΔRT_{NDT} , consists of a physical transition temperature shift, i.e., for example shift in T_0 , and an apparent transition temperature shift caused by the decrease in upper shelf energy. One can also see in Fig. 9 that this effect is stronger for the materials with low upper shelf energies. The difference in RT_{NDT} values of the curves with upper shelf energies of 50 and 100 J is larger than those of 100 and 200 J, and 200 and 300 J.

The apparent transition temperature shift, $\Delta T_{\text{apparent}}$, can be estimated using the upper shelf toughness energies, USE_u and USE_i , before and after irradiations, respectively, as follows:

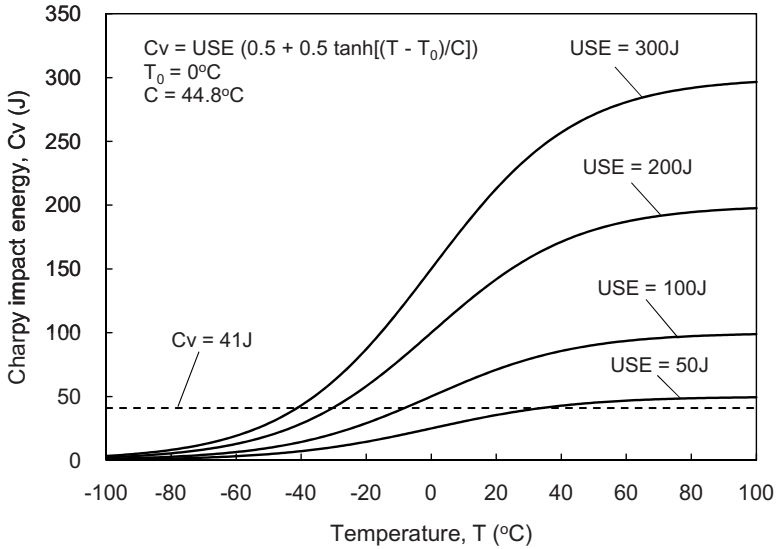


FIG. 9—Effect of upper shelf energy on the transition temperature determination at 41 J.

$$\Delta T_{\text{apparent}} = \left[\tanh^{-1} \left(\frac{82}{\text{USE}_i} - 1 \right) - \tanh^{-1} \left(\frac{82}{\text{USE}_u} - 1 \right) \right] \times C \quad (15)$$

where:

C = parameter determined by the fit of hyperbolic tangent curve of the following form to the experimental data:

$$C_v = \text{LSE} + (\text{USE} - \text{LSE}) \times \left(0.5 + 0.5 \cdot \tanh \left(\frac{T - T_0}{C} \right) \right) \quad (16)$$

where:

LSE = lower shelf energy.

The number 82 in Eq 15 comes from the 41 J divided by 0.5. The mean value for C is found to be 44.8°C for the RPV steels investigated. The predictions of CRIEPI model for the Linde 80 materials adjusted using the apparent transition temperatures calculated from the Eq 15 are plotted in Fig. 10 in solid symbols together with the as-predicted values in open circles. The under-prediction tendency of the as-predicted values for the Linde 80 weld metals is improved.

The embrittlement model that we are applying in the CRIEPI model is based on the hardening mechanism of the materials, and it has been pointed out by McElroy et al. that such model has some difficulty to be applied to such materials like Linde 80 welds, in which hardening and $\Delta \text{RT}_{\text{NDT}}$ do not have necessarily good linear correlation [27]. Some modification of the prediction method would be necessary for the accurate predictions of the $\Delta \text{RT}_{\text{NDT}}$ values of the low upper shelf toughness materials, though this is not a major concern

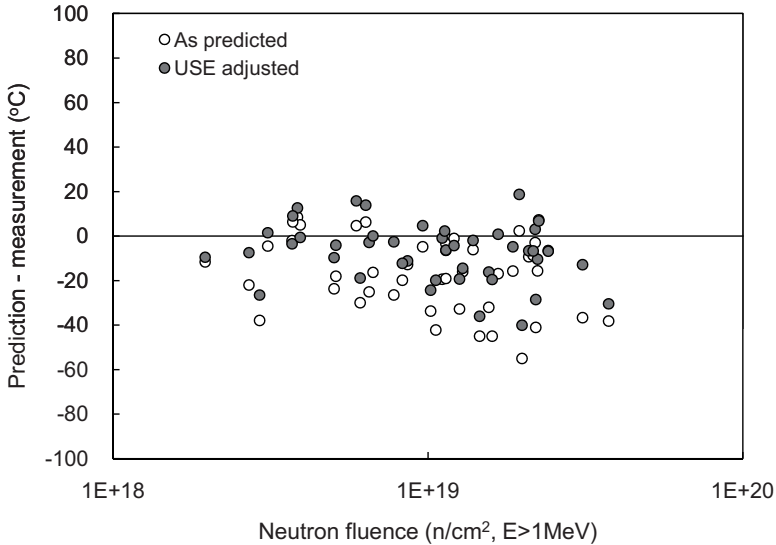


FIG. 10—Upper shelf adjustment for the prediction of Linde 80 weld metals.

for the Japanese RPV steels at the present time. Making the coefficient of the Cu-related term for weld metals larger, as has been done in the U.S. exercises, will be a useful way.

Finally, the comparison of the CRIEPI model predictions with the measured values of forgings is shown in Fig. 11. Unlike the previous plots, the vertical axis is the prediction, and the horizontal axis is the measured value. As-predicted values are the data points shown in open circles, while the predictions applied the offset adjustments are shown in solid circles. Offset adjustment was applied only when the plant has more than two surveillance data points for the same heat of material. As shown in Fig. 11, as-predicted values tend to be larger than the measurement in the case of forgings, but adjusted predictions agree well with the measurements, suggesting that the CRIEPI model well reproduces the embrittlement trend of the surveillance data.

In order to look at this situation on a plant-by-plant basis, two typical cases are shown in Figs. 12 and 13. Figure 12 shows the surveillance data of LT and TL directions, defined in ASTM E399-09 [28], of the material from CB1 plant together with the CRIEPI model predictions with and without offset adjustments as well as the ASTM E900-02 prediction. ASTM E900-02 has a good prediction for the TL data, but the prediction for the LT data is not sufficient. The negative shift of LT data of the first capsule cannot be explained. On the other hand, predicted values of the CRIEPI model predictions are larger than both of the LT and TL data. However, if we apply the offset adjustment to the CRIEPI model predictions by shifting the curve in the vertical direction, the curve just runs on the LT and TL data points. The CRIEPI model reproduces the embrittlement trend of LT and TL data sets and also explains that the negative shift data of the LT data at the first capsule are very meaningful in the sense of the embrittlement trend. In the case of SQ1 in Fig. 13, the embrittle-

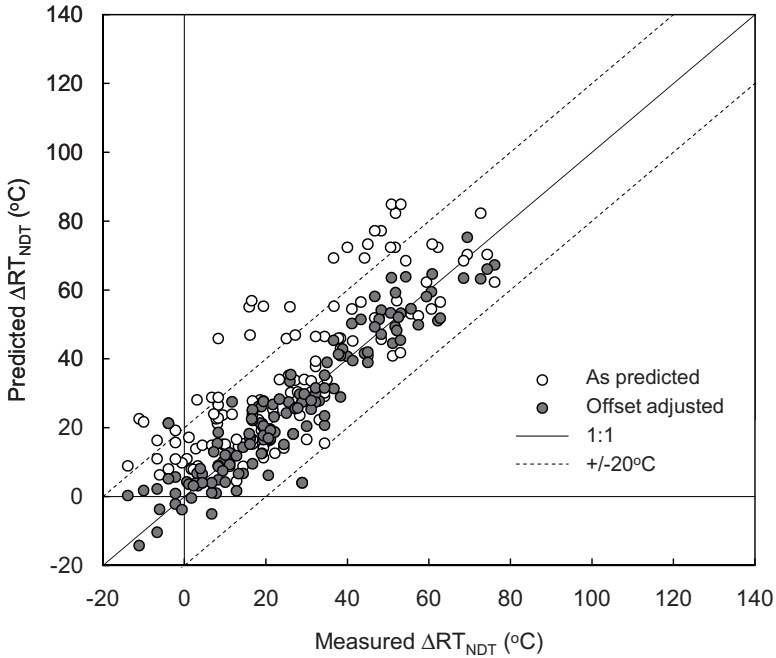


FIG. 11—Offset adjustment for the U.S. forgings.

ment of the forging material with 0.13 wt % Cu and 0.76 wt % Ni is well predicted by the CRIEPI model for both TL and LT directions, and ASTM E900-02 correlation gives smaller values. We found that offset values for the forging materials tend to be negative, while offset values have in general normal distribution with mean value of nearly zero for plates and weld metals. It may be worth investigating the initial mechanical properties of forgings.

Conclusion

Microstructural analyses of Japanese surveillance materials were conducted using state-of-the-art experimental techniques to enhance our understanding of the embrittlement mechanisms. We found that (1) solute atom clusters with little or no copper are formed in medium nickel materials at low to medium fluences, (2) the effect of low-flux irradiation on copper-containing materials is to enhance the growth of copper-enriched solute atom clusters as well as to increase the number density, and (3) the square root of the volume fraction of the solute atom clusters has good correlation with the transition temperature shift.

A new embrittlement correlation method was developed on the basis of the understanding of the embrittlement mechanisms. Microstructural changes during irradiation are modeled using rate equations, and the predicted microstructural changes are correlated with the transition temperature shift using a

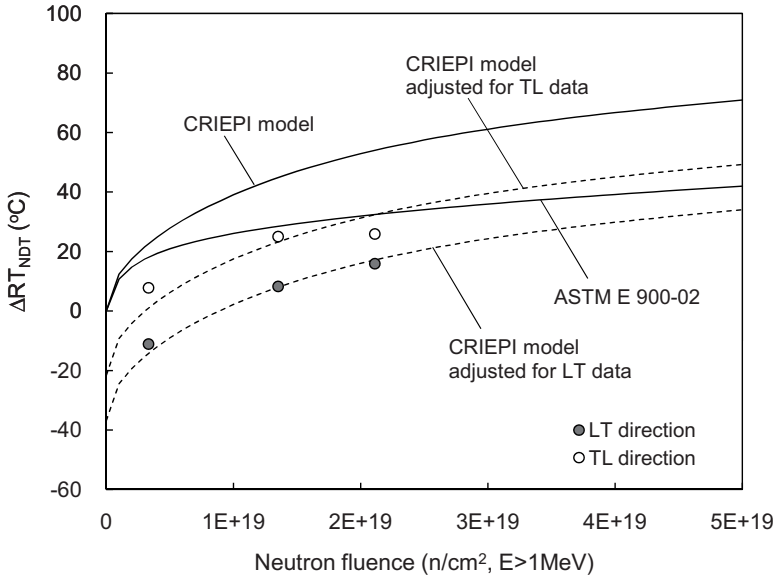


FIG. 12—Comparison of the predictions and surveillance data of CB1. Cu and Ni contents are 0.09 and 0.845 wt %, respectively.

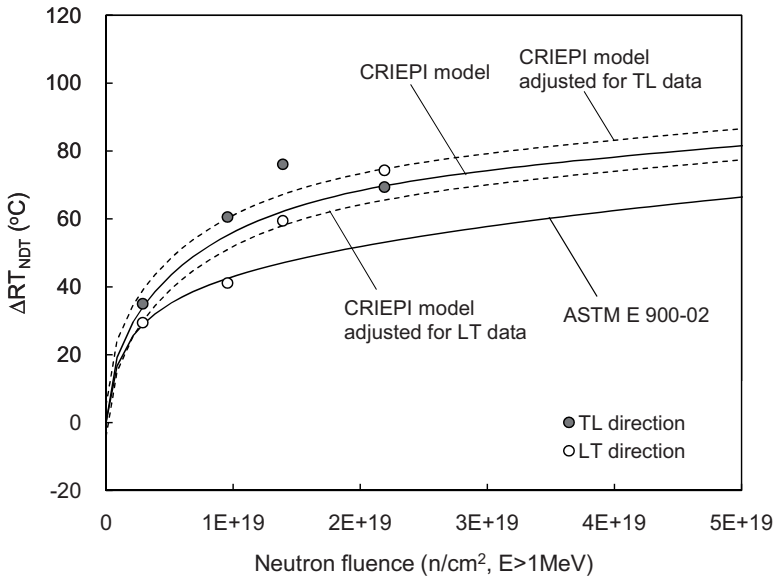


FIG. 13—Comparison of the predictions and surveillance data of SQ1. Cu and Ni contents are 0.13 and 0.76 wt %, respectively.

TABLE 3—Coefficients for the embrittlement correlation method. Since different time integration methods result in different predicted values, these coefficients must be used together with the source code in Fig. 14.

Coefficient	Value
ξ_1	7.8389×10^{-06}
ξ_2	2.6450×10^{-04}
ξ_3	3.4068×10^{-01}
ξ_4	7.1620×10^{-01}
ξ_5	$7.6028 \times 10^{+00}$
ξ_6	7.6159×10^{-01}
ξ_7	$3.3033 \times 10^{+00}$
ξ_8	$2.7840 \times 10^{+02}$
ξ_9	2.9500×10^{-25}
ξ_{10}	2.4093×10^{-02}
ξ_{11}	6.6826×10^{-01}
ξ_{12}	6.0732×10^{-05}
ξ_{13}	7.3670×10^{-01}
ξ_{14}	$2.4264 \times 10^{+00}$
ξ_{15}	7.3319×10^{-01}
ξ_{16}	$2.3457 \times 10^{+02}$
ξ_{17}	$1.7241 \times 10^{+00}$

simple equation. The coefficients of the equations are optimized using the most recent Japanese surveillance data. A new concept of offset adjustment was proposed to adjust the predictions to the surveillance data. This adjustment was found to work very well for the Japanese surveillance data.

Some comparisons were made between the predictions of the new correlation and the U.S. new correlation and surveillance database. It was found that, in general, the present correlation works well for the U.S. surveillance data with two exceptions of CE plates and Linde 80 welds. The prediction of U.S. forging data was discussed in the light of offset adjustment concept, and the necessity to investigate the start-of-life properties of forgings was suggested.

The new embrittlement correlation method was adopted in the new revision of the JEAC4201-2004 and now is referred to as JEAC4201-2007 [29].

Acknowledgments

The writers acknowledge the support of Tokyo Electric Power Co., Kansai Electric Power Co., Hokkaido Electric Power Co., Tohoku Electric Power Co., Chubu Electric Power Co., Hokuriku Electric Power Co., Chugoku Electric Power Co., Shikoku Electric Power Co., Kyushu Electric Power Co., and Japan Atomic Energy Co. The writers acknowledge helpful discussions with the members of the Working Group of Fracture Toughness of Japan Electric Association. The writers would like to express special thanks to Prof. Naoto Sekimura of the University of Tokyo, Dr. Colin English of National Nuclear Laboratory,

```

1 /*=====
2 Charpy Transition Temperature Shift Calculator
3   for Reactor Pressure Vessel Materials
4 developed by N.Soneda, A.Nomoto, K.Dohi, S.Ishino (GZEPF)
5 Copyright 2007 (C) Central Research Institute of Electric Power Industry. All right reserved.
6 April 10, 2007
7 =====*/
8
9
10 #define WASTEPS 500
11 #define CU_SOLUBILITY 0.040
12 #define CU_MAX_SOLUBILITY 0.50
13
14 double max(double x, double y)
15 {
16   if (x > y) return x;
17   else return y;
18 }
19
20 double min(double x, double y)
21 {
22   if (x < y) return x;
23   else return y;
24 }
25
26 double *CalcShift( char *ID, double Fluence, double Flux, double Trrad, double Cu, double Nf,
27                   double *t_md, double *t_c, double *t_ind, double *t_emb, double *t_sc,
28                   double *C_ind[MWASTEPS], Cu_mat[MWASTEPS],
29                   double C_sc_ind[MWASTEPS], delta_C_ind[MWASTEPS], C_emb[MWASTEPS], delta_C_emb[MWASTEPS];
30                   double vfc[MWASTEPS], C_md[MWASTEPS];
31                   double vfc_emb[MWASTEPS], vfc_ind[MWASTEPS], vfc_emb[MWASTEPS], vfc[MWASTEPS];
32                   double D_Cu, Cu_sol;
33                   double P, q, s;
34                   double delta_ft, delta_tn, delta_t;
35                   double *prediction;
36                   int i;
37                   int flag = 0;
38
39 /* initialize */
40 delta_ft = delta_t = Flux;
41 delta_tn = delta_t / 5.0e-11;
42 Cu_sol = CU_SOLUBILITY;
43 Cu_max = CU_MAX_SOLUBILITY;
44 Cu_mat[0] = 0.75 * P + 0.52;
45 Cu_avai[0] = max( Cu_mat[0] - Cu_sol, 0.0 );
46 delta_C_ind[0] = 0.0;
47 delta_C_emb[0] = 0.0;
48 C_md[0] = 0.0;
49 C_emb[0] = 0.0;
50 Ft[0] = 0.0;
51 p = gz[4] + pow( (1.869 - 0.00457 * Trrad) / (1.869 - 0.00457 * 288), 2.0 )
52 + D_Cu * Cu * pow( (1.0 + gz[7] * Nf), 0.6 );
53 q = pow( (1.0 + gz[13] * pow( Nf, gz[14] )) / (1.0 + gz[7] * 0.6), 2.0 ) * gz[8];
54 s = pow( (1.0 + gz[13] * pow( 0.6, gz[14] )) * gz[15], 2.0 );
55
56 for ( i = 1; i < WASTEPS; i++) {
57   /*=====
58   MICROSTRUCTURE EVOLUTION
59   =====*/
60
61   /* calculate Fluence */
62   ft[i] = ft[i-1] + delta_ft;
63   Ft[i] = Ft[i-1] + delta_tn;
64
65   /* calculate increment of irradiation-induced solute atom clusters */
66   delta_C_ind[i] = min( (Cu_mat[i-1] + 0.02) * D_Cu + 0.0003
67                       * (delta_ft * p + C_md[i-1] * delta_tn)
68                       + gz[3], delta_ft * p + C_md[i-1] * delta_tn );
69   C_ind[i] = C_ind[i-1] + delta_C_ind[i];
70
71   /* calculate increment of irradiation-enhanced solute atom clusters */
72   delta_C_emb[i] = Cu_avai[i-1] + delta_C_emb[i];
73   C_emb[i] = C_emb[i-1] + delta_C_emb[i];
74
75   /* calculate SC number density */
76   C_sc[i] = C_ind[i] + C_emb[i];
77
78   /* calculate Cu content in solution */
79   vfc[i] = (min( Cu, Cu_max) - Cu_mat[i]) / C_sc[i];
80   vfc_emb[i] = (vfc[i] * gz[9]) / (1.0 + gz[10] * D_Cu) + (vfc[i] * gz[11] + gz[12]) * s;
81   vfc_ind[i] = vfc[i] + C_emb[i];
82   vfc_emb[i] = vfc_ind[i] + vfc_emb[i];
83
84   /*=====
85   MECHANICAL PROPERTY CHANGE
86   =====*/
87   t_md[i] = gz[16] * sqrt(vfc_ind[i]);
88   t_sc[i] = gz[16] * sqrt(vfc[i]);
89   t[i] = sqrt( t_sc[i] * t_sc[i] + t_md[i] * t_md[i] );
90
91   /* INTERPOLATION OF TEMPERATURE SHIFT
92   =====*/
93   pred = 0.0; prediction = NULL;
94   if (Fluence == 0.0) {
95     prediction = &pred;
96     prediction = NULL;
97   } else {
98     for ( i = 1; i < WASTEPS; i++) {
99       if (Fluence < Ft[i]) {
100         Flag = 1;
101         r1 = (Fluence - Ft[i-1]) / (Ft[i] - Ft[i-1]);
102         r2 = (Ft[i] - Fluence) / (Ft[i] - Ft[i-1]);
103         pred = r1 * r1 + r2 * r2;
104         break;
105       }
106       if (Flag == 1)
107         prediction = &pred;
108     }
109   }
110
111   /*=====
112   INTERPOLATION OF TEMPERATURE SHIFT
113   =====*/
114   pred = 0.0; prediction = NULL;
115   if (Fluence == 0.0) {
116     prediction = &pred;
117   } else {
118     for ( i = 1; i < WASTEPS; i++) {
119       if (Fluence < Ft[i]) {
120         Flag = 1;
121         r1 = (Fluence - Ft[i-1]) / (Ft[i] - Ft[i-1]);
122         r2 = (Ft[i] - Fluence) / (Ft[i] - Ft[i-1]);
123         pred = r1 * r1 + r2 * r2;
124         break;
125       }
126       if (Flag == 1)
127         prediction = &pred;
128     }
129   }
130
131   /*=====
132   MICROSTRUCTURE EVOLUTION
133   =====*/
134
135 }

```

FIG. 14—Computer code to calculate the predicted transition temperature shifts.

Mrs. Bob Carter and Stan Rosinski of EPRI, and Mr. Bill Server of ATI Consulting and Dr. Randy Lott of Westinghouse for their fruitful discussions and suggestions through the development of the new correlation method.

Appendix: Calculation of Transition Temperature Shift

The final set of coefficients together with the computer code used to integrate the rate equations can be found in Table 3 and Fig. 14.

References

- [1] JEAC4201-2004, December 21, 2004, "Method of Surveillance Tests for Structural Materials of Nuclear Reactors," Japan Electric Association, Chiyoda-ku, Tokyo, Japan.
- [2] Eason, E. D., Wright, J. E., and Odette, G. R., "Improved Embrittlement Correlations for Reactor Pressure Vessel Steels," *Report No. NUREG/CR-6551*, U.S. Nuclear Regulatory Commission, Washington, D.C., November 1998.
- [3] ASTM E900-02, 2002, "Standard Guide for Predicting Radiation-Induced Transition Temperature Shift for Reactor Vessel Materials, E706(IIF)," *Annual Book of ASTM Standards*, Vol. 12.02, ASTM International, West Conshohocken, PA.
- [4] Eason, E. D., Odette, G. R., Nanstad, R. K., and Yamamoto, T., "A Physically Based Correlation of Irradiation-Induced Transition Temperature Shifts for RPV Steels," *Report No. ORNL-TM-2006/530*, U.S. Nuclear Regulatory Commission, Washington, D.C., 2007.
- [5] For example, Odette, G. R. and Lucas, G. E., *Radiat. Eff. Defects Solids*, Vol. 144, 1998, pp. 189–231.
- [6] Miller, M. K. and Burke, M. G., "Fine-Scale Microstructural Characterization of Pressure Vessel Steels and Related Materials Using APFIM," *Effects of Radiation on Materials: 14th International Symposium (Volume II)*, ASTM STP 1046, N. H. Packan, R. E. Stoller, and A. S. Kumar, Eds., ASTM International, West Conshohocken, PA, 1990, p. 107.
- [7] Auger, P., Pareige, P., Akamatsu, M., and Blavette, D., "APFIM Investigation of Clustering in Neutron-Irradiated Fe–Cu Alloys and Pressure Vessel Steels," *J. Nucl. Mater.*, Vol. 225, 1995, pp. 225–230.
- [8] Carter, R. G., Soneda, N., Dohi, K., Hyde, J. M., English, C. A., and Server, W. L., "Microstructural Characterization of Irradiation-Induced Cu-Enriched Clusters in Reactor Pressure Vessel Steels," *J. Nucl. Mater.*, Vol. 298, 2001, p. 211–224.
- [9] Hawthorne, J. R., "Significance of Nickel and Copper Content to Radiation Sensitivity and Post-irradiation Heat Treatment Recovery of Reactor Vessel Steels," *Effects of Radiation on Materials: 11th Conference*, ASTM STP 782, H. R. Brager and J. S. Perrin, Eds., ASTM International, West Conshohocken, PA, 1982, p. 375.
- [10] Carter, R. G., "Conclusions from the EPRI-CRIEPI Workshop on Dose Rate Effects in RPV Materials," *Conference Proceedings of Workshop on Dose Rate Effects in Reactor Pressure Vessel Materials*, EPRI 1006981, CRIEPI T980203, Squaw Creek Resort, Olympic Valley, CA, November 12–14, 2001, Electric Power Research Institute, Palo Alto, CA and Central Research Institute of Electric power Industry, Komae Tokyo, Japan, pp. 1.1–1.9.
- [11] Odette, G. R., "Microstructure Induced Microstructural Evolution in Reactor Pres-

- sure Vessel Steels," *Microstructure of Irradiated Materials, MRS Symp. Proc.*, Vol. 373, I. M. Robertson, L. E. Rehn, S. J. Zinkle, and W. J. Phythian, Eds., MRS, Pittsburgh, PA, 1995, p. 137.
- [12] Odette, G. R., Liu, C. L., and Wirth, B. D. "On the Composition and Structure of Nanoprecipitates in Irradiated Pressure Vessel Steels," *Microstructure Evolution During Irradiation, MRS Symp. Proc.*, Vol. 439, I. M. Robertson, G. S. Was, L. W. Hobbs, and T. Diaz de la Rubia, Eds., MRS, Pittsburgh, PA, 1997, p. 547.
- [13] Soneda, N., Dohi, K., Nomoto, A., Nishida, K., and Ishino, S., "Development of Neutron Irradiation Embrittlement Correlation of Reactor Pressure Vessel Materials of Light Water Reactors," *Report No. CRIEPI Q06019*, Central Research Institute of Electric Power Industry, Komae, Tokyo, Japan, April 2007.
- [14] Auger, P., Pareige, P., Akamatsu, M., and Van Duysen, J.-C., "Microstructural Characterization of Atom Clusters in Irradiated Pressure Vessel Steels and Model Alloys," *J. Nucl. Mater.*, Vol. 211, 1994, pp. 194–201.
- [15] Otaka, M. and Osaki, T., "Reduction of Upper Shelf Energy of Highly Irradiated RPV Steels," *Conference Proceedings of the 30th MPA-Seminar in Conjunction with the Ninth German-Japanese Seminar*, Paper No. 9.1, Stuttgart, October 6–7, 2004, Materials Testing Institute, University of Stuttgart, Stuttgart.
- [16] Soneda, N., Dohi, K., Nishida, K., Nomoto, A., Tomimatsu, M., and Matsuzawa, H., "Microstructural Characterization of RPV Materials Irradiated to High Fluences at High Flux," *J. ASTM Int.*, Vol. 6, No. 7, 2009, Paper ID JAI102128.
- [17] Nuclear and Industrial Safety Agency (NISA), "Basic Concept on the Enhancement of the Ageing Management," April 6, 2005, Ministry of Economy, Trade and Industry, Chiyoda-ku, Tokyo, Japan (in Japanese).
- [18] Fisher, S. B., Harbottle, J. E., and Aldridge, N., "Radiation Hardening in Magnox Pressure Vessel Steels," *Philos. Trans. R. Soc. London, Ser. A*, Vol. 315, 1985, pp. 301–332.
- [19] Fisher, S. B. and Buswell, J. T., "A Model for PWR Pressure Vessel Embrittlement," *Int. J. Pressure Vessels Piping*, Vol. 27, 1987, pp. 91–135.
- [20] Soneda, N., Ishino, S., Takahashi, A., and Dohi, K., "Modeling the Microstructural Evolution in bcc-Fe During Irradiation Using Kinetic Monte Carlo Computer Simulation," *J. Nucl. Mater.*, Vol. 323, 2003, pp. 169–180.
- [21] Hiranuma, N., Soneda, N., Dohi, K., Ishino, S., Dohi, N., and Ohata, H., "Mechanistic Modeling of Transition Temperature Shift of Japanese RPV Materials," *30th MPA-Seminar in Conjunction with the Ninth German-Japanese Seminar*, Paper No. 3.1, Stuttgart, October 6–7, 2004, Materials Testing Institute, University of Stuttgart, Stuttgart.
- [22] Jones, R. B. and Williams, T. J., "The Dependence of Radiation Hardening and Embrittlement on Irradiation Temperature," *Effects of Radiation on Materials: 17th International Symposium, ASTM STP 1270*, D. S. Gelles, R. Nanstad, A. S. Kumar, and E. A. Little, Eds., ASTM International, West Conshohocken, PA, 1996, p. 569.
- [23] Debarberis, L., Acosta, B., Sevini, F., Krykov, A., Gillemot, G., Valo, M., Kikolaev, A., and Brumovsky, M., "Role of Nickel in a Semi-Mechanistic Analytical Model for Radiation Embrittlement of Model Alloys," *J. Nucl. Mater.*, Vol. 336, 2005, pp. 210–216.
- [24] Japan Power Engineering and Inspection Corporation (JAPEIC), "Annual Report on PLIM Project," JAPEIC, Minato-ku, Tokyo, March 2003.
- [25] Soneda, N., English, C., and Server, W., "Use of an Offset in Assessing Radiation Embrittlement Data and Predictive Models," *Proceedings of PVP2006-ICPVT-11, 93369, 2006 ASME Pressure Vessels and Piping Division Conference*, Vancouver, BC,

Canada, July 23–27, 2006, American society of Mechanical Engineers, New York, NY.

- [26] “BWR VIP-178NP: BWR Vessel and Internal Project, Nonproprietary Report of Material Test Results from the BWR Integrated Surveillance Program (ISP),” *Report No. 1015504*, Epri, Palo Alto, CA, 2007.
- [27] McElroy, R. J. and Lowe, A. L., Jr., “Irradiation Embrittlement Modelling of Linde 80 Weld Metals,” *ASTM STP1270*, D. S. Gelles, R. Nanstad, A. S. Kumar, and E. A. Little, Eds., ASTM International, West Conshohocken, PA, 1996, pp. 68–85.
- [28] ASTM E399-09, 2009, “Standard Test Method for Linear-Elastic Plane-Strain Fracture Toughness K_{Ic} of Metallic Materials,” *Annual Book of ASTM Standards*, Vol. 03.01, ASTM International, West Conshohocken, PA.
- [29] JEAC4201-2007, 2007, “Method of Surveillance Test for Structural Materials of Nuclear Reactors,” Japan Electric Association, Chiyoda-ku, Tokyo, Japan.

DISCUSSION - JAI102127, Embrittlement Correlation Method for the Japanese Reactor Pressure Vessel Materials, published online in the Journal of ASTM International (JAI), Volume 7, Issue 3 (March 2010) and included in STP1513, Effects of Radiation on Nuclear Materials and the Nuclear Fuel Cycle: 24th Volume.

To Whom It May Concern:

During the recent months, there has been considerable discussion on the paper, "Embrittlement Correlation Method for the Japanese Reactor Pressure Vessel Materials" published in the Vol. 7, Issue 3 (March 2010) of the Journal of ASTM International (JAI) and included in STP 1513, Effects of Radiation on Nuclear materials and the Nuclear Fuel Cycle: 24th Volume.

Specifically, technical concerns were raised about some of the terminology and application of the data used by Dr. Soneda and colleagues. ASTM, JAI, and the chairman of STP 1513 have taken a detailed and sincere analysis of the exchange. Additional referees were provided and a technical dialogue continued. The resulting exchange is listed below for formal archive and consideration by future online readers of this paper.

As the chairman of the 24th ASTM Symposium on Effects of Radiation on Materials and Nuclear Fuel Cycle, I believe it is of high importance to address and examine papers when such technical concerns are raised. In this case, recent developments and understanding in Japanese data and guidelines have evolved beyond the proposals in this particular paper. Indeed, new data or interpretations are often drivers of changes in theory or mechanistic understanding in all fields of research and this is a valuable part of the scientific process.

I would like to thank Prof. Koiwa and Dr. Soneda for the insightful and detailed debate and discussion to both help resolve this issue and to further our knowledge.

Sincerely,

Jeremy T. Busby

A comment on the paper entitled:

Embrittlement Correlation Method for the Japanese Reactor Pressure Vessel Materials

by Soneda N., Dohi K., Nomoto A., Nishida K., Ishino S.

published in Journal of ASTM International (JAI) - 2010 - Volume 7, Issue 3.

In the paper the authors have developed a new embrittlement correlation method for the Japanese reactor pressure vessel steels. The method consists of two parts. First the microstructural changes during irradiation are modeled using rate equations to derive the concentrations of “solute clusters” C_{SC} and of the “matrix damage” C_{MD} . In the second step, the transition temperature shift ΔT is related to the defect concentrations C_{SC} and C_{MD} .

The first rate equation describing the rate of increase in C_{SC} is given as

$$\frac{\partial C_{SC}}{\partial t} = \xi_3 \cdot \left((C_{Cu}^{mat} + \varepsilon_1) \cdot D_{Cu} + \varepsilon_2 \right) \cdot C_{MD} + \xi_8 \cdot \left(C_{Cu}^{avail} \cdot D_{Cu} \cdot \left(1 + \xi_7 \cdot C_{Ni}^0 \right) \right)^2.$$

The first term in the above equation describes the formation of irradiation–*induced* solute atom clusters: copper atoms in solid solution migrate to matrix damage to form (nucleate) solute clusters. The second term describes the formation of irradiation–*enhanced* solute atom clusters: enhancement by vacancies due to irradiation will be included as the increase in diffusion coefficient of copper. Here the authors state: “Therefore, it is described as the square of the product of the concentration of copper atoms in supersaturation and the diffusivity.”

According to the random walk theory, the frequency of association of two moving entities is expressed by the product of the diffusivity* and the square of the concentration of the moving entity. The diffusion coefficient should appear simply as D , but not as D^2 . The inadequacy becomes evident by comparing the two terms after dropping less significant quantities as shown below.

The first term $D_{Cu} \cdot C_{Cu}^{mat} \cdot C_{MD}$

The second term $\left(D_{Cu} \cdot C_{Cu}^{avail} \right)^2$

Needless to say, the dimensions of the two terms should be the same.

This error is rather elementary yet fatal: the error in the basic equation inevitably invalidates whole the result of the subsequent analysis. The paper should be withdrawn.

*More properly, “jump frequency” should be used here, instead of “diffusivity”.

Masahiro Koiwa* and Hiromitsu Ino**

*** Professor Emeritus, Kyoto University**

**** Professor Emeritus, the University of Tokyo**

Editor’s response to comment on the paper entitled:

**Embrittlement Correlation Method for the Japanese Reactor Pressure Vessel
Materials**

by Soneda N., Dohi K., Nomoto A., Nishida K., Ishino S.

published in Journal of ASTM International (JAI) - 2010 - Volume 7, Issue 3.

All,

I have asked several other experts in RPV steels and physics of radiation damage to look at this paper and the recent comments. The comments in the letter do have merit and we could all see their concern in the development of the equations as they do not follow the generally accepted theory for such phenomena. Further, given the current state of awareness around the world on reactor integrity, such concerns are understandable.

While the proposed in the manuscript "model" may not be considered as a physically-based model, the ability of this "model" to describe large

Japanese surveillance database is a worthy accomplishment. I am copying this to the author of this paper and recommending him in the future to use better wording. For example, use of "estimation" instead of "modeling" for clarity. Indeed, you are using those equations to estimate microstructural changes during irradiation and their contribution to embrittlement correlation method.

It is apparent from the paper, that these estimations are doing good job of describing the large database. Modeling, on the other hand, is based on more basic, fundamental relations and is extremely important for understanding such complicated phenomena. However, straight-forward inserting of a pure physically-based model into a regulatory correlation method may be difficult to achieve at this point.

As the editor/chair of this conference, I am hesitant to endorse removal of the paper from the proceedings or the online database. Additional research will judge the relationship on its own merit and either strengthen the findings or disprove them. I'm not sure our role as publisher's/editors is to make that judgment on our own in advance.

Jeremy Busby

Author's Response to A comment on the paper entitled:

**Embrittlement Correlation Method for the Japanese Reactor Pressure Vessel
Materials**

by Soneda N., Dohi K., Nomoto A., Nishida K., Ishino S.

published in Journal of ASTM International (JAI) - 2010 - Volume 7, Issue 3.

Dear All,

Thank you very much for copying me your discussions.

I would appreciate if you could allow me to add some comments.

I agree with Jeremy Busby and other experts he consulted with that the generally accepted form is $D \times C_{cu} \times C_{cu}$, not $D^2 \times C_{cu} \times C_{cu}$. But this is true for C_{cu}^2 , which is the number density of di-Cu, in terms of the fundamental physics (or rate theory) point of view. Our equation is for the time evolution of C_{sc} , which is the number density of well-grown solute atom clusters, that can be detected by atom probe tomography and consist of hundreds or thousands of solute atoms. In other words, our equation is for the precipitation process. Our equation is still not purely fundamental physics based, but exact expression of precipitation process using a simple single term, like irradiation-enhanced clustering term in our equation, is impossible anyway, and our equation is a correlation or approximation. In this sense, the suggestion of the letter to use D in stead of D^2 (the letter says we "should" use D) is not necessarily correct. We can just say that the term works or not.

The goal of our paper and equations is to develop a PRACTICAL engineering correlation method that can be used to describe the amount of embrittlement of the Japanese RPV steels. Our objective is not to develop a purely physics based theory, which I believe impossible with a few simple equations.

I would appreciate if you could consider these points.

Best regards,

Naoki Soneda
Materials Science Research Laboratory
NPP Maintenance Rsearch Team
CRIEPI

Ms Kathy Dernoga
Managing Editor, Books and Journals
ASTM International

Dear Ms Kathy Dernoga,

Thank you for your mail of September 10, 2012. I read the mail carefully, but I feel it necessary to write you again to explain the situation more clearly.

As stated at the end of the paper by Soneda et al, "the new Embrittlement Correlation Method" was adopted in JEAC4201-2007. Recently, at the committee meeting of Nuclear and Industrial Safety Agency (NISA), the Institute of Electric Power Industry (CRIEPI), together with the Federation of Electric Power Companies of Japan and Central Research, reported the result of preliminary analysis on Embrittlement Correlation Method or JEAC4201-2007. The fitting parameters of the CRIEPI model were optimized to new Japanese surveillance database. It turned that the new parameter set is widely different from that (Table 3 in the paper by Soneda et al) adopted in JEAC4201-2007. Note that even the new set does not predict correctly the

increase in the ductile-brittle transition temperature obtained for the specimen irradiated in No. 1 reactor at Genkai plant. For your reference, the table of the parameters is given at the end of this note. This clearly shows the fragility of the method, in contradiction to the opinion of the symposium chairman, Jeremy Bushy:

(1) the ability of this "model" to describe large Japanese surveillance database is a worthy accomplishment.

(2) these estimations are doing good job of describing the large database.

I understand that JAI is no longer published, and May 2012 was its last published issue. Yet, I have to point out that the journal is still on line, and is still available to researchers, as shown in http://www.astm.org/DIGITAL_LIBRARY/JOURNALS/JAI/jai_about.html

Thus, I do believe that the option suggested by Dr Sheldon Dean is most relevant:

“The only other option that I can suggest is that we attach a discussion to the archived paper. That would at least alert the readership that the paper is controversial, but it does not alert the folks who have seen the original paper that the problem exists. “

I believe that the publishers are responsible for distributing right information and quickly correct them in case of any mistakes. I do hope you reconsider your decision.

Yours sincerely,
Masahiro Koiwa,
Professor Emeritus, Kyoto University

変数	JEAC4201-2007	Case III
ξ_1	7.8389E-06	9.7208E-06
ξ_2	2.6450E-04	3.7232E-04
ξ_3	3.4068E-01	1.4231E+00
ξ_4	7.1620E-01	7.1620E-01
ξ_5	7.6028E+00	2.1943E+00
ξ_6	7.6159E-01	1.1885E+00
ξ_7	3.3033E+00	5.6817E+00
ξ_8	2.7840E+02	7.1272E+02
ξ_9	2.9500E-25	3.9940E-25
ξ_{10}	2.4093E-02	0.0000E+00
ξ_{11}	6.6826E-01	6.6826E-01
ξ_{12}	6.0732E-05	2.0039E-05
ξ_{13}	7.3670E-01	1.4434E-01
ξ_{14}	2.4264E+00	4.7000E+00
ξ_{15}	7.3319E-01	7.3319E-01
ξ_{16}	2.3457E+02	3.0277E+02
ξ_{17}	1.7241E+00	2.2404E+00
η_1	7.0000E-06	1.8709E-07
η_2	5.2000E-01	6.3156E-01

In the above the right column indicated as Case III is said to give a better fit to the new database.

Dear All,

Thank you for including me in this discussion.

Let me say a few words about the letter from Prof. Koiwa.

1. He says "It turned that the new parameter set is widely different from that (Table 3 in the paper by Soneda et al) adopted in JEAC4201-2007." What we did in this work was to calibrate our embrittlement correlation method to the new database by changing the coefficients. Since we have almost 20 coefficients in the equation set, it is very natural that the change in the value of one coefficient is compensated by the change in the value(s) of another coefficient(s). This may result in a non-trivial change of the values of some of the coefficients. The amount of change will depend on the sensitivity of the calculated transition temperature shift to the coefficients.
2. He says "Note that even the new set does not predict correctly the increase in the ductile-brittle transition temperature obtained for the specimen irradiated in No. 1 reactor at Genkai plant." I do not understand the quantitative meaning of "correctly". We are working on the commercial steels, in which we always see a lot of scatter in the data. In the RPV steels case, since the transition temperature shift of RPV steels is measured by the Charpy impact test, the measured shifts are always accompanied with some uncertainties at least due to the test method itself. According to my experience with the Japanese and also US surveillance database, the error of the new prediction is well within the acceptable uncertainty band.

Thank you for your patience to my long message.

Best regards,
Naoki Soneda
Materials Science Research Laboratory
NPP Maintenance Research Team
CRIEPI

M. R. Wootton,¹ R. Moskovic,¹ C. J. Bolton,¹ and
P. E. J. Flewitt¹

Magnox Steel Reactor Pressure Vessel Monitoring Schemes—An Overview

ABSTRACT: The steel pressure vessel Magnox reactors were designed in the 1950s and were made from C–Mn plate steel and forgings welded together using a mixture of submerged-arc and manual metal arc weld metals. Each reactor contained surveillance capsules with specimens of plate steel, forgings, and the different weld metals to monitor the effects of irradiation on the Charpy impact and tensile properties. Canisters were withdrawn over the operating life and measurements were taken. During the lifetime of the fleet, there were developments in testing, observed changes in properties, and understanding of the radiation damage process that challenged the safety cases to support the operation of the stations. At the time the reactors were designed, the concept of fracture toughness was only beginning to be investigated, yet during the lifetime of the stations, fracture toughness testing was successfully adopted as standard practice as an input to fracture mechanics based assessment of the steel vessels. Both hardening and non-hardening embrittlements, the latter due to impurity phosphorus segregation in weld metal, were successfully addressed. At a relatively late stage the contribution of “thermal neutrons” to embrittlement was identified as being significant and was successfully incorporated into the assessment process. This led to the adoption of sophisticated statistical techniques to assess changes in properties of the most critical construction material—submerged-arc weld metal. A large scale sampling and testing programme of submerged-arc weld metal from a decommissioned reactor validated the assessment process. As a result of successfully addressing these and other challenges when the last two steel pressure vessel stations closed in December 2006, they had achieved lifetimes of nearly 40 years.

Manuscript received June 17, 2008; accepted for publication September 23, 2009; published online January 2010.

¹ Magnox Electric, Ltd., Oldbury Naite, Oldbury-on-Severn, Bristol, BS35 1RQ United Kingdom.

Cite as: Wootton, M. R., Moskovic, R., Bolton, C. J. and Flewitt, P. E. J., “Magnox Steel Reactor Pressure Vessel Monitoring Schemes—An Overview,” *J. ASTM Intl.*, Vol. 7, No. 1. doi:10.1520/JAI101948.

Copyright © 2010 by ASTM International, 100 Barr Harbor Drive, PO Box C700, West Conshohocken, PA 19428-2959.

KEYWORDS: steel reactor pressure vessel, monitoring programme, Magnox power station, carbon-manganese steel, neutron irradiation

Introduction

In the period between 1962 and 1966, the Central Electricity Generation Board (CEGB) commissioned six Magnox nuclear power stations in the United Kingdom each with two steel reactor pressure vessels (RPVs). Commissioning and cessation of generation dates for these power stations are presented in Table 1.

With the exception of Berkeley, all of the stations had spherical RPVs approximately 20 m in diameter (Fig. 1) and fabricated from 75 to 100 mm thick plain carbon-manganese steel plates and forgings joined together by a mixture of manual metal arc and semi-automatic submerged-arc weld metals. This spherical shell contained carbon dioxide coolant gas and operated typically at pressures of between 10 and 20 bars depending on the design with core gas inlet and outlet temperatures of approximately 190 and 360°C, respectively. The design of the two reactors at Berkeley was based on those of the earlier stations at Calder Hall and Chapelcross and had cylindrical pressure vessels of approximately 11 m in diameter and material of 50 mm thickness. The pressure of carbon dioxide in the reactor circuit was only 7 bars, while the core inlet and outlet temperatures (150 and 350°C) were similar to the later stations (see Table 1).

As with any structure of this type, it is the welds that are judged to be the areas of the vessel most likely to contain any potential defects, albeit they are designed to be tolerant of defects. At the time of their construction, there was no specific nuclear code available, and the vessels were designed, constructed, inspected, and tested to the conventional non-nuclear code BS1500 Class 1. Thus, the original safety case assessments were based on the fact that they had been built to an established code of practice with particular attention given to quality control, fabrication, and inspection techniques.

All of these stations were designed in the 1950s when little was known about the effects of neutron irradiation on ferritic steel beyond the fact that steels would become hardened and embrittled when exposed to increasing amounts of neutron irradiation [1,2]. In addition, this also predated the adoption of fracture mechanics approaches to integrity assessment. In order to avoid the possibility of brittle fracture of the pressure vessel, it was stipulated [2] that the vessels should be never be pressurized at any temperature at which

TABLE 1—*Ex-CEGB Magnox power stations with steel RPVs.*

Station	Year Commissioned	Year Closed
Berkeley	1962	1989
Bradwell	1962	2002
Dungeness A	1965	2006
Hinkley point A	1965	1999
Trawsfynydd	1965	1991
Sizewell A	1966	2006

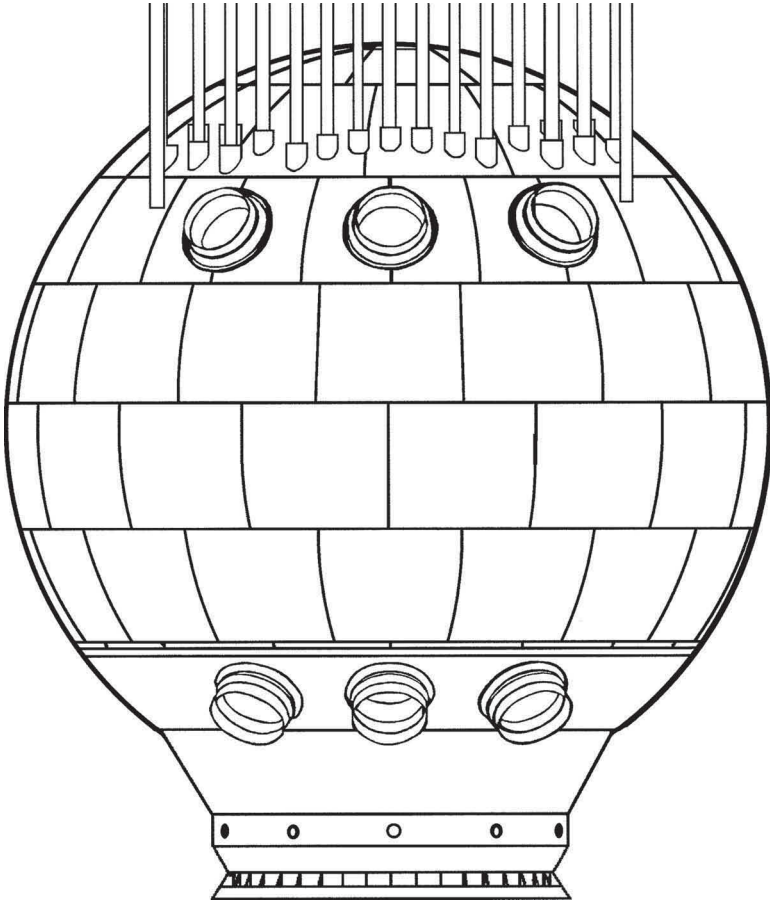


FIG. 1—Schematic Magnox steel RPV.

a brittle crack could propagate. The critical temperature for the start-of-life condition of the structural materials was determined by Robertson crack arrest tests [3], but it was recognized that it would be impossible to carry out tests of this nature on irradiated material. For this reason steel pressure vessel monitoring schemes, consisting of steel canisters containing test specimens made from the various RPV structural steels, were included in the reactors at all of these Magnox stations. The positions of the canisters generally meant that they had accrued similar neutron doses to the adjacent vessel, but there were a few locations where the vessel had a higher dose than the appropriate surveillance canister locations by a factor of about two. The intention was to periodically remove these canisters over the life of each reactor and add the increase in the Charpy ductile to brittle transition temperature ($\Delta T_{40 J}$) to the initial crack arrest temperature to allow for the effects irradiation and ageing effects [2]. No design life was ever specified for these stations, but predictions of the combined

affects of ageing and neutron irradiation [2] indicate that 20 years was considered as achievable.

Safety arguments were revised in the early 1980s using fracture mechanics methodology. Monitoring of properties continued, the arguments became more sophisticated, and further modifications had to be made to vessel operating procedures.

A deterministic assessment method was developed to replace the original assessment based on the Robertson crack arrest temperature. Briefly, this was a fracture mechanics approach based on the R6 [4] two criteria failure avoidance procedure. The main inputs to the fracture mechanics assessment were depth, shape, and position of a potential defect, materials properties, loading conditions, and the geometry and dimensions of the plant component. The procedure was used to determine the minimum failure pressure as a function of vessel temperature, defined as the pressure limit line, for different locations on the vessel. By comparing this failure line with the pressure and temperature limits set by the operating rules for a reactor, it was possible to derive temperature margins and pressure reserve factors for the plant. Since the temperature and neutron flux were not uniform over the pressure vessel, these assessments had to be undertaken at bounding and key locations.

As noted above material property data was one of the key input parameters into the deterministic fracture mechanics assessment of defects in the steel RPVs. This included start-of-life properties including yield stress, ultimate tensile stress, and fracture toughness. Before entering service, tensile properties had been measured at ambient temperature, and Charpy impact energies had been measured at only -10°C . Being able to predict changes in a material's tensile and fracture toughness properties after exposure to the service environment was an essential contribution to the overall structural integrity assessment. The fact that temperature and neutron dose were not uniform over the pressure vessels meant that generic methods had to be developed for predicting changes in tensile and fracture toughness properties. Although this information was required for all structural materials, the understanding of the variation in the properties of submerged-arc weld metal would rapidly become of prime importance in the assessment process. The data obtained from testing specimens contained in the various RPV surveillance canisters was invaluable in the development of means for predicting the properties of neutron irradiated RPV structural materials.

During the lifetime of the stations, trends in the data from the surveillance programmes and the advent of new assessment techniques based on fracture mechanics concepts all presented significant challenges to the continued operation of the Magnox fleet. At the same time, improved understanding of the effects of neutron irradiation on the properties of steels helped in the interpretation of these trends in behavior. As a consequence, it was possible to successfully address these challenges to the extent that when the last steel pressure vessel stations were closed in December 2006, lifetimes of up to 40 years had been achieved (Table 1).

TABLE 2—Typical chemical compositions (wt %).

Material	C	Mn	Si	S	P	Cu
Plate	0.09–0.17	1.04–1.32	0.10–0.60	0.02–0.04	0.01–0.04	0.03–0.15
Forgings	0.18	1.30	0.36	0.024	0.024	0.10
Manual metal arc weld	0.086	0.91	0.42	0.022	0.025	0.08
Submerged-arc weld	0.088	1.49	0.52	0.037	0.031	0.23

Design of the Monitoring Schemes

The Magnox RPVs (Fig. 1) were made of plain carbon-manganese plate steels and forgings and welded by a mixture of manual metal arc and semi-automatic submerged-arc weld metals. Typical compositions of these materials are summarized in Table 2.

The steels in the Magnox RPVs experienced a wide range of dose and thermal conditions, and the RPV surveillance schemes were designed to cover this range of conditions (Table 3). In the long term this was to prove an advantage as it led to a good understanding of the effects of each variable on the response of steels to neutron irradiation. However, the design also meant that there were problems in assessing all of the required RPV locations and there were gaps in the data where interpolation and others where some extrapolation of properties were needed. Nevertheless, the understanding of the science behind the behavior of the materials gave confidence in the predictions.

A typical original surveillance scheme canister is shown in Fig. 2. These contained a mixture of Charpy and tensile specimens. At the time the schemes were designed, testing of Charpy impact specimens was the only realistic method for following the embrittlement of steel. The concept of fracture mechanics and fracture toughness testing was not developed until the mid to late 1960s.

Each surveillance canister contained nickel and cobalt activation flux monitors. The measured fluxes were compared with the predictions from the three-dimensional computer model MCBEND [5], and there was generally very good agreement between measured and predicted values. Hence, there was validation of the model as applied to the RPVs.

In the late 1970s and early 1980s, the original schemes were augmented by some additional surveillance canisters containing tensile specimens together with Charpy geometry and some compact tension fracture toughness specimens all made from station specific plate and submerged-arc weld materials.

TABLE 3—Range of RPV surveillance conditions.

Canister Location	Irradiation Temp. (°C)	Dose Rate (dpa·s ⁻¹ × 10 ¹³)
Above core	330–360	3.2–4.9
Beside core	198–355	7.3–26
Below core	165–223	0.94–49

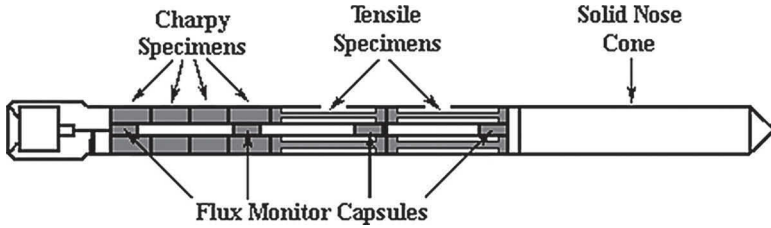


FIG. 2—Typical Magnox RPV steels surveillance canister.

Scheme Challenges and Solutions

Challenges

It had initially been estimated [2] that the combined effect of neutron irradiation and in-service ageing would give a total shift in the crack arrest temperature of 100° . As more data became available, this was reduced to 40° [6]. The development of embrittlement following each periodic withdrawal of appropriate surveillance scheme specimens was checked by reference to changes in the Charpy impact energy ductile to brittle transition temperature ($\Delta T_{40 J}$). By the late 1970s/early 1980s, data from the surveillance schemes revealed the following:

- Submerged-arc weld metal samples from the lead station, in terms of dose, were showing values of $\Delta T_{40 J}$ greater than 40°C , i.e., the shift allowance [6] had been exceeded [7,8];
- The rates of hardening and embrittlement for all materials as a function of dose expressed in $\text{n}\cdot\text{cm}^{-2}$ were greater for below reactor core specimens than for those irradiated in side-core locations at the same irradiation temperature;
- Submerged-arc weld metal was showing much greater hardening and embrittlement with radiation dose than plate, forged steel, and manual metal arc weld metal irradiated under the same conditions; and
- Submerged-arc weld metal surveillance specimens exposed in the high temperature surveillance locations ($\sim 360^{\circ}\text{C}$) in the reactors at one station were also showing high rates of embrittlement accompanied by small amounts of hardening.

At the same time that the above issues were becoming apparent, an additional complicating factor arose in that the change to integrity assessments based on fracture mechanics was required. The CEBG had developed and adopted the R6 procedure [4], and fracture toughness was an essential input into this. The adoption of fracture toughness for integrity assessment purposes had led to the declaration by the CEBG and the regulator [the Nuclear Installations Inspectorate (NII)] that during operation, the RPVs would at all times be operating on the fracture toughness upper shelf. This was in essence a restatement of the early Operating Rule that the RPVs should never be pressurized at temperature where potentially a brittle crack could propagate [2]. In the early days of using R6, the CEBG had no direct measurements of the fracture tough-

ness for irradiated material, although fracture toughness values for unirradiated materials were obtained from testing archive welds, plates, and forgings. Values of upper shelf toughness for irradiated material were predicted using correlations based on upper shelf Charpy energy and yield stress [7]. It became clear that continued use of these correlations would soon cause the upper shelf operating margins in key locations to be eroded with the associated threat of plant closures [8].

Solutions

Exceeding Shift Allowance—As noted above [2], the original way of assessing the integrity of key locations in the RPVs had been to add values of $\Delta T_{40 J}$ to the Robertson crack arrest temperatures for the appropriate steels and monitor these changes against an estimated shift to end of life. Using this approach, the finding from the surveillance programme had very serious consequences for the continued operation of the plant. Fortunately, developments in the way the resistance of material to brittle fracture were measured had moved on from the Robertson crack arrest test with the development of the concept of fracture toughness. The parallel development of the R6 procedure [4] for assessing integrity, in which fracture toughness was an essential input, helped to ameliorate the consequences of the unexpectedly high changes in the Charpy ductile to brittle transition temperature being found in the surveillance scheme and restored operating margins.

A critical part of this whole process was being able to predict the fracture toughness of the RPV materials after irradiation. The CEGB developed its own in-house methodology CUSURV [7], but this required the ability to predict irradiation induced changes in the ductile to brittle transition toughness temperature ($\Delta T_{100 \text{ MPa},m}$). Attempts to do this by direct measurement were unsuccessful, and consequently this was done indirectly by assuming that the value of $\Delta T_{100 \text{ MPa},m}$ for a given set of irradiation conditions was the same as the change in the Charpy ductile to brittle transition temperature $\Delta T_{40 J}$. However it was necessary to be able to predict this for any combination of irradiation dose and temperature and thereby each assessment location. This resulted in the development of dose damage relationships (DDRs) or trend lines that related $\Delta T_{40 J}$ and changes in yield stress to accrued radiation dose and temperature for different materials. The data used to develop these DDRs came largely from the RPV surveillance programme. At a stroke, the purpose of the surveillance schemes changed from simply monitoring the condition of the vessels at certain locations to providing experimental data that could be used to predict the state of any location in any plant. The development and maintenance of these relationships became a vital part of the continued operation of the Magnox steel pressure vessel fleet.

Differences in Hardening and Embrittlement in Sub- and Side-Core Locations—The difference in behavior between specimens after irradiation in sub- and side-core locations was a complicating problem, albeit one that did not necessarily threaten the life of the reactor fleet. The main effect arising

from this difference in behavior was that it was not possible to produce generic DDRs for each material and as the result was a series material and location specific relationships. The need for these DDRs was removed when it was established [9,10] that the reason for the different behavior between specimens irradiated in sub- and side-core locations lay in the differences between the neutron spectra in these areas. It was found that the neutron spectra at any location depended on the thickness of the graphite moderator and the presence of various in-vessel structural components. Measuring fluence in terms of displacements per atom (dpa) of iron rather than $n \cdot \text{cm}^{-2}$ enabled the due allowance to be made for the differences in neutron spectra. Consequently it was possible to combine Charpy and tensile data from different locations [7] to produce generic DDRs. Unfortunately, changing from $n \cdot \text{cm}^{-2}$ to dpa did not remove the necessity for material specific relationships.

The change from $n \cdot \text{cm}^{-2}$ to dpa as a measure of fluence initiated a large programme of work to establish dpa doses for all assessment and surveillance locations in all of the RPVs. These were estimated using the neutron transport computer model MCBEND [9,10] and were subjected to periodic revision over the remaining life of the stations. Neutron dose predictions were compared with measurements from a wide range of sources, e.g., steel monitoring wires wrapped around the RPV, individual surveillance specimens, drillings from RPV components, debris, and multi-foil activation packs. In the overwhelming majority of cases, there was very good agreement between measurements and predictions.

Submerged-Arc Weld Metal Irradiated at Temperatures Less than 290°C—The enhanced hardening and embrittlement of submerged-arc weld metal were unexpected and would remain a problem throughout the life of these Magnox power stations. It was finally discovered that this behavior was due to radiation-enhanced nanoscale precipitation of copper-rich particles [11], a process that occurs very slowly in the absence of neutron dose under the thermal conditions encountered in a Magnox RPV. A theoretical model describing the process was developed, and this was validated using a range of microstructural techniques [11–13]. Given the relatively high level of copper in the submerged-arc weld metal (Table 2), which arises from the copper coating of the welding wire, it is obvious why radiation-enhanced copper precipitation became a major problem in submerged-arc weld metal. However, the copper levels present in other RPV materials (Table 2) meant that the contribution of radiation-enhanced precipitation of copper to hardening and embrittlement could not be neglected in the derivation of DDRs.

Irradiation of Submerged-Arc Weld Metal at Temperatures above 360°C—The response of submerged-arc weld metal after irradiation at temperatures of $\sim 360^\circ\text{C}$ and above presented a rather different problem to that at lower temperatures. In this case while the material showed significant embrittlement, this was accompanied by much smaller than expected changes in yield stress (hardening) [8,14]. Under the same irradiation conditions, only small changes in the values of T_{40J} were observed in manual metal arc weld metal with zero values for plate steels. Indeed, neither of these materials showed significant

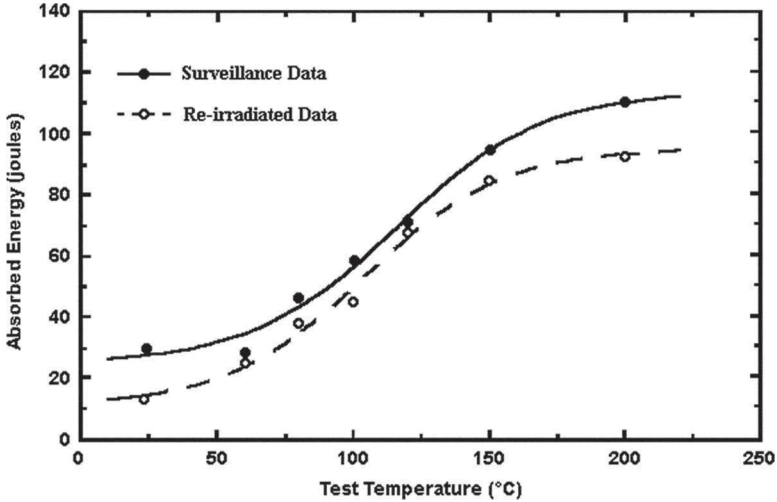


FIG. 3—Data from Charpy submerged-arc weld specimens before and after re-irradiation (high dose rate and same irradiation temperature).

irradiation hardening. It was therefore concluded that submerged-arc weld surveillance specimens were experiencing non-hardening embrittlement. This was confirmed when scanning electron microscopic examination of the fracture surfaces of submerged-arc weld specimens tested on the lower shelf showed that the embrittlement was associated with extensive intergranular failure (IGF) rather than transgranular cleavage. Complementary Auger spectroscopic studies showed that the IGF was associated with phosphorus segregation to the grain boundaries [14]. Scoop sampling of submerged-arc and manual metal welds [15,16] from the station's RPVs showed that the bulk phosphorus contents were similar to those found in the surveillance specimens. Detailed microstructural examination of the scoop samples also confirmed the presence of significant amounts of IGF, and Auger spectroscopic analyses showed associated elevated levels of phosphorus on the grain boundaries. Similar examination of the scoop samples of manual metal arc welds revealed that both the amount of IGF and level intergranular phosphorus were much less than for the submerged-arc weld metal [16].

Detailed modelling of the segregation processes over the temperature range of interest [14] showed that phosphorus segregation was dominated by thermal rather than irradiation processes. (The dominance of thermal over radiation processes at this temperature was consistent with the behavior of the specimens following the down rating of the station's operating temperature in 1969 [8].) In order to confirm the importance thermal over irradiation processes in this temperature regime, submerged-arc Charpy specimens from a high temperature surveillance canister from the station of interest were re-irradiated. The irradiation dose to the specimens was increased by an order of magnitude while keeping the irradiation temperature constant. The resulting Charpy results from the specimens before and after re-irradiation are shown in Fig. 3

where it can be seen that the ten-fold increase in dose caused only a small increase in the Charpy impact energy temperature shift.

On the basis of the results of the above experiment and the understanding of the processes involved, a DDR for these conditions was developed where embrittlement was described as a function of time and temperature [14]. Additional surveillance canisters were removed from the high temperature surveillance locations at this station over the remaining life of the plant to check for any deviations from predicted behavior. None were ever found, and the plant ceased generation after approximately 40 years of operation.

Upper Shelf Fracture Toughness—In the early 1980s a radiation shielded rig for carrying out unloading compliance fracture toughness tests was commissioned at the then Berkeley Nuclear Laboratories [17]. Test results showed that the values of upper shelf fracture toughness predicted using the correlations with upper shelf Charpy impact energy data and yield stress were overly conservative. DDRs for upper shelf fracture toughness for RPV materials based on fracture toughness measurements made using this facility were developed. These data was then incorporated into the fracture mechanics based assessment process.

Dose Damage Relationships

DDRs are used to predict changes in radiation-induced changes in yield stress (hardening) or embrittlement (Charpy impact energy transition temperature or fracture toughness transition temperature) as a function of radiation dose and temperature, and they were a critical input into the assessment process [8]. In the 1980s the CEGB investigated several different types of DDR including empirical relationships, e.g., U.S. Regulatory Guide 1.99 [18]. Two term relationship based on an understanding of the mechanism whereby neutron irradiation causes hardening and embrittlement of ferritic steels [11–13] was finally adopted [8] to model both hardening ($\Delta\sigma$) and embrittlement ($\Delta T_{40 J}$) and had the form

$$\left. \begin{array}{l} \Delta T_{40 J} \\ \text{or} \\ \Delta\sigma \end{array} \right\} = \Delta_{\text{copper}} + \Delta_{\text{matrix}} \quad (1)$$

In this relationship, Δ_{copper} represents the contribution of nanoscale copper precipitation to the property change, and Δ_{matrix} represents the contribution from matrix hardening arising from the production of point defects by neutron irradiation. The advantage of this approach was that the derived relationships could be used with confidence when limited extrapolation was required into regions of neutron dose, dose rate, or irradiation temperatures that were not specifically included in the surveillance database.

A key assumption in this relationship, which was supported up by modeling and microstructural studies [12,13], was that under RPV conditions of irradiation dose and temperature, the copper contribution (Δ_{copper}) had peaked [12]. Hence the contribution from nanoscale copper precipitation to the prop-

erty change remained constant, assuming that there is no overageing of these precipitates. On this basis pragmatic DDRs of the form

$$\left. \begin{array}{l} \Delta T_{40 \text{ J}} \\ \text{or} \\ \Delta \sigma \end{array} \right\} = B + AF_T \sqrt{D} \quad (2)$$

were adopted. In this equation B represents the material specific copper precipitate contribution to the property change with the matrix damage contribution being given by $AF_T \sqrt{D}$. In this term A is a material specific constant, D is the dpa dose, and F_T is the temperature dependence [8,19]. This was derived from data contained in open literature and is given by

$$F_T = 1.869 - 4.57 \times 10^{-3} T \quad (3)$$

where:

T = irradiation temperature in °C.

DDR's were derived for the different RPV materials (Table 1) over the years. They were revised as and when new Charpy impact energy or tensile test data became available or following revisions to the neutron doses accrued by the surveillance specimens. However, the main effort was concentrated on developing and refining the embrittlement DDR for submerged-arc weld metal to address new challenges as they arose.

Challenges to Dose Damage Relationships and Their Resolution

Intergranular Fracture

The two term DDRs worked well. The application of the embrittlement DDR for submerged-arc weld metal to doses outside those in the surveillance database had been justified by including data from accelerated irradiation programmes in its derivation. However, there was increasing concern that the latter data was not compatible with those emerging from the surveillance schemes. The decision was made to remove the accelerated data from the database used to derive the DDR. This made it necessary to extend the application of the submerged-arc weld metal DRR to doses beyond those available from the surveillance programme. In order to validate this extrapolation, surveillance specimens were re-irradiated to doses beyond those needed for assessment purposes. These specimens showed unexpectedly high values of $\Delta T_{40 \text{ J}}$. High resolution fractography of test specimens showed significant amounts of IGF in the fine grained regions of the weld metal, and the accompanying Auger spectroscopic studies revealed high concentrations of phosphorus at the grain boundaries [20]. Modelling of radiation-enhanced diffusion of phosphorus to grain boundaries indicated that there could be a breakaway to high rates of embrittlement above a critical dose. In order to allow for this possibility, a three term embrittlement DDR was proposed [8], which included a contribution from non-hardening embrittlement (Δ_{IGF}), viz.

$$\Delta T_{40 J} = \Delta_{\text{copper}} + \Delta_{\text{matrix}} + \Delta_{\text{IGF}} \quad (4)$$

The development of this DDR was accompanied by an extensive programme of work studying the development of IGF and the diffusion of phosphorus to grain boundaries as a function of irradiation dose.

The three term DDR had a big drawback in that it implied that there could be regions of the RPVs where there could be dramatic reductions in toughness. Uncertainty about when such a contribution would intervene was a major problem and contributed to the decision to close the lead irradiation dose power station (Trawsfynydd) in 1991.

The importance of the possibility of non-hardening embrittlement meant that fractographic and grain boundary composition studies on IGF, predominantly on submerged-arc weld surveillance specimens and to a lesser extent on other RPV materials, continued following the closure of Trawsfynydd. As a result of these studies, the following important conclusions were reached at that time.

- IGF was found in fine grained regions of all submerged-arc weld metal irrespective of irradiation dose. It was difficult to assess columnar regions of the microstructure.
- Grain boundary phosphorus levels did not increase systematically with neutron dose.
- Negligible amounts of IGF were found in other RPV materials.

These observations were all extremely important. The first conclusion meant that the existence of IGF and its contribution to embrittlement could not be ignored in any future submerged-arc weld metal DDR. The second implied that any IGF existing under conditions covered by the RPV surveillance data was unlikely to significantly increase with radiation dose, while the third indicated a priori that IGF would be a much less serious problem for other RPV steels. (To some degree these observations anticipated some of the findings of the European Union Fifth Framework project Phosphorus Influence on Steels Ageing (PISA) [21] and the work of Faulkner et al. [22].)

The closure of Trawsfynydd in 1991 was an important decision since it had been the intention to continue operation of this station based on the proposed three term DDR. Since the projected doses to critical areas of the remaining steel RPV stations lay within the range of doses in the surveillance database, the closure of this station removed the need for accelerated radiation data. Hence, a DDR could be derived that used surveillance data alone. However, since IGF was always present in the surveillance specimens, this factor had to be taken into account when deriving a surveillance only DDR. The surveillance database was consequently subjected to rigorous analysis, and no separate IGF term, as presented in Eq 4, was found. The surveillance-only submerged-arc weld DDR therefore reverted to the original two term form (Eq 2), and it was accepted that the effects of IGF were contained within the constant for the matrix damage contribution to the relationship. Since IGF had also been found to some degree in all of the other RPV materials, albeit to a much lesser extent than in submerged-arc weld metal, it was also accepted that the matrix damage regression constant in the DDRs for these materials also subsumed any effects of IGF.

Dosimetry Challenge—“Thermal” Neutrons

When the change was made expressing neutron dose in dpa rather than $n \cdot \text{cm}^{-2}$ [8–10], the values of dpa were calculated for neutrons with energies $E > 1$ keV (so called “fast” neutrons). It was acknowledged that thermalized neutrons with lower energies (thermal neutrons) could potentially contribute to the damage process, but it was considered that this bounding energy provided an adequate parameter for describing the properties in the Magnox RPV materials surveillance database. However, on-going validated calculations using the MCBEND computer model [8] showed that the percentage dpa contribution from thermal neutrons was higher at RPV side-core locations (50–100 %) compared to that at the top or bottom (sub-core locations) of the RPV (0.5–5 %). These observations suggested that thermal neutrons could make a significant contribution to the irradiation damage. As a result, an ambitious irradiation experiment was set up in the heavily thermalized reflector region of the heavy water moderated Halden reactor in Norway [8,23] to assess the contribution of thermal neutrons to the radiation damage process. It is noteworthy that the neutron spectra in the Magnox stations did not contain a sufficiently high thermal component for this experiment to be carried out in the Magnox fleet. The materials in the programme included both unirradiated steels and pre-irradiated specimens taken from the RPV surveillance programmes [24].

The results from the Halden programme [23,24] confirmed that thermal neutrons were indeed making a significant contribution to irradiation hardening and embrittlement [8]. It was established that to allow for extra displacements from low energy recoils (approximately 500 eV), a thermal neutron effectiveness factor (k) needed to be introduced to modify the dose term in each material DDR. This meant that the general form of the two term DDRs for both embrittlement and hardening (Eq 2) became

$$\left. \begin{array}{l} \Delta T \\ \text{or} \\ \Delta \sigma \end{array} \right\} = B + AF_T \sqrt{D_f + kD_t} \quad (5)$$

In this equation, the definitions of B , A , and F_T remained unchanged, but the single dose term, D , was replaced by $(D_f + kD_t)$, where D_f and D_t are the fast and thermal dpa doses, respectively; the constant k is the thermal neutron effectiveness factor for the material. The thermal neutron effectiveness factor was found to be material dependent [23], and separate values were estimated for the different RPV materials.

As a result of this experiment, estimates of thermal neutron dose had to be made for all RPV surveillance canisters and assessment locations [25], as a consequence of which all the different DDRs had to be revised.

Thermal Neutrons and Submerged-Arc Weld Metal

Incorporating a contribution from thermal neutrons in the DDRs for manual metal arc weld metal, plate steels, and forgings had little impact on the integrity assessment of key locations since the properties of submerged-arc weld metal in these areas remained life limiting. However, it soon became obvious that the

inclusion of thermal neutrons into the submerged-arc weld metal DDR would result in bounding upper shelf margins in certain key side-core locations being seriously eroded. The reduction in these margins would immediately threaten the continued operation of the fleet. In a review of the derivation of the submerged-arc weld DDR [26], it was recognized that lower bound properties for the DDR were not calculated in a rigorous way and a more defensible procedure was possible. The submerged-arc weld database was re-analyzed using the Burr function to describe the relationship between Charpy impact energy and test temperature; statistical fitting was carried out in a Bayesian framework using a technique based on Markov Chain Monte Carlo sampling [26–30] to give the embrittlement form of Eq 5. It was argued that since the fracture surfaces of the test specimens showed significant IGF, in fitting this equation there was the underlying implication that the values of A , B , and F_T might be modified in comparison to those that would be obtained if only copper precipitation and matrix damage occurred. As a result a submerged-arc weld metal embrittlement, specific temperature dependence, F_T' , was deduced

$$F_T' = 1.200 - 1.06 \times 10^{-3} T \quad (6)$$

A major outcome from this revised analytical approach was that it justified tighter uncertainty allowances for the DDR than had been possible with the earlier derivations. The tighter uncertainty of the DDR when combined with the scatter in start-of-life transition fracture toughness resulted in reduced scatter in the fracture toughness of irradiated material. This maintained margins for on upper shelf operation at critical RPV locations.

This radical approach was subjected to rigorous peer review, and its acceptance by the regulator (NII) was a major achievement.

Validation of the Prediction of the Fracture Toughness of Reactor Pressure Vessel Submerged-Arc Weld Metal

In the early 1990s the question was asked as to how well the predicted fracture toughness of submerged-arc weld metal, for a given neutron dose and irradiation temperature, compared with measured values. The comparison with results from the submerged-arc weld metal samples in the RPV surveillance programme gave a degree of confidence, but there were some areas of concern, viz.

- The welds adopted were reproduction welds specially made using similar consumables and welding parameters that had been used in constructing the various RPVs.
- Data from the surveillance scheme had been used in deriving the predictive method and as such could not be considered to provide unbiased validation.

In other words, the procedure for predicting fracture toughness needed to be validated against fracture toughness results obtained from service exposed RPV submerged-arc weld metal. Sampling of RPV welds would also be useful since it could be used to validate the assumed dose attenuation through the vessel wall and give information on chemical composition and the quality of the welds. It would also show how well the fracture toughness of the

submerged-arc weld metal in the surveillance schemes compared with that of structural RPV welds.

In planning of this particular programme, it was fortunate that the station containing submerged-arc welds with the highest accrued radiation doses was part of a pressure vessel that had been decommissioned at Trawsfynydd in 1991. (Results from submerged-arc weld metal specimens in the RPV programme for this station also constituted a large proportion of the surveillance scheme databases.) The highest dose submerged-arc welds in the Trawsfynydd RPVs were in the side-core regions of the reactors, and the neutron spectra for these regions contained a significant proportion of thermal neutrons in the accrued dose. These two factors made these welds potentially extremely attractive for sampling. Unfortunately, the neutron dose to these welds showed large variations over relatively short distances. This would have made interpretation of fracture toughness test data extremely difficult, and these welds were not sampled. Instead, attention was focused on the four submerged-arc welds in the south pole of the RPVs where the doses were also high but sensibly constant along the length of each weld [31,32] and the irradiation temperature was essentially constant.

The removal of the weld samples was technically extremely challenging [33] because of the hostile irradiation environment. This was compounded by access being restricted, samples needed to be removed without heating them above the irradiation temperature ($\sim 190^{\circ}\text{C}$) (achieved by using ultra high pressure water jet cutting), and it was necessary to restore vessel integrity after the samples had been removed. In spite of these challenges, four through-wall thickness trepans of about 150 mm diameter were successfully removed from each weld. Two Charpy geometry specimens were made at each of four depths through the wall. Additional samples were cut for chemical analysis, microstructural examination, and dose measurements [31,32]. The Charpy geometry specimens were notched, side-grooved, pre-fatigued, and fracture toughness tested in the unloading compliance mode [17]. After testing, the specimens were heat tinted and fractured after cooling in liquid nitrogen. The fracture faces were recorded for crack growth measurements and then removed from the broken pieces. The halves of each specimen were then reconstituted using a stud welding technique, re-machined, notched, side-grooved, pre-fatigued, and re-tested at different temperatures [31,32]. These two temperatures were different from the original specimen test temperature. In this way each original Charpy geometry specimen could potentially generate three results, meaning that in all, approximately 400 fracture toughness tests were carried out.

The resulting fracture toughness results were compared with the predicted fracture toughness for the appropriate irradiation dose and temperature. Two typical sets of results are shown in Figs. 4 and 5. There is clearly good agreement between measured and predicted values (the solid line is the 50 percentile predicted values, and the broken lines are the 5 and 95 percentile values). By normalizing all of the results to a standard irradiation condition, it is possible to present the fracture toughness results from all of the welds on a single figure. This is done in Fig. 6 and shows that there is good agreement between the measured fracture toughness values and predictions made prior to data acquisition.

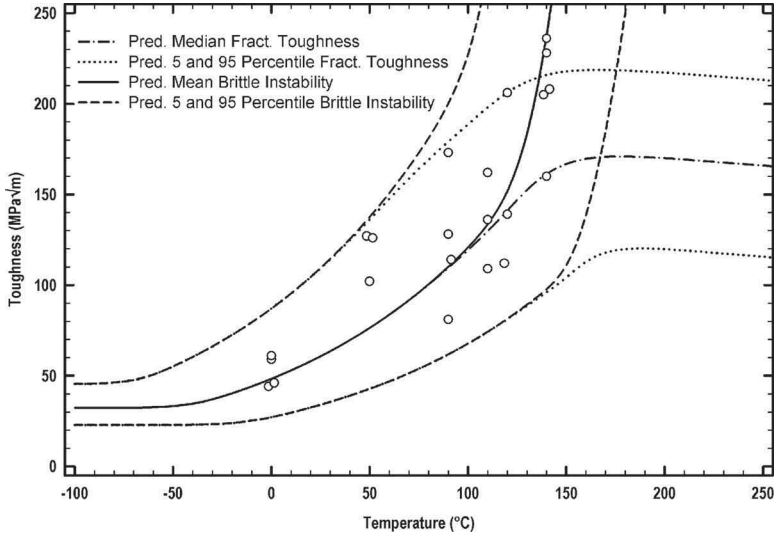


FIG. 4—Weld 4 level 1 fracture toughness results and predicted curves.

A similar normalizing process enabled the fracture toughness measurements obtained from surveillance specimens to be compared with those for the RPV welds, and this is shown in Fig. 7. There is again good agreement between measured and predicted values, and this shows that the welds in the surveillance scheme were representative of the RPV welds.

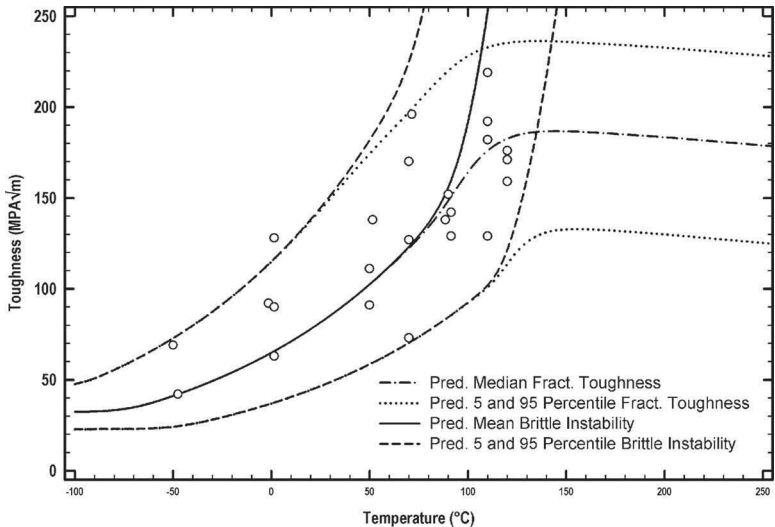


FIG. 5—Weld 4 level 4 fracture toughness results and predicted curves.

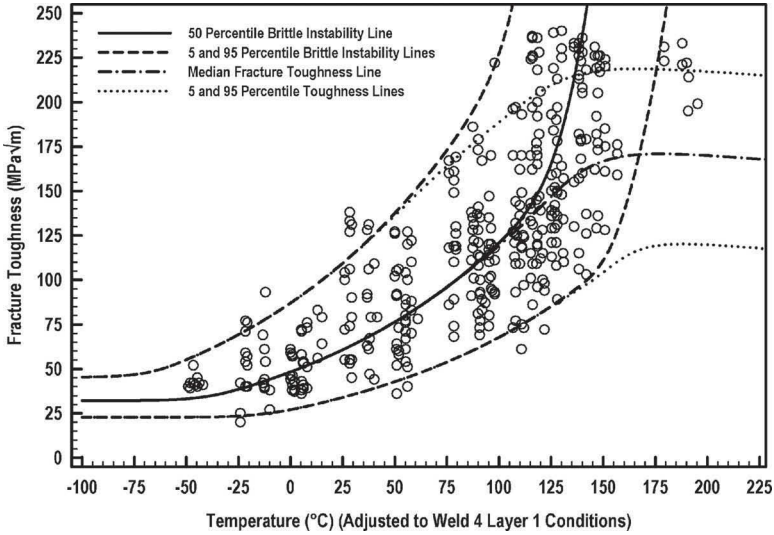


FIG. 6—Fracture toughness data from submerged-arc welds from Trawsfynydd RPV.

Other information provided by the weld sampling programme validated other aspects of the assessment process [31,32]. There was good agreement between measured and predicted neutron doses, and comparison of the measured and predicted doses at the various depths within the welds confirmed the predicted attenuation of dose through the thickness of the RPV wall modelled

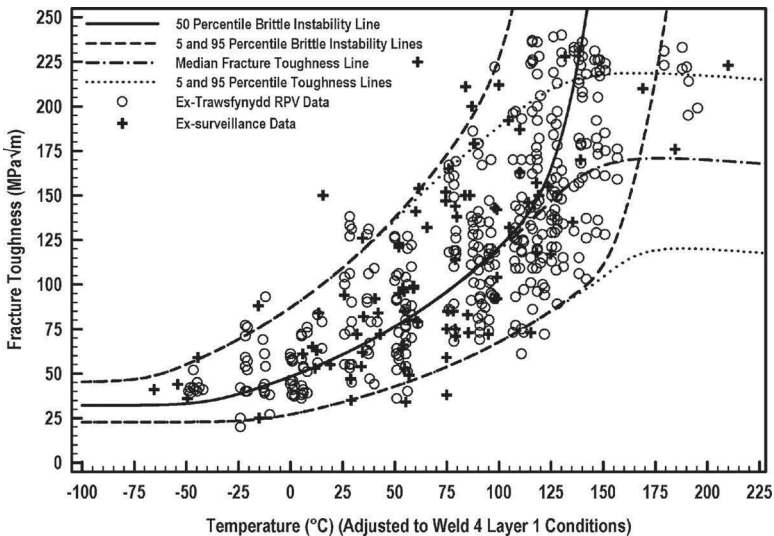


FIG. 7—Fracture toughness data from Trawsfynydd RPV and surveillance submerged-arc weld metal.

by MCBEND. Etched sections of the welds confirmed that the welds were of high quality and showed the expected microstructural features. In addition, the chemical composition of the weld metal was remarkably uniform.

Microscopic examination and measurements of the fracture faces of the tested specimens produced some interesting and also unexpected results. The most surprising observation was that the fracture toughness for a given dose was correlated with the amount of fine grained material in the crack front in that the higher the percentage of fine grained material, the higher the fracture toughness. This was despite the fact that, as expected, the fine grained regions of the welds contained significant amounts of IGF irrespective of dose. This explains why IGF is not as significant for these types of welds as was originally thought when the phenomenon was first seen in submerged-arc weld metal [8].

Concluding Remarks

The six Magnox stations with steel pressure vessels were designed and built during the 1950s and 1960s from simple carbon-manganese steels and fabricated using a mixture of manual metal arc and semi-automatic submerged-arc weld metal. At that time, the understanding and study of the effect of prolonged exposure of ferritic steels to neutron irradiation were in its infancy and predated fracture mechanics methods for assessing the integrity of such pressure vessels. The foresight of the scientists and design engineers to include steel pressure vessel monitoring schemes in the reactors was to prove invaluable. These schemes provided warnings of effects such as the enhanced sensitivity of submerged-arc weld metal to neutron irradiation and experimental data that was vital to the development of the means to predict the state of plant as assessment methodologies to demonstrate safe operation evolved. They also provided a source of specimens that were re-irradiated to provide hardening and embrittlement information at irradiation somewhat beyond anticipated doses to critical locations, thereby minimizing the amount of extrapolation required for assessment purposes. Without these specimens, such experiments would have been practical only if significantly enhanced dose rates had been used. The surveillance schemes played a pivotal role in helping two of the steel pressure vessel stations operate into the 21st century, with all of the stations operating beyond their perceived design life with some extending to approximately 40 years.

Acknowledgments

The writers would like to acknowledge the contributions of many colleagues, both scientific and technical support, over the years to this programme of work. It is hoped that their dedication and innovation are reflected in this paper. This paper is published with the permission of the Head of Engineering, Waste, Strategy and Technical, Magnox Electric, Ltd.

References

- [1] Cottrell, A. H., "Theoretical Aspects of Radiation Damage and Brittle Fracture in Steel Pressure Vessels," *Steels for Reactor Pressure Circuits, Special Report No. 69*, Iron and Steel Institute, London, 1961, pp. 281–296.
- [2] Harries, D. R., Nichols, R. W., and Judge, C., "The Effect of Neutron Irradiation on the Ductile-Brittle Transition of Steels and Its Relevance to Reactor Pressure Vessels," *Steels for Reactor Pressure Circuits, Special Report No. 69*, Iron and Steel Institute, London, 1961, pp. 297–327.
- [3] Robertson, T. S., "Propagation of Brittle Fracture in Steel," *J. Iron Steel Inst., London*, Vol. 175, 1953, pp. 361–374.
- [4] Milne, I., Ainsworth, R. A., Dowling, A. R., and Stewart, A. T., "Assessment of the Integrity of Structures Containing Defects," *CEGB Report No. R/H/R6, Revision 3*, Central Electricity Generating Board, London, 1986.
- [5] Chucas, S. J., "MCBEND, A Monte Carlo Program for General Radiation Transport Solutions," *ANSWERS Software Service*, AEA Technology.
- [6] Flewitt, P. E. J., Williams, G. H., and Wright, M. B., "Integrity of Magnox Reactor Steel Pressure Vessels," *Mater. Sci. Technol.*, Vol. 9, 1993, pp. 75–82.
- [7] Bolton, C. J., Charnock, W., and Priest, R. H., "The Effect of Irradiation on Fracture Toughness Transition Temperature of Magnox Reactor Pressure Vessels," *Proceedings of the International Conference on Nuclear Power Plant Extension*, Snowbird, UT, 1988, ANS Idaho, Idaho Falls, ID.
- [8] Jones, R. B. and Bolton, C. J., "Neutron Radiation Embrittlement Studies in Support of Continued Operation and Validation by Sampling of Magnox Reactor Steel Pressure Vessels and Components," *24th Water Reactor Safety Information Meeting*, Bethesda, 1996, NRC, Bethesda, MD, Vol. 2, pp. 25–48.
- [9] Heffer, P. J. H., Jones, L. T., Thornton, D. A., Avery, A., Smith, N., and Ziver, K., "Magnox Pressure Vessel Dosimetry—A New Assessment," *Seventh ASTM-Euratom Symposium on Reactor Dosimetry*, Strasbourg, Euratom Working Group on Reactor Dosimetry and ASTM, Kluwer Academic Publishers, Dordrecht and Boston, 1990, pp. 13–20.
- [10] Mossop, J. R., Thornton, D. A., and Lewis, T. A., "Validation of Neutron Transport Calculations on Magnox Power Plant," *Reactor Dosimetry, ASTM STP 1228*, ASTM International, West Conshohocken, PA, 1994, pp. 384–391.
- [11] Fisher, S. B., Harbottle, J. E., and Aldridge, N., "Radiation Hardening in Magnox Pressure Vessel Steels," *Philos. Trans. R. Soc. London, Ser. A*, Vol. 315, 1985, pp. 301–332.
- [12] Buswell, J. T. and Jones, R. B., "The Modelling of Radiation Hardening and Embrittlement in Magnox Mild Steel Submerged-Arc Welds," *16th International Symposium on Effects of Radiation on Materials, ASTM STP 1175*, Aurora, 1992, ASTM International, West Conshohocken, PA, 1994, pp. 424–443.
- [13] Bolton, C. J., Buswell, J. T., Jones, R. B., Moskovic, R., and Priest, R. H., "The Modelling of Irradiation Embrittlement in Submerged-Arc Welds," *17th International Symposium on Effects of Radiation on Materials, ASTM STP 1270*, Sun Valley, ID, 1994, ASTM International, West Conshohocken, PA, 1996, pp. 103–118.
- [14] Beere, W. B., Fidler, R. S., Bolton, C. J., Fenton, S. T., and Jones, R. B., "The Ductile-Brittle Transition Behaviour of Submerged-Arc Weldments Following High Temperature Exposure," *18th International Symposium on Effects of Radiation on Materials, ASTM STP1325*, Hyannis, MA, 1996, ASTM International, West Conshohocken, PA, 1999, pp. 223–232.

- [15] Bischler, P. J. E. and Stump, J. M., "The Development of Techniques to Examine RPV Scoop Samples Removed from Bradwell R1," *International Conference on Nuclear Plant Life Management and Extension (PLIM/PLEX)*, Nice, France, November 27–30, 1995, Atomic Energy Agency, Vienna.
- [16] Bischler, P. J. E., Knowles, G., Spellward, P., Scowen, R. J., Lee, B. J., Stump, J. M., and Mowles, S. J., "An Examination of Irradiated Scoop Samples Removed from Bradwell Reactor 1 Pressure Vessel," *International Conference on Nuclear Plant Life Management and Extension (PLIM/PLEX)*, Nice, France, November 27–30, 1995, Atomic Energy Agency, Vienna.
- [17] Neale, B. K. and Priest, R. H., "The Unloading Compliance Method for Crack Length Measurement Using Compact Tension and Precracked Charpy Specimens," *Elastic-Plastic Fracture Test Methods—The User's Experience*, ASTM STP 856, ASTM International, West Conshohocken, PA, 1985, pp. 375–393.
- [18] "Radiation Embrittlement of Reactor Vessel Materials," *Regulatory Guide 1.99, Rev. 2*, United States Nuclear Regulatory Commission, Washington, DC, 1988.
- [19] Jones, R. B. and Williams, T. J., "The Dependence of Radiation Hardening and Embrittlement on Irradiation Temperature," *17th International Symposium on Effects of Radiation on Materials*, ASTM STP 1270, Sun Valley, ID, 1994, ASTM International, West Conshohocken, PA, 1996, pp. 569–590.
- [20] Bischler, P. J. E. and Wild, R. K., "A Microstructural Study of Phosphorus Segregation and Intergranular Fracture in Neutron Irradiated Submerged-Arc Welds," *17th International Symposium on Effects of Radiation on Materials*, ASTM STP 1270, Sun Valley, ID, 1994, ASTM International, West Conshohocken, PA, 1996, pp. 260–273.
- [21] Fifth Framework of the European Atomic Energy Community, "Project PISA—Phosphorus Influence on Steels Ageing—Final Report," *Report No. PISA/PISA/R/(15)*, Issue 1, European Commission, Brussels, July 2005.
- [22] Faulkner, R. G., Jones, R. B., Lu, Z., and Flewitt, P. E. J., "Grain Boundary Impurity Segregation and Neutron Irradiation Effects in Ferritic Alloys," *Philos. Mag.*, Vol. 85(19), 2005, pp. 2065–2099.
- [23] Jones, R. B., Edens, D. J., and Wootton, M. R., "Influence of Thermal Neutrons on the Hardening and Embrittlement of Plate Steels," *19th International Symposium on Effects of Radiation on Materials*, ASTM STP 1366, Seattle, WA, 1998, ASTM International, West Conshohocken, PA, 2000, pp. 366–382.
- [24] Jones, R. B., Cowan, J. R., Corcoran, R. C., and Walmesly, J. R., "Embrittlement, Hardening and Grain Boundary Composition in an Irradiated and Thermally Aged Fe–P–C Alloy," *19th International Symposium on Effects of Radiation on Materials*, ASTM STP 1366, Seattle, WA, 1998, ASTM International, West Conshohocken, PA, 2000, pp. 473–491.
- [25] Lewis, T. A., Hopper, S. E., Mossop, J. R., Thornton, D. A., and Whiley, G. S., "The Prediction of Fast and Thermal Neutron Dose Rates for the Pressure Vessels of Magnox Power Plant," *Proceedings of the Ninth International Symposium on Reactor Dosimetry*, Prague, 1996, World Scientific, Singapore, 1998, pp. 600–607.
- [26] Moskvic, R., Windle, P. L., and Smith, A. F. M., "Modelling Charpy Impact Energy Changes Using a Bayesian Method," *Metall. Mater. Trans. A*, Vol. 28, 1997, pp. 1181–1193.
- [27] Stephens, D. A., Smith, A. F. M., and Moskvic, R., "Charpy Impact Energy: A Markov Chain Monte Carlo Analysis," *J. R. Stat. Soc., Ser. C, Appl. Stat.*, Vol. 46, 1997, pp. 477–492.
- [28] Moskvic, R. and Flewitt, P. E. J., "An Overview of the Principles of Modelling Charpy Impact Energy Data Using Statistical Analyses," *Metall. Mater. Trans. A*,

Vol. 28, 1997, pp. 2609–2623.

- [29] Moskovic, R., Jordinson, C., Stephens, D. A., and Smith, A. F. M., “A Bayesian Analysis of the Influence of Neutron Irradiation on Embrittlement in Ferritic Submerged Arc Weld Metal,” *Metall. Mater. Trans. A*, Vol. 31, 2000, pp. 445–459.
- [30] Moskovic, R. and Jordinson, C., “Influence of Thermal Neutrons on Embrittlement and Hardening in Weld Metals,” *Modell. Simul. Mater. Sci. Eng.*, Vol. 7, 1999, pp. 503–523.
- [31] Bischler, P. J. E., Wootton, M. R., and Bolton, C. J., “Fracture Toughness of Submerged-Arc Weld Samples from a Decommissioned Magnox Reactor Pressure Vessel: Initial Results,” *19th International Symposium on Effects of Radiation on Materials, ASTM STP 1366*, Seattle, WA, 1998, ASTM International, West Conshohocken, PA, 2000, pp. 295–305.
- [32] Bolton, C. J., Bischler, P. J. E., Wootton, M. R., Moskovic, R., Morri, J. R., Pegg, H. C., Haines, A. B., and Woodman, R., “Fracture Toughness of Weld Samples Removed from a Decommissioned Magnox Reactor Pressure Vessel,” *Int. J. Pressure Vessels Piping*, Vol. 79, 2002, pp. 685–692.
- [33] Curry, A. and Clayton, R., “Remote Through-Wall Sampling of the Trawsfynydd Reactor Pressure Vessel: An Overview,” *Nucl. Energy*, Vol. 36, 1997, pp. 59–64.

Hans-Werner Viehrig,¹ Jan Schuhknecht,² Udo Rindelhardt,³
and Frank-Peter Weiss⁴

Investigation of Beltline Welding Seam of the Greifswald WWER-440 Unit 1 Reactor Pressure Vessel

ABSTRACT: The investigation of reactor pressure vessel (RPV) materials from decommissioned nuclear power plants (NPP) offers the unique opportunity to scrutinize the irradiation behavior under real conditions. The paper describes the investigation of trepans taken from the decommissioned WWER-440 RPVs of the Greifswald NPP. The key part of the testing is aimed at the determination of the reference temperature T_0 following the ASTM Test Standard E1921 to determine the fracture toughness of the RPV steel in different thickness locations. In a first step, the trepan taken from the RPV Greifswald Unit 1 containing the multilayer welding seam located in the beltline region was investigated. This welding seam represents the irradiated, recovery annealed, and reirradiated condition. It is shown that the Master Curve approach as adopted in ASTM E1921 is applicable to the investigated original WWER-440 weld metal. The evaluated T_0 varies through the thickness of the welding seam. After an initial increase of T_0 from 10°C at the inner surface to 49°C at 22 mm distance from it, T_0 decreases to -32°C at a distance of 70 mm, finally increasing again to 61°C near the outer RPV wall. The lowest T_0 value was measured in the root region of the welding seam representing a uniform fine grain ferritic structure. The highest T_0 of the weld

Manuscript received June 6, 2008; accepted for publication March 18, 2009; published online April 2009.

¹ Ph.D., Forschungszentrum Dresden-Rossendorf, Institute for Safety Research, Department Materials and Components Safety, P.O. Box 510119, 01314 Dresden, Germany, e-mail: H.W.Viehrig@fzd.de

² Forschungszentrum Dresden-Rossendorf, Institute for Safety Research, Department Materials and Components Safety, P.O. Box 510119, 01314 Dresden, Germany.

³ Professor, Ph.D., Forschungszentrum Dresden-Rossendorf, Institute for Safety Research, P.O. Box 510119, 01314 Dresden, Germany.

⁴ Professor, Ph.D., Forschungszentrum Dresden-Rossendorf, Institute for Safety Research, P.O. Box 510119, 01314 Dresden, Germany.

Cite as: Viehrig, H.-W., Schuhknecht, J., Rindelhardt, U. and Weiss, F.-P., "Investigation of Beltline Welding Seam of the Greifswald WWER-440 Unit 1 Reactor Pressure Vessel," *J. ASTM Intl.*, Vol. 6, No. 5. doi:10.1520/JAI101925.

Copyright © 2009 by ASTM International, 100 Barr Harbor Drive, PO Box C700, West Conshohocken, PA 19428-2959.

seam was not measured at the inner wall surface. This is important for the assessment of ductile-to-brittle temperatures measured on subsize Charpy specimens made of weld metal compact samples removed from the inner RPV wall. Our findings imply that these samples do not represent the most conservative condition. Nevertheless, the Charpy transition temperature, TT_{41J} , estimated with results of subsize specimens after the recovery annealing, was confirmed by the testing of standard Charpy V-notch specimens.

KEYWORDS: Russian WWER-type reactor, reactor pressure vessel steel, beltline welding seam, weld metal, trepans, fracture toughness, Master Curve, integrity assessment

Introduction

Nuclear plant operators must demonstrate that the structural integrity of a nuclear reactor pressure vessel (RPV) is assured during routine operations or under postulated accident conditions. The aging of the RPV steels is monitored with surveillance program results or predicted by trend curves. Embrittlement forecast with trend curves and surveillance specimens may not reflect the reality. Accordingly, the most realistic evaluation of the toughness response of RPV material to irradiation is done directly on RPV wall samples from decommissioned nuclear power plants (NPP). Such a unique opportunity is now offered with material from the decommissioned Greifswald NPP (WWER-440/V-230). The four Greifswald NPP units representing the first generation of WWER-440/V-230 reactors were shut down in 1990 after 11–17 years of operation [1,2]. Table 1 presents the operation characteristics of the Units 1 to 4 and the expected neutron fluences. RPVs in three different conditions are available:

- Unit 1 is irradiated, annealed and reirradiated (IAI).
- Units 2 and 3 are irradiated and annealed (IA).
- Unit 4 is irradiated.

The well documented different irradiation/annealing states of the four decommissioned Greifswald RPVs [2] allows the validation of material properties

TABLE 1—Operation characteristics and expected maximum neutron fluences of Greifswald Units 1 to 4.

Operation Period					Azimuthal Maximum of $N_{E>0.5 \text{ MeV}}$ in Units of 10^{19} n/cm^2			
Unit	Date	Cycles	Effective Days	Annealed In	Inner Wall Axial Maximum	Inner Wall Weld 4	Outer Wall Axial Maximum	Outer Wall Weld 4
1	1974–1988	13	4205.0	1988	5.53	3.93	1.4	0.96
1 ^a	1988–1990	2	627.4	...	0.16	0.1	0.05	0.03
2	1975–1990	14	4067.4	1990	6.68	4.7	1.70	1.16
3	1978–1990	12	3581.8	1990	4.4	3.4	0.68	0.50
4	1979–1990	11	3207.9	not	4.0	3.1	0.62	0.45

^aReirradiated.

Note: $N_{E>0.5 \text{ MeV}}$ = neutron fluence, $E > 0.5 \text{ MeV}$.

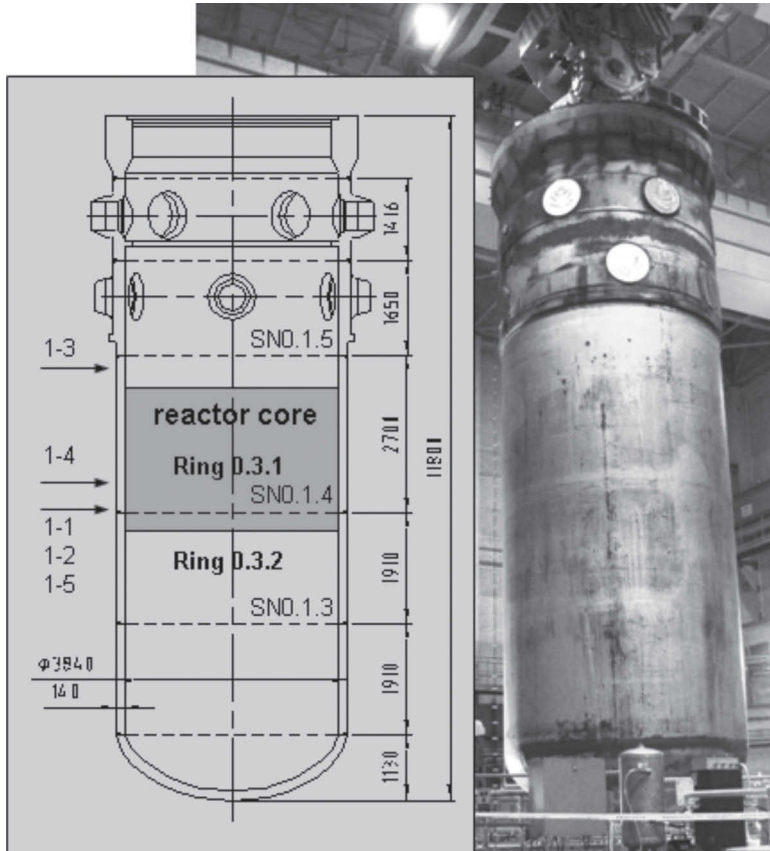


FIG. 1—RPV VVER 440 Greifswald Unit 1 and locations of the sampled trepanns.

under long term, low flux irradiation, during industrial recovery annealing and during subsequent reirradiation. Trepanns were already extracted from Units 1, 2, and 4. This paper presents the results of the investigation of the first trepan taken from the RPV welding seam in the beltline region of Greifswald Unit 1.

Material and Specimens

The material investigated was extracted from the circumferential beltline welding seam No. SN0.1.4 of Greifswald Unit 1 RPV (Fig. 1). The so-called critical temperature of brittleness of this welding seam was estimated by predicting formulas for the initial condition, T_{K0} , at 46°C, and after 13 campaigns of operation at 186°C (T_K) [2,3]. In this state, the RPV was subjected to a heat treatment at 475°C for 152 hours in order to anneal the irradiation embrittlement in 1988. The RPV was heat treated within a region of 0.7 m above and below the circumferential beltline welding seam No. SN0.1.4. After the annealing, compact specimens were taken from the weld metal directly at the inner

surface of vessel wall. Subsize Charpy specimens were machined and tested. With these specimens a critical temperature of brittleness T_K of $+30^\circ\text{C}$ was measured [3]. After the annealing, the operation of Unit 1 was continued for another two years (Table 1). Unit 1 was shut down in 1990.

Trepans representing the IAI condition were extracted from the decommissioned Unit 1 RPV in 2005. The custom-built trepanning device and the trepanning procedure are described elsewhere [4]. Figure 1 shows the location of the trepans taken from the RPV of Greifswald Unit 1. Trepans were taken from the circumferential beltline welding seam No. SN0.1.4, and the base metal ring 0.3.1. The neutron flux through the RPV was calculated [1] with TRAMO [5], which is a multi-group Monte Carlo code for neutron and gamma transport calculations.

At first, the trepan 1-1 representing the IAI condition of the beltline welding seam was investigated. The WWER-440 RPV welding seams are X-butt multilayer submerged arc welds. They consist of a welding root welded with an unalloyed wire Sv-08A and the filler material welded with the alloyed wire Sv-10KhMFT. Table 2 contains the chemical composition of the weld metal within trepan 1-1 in different thickness locations and the specifications of the manufacturing protocol [2]. The chemical composition was measured by inductively coupled plasma mass spectrometry on irradiated samples from three thickness locations of the alloyed filler material. In principle the measured chemical composition agrees with the information in the manufacturing protocol. The copper and phosphorus contents are within the range as specified in the manufacturing guidelines of the WWER-440/V-230 generation 1, but both are clearly higher than in the specification of next generation (WWER-440/V-213) with maximum allowed P and Cu contents of 0.01 % and 0.1 %, respectively [6,7]. The composite material of the welding root was not analyzed.

Figure 2 shows the scheme with the location of the welding seam within the trepan 1-1 and the picture of it. The location of the welding seam within trepan 1-1 was metallographically examined and is depicted in Fig. 3 together with the exemplified cutting scheme of the disk 1-1.1 (Table 3). The welding root is located within a distance of about 60 mm to 80 mm relative to the inner RPV wall. The trepan 1-1 was cut into disks each of a thickness of 10 mm using a wire traveling electro-erosion discharging machine (EDM). From one disk ten Charpy size SE(B) specimens were machined.

The Charpy size SE(B) specimens were precracked ($a/W=0.5$) and 20 % side-grooved. As shown in Fig. 3 the orientation of the SE(B) specimen is TS (specimen axis axial and crack growth direction across the vessel wall) according to ASTM E1823 [8]. The TS orientation is in correspondence with the surveillance specimens in Russian WWER-440/V-213 second generation reactors. From the broken halves of the tested SE(B) specimens Charpy V-notch specimens according to DIN EN 10045-1 (1991) [9] were manufactured by the reconstitution technique.

Testing and Evaluation

SE(B) specimens from eleven thickness locations (Table 3) were tested and evaluated according to ASTM E1912-08 [10]. The precracked and side-grooved

TABLE 2—Chemical composition of trepan 1-1 (Mass %).

No. Disk protocol ^b	Thickness Location ^a mm	C	Si	Mn	Cr	Ni	Mo	V	P	Cu
		0.05	0.47	1.22	1.48	0.23	0.41	0.16	0.037	0.103
1-1.1	8			1.06	1.49	0.22	0.40	0.14	0.038	0.125
1-1.3	22			0.97	1.35	0.19	0.43	0.14	0.030	0.141
1-1.12	94			0.93	1.23	0.22	0.40	0.09	0.029	0.141

^aDistance of disk center from the inner surface.

^bManufacturing protocol of the RPV Unit 1—welding seam SN0.1.4.

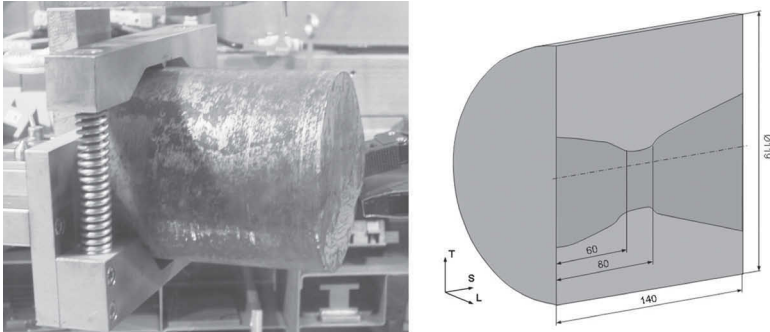


FIG. 2—Scheme and picture of trepan 1-1 with the location of the welding seam.

Charpy size SE(B) specimens were monotonically loaded until they failed by cleavage instability. Standard Master Curve (MC) reference temperatures T_0 were evaluated with the measured J integral based cleavage fracture toughness values, K_{Jc} , applying the multitemperature procedure of ASTM E1921-08 [10]. In addition, the modified MC analysis of the SINTAP procedure [11] was used for the evaluation of the measured K_{Jc} values. The SINTAP lower tail analysis contains three steps, and guides the user towards the most appropriate estimate of the reference temperature, T_0^{SINTAP} , describing the population having the lower toughness [12,13].

Instrumented Charpy V-notch impact tests on reconstituted specimens were performed according to DIN EN 10045-1 [9] and EN ISO 14556 [14]. The impact energy, lateral expansion, and fracture appearance temperature curves were fitted by the hyperbolic tangent approach. Charpy-V parameters as transition temperatures and the upper shelf energy were evaluated on specimens from five thickness locations.

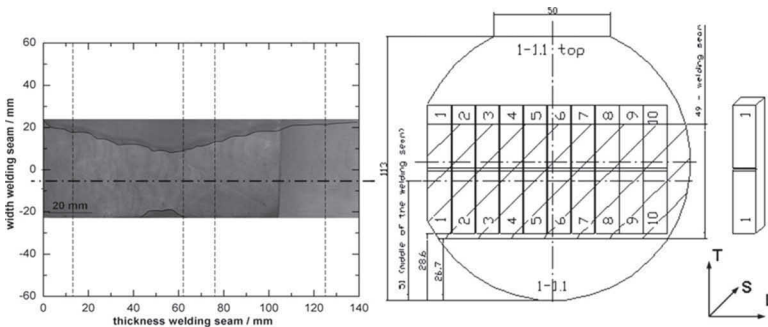


FIG. 3—Metallographic section of the welding seam within trepan 1-1 and cutting scheme of disk 1-1.1.

TABLE 3—Location of the investigated disks within trepan 1-1, neutron fluences, MC test results according to ASTM E1921-05 and SINTAP and Charpy-V parameters.

Code Disk	Distance from Inner Surface (Center Disk) mm	$N_{E>0.5 \text{ MeV}}$		E1921-08		SINTAP	Charpy-V	
		Before ^a 10^{19} n/cm^2	After ^a 10^{19} n/cm^2	T_0 °C	σT_0 K	T_0^{SINTAP} °C	TT_{41J} °C	USE J
1-1.1	8	3.90	0.182	10.3	7.5	32.5	51.4	130.8
1-1.3	22	3.66	0.113	49.1	7.2	49.1	32.6	153.4
1-1.5	36	3.32	0.103	33.8	7.5	33.8	14.6	154.7
1-1.6	42	3.13	0.098	-4.8	7.5	-4.8		
1-1.8	60	2.66	0.085	-4.5	7.2	5.0		
1-1.9	70	2.40	0.077	-31.7	6.1	-16.4		
1-1.11	84	2.07	0.068	-34.0	8.4	18.6		
1-1.12	94	1.85	0.061	22.7	7.5	45.1	20.1	120.3
1-1.14	107	1.59	0.053	-32.6	8.5	-32.6	13.1	149.8
1-1.15	118	1.40	0.047	-8.7	7.5	-8.7		
1-1.17	131	1.16	0.040	61.4	8.4	61.4		

^aAccumulated neutron fluence before and after the recovery annealing; the weld metal investigated represents the IAI condition.

Results and Discussion

Table 3 summarizes the MC and Charpy-V test results of the investigated disks of trepan 1-1. The table also contains the location of the disks within the trepan and the calculated neutron fluences in the center of the disks. The test results comprise the reference temperatures, T_0 , evaluated according to ASTM E1921-08 [10] and the SINTAP procedure [11–13], T_0^{SINTAP} , as well as the Charpy-V parameters transition temperature related to a Charpy-V energy of 41J, TT_{41J} , and upper shelf energy, USE, of five thickness locations. T_0 data presented in Table 3 and depicted in Fig. 4 vary through the thickness of the trepan 1-1 and, thus, the welding seam. Through the wall thickness, T_0 shows a wavelike behavior. After an initial increase of T_0 from 10.3°C at the inner surface to 49.1°C at 22 mm distance from it, T_0 decreases to -31.7°C at a distance of 70 mm, finally increasing again to a maximum 61.4°C near the outer RPV wall. The lowest T_0 value was measured in the root region of the welding seam representing a uniform fine grain ferritic structure. Beyond the welding root T_0 shows also a wavelike behavior with a span of about 50 K.

Figure 5 shows the K_{Jc} values versus the test temperature normalized to T_0 of the individual thickness location. The K_{Jc} values generally follow the course of the MC, though the scatter is large. Nevertheless, only two out of about 100 K_{Jc} values lie below the 2 % fracture probability line. Additionally, the MC SINTAP procedure was applied to determine T_0^{SINTAP} representing the brittle fraction of the dataset. For some thickness locations there are remarkable differences between T_0 and T_0^{SINTAP} (Table 3). That strongly indicates that the material is not fully homogeneous, which is not unusual for the investigated multilayer weld metal.

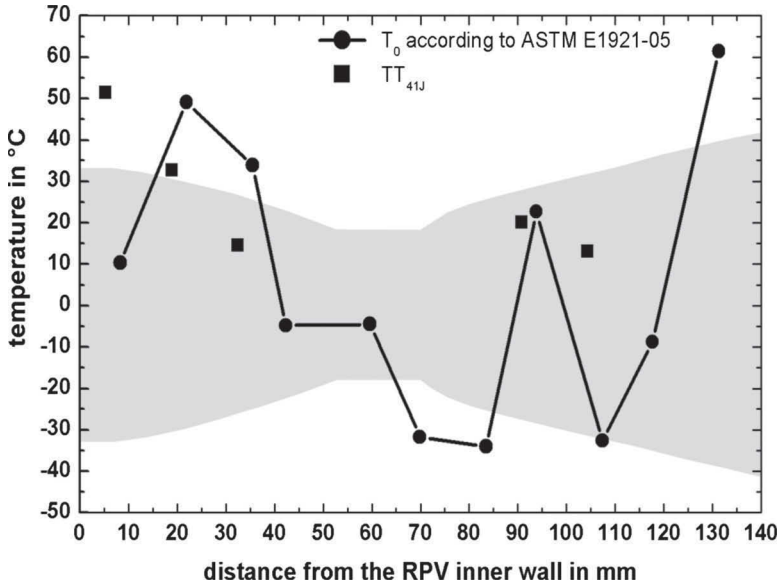


FIG. 4—Course of the reference temperatures T_0 through the welding seam SN0.1.4 of Greifswald Unit 1.

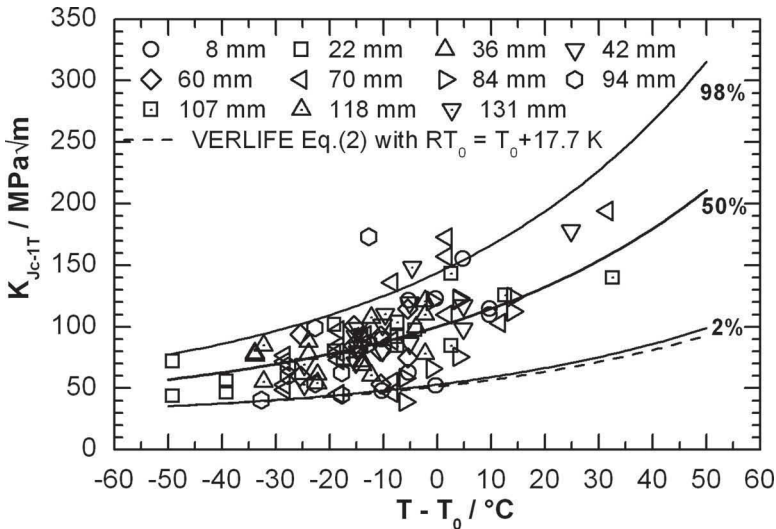


FIG. 5— K_{Jc} values measured on Charpy size SE(B) specimens, adjusted to 1T (25.4 mm) specimen size, versus the test temperature normalized to T_0 of the individual disks, and Master Curves for 2, 50, and 98 % fracture probability.

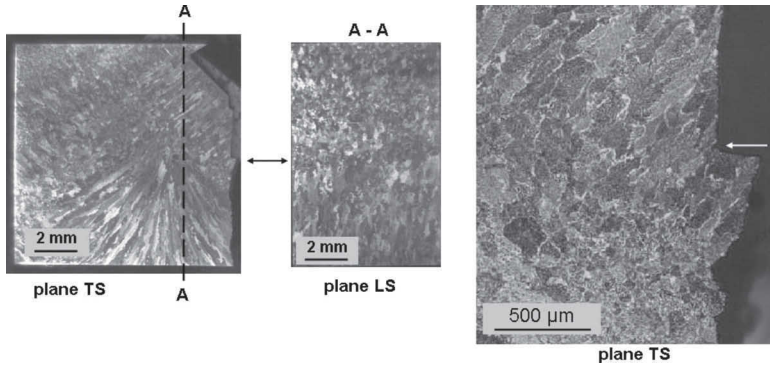


FIG. 6—Metallographic sections of the TS oriented SE(B) specimen from the thickness location 22 mm ($T_0=49.1^\circ\text{C}$, Table 3), arrow at fatigue crack tip location.

As mentioned above, the beltline welding seam of Greifswald Unit 1 was recovery annealed and re-irradiated to low fluences (Table 3). Taking into account a T_K of 186°C after 13 campaigns operation [2] the results presented here and the results determined on subsize impact specimens [3] show that the embrittlement was almost fully mitigated due to the recovery annealing. The re-embrittlement during two campaign operations can be assumed to be low. Hence, the variation of T_0 measured through the thickness of the multilayer welding seam No. SN0.1.4 results basically from differences in the structure of the welding beads. Figures 6 and 7 depict the structure in the vicinity of the crack tip of TS oriented SE(B) specimens at 22 mm and 70 mm depth, respectively. Generally, TS oriented specimens have a uniform structure along the fatigue crack front (plane LS), thus the crack tip is located in varying welding beads. Figure 6 shows the structure of a specimen from the thickness location 22 mm (disk 1-1.3, Table 3). The crack tip is located in a coarse grain bainitic structure whose grains are framed with proeutectoid ferrite. This coarse grain

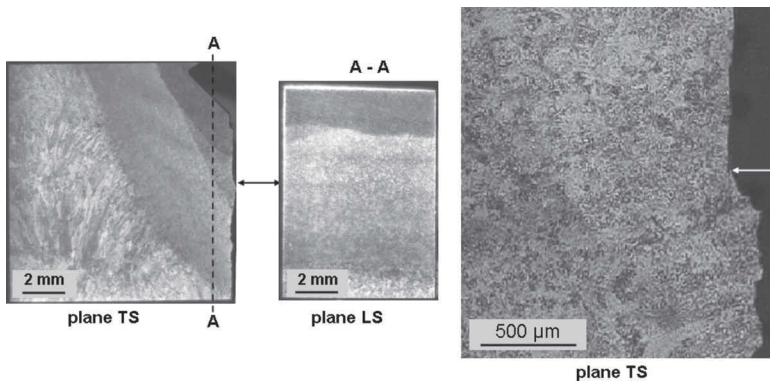


FIG. 7—Metallographic sections of the SE(B) specimen (TS) from the welding root location 70 mm ($T_0=-31.7^\circ\text{C}$, Table 3), arrow marks the position of the fatigue crack tip.

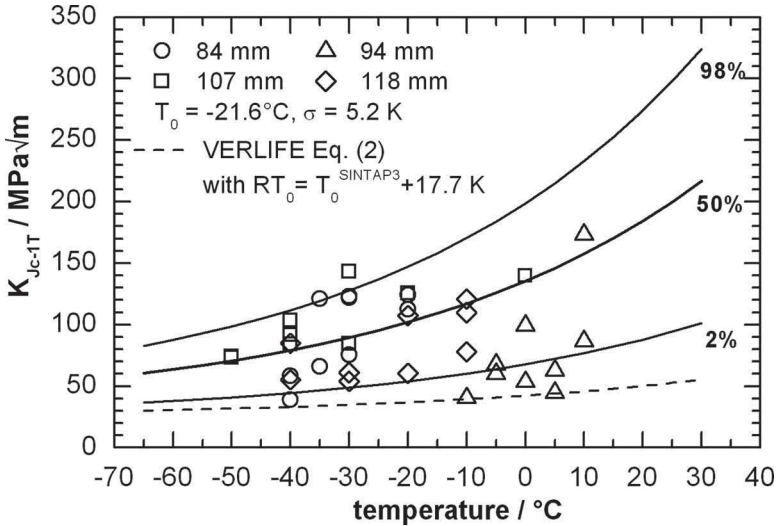


FIG. 8— K_{Jc} values measured on Charpy size SE(B) specimens from the thickness locations beyond the welding root, adjusted to 1T (25.4 mm) specimen size, versus the test temperature, Master Curves for 2, 50, and 98 % fracture probability and VERLIFE lower bound curve.

structure results in a T_0 of 49.1 °C. For comparison, Fig. 7 shows the structure in the region of the welding root in a thickness location of 70 mm, where a T_0 of -32 °C was determined (Table 3). There, the crack tip is located directly in a fine grain structure of high ferrite content which was welded with the unalloyed wire Sv-08A. This example shows the effect of the specimen orientation in a multilayer welding seam. Unlike TS specimens, the structure of TL specimens varies along the fatigue crack front (plane LS), which is featured in the welding root region depicted in Fig. 7. It means TS and TL specimens have a differentiating and integrating behavior, respectively. Therefore, TS specimens are more sensitive to variations in the structure of the multilayer weld metal. The wide range of T_0 values spanning about 50 K can be explained by the location of the crack tip in the different structures of the welding beads. According to the Russian regulatory guide PNAE-G-7-002-086 [15] the surveillance specimens of weld metal of a WWER-440/V-213 RPV should come from thickness locations beyond the welding root. Therefore, the K_{Jc} values of the Sv-10KhMFT filling layers (disks 1-1.11, 1-1.12, 1-1.14, and 1-1.15, Table 3) were evaluated separately. The overall T_0 for those locations, according to ASTM E1912-08 [10], is -21.6 °C (Fig. 8), while T_0^{SINTAP} evaluated with SINTAP Step 2 is -3.7 °C and that for the more conservative Step 3 is 22.3 °C. As shown in Fig. 8 the majority of the K_{Jc} values from thickness location 94 mm (disk 1-1.12) are below the MC for 2 % fracture probability. The T_0 of that layer is clearly higher compared with the neighbor disks (Table 3, Fig. 4). Hence, within the welding seam are brittle zones. Due to the differentiating character of the precracked TS specimen very small brittle zones can be detected. That implication is con-

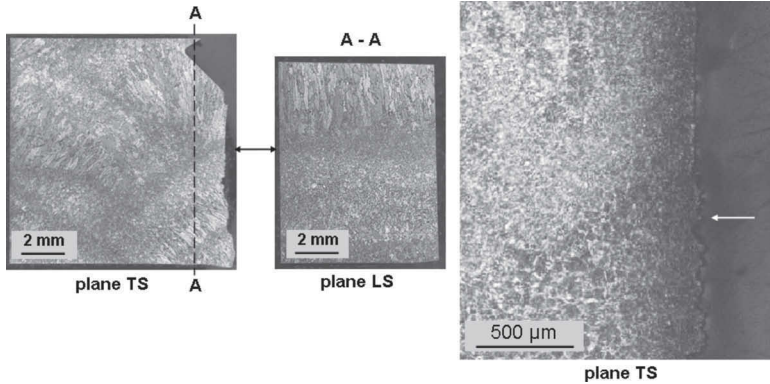


FIG. 9—Metallographic sections of the SE(B) specimen (TS) from the thickness location 94 mm ($T_0=22.7^\circ\text{C}$, Table 3), arrow at fatigue crack tip location.

firmed by the metallographic section shown in Fig. 9, where it can be clearly seen that the crack tip is directly located in a fusion zone between two welding beads.

Table 3 also contains the Charpy-V parameters, ductile-to-brittle transition temperatures TT_{41J} , and upper shelf energies from the filling layers of the welding seam. The evaluated TT_{41J} is 51.4°C at the location near the inner RPV wall and, thus, close to the reported T_{K0} of 46°C [2,3]. The evaluated upper shelf energy is on the level expected for WWER-440 weld metal. As mentioned before a T_K of 30°C was estimated with subsized impact specimens (type KLST according to DIN EN 10045-1 [9]). This T_K is based on a correlation between the $TT_{1.9J}$ transition temperature determined with KLST specimens and the TT_{41J} transition temperature of standard Charpy-V specimens [16]. The scatter of this correlation $\pm 35\text{ K}$ is rather high and therefore the uncertainty of the applied conversion is also high. Taking into account the difference in the orientation of the specimens and the reirradiation of two cycles the TT_{41J} estimated with KLST specimens after the recovery annealing is realistic. In this case the reirradiation causes an increase of TT_{41J} by 21 K. The TT_{41J} transition temperatures of the other thickness locations are lower. A direct correlation between T_0 and TT_{41J} of the investigated weld metal is questionable due to the different thickness location (S) of the crack tip and notch root in precracked SE(B) and reconstituted Charpy-V specimens, respectively. In addition the notch root of the reconstituted Charpy-V specimens is at a different axial position (T). Hence, the structures at the crack tip and notch root are different. This becomes apparent for the thickness layer 94 mm (disk 1-1.12) where T_0 agrees with TT_{41J} . Normally, T_0 is expected to be about 40 K lower than TT_{41J} .

Based on the results presented here a low re-embrittlement can be stated for thickness locations close to the inner RPV wall. This is more obvious for the Charpy-V results. The fracture toughness based T_0 shows a higher inherent scatter which is caused by the differentiating character of precracked TS specimens.

The MC approach and the associated reference temperature, T_0 , as defined in the test standard ASTM E1921, is rapidly moving from the research laboratories to application in integrity assessment of components and structures. For WWER reactors the “Unified Procedure for Lifetime Assessment of Components and Piping in WWER NPPs—VERLIFE” [17] defines a reference temperature, RT_0 , used in integrity assessment of WWER reactors as:

$$RT_0 = T_0 + \sigma \quad (1)$$

where

T_0 reference temperature according to ASTM E1912-08 [10]

σ is a margin $\sigma = \sqrt{\sigma_1^2 + \delta T_M^2}$

σ_1 standard deviation according to ASTM E1912-08 [10]

δT_M considers the scatter in the materials; if this value is not available the application of the following values is suggested

$\delta T_M = 10^\circ\text{C}$ for the base material,

$\delta T_M = 16^\circ\text{C}$ for weld metals.

The VERLIFE procedure [17] suggests the following RT_0 indexed lower bound curve for WWER base and weld metal:

$$K_{Jc}^5 \% (T) = \min\{25.2 + 36.6 \cdot e^{[0.019 \cdot (T - RT_0)]}; 200\} \text{ in MPa}\sqrt{\text{m}} \quad (2)$$

Equation 2 agrees with the standard MC for 5 % fracture probability in ASTM E1921-05 [10].

The VERLIFE [17] lower bound curve indexed with the RT_0 based on an average standard deviation according to ASTM E1921-08 [10] is depicted in Fig. 5. It is comparable with the MC of 2 % fracture probability. The K_{Jc} values adjusted to a specimen thickness of $1T$ are not completely enveloped by the VERLIFE WWER lower bound fracture toughness curve. The application of $T_0^{\text{SINTAP}^3}$ instead of T_0 in Eq 1 ensures that all measured K_{Jc} values are now enveloped by VERLIFE [17] lower bound fracture toughness curve. The same conclusion can be drawn for the specimens from the surveillance specimen locations in Fig. 8, whose K_{Jc} values are also enveloped by the VERLIFE lower bound curve based on $T_0^{\text{SINTAP}^3}$.

Summary and Conclusions

This paper presents first results of the post mortem investigations performed into the reactor pressure vessels (RPV) of the Russian WWER-440 type reactors. Trepan were taken from the beltline weld and the base metal of the Unit 1 RPV. This RPV was annealed after 15 years of operation and operated for two more years. At first the trepan of the beltline welding seam was investigated by Master Curve (MC) and Charpy V-notch testing. Specimens with TS orientation from eleven locations through the thickness of the welding seam were tested and evaluated according to ASTM E1921-05/08 [10]. The reference temperature T_0 was calculated with the measured fracture toughness values, K_{Jc} , at brittle failure of the specimen. Generally the K_{Jc} values measured on precracked and side-grooved Charpy size SE(B) specimens of the investigated weld metal follows the course of the Master Curve. The K_{Jc} values show a remarkable scatter.

T_0 shows a wavelike behavior through the welding seam. It increases from 10.3°C at the inner surface to 49.1°C at 22 mm distance and again decreases to -31.7°C at a distance of 70 mm, finally increasing again to a maximum 61°C toward the outer RPV wall. The lowest T_0 value was measured in the root region of the welding seam representing a uniform fine grain ferritic structure. Beyond the welding root T_0 shows a span of about 50 K. The differences in T_0 through the beltline welding seam are not the result of the low reirradiation but, rather caused by the nonhomogenous structure of the multilayer welding seam. Due to the differentiating character of the precracked TS specimen very small brittle zones can be detected. With the application of the MC modification in the SINTAP procedure [11–13] a reference temperature T_0^{SINTAP} can be evaluated which is based on the brittle constituent of a dataset. There are remarkable differences between T_0 and T_0^{SINTAP} indicating macroscopic inhomogeneous weld metal for some thickness locations.

Generally the effect of the recovery annealing was confirmed with the fracture toughness and Charpy-V testing. The TT_{41J} estimated with subsized KLST impact specimens after the annealing was confirmed by the testing of standard Charpy V-notch specimens.

The VERLIFE [17] procedure prepared for the integrity assessment of WWER RPV was applied on the measured results. It enables the determination of a reference temperature, RT_0 to index a lower bound fracture toughness curve. This curve agrees with the MC 5 % fractile as specified in ASTM E1912-08 [10]. The measured K_{Jc} values are not enveloped by this lower bound curve. However, the VERLIFE lower bound curve indexed with the SINTAP reference temperature RT_0^{SINTAP} envelops the K_{Jc} values. Therefore, for a conservative integrity assessment the fracture toughness curve indexed with a RT representing the brittle fraction of a dataset of measured K_{Jc} values has to be applied.

Acknowledgments

This study was funded by the German Federal Ministry of Economics and Technology, (Reactor Safety Research Project Grant No. 1501331).

References

- [1] Konheiser, J., Rindelhardt, U., Viehrig, H.-W., Böhmer, B., and Gleisberg, B., "Pressure Vessel Investigations of the Former Greifswald NPP: Fluence Calculations and Nb Based Fluence Measurements," *ICONE14/FEDSM2006 Proceedings*, Contribution ICONE 14-89578, 2006M.
- [2] Böhmer, B., Böhmert, J., Müller, G., Rindelhardt, U., and Utke, H., "Embrittlement Studies of the Reactor Pressure Vessel of the Greifswald -440 Reactors," Technical Report Task 4: Data Collection, Project Reference: NUCRUS96601 Technical Report, published October 1999, TACIS Service DG IA, European Commission, TACIS Information Office, European Commission, Aarlenstraat 88 1/06 Rue d' Arlon, 1040 Brussels, Belgium.

- [3] Ahlstrand, R., Klausnitzer, E. N., Langer, D., Leitz, Ch., Pastor, D., and Valo, M., "Evaluation of the Recovery Annealing of the Reactor Pressure Vessel of NPP Nord (Greifswald) Units 1 and 2 by Means of Subsize Impact Specimens," *Radiation Embrittlement of Nuclear Reactor Pressure Vessel Steels: An International Review (4th Volume)*, ASTM STP 1170, Lendell E. Steel, Ed., ASTM International, West Conshohocken, PA, 1993, pp. 321–343.
- [4] Viehrig, H.-W., Rindelhardt, U., and Schuhknecht, J., "Post Mortem Investigations of the NPP Greifswald WWER-440 Reactor Pressure Vessels," *Proceedings of the 19th International Conference on Structural Mechanics in Reactor Technology*, American Association for Structural Mechanics in Reactor Technology, 12–17 Aug. 2007, Toronto, Canada.
- [5] Barz, H.-U., Böhmer, B., Konheiser, J., and Stephan, I., "High-Precision Monte Carlo Calculations, Experimental Verification and Adjustment of Fluences in the Pressure Vessel Cavity of a VVER-1000," *Proceedings, 1998 ANS Radiation Protection and Shielding Division Topical Conference Technologies for the New Century*, 19–23, April 1998, Nashville, TN, Vol. 1, pp. 447–454.
- [6] Davies, L. M., "A Comparison of Western and Eastern Nuclear Reactor Pressure Vessel Steels," AMES Report No. 10, EUR 17327, European Commission, Luxembourg, 1997, Catalogue Number: CD-NA-17327 EN-C.
- [7] Brumovský, M., Valo, M., Kryukov, A., Gillemot, F., Debarberis, L., and Kang, K., "Guidelines for Prediction of Irradiation Embrittlement of Operating WWER-440 Reactor Pressure Vessels," *IAEA-TECDOC-1442*, IAEA, Vienna, 2005.
- [8] ASTM E1823-07, "Standard Terminology Relating to Fatigue and Fracture Testing," *Annual Book of ASTM Standards*, ASTM International, West Conshohocken, PA, 2007.
- [9] DIN EN 10045-1 (1991), "Metallic Materials: Charpy Impact Test, Part 1," *DIN-Taschenbuch 19, Werkstoffprüfnormen für metallische Werkstoffe 1*, Beut Verlag GmbH, 2003.
- [10] ASTM E1912-08, "Standard Test Method for Determination of Reference Temperature, T_0 , for Ferritic Steels in the Transition Range," *Annual Book of ASTM Standards*, ASTM International, West Conshohocken, PA, 2008.
- [11] SINTAP, Structural Integrity Assessment Procedures for European Industry (SINTAP), Final Version: WEM/SINTAP/PROC_7/CONTENTS REGP (05/11/99), Nov. 1999.
- [12] Wallin, K., Nevasmaa, P., Laukkanen, A., and Planman, T., "Master Curve Analysis of Inhomogeneous Ferritic Steels," *Eng. Fract. Mech.*, Vol. 71, Issues 16–17, Nov. 2004, pp. 2329–2346.
- [13] Pisarski, H. G., and Wallin, K., "The SINTAP Fracture Toughness Estimation Procedure," *Eng. Fract. Mech.*, Vol. 67, No. 6, Dec. 2000, pp. 613–624.
- [14] EN ISO 14556 (2000), "Steel—Charpy V-Notch Pendulum Impact Test—Instrumented Test Method," *DIN-Taschenbuch 19, Werkstoffprüfnormen für metallische Werkstoffe 1*, Beut Verlag GmbH, 2003.
- [15] PNAE-G-7-002-086, "Regulatory Guide for Strength Calculation of Nuclear Power Plant Equipments and Piping," ATOMENERGOISDAT, Moscow, 1989 (in Russian).
- [16] Klausnitzer, E., Kristof, H., and Leistner, R., "Assessment of Toughness Behaviour of Low Alloy Steels by Subsize Impact Specimens," *Transactions of the 8th International Conference of Structural Mechanics in Reactor Technology (SMIRT)*, Vol. G, 1985, pp. 33–37.
- [17] Brumovský, M., "Unified Procedure for Lifetime Assessment of Component and Piping in WWER NPPs 'VERLIFE'," European Commission, Final Report, Contract No. FIKS-CT-2001-20198, Sept. 2003.

Naoki Soneda,¹ Kenji Dohi,² Kenji Nishida,² Akiyoshi Nomoto,²
Minoru Tomimatsu,³ and Hiroshi Matsuzawa⁴

Microstructural Characterization of RPV Materials Irradiated to High Fluences at High Flux

ABSTRACT: Understanding the embrittlement of reactor pressure vessel (RPV) steels at high fluence region is very important for the long term operation of nuclear power plants. In this study, extensive microstructural analyses were performed on the RPV steels irradiated to very high fluences beyond 10^{20} n/cm², $E > 1$ MeVat high fluxes under the Pressurized Thermal Shock and Nuclear Power Plant Integrity Management projects in Japan. Three dimensional atom probe analyses were performed to characterize the solute atom cluster formation in these materials. The effects of fluence, flux, and chemical compositions on the characteristics of clusters were analyzed. The formation of dislocation loops was identified in the transmission electron microscopy analyses of high and low Cu steels, and the changes in loop size and number density with fluence were studied. P segregation on grain boundaries was also studied by surface analyses as well as grain boundary chemical analyses. We found that nonhardening embrittlement due to grain boundary fracture is not a major contributor to the embrittlement in these materials and irradiation conditions. The correlation of the microstructural changes and the Charpy transition temperature shifts was studied. The volume fraction of solute atom clusters has an excellent correlation with the transition temperature shifts. The Orowan model calculations of the contribu-

Manuscript received September 18, 2008; accepted for publication June 2, 2009; published online August 2009.

¹ Central Research Institute of Electric Power Industry, 2-11-1 Iwado-kita, Komae, Tokyo 201-8511, Japan. (Corresponding author), e-mail: soneda@criepi.denken.or.jp

² Central Research Institute of Electric Power Industry, 2-11-1 Iwado-kita, Komae, Tokyo 201-8511, Japan.

³ Mitsubishi Heavy Industries, Ltd., 1-1-1 Wadasaki-cho, Hyogo-ku, Kobe 652-8585, Japan.

⁴ Japan Nuclear Energy Safety Organization, TOKYUREIT Toranomon Building, 3-17-1 Toranomon, Minato-ku, Tokyo 105-0001, Japan.

Cite as: Soneda, N., Dohi, K., Nishida, K., Nomoto, A., Tomimatsu, M. and Matsuzawa, H., "Microstructural Characterization of RPV Materials Irradiated to High Fluences at High Flux," *J. ASTM Intl.*, Vol. 6, No. 7. doi:10.1520/JAI102128.

Copyright © 2009 by ASTM International, 100 Barr Harbor Drive, PO Box C700, West Conshohocken, PA 19428-2959.

tions of dislocation loops to the transition temperature shifts show that in low Cu materials, dislocation loops may be a major contributor, but in Cu containing materials its contribution is weak. Root-sum-square of the contributions of solute atom clusters and dislocation loops seems to be a reasonable model to describe the total ΔRT_{NDT} .

KEYWORDS: reactor pressure vessel, neutron irradiation embrittlement, high fluence, atom probe tomography, transmission electron microscopy

Introduction

The safe operation of nuclear power plants requires the determination of the appropriate operation conditions of reactor pressure vessels (RPVs) with consideration of the neutron irradiation embrittlement of RPV steels. The accurate prediction of embrittlement is thus very important for the long term operation of the nuclear power plants. The embrittlement of RPV steels is normally predicted and monitored by the embrittlement correlation method as well as the surveillance program where the mechanical property changes in the test specimens irradiated in a capsule located inside the RPVs are measured. At present time, the maximum neutron fluence of the irradiated specimens in the Japanese surveillance program database is about 6×10^{19} n/cm², $E > 1$ MeV. However, the expected maximum neutron fluence after the long term operation of 60 years or more may be beyond 1×10^{20} n/cm², $E > 1$ MeV, for some plants, and it is necessary to understand the mechanical property changes in RPV materials at high neutron fluences. Since we need to wait for a long time until the sufficient number of high fluence surveillance data is accumulated, an accelerated irradiation of RPV steels utilizing materials testing reactors will be the only way to obtain such mechanical property change database in a short time period. However, the effect of high flux irradiation of test reactors is always the issue that we need to address very carefully, and thus not only obtaining the information of mechanical property changes but also studying the mechanism of embrittlement at very high flux and at very high fluences are very important for the future development of accurate embrittlement correlation methods.

With respect to the high fluence irradiation, we had two major projects in Japan in the past, i.e., Pressurized Thermal Shock (PTS) and Nuclear Power Plant Integrity Management (PLIM) technology projects. The PTS project was conducted by Japan Power Engineering and Inspection Corporation in the late 1980s to study the transition temperature shifts in several RPV steels irradiated in the Japan Materials Testing Reactor (JMTR). The results of the PTS project were used to develop a Japanese embrittlement correlation equation, Japan Electric Association Code JEAC4201-1991 [1]. The PLIM project, on the other hand, was conducted by Japan Nuclear Safety Organization (JNES) in the early 2000s to obtain the data to develop an embrittlement correlation equation for the Charpy upper shelf energy changes. In the PLIM project, the irradiation of the RPV materials of both plates and weld metals with systematically controlled chemical composition was performed to obtain the mechanical property

TABLE 1—Chemical composition of the PTS and PLIM materials.

ID	Project	Product Form	Chemical Composition (wt %)								
			C	Si	Mn	P	S	Ni	Cr	Mo	Cu
B1	PLIM	Plate	0.24	0.17	1.55	0.009	0.018	0.63	0.14	0.52	0.21
B4			0.23	0.15	1.51	0.009	0.022	0.62	0.15	0.52	0.17
B5			0.24	0.14	1.52	0.009	0.020	0.59	0.13	0.51	0.10
B6			0.22	0.13	1.47	0.008	0.022	0.92	0.13	0.52	0.10
B7			0.24	0.14	1.53	0.017	0.024	0.63	0.13	0.51	0.10
B8			0.22	0.32	1.53	0.009	0.020	0.63	0.14	0.51	0.10
B9			0.19	0.22	1.50	0.003	0.006	0.62	0.11	0.51	0.04
S1			...	0.26	...	0.007	...	0.62	0.09
S2			...	0.23	1.48	0.011	...	0.64	0.17
W1	Weld metal	0.046	0.30	1.19	0.016	0.021	0.88	0.02	0.52	0.20	
W2		0.053	0.30	1.21	0.016	0.016	0.86	0.03	0.52	0.13	
W3		0.064	0.27	1.19	0.016	0.006	0.88	0.02	0.49	0.10	
W4		0.061	0.28	1.23	0.008	0.004	0.84	0.03	0.45	0.02	
P1B		PTS	Plate	0.20	0.21	1.46	0.008	0.008	0.58	...	0.46
P2B	0.18			0.21	1.43	0.007	0.005	0.59	...	0.47	0.25
P3B	0.19			0.22	1.44	0.018	0.006	0.57	...	0.47	0.06
P4B	0.20			0.24	1.44	0.009	<0.005	1.78	...	0.48	0.06

data. Although the objective of the PLIM project was focused on the upper shelf energy, the full curves of Charpy impact tests were obtained for all the materials, and thus the database is also suitable to study the transition temperature shifts.

Under this situation, JNES started in 2005 a new project named Prediction of Radiation Embrittlement (PRE) for High Fluence Range project to study the mechanism of RPV embrittlement irradiated to high fluences using the materials irradiated in PTS and PLIM projects. Extensive microstructural analyses utilizing three dimensional atom probe (3DAP) tomography, positron annihilation (PA) spectroscopy, and transmission electron microscopy (TEM) are planned in the PRE project to characterize the microstructural changes in the materials in terms of solute atom behavior and point defect cluster formation as a function of environmental and metallurgical variables. In this paper, the first stage results of the PRE project on the microstructural analyses are presented.

Experiments

Materials and Irradiation Conditions

The chemical compositions and irradiation conditions of the steels of PLIM and PTS projects are shown in Tables 1 and 2. In the PLIM project [2], plates and weld metals with the wide range of copper contents are irradiated. There

TABLE 2—Irradiation conditions and mechanical property changes.

ID	Chemical Composition				Fluence ($\times 10^{19}$ n/cm ²)	Flux ($\times 10^{12}$ n/cm ² ·s)	ΔT_{NDT} (°C)	ΔFATT (°C)	USE (J)	ΔUSE (J)	ΔH_V	SD of ΔH_V
	Cu	Ni	P	Si								
B1-1	0.21	0.63	0.009	0.17	3.1	5	106	96	87	17	16	25
B1-2	0.21	0.63	0.000	0.00	6.4	5	125	108	78	26	29	23
B1-3	0.21	0.63	0.000	0.00	12.1	5	165	142	64	40	87	20
B4-1	0.17	0.62	0.009	0.15	3.2	5	89	83	68	14	16	8
B4-2	0.17	0.62	0.000	0.00	6.4	5	119	103	64	18	71	14
B4-3	0.17	0.62	0.009	0.14	12.9	5	160	136	51	31	74	10
B5-1	0.1	0.59	0.009	0.14	3.1	5	72	65	91	11	21	25
B5-2	0.1	0.59	0.009	0.14	6.4	5	104	90	80	22	43	21
B5-3	0.1	0.59	0.009	0.14	12.0	5	137	122	73	29	72	22
B6-1	0.1	0.92	0.008	0.13	8.6	5	126	122	77	43	62	28
B7-1	0.1	0.63	0.017	0.14	8.6	5	116	105	72	21	72	29
B8-1	0.1	0.63	0.009	0.32	8.7	5	98	93	79	22	65	19
B9-1	0.04	0.62	<0.005	0.22	3.1	5	16	37	244	21	23	13
B9-2	0.04	0.62	<0.005	0.22	6.3	5	29	46	239	26	-2	9
B9-3	0.04	0.62	<0.005	0.22	12.1	5	66	77	205	60	38	16
S1-1	0.09	0.62	0.007	0.26	3.2	5	45	12	176	14	13	13
S1-2	0.09	0.62	0.007	0.26	5.9	5	79	59	168	22	35	16
S1-3	0.09	0.62	0.007	0.26	11.7	5	128	92	134	56	90	20
S1s-1	0.09	0.62	0.007	0.26	3.0	0.1	9	17
S1s-2	0.09	0.62	0.007	0.26	6.0	0.1	38	26
S2-1	0.14	0.72	0.010	0.21	4.4	5	21	23
P1B-1	0.06	0.58	0.008	0.21	6.7	10	48	41	121	16	26	24
P1B-2	0.06	0.58	0.008	0.21	12.9	10	71	54	111	26	23	16
P2B-1	0.25	0.59	0.007	0.21	7.0	10	140	110	109	38	47	20
P3B-1	0.06	0.57	0.018	0.22	5.4	10	56	59	145	12	20	15

TABLE 2— (Continued.)

ID	Chemical Composition				Fluence ($\times 10^{19}$ n/cm 2)	Flux ($\times 10^{12}$ n/cm 2 ·s)	ΔRT_{NDT} ($^{\circ}\text{C}$)	ΔF_{ATT} ($^{\circ}\text{C}$)	USE (J)	Δ USE (J)	ΔH_{V}	SD of ΔH_{V}
	Cu	Ni	P	Si								
P4B-1	0.06	1.78	0.009	0.24	7.1	10	180	151	106	57	38	26
W1-1	0.2	0.88	0.016	0.30	3.3	5	119	110	103	36	40	10
W1-2	0.2	0.88	0.016	0.30	8.6	5	151	144	82	57	28	10
W1-3	0.2	0.88	0.016	0.30	11.8	5	175	164	79	60	74	10
W2-1	0.13	0.86	0.016	0.30	3.2	5	80	69	129	45	84	12
W2-2	0.13	0.86	0.016	0.30	8.9	5	139	114	111	63	70	11
W2-3	0.13	0.86	0.016	0.30	11.2	5	150	135	96	78	100	12
W3-1	0.1	0.88	0.016	0.27	3.1	5	49	60	167	28	18	9
W3-2	0.1	0.88	0.016	0.27	8.3	5	98	100	138	57	12	10
W3-3	0.1	0.88	0.016	0.27	11.3	5	131	120	126	69	48	8
W4-1	0.02	0.84	0.008	0.28	3.1	5	32	18	221	41	-6	9
W4-2	0.02	0.84	0.008	0.28	9.0	5	58	58	199	63	6	11
W4-3	0.02	0.84	0.008	0.28	13.0	5	88	88	170	92	21	12

are two kinds of plate materials in the PLIM projects. The plates with IDs starting with “B” are those newly produced for the PLIM project, while the two plates with IDs starting with “S” are two standard reference materials used in the surveillance programs in Japan. It should be noted that the B-series plates except for the B9 plate are fabricated so that the upper shelf toughness is relatively low because the primary objective of the PLIM project was to generate a database for the use of the development of the embrittlement correlation method of upper shelf energy reduction. This was done by increasing the sulfur content in these plates. Among the B-series plates, the chemical compositions of B6, B7, and B8 are basically similar to B5 material, except for nickel, phosphorus, and silicon contents, respectively. The materials with IDs starting with “W” are weld metals. All the plates and weld metals except for S1s materials were irradiated in the Halden Reactor at the neutron flux of 5×10^{12} n/cm²·s, $E > 1$ MeV, up to the neutron fluence of $> 1 \times 10^{20}$ n/cm², $E > 1$ MeV. S1s material was irradiated in commercial reactors in Japan at the neutron flux of $\sim 1 \times 10^{11}$ n/cm²·s, $E > 1$ MeV. The irradiation temperature of the materials was controlled to be 290°C +/−10°C.

Four materials were selected from those irradiated in the PTS projects [3]. P1B material is the 1B material of the PTS project, which is a plate with relatively low Cu content. P2B material is the 2B material of the PTS project, which is a plate with high Cu content of 0.25 wt %. The chemical contents of P3B and P4B materials, which are 3B and 4B materials of PTS project, respectively, are basically the same as that of P1B materials except for the P and Ni contents. The Ni content of P4B material is 1.78 wt %, which is far beyond the required range for Ni content of A533B Cl.1 plate materials. These materials were irradiated in the JMTR at the neutron flux of 1×10^{13} n/cm²·s, $E > 1$ MeV, up to the neutron fluence of $> 1 \times 10^{20}$ n/cm², $E > 1$ MeV. The irradiation temperature of the materials was also controlled to be 290°C +/−10°C.

Microstructural Characterization

3DAP tomography, PA spectroscopy, and TEM were used to characterize the features of nanometer size generated in the steels. For the 3DAP, LEAP 3000 X of Imago Scientific Instruments, which is equipped with a local electrode and a high frequency (200 kHz) voltage pulse as well as a laser pulse module, was used [4]. For the 3DAP measurement, materials were cut into bars with size of $0.3 \times 0.3 \times 10$ mm³, and then conventional electropolishing technique [5] was used to sharpen the bars into needle-shaped specimens with tip diameter of around 100 nm. Specimens were cooled down to 50 K at the measurement, and only voltage pulse mode was used to collect ions. Cluster analysis was done using the recursive search algorithm [6]. In our application of the algorithm, a series of core atoms, i.e., Cu, Ni, Mn, and Si, which are within the separation of 0.5 nm, is searched first, and then, periphery atoms, which are again within the separation of 0.5 nm from the core atoms, are searched. Finally, periphery atoms that have less than three core atoms within a 0.5 nm distance are removed. Cluster size is defined using a Guinier radius, which is a radius of gyration multiplied by $(5/3)^{1/2}$.

PA experiments were done using the positron source of ^{22}Na with the radioactive intensity of 1.7 MBq. A positron lifetime spectrum was obtained by accumulating the time difference between the positron generation signal of 1275 keV γ -ray and the PA signal of 511 keV γ -ray using a BaF_2 scintillator coupled with a photomultiplier tube. The time resolution of the system used is 260 ps. Decomposition of the positron lifetime spectrum was performed using the positron lifetime analysis software *Resolution* [7]. Since it is very difficult to decompose the lifetime spectrum of commercial steels into more than two components in addition to the component of polyimide film used to seal the ^{22}Na solution in the commercial steels, we normally decompose the spectrum into two lifetime components: one is for the average lifetime of radiation damage and the other is for polyimide, which is fixed to be 350 ps in this study.

Analyses of very fine scale dislocation loops as well as the grain boundary chemistry were performed using 200 keV field emission gun–transmission electron microscope equipped with the energy dispersive x-ray spectroscopy apparatus. Dislocation loops were identified as white and black dots by performing bright image and weak-beam dark image analyses using several different diffraction vectors. The sample thickness was measured using the convergent beam electron diffraction method to estimate the volume of the view, which is used in the number density calculations. Chemical analyses of grain boundaries were done using electron beam of 1 nm ϕ , and the target elements were Fe, Ni, Si, P, Mn, and Cu.

Mechanical Property Data

As stated above, the materials from the PLIM project were fabricated to reinforce a database for the correlation equation development of upper shelf toughness reduction. The chemical composition, in particular S content, and manufacturing process of these materials were controlled so that the upper shelf toughness becomes low to simulate the mechanical properties of RPVs of the first generation. Here, we first summarize the mechanical property data of PLIM and PTS projects to see the consistency among the data. Table 2 shows the mechanical property data including Charpy temperature shift at 41 J, upper shelf toughness, temperature shift at 50 % shear fracture surface, and the Vickers hardness increase measured by 1 kgf weight.

Figure 1(a) and 1(b) shows the $\Delta\text{RT}_{\text{NDT}}$ values of plates and weld metals, respectively, plotted against the neutron fluence. In both plots, materials with high Cu contents show larger shifts, which increase with increasing fluence, indicating no saturation of embrittlement. When we compare the plates and weld metals, weld metals show in general larger shifts than the plates with similar Cu content. This can be due to the product form effect, but on the other hand, this may be due to the effect of Ni content because weld metals have higher Ni content, typically 0.88 wt %, than plates, typically 0.60 wt %, as shown in Table 2. This Ni effect can also be seen in the comparison between B5 and B6 plates, where B6 plate with 0.92 wt % Ni shows larger shift than B5 plate with 0.59 wt % Ni, though the difference is small. The synergetic effect between Cu and Ni has been well known and accepted [8], and thus above

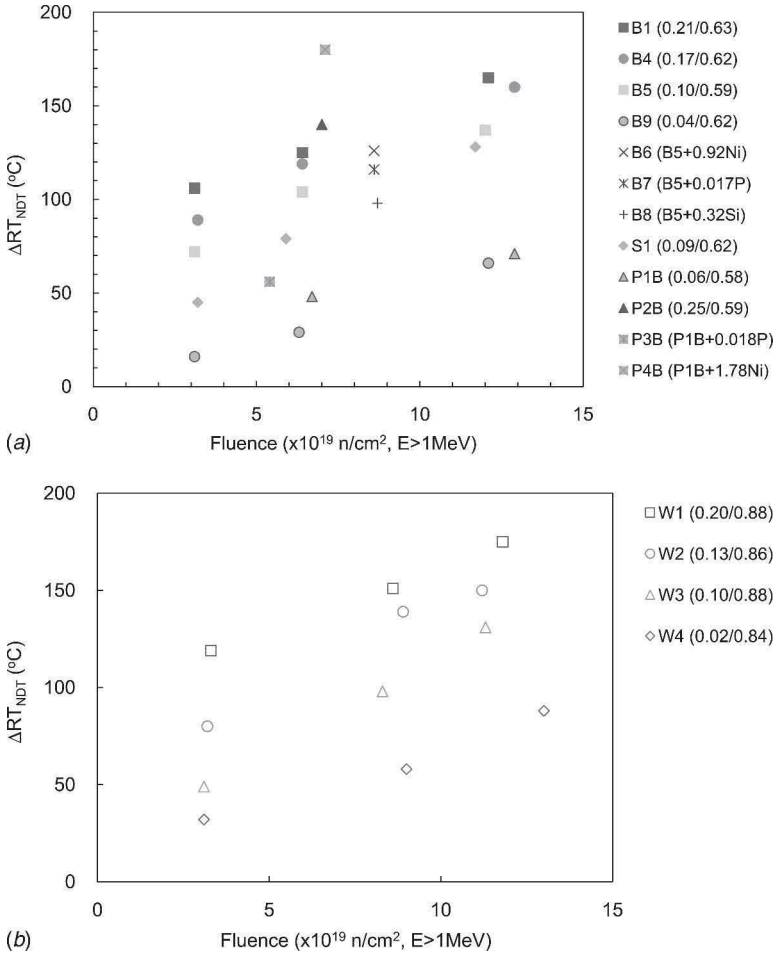


FIG. 1—Effect of neutron fluence on the transition temperature shifts in terms of ΔRT_{NDT} for various materials.

observations can be due to this synergetic effect. When we compare the results of P1B and P4B, the P4B plate, which has very high Ni content of 1.78 wt %, shows much larger shift than P1B with 0.58 wt % Ni, though the Cu content of these plates are as low as 0.06 wt %. This comparison suggests that Ni alone can cause embrittlement in addition to the synergetic effect with Cu. The effect of P can be observed in the comparisons between B5 and B7 and between P1B and P3B. The P effect looks small in the comparison of B5 and B7, both of which have medium Cu content of 0.1 wt %, while there is some difference between P1B and P3B, both of which have low Cu content of 0.06 wt %. The P3B plate with higher P content shows larger shift than the P1B plate.

With respect to the upper shelf energy, one can see in Table 2 that the plates from B1 to B8 of the PLIM project have low initial values of upper shelf energy

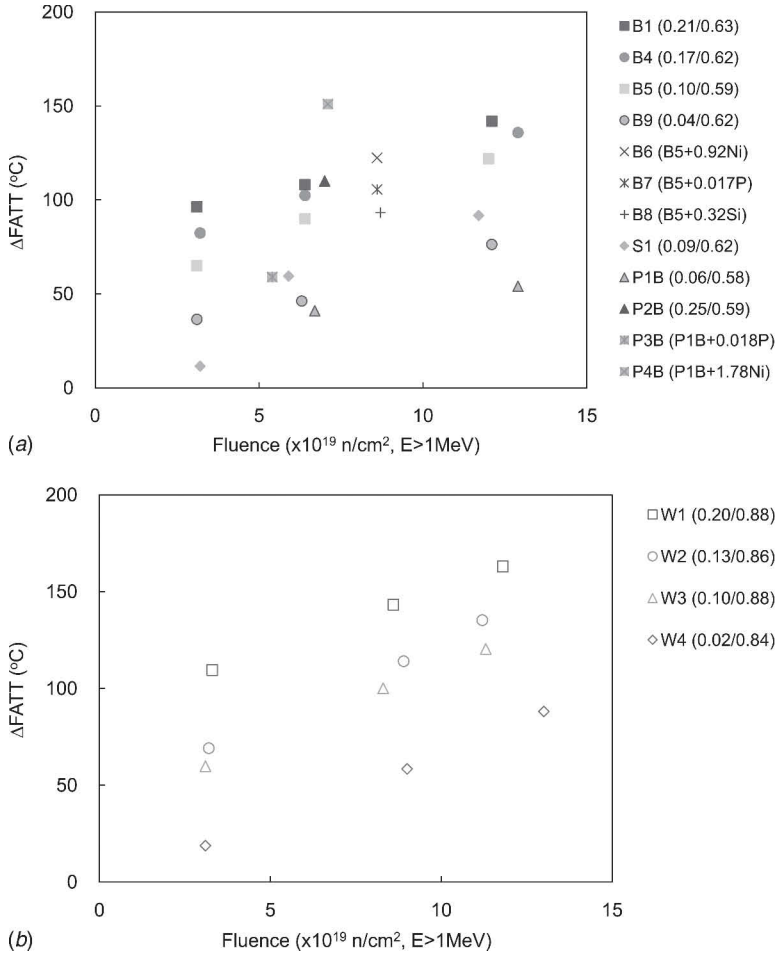


FIG. 2—Effect of neutron fluence on the transition temperature shifts in terms of $\Delta FATT$ for various materials.

below 100 J, and the values decrease with irradiation. Since the ΔRT_{NDT} index is defined as the temperature shift of the Charpy energy at 41 J, the ΔRT_{NDT} value is affected by the decrease in upper shelf energy, in particular in low upper shelf energy materials. Therefore, we discuss here another index of embrittlement, $\Delta FATT$ (fracture appearance transition temperature), which is defined as the temperature shift at 50 % shear fracture surface. Figure 2(a) and 2(b) shows the $\Delta FATT$ values as a function of fluence. The same tendency that was found in Fig. 1 can also be observed in Fig. 2. Figure 3 is a comparison between ΔRT_{NDT} and $\Delta FATT$. In general, ΔRT_{NDT} values are larger than those of $\Delta FATT$ at larger shift region. This tendency is more evident in plates having lower upper shelf energy than in weld metals having higher upper shelf energy. Note that the differences between ΔRT_{NDT} and $\Delta FATT$ values are large in B9

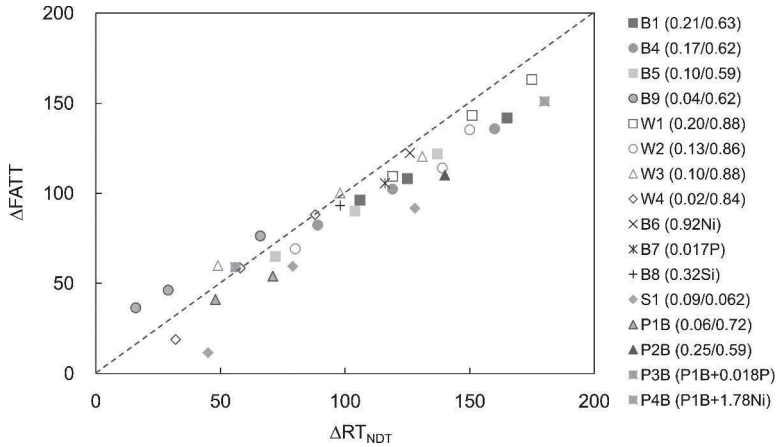


FIG. 3—Comparison of ΔRT_{NDT} and $\Delta FATT$ values.

and S1 plates. In particular, in B9 material, ΔRT_{NDT} values are smaller than $\Delta FATT$ values, suggesting some scatter in the initial values of these indexes.

Microstructural Characterization

Formation of Solute Atom Clusters

Figure 4 shows results obtained for the B1 and B9 materials using 3DAP. In the B1 material with high Cu content of 0.21 wt %, it is clearly observed that high number densities of solute atom clusters enriched with Cu, Ni, Mn, and Si are uniformly formed in the matrix, as shown in Fig. 4(a). This observation is very consistent with those in literatures [9–11]. However, if there are dislocation lines, the Cu-enriched solute atom clusters are preferentially formed right on the dislocation lines, as shown in Fig. 4(b). On the other hand, in B9 material with low Cu content of 0.04 wt %, one can also see the formation of solute atom clusters, as shown in Fig. 4(c). A very different characteristic of B9 plate from B1 plate is that the clusters are enriched with Ni, Mn, and Si but no Cu. The number density of the solute atom clusters in B9 material is much lower than in B1. This type of characterization of solute atom clusters was done for all the materials listed in Table 2. It should be noted that no nanoscale fine features associated with S atoms were observed by 3DAP in the B1, B5, B6, B7, and B8 plates, which have high S contents. This suggests that S has an effect to make the initial upper shelf toughness low but essentially has no effect on embrittlement. In this section, we will discuss the characteristics of the solute atom clusters in terms of bulk chemical compositions and irradiation conditions of the materials.

Figure 5(a) and 5(b) shows the cluster number density of plates and weld metals as a function of neutron fluence. In terms of the Cu effect on the number density, it is clear that the cluster number density is larger in higher Cu mate-

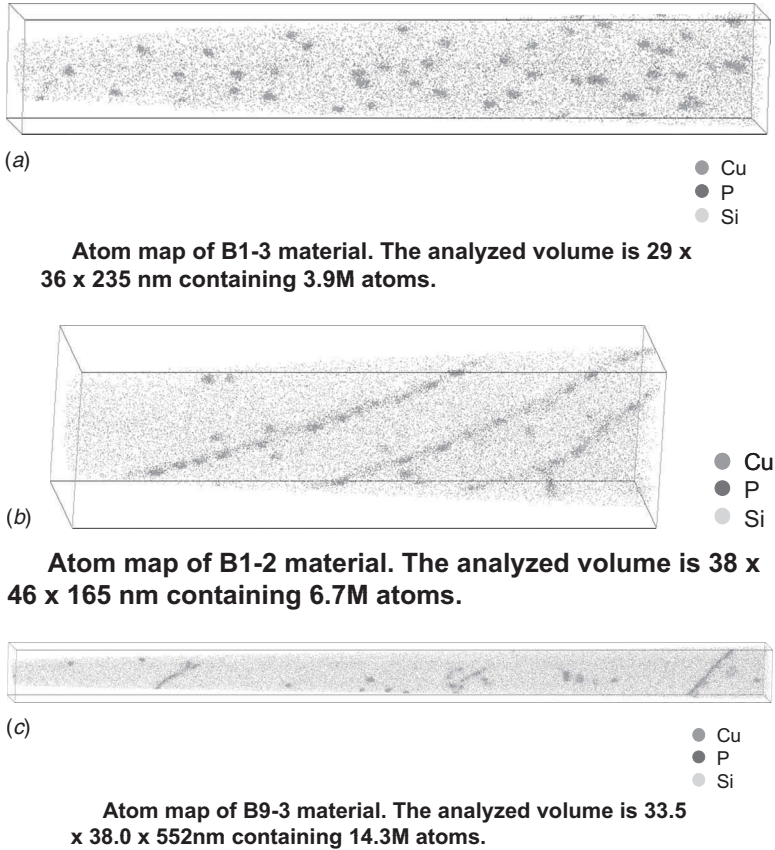


FIG. 4—Atom map obtained by 3DAP measurement for B1 and B9 materials.

rials at fluences around 3×10^{19} n/cm², $E > 1$ MeV, in both plates and weld metals. When we compare the plates and weld metals, weld metals have in general larger number densities than plates. This may be due to the difference in Ni content between plates and weld metals. In fact, the cluster number densities in B6 and P4B materials having higher Ni contents are also larger than the same class of materials, B5 and P1B, with lower Ni contents. More precisely, the cluster number density in B6 plate with 0.92 wt % Ni is almost two times larger than that of B5 plate with 0.59 wt % Ni, and the cluster number density of P4B plate with 1.78 wt % Ni is more than ten times larger than that of P1B material. These results suggest that an increase in Ni content enhances the nucleation of solute atom clusters. Phosphorus content also looks to have similar effect. When we make comparisons between B7 plate with 0.017 wt % P and B5 plate with 0.009 wt % P and between P3B plate with 0.018 wt % P and P1B plate with 0.008 wt % P, the cluster number densities of higher P content plates are almost two times larger than lower P content plates in both cases. The effect of Si is not evident.

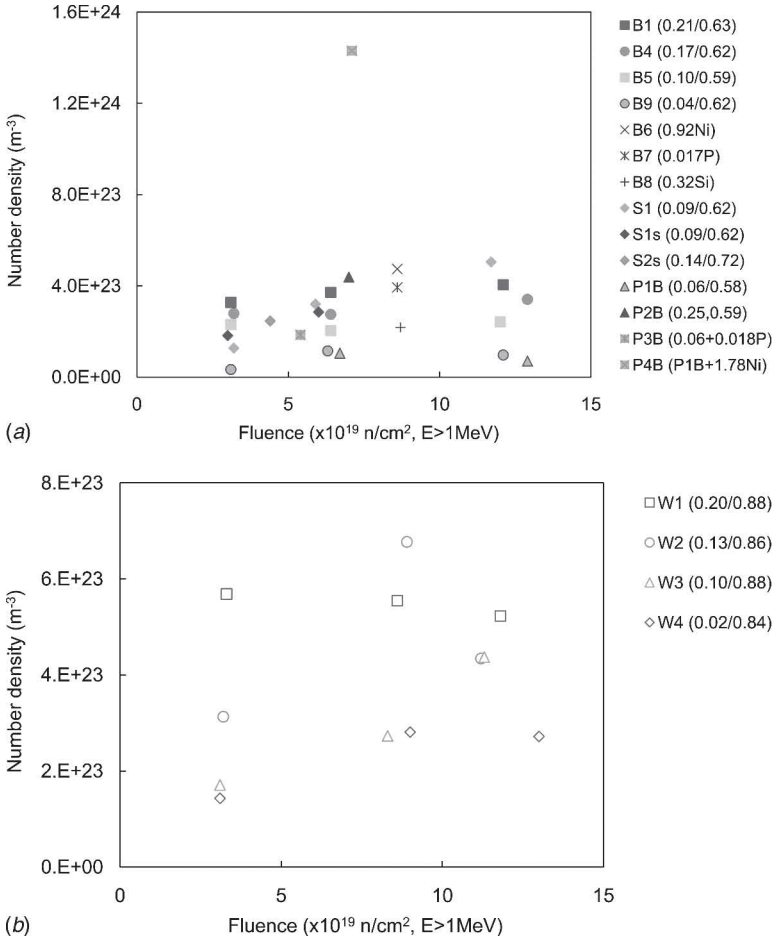


FIG. 5—Changes in the number density of solute atom clusters with fluence.

With respect to the effect of fluence, high number density of solute atom clusters are readily formed at low fluences around 3×10^{19} n/cm², $E > 1$ MeV. However, at higher fluences, the number density does not necessarily increase with fluence. In high Cu materials, an increase in number density saturates at 3×10^{19} n/cm², $E > 1$ MeV, while in low Cu materials saturation looks to occur at around 6×10^{19} n/cm², $E > 1$ MeV, with one exception of S1 plate, in which the number density increases with increasing fluence up to the highest fluence. Regarding the flux effect, on the other hand, the comparison of S1 plate irradiated in MTR at 5×10^{12} n/cm²·s, $E > 1$ MeV, with S1s plate irradiated in a commercial reactor at $\sim 1 \times 10^{11}$ n/cm²·s, $E > 1$ MeV, shows similar number density in spite of the 50 times difference in the magnitude of flux. In spite of a slight difference in chemical compositions, comparisons between B1 plate and P2B plate and between B9 plate and P1B plate might be

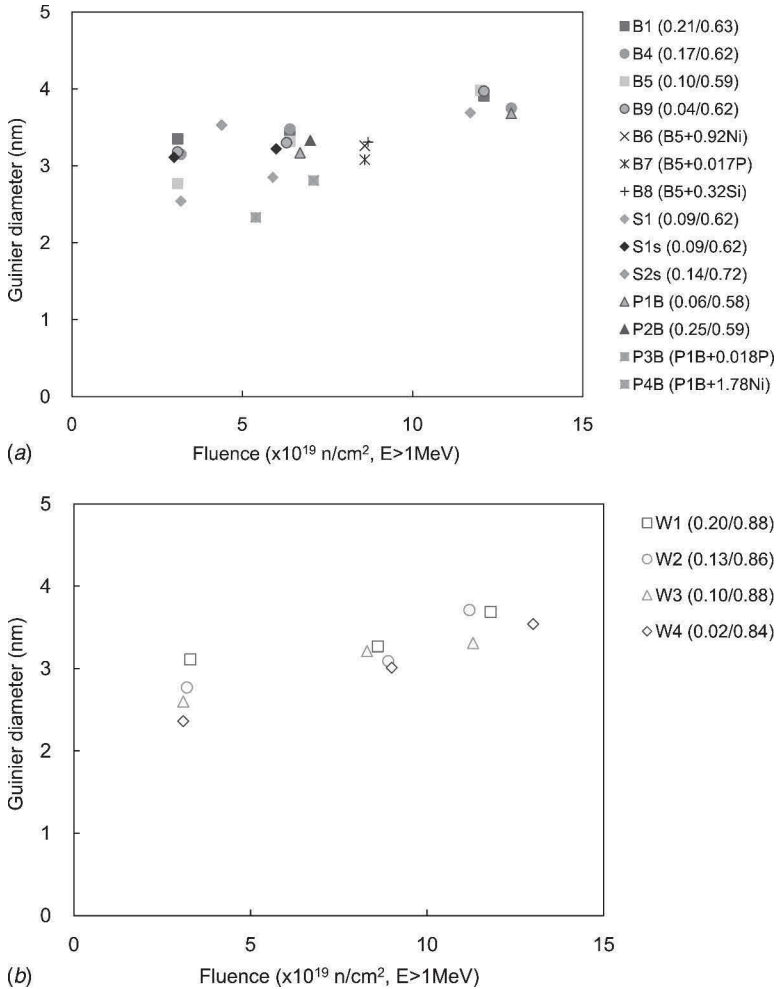


FIG. 6—Changes in the Guinier diameter of solute atom clusters with fluence.

useful. The flux of B1 and B9 plates is 5×10^{12} n/cm²·s, $E > 1$ MeV, while that of P2B and P1B is 1×10^{13} n/cm²·s, $E > 1$ MeV. The comparisons do not show significant difference in the cluster number densities.

Figure 6(a) and 6(b) shows the change in cluster diameter as a function of fluence. The general trend is that the cluster diameter in terms of the Guinier diameter consistently increases with fluence. This suggests that the clusters formed at lower fluences grow in size due to segregation of solute atoms to the clusters during irradiation to higher fluences. It should be noted that the cluster volume is proportional to the cube of the cluster diameter. This means that the difference of 3 and 4 nm in diameter means more than two times difference in volume, and a slight increase in diameter in Fig. 6 corresponds to a large increase in volume. The effect of Cu on cluster diameter is not necessarily clear,

but in weld metals irradiated to lower fluences, cluster diameter is larger in higher Cu content materials. When we compare the plates and weld metals, cluster diameters of weld metals are in general smaller than those of plates. As we saw above, this may be again due to difference in Ni content, i.e., higher Ni contents in weld metals make the diameters smaller than in plates with lower Ni contents. In fact, B7 and P4B, in particular P4B, have smaller cluster diameters maybe due to their high Ni contents. This is very consistent observation in the sense that the amount of solute atom segregation per cluster is less in the materials with higher number density of solute atom clusters, which act as segregation sites of solute atoms. Similar observation can be found in high P materials: the cluster diameters of B7 and P3B plates are smaller, but the number densities of clusters are larger in these plates.

The flux effect on the cluster size is evident in comparison between S1s and S1 materials, where the cluster size in S1s plate irradiated at lower flux is larger than S1 plate irradiated at higher flux. The same tendency can be found in the comparisons between B1 and P2B plates and between B9 and P1B plates irradiated in two different MTRs with different fluxes. B1 and B9 plates irradiated at lower flux have larger diameters. Flux effect can be caused due to differences in (1) irradiation time and (2) intercascade interaction, but in the high flux irradiation regime, the effect of intercascade interaction may be dominant. When the intercascade interaction becomes stronger at higher fluxes, the fraction of pair recombination increases at higher fluxes, resulting in the decrease in the amount of diffusion of point defects, in particular, vacancies, which are the carriers of solute atoms. This could be the mechanism of the difference in microstructure between the two fluxes at high flux regime. There should be some effect of irradiation time, but since the total fluence is very high in these materials, the diffusion of solute atoms due to irradiation-induced point defects should be much larger compared to that due to the thermal vacancies, and thus the effect of irradiation time would be negligible.

Figure 7(a) and 7(b) shows the change in volume fraction of the solute atom clusters. The volume fraction is calculated by assuming that the clusters are the complete spheres with the measured average Guinier radius, and the sum of all the cluster volumes divided by the total volume of the measured area is the volume fraction. The changes in cluster volume fraction are very similar to the change in transition temperature shifts in qualitative sense, and this will be discussed later.

Formation of Dislocation Loops

Another well-accepted contributor to embrittlement is the so-called matrix damage, which can be vacancy clusters, dislocation loops, and solute atom–point defect complexes. Extensive analyses by PA lifetime measurements show that the average lifetimes for all the materials are less than 180 ps, and in particular in low Cu materials, the average lifetime is less than 160 ps, suggesting that large vacancy clusters, or nanovoids, are not formed in these materials. Thus the possibility of vacancy clusters as matrix damage can be ruled out in these materials. Solute atom–point defect complex is another possibility for matrix damage, but it is very likely that such kind of damage with solute atoms

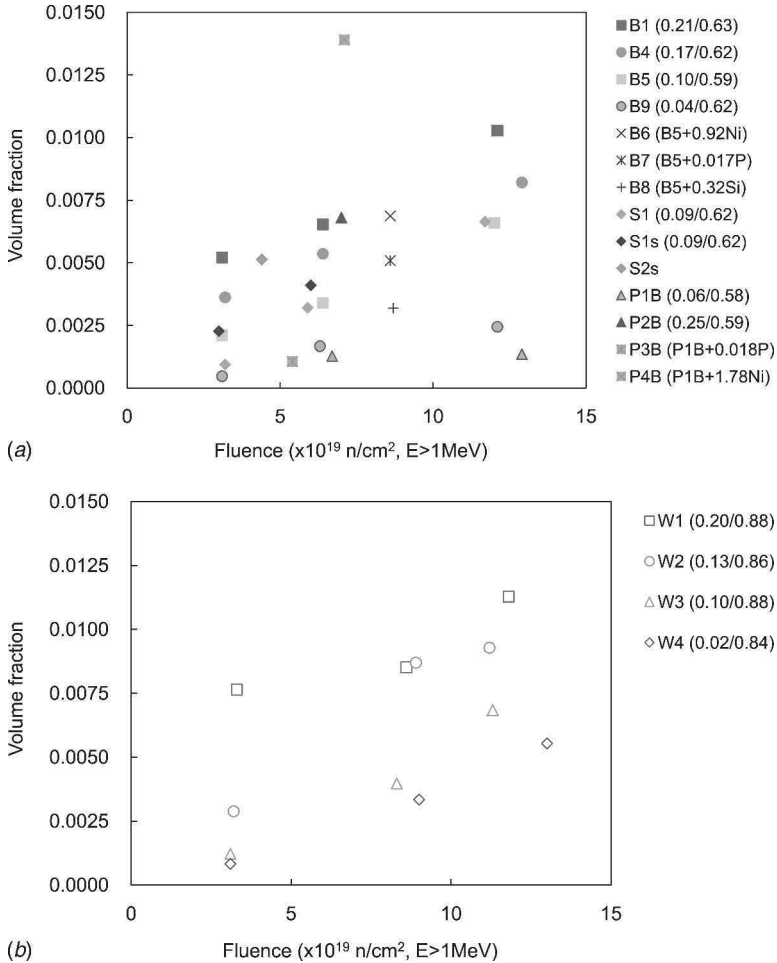


FIG. 7—Changes in the volume fraction of solute atom clusters with fluence.

can be detected by 3DAP. Therefore, in this section, we will discuss TEM measurement results to consider the remaining possible candidate for the matrix damage, i.e., dislocation loops.

TEM observations were performed on B1, S1, B9, and P1B plates. Examples of TEM observations of B9 and P1B materials are shown in Fig. 8. Both low Cu B9 plate and high Cu P1B plate have a number of dislocation loops, and the loops are well developed at higher fluences as shown in Fig. 8(b) and 8(d). It is interesting to see that some of the dislocation loops are formed preferentially near dislocation lines, and this may suggest source hardening though we see no enhanced yield drop in the stress-strain curve of these materials. Figure 9 shows the change in dislocation number density as a function of neutron fluence. The number densities increase with fluence in all the four materials. The number density of S1 plate with 0.09 wt % Cu is the smallest, those of B1 plate

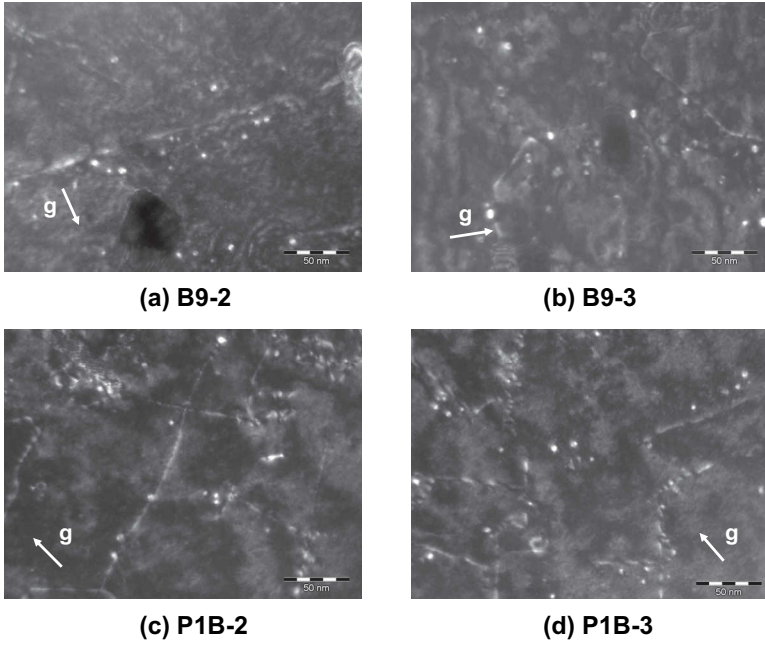


FIG. 8—TEM images of B9 and P1B materials irradiated at two different fluences ($\times 300\ 000$).

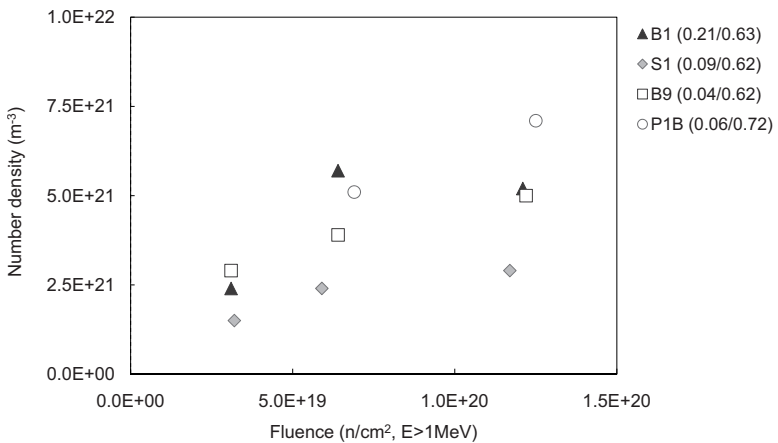


FIG. 9—Changes in the number density of dislocation loops with fluence.

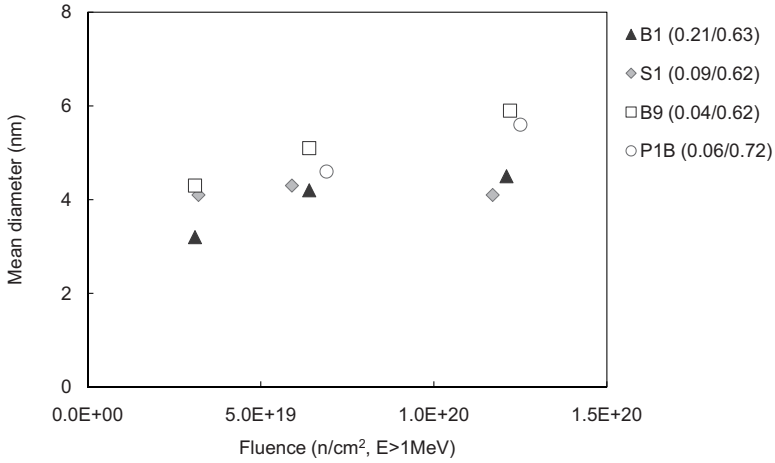


FIG. 10—Changes in mean diameter of dislocation loops with fluence.

with 0.21 wt % Cu and B9 plate with 0.04 wt % Cu are in similar magnitude, and that of P1B plate with 0.06 wt % Cu is the largest. Since the flux of P1B is two times faster than the other three materials, this might be due to the effect of flux, but there is no evidence. The effect of Cu content on the loop number density is not clear.

Figure 10 shows the average loop diameters as a function of neutron fluence. The average loop size increases with increasing fluence in all the materials. B9 and P1B plates with lower Cu contents have larger average loop size than B1 and S1 plates having higher Cu contents. Since B1 and S1 plates have solute atom clusters of larger number densities, the interaction between the solute atom clusters and point defects can be much larger in B1 and S1 materials than in B9 and P1B materials. This larger possibility of solute atom cluster–point defect interaction may suppress the growth of dislocation loops in B1 and S1 materials.

Grain Boundary Fracture

Grain boundary fracture due to P segregation at grain boundaries is a nonhardening type of embrittlement that may occur in high P materials irradiated to high fluences. In order to investigate if this occurred in the materials considered in this study, we performed fracture surface observations as well as grain boundary chemical analyses for the pairs of materials, B5 (0.009 wt % P) and B7 (0.017 wt % P) plates and P1B (0.008 wt % P) and P3B (0.018 wt % P) plates. No grain boundary fracture was observed in P3B plate, while very small amount of grain boundary fracture was observed in B5, B7, and P1B plates. The number of locations of grain boundary fracture in B7 is the largest, and P1B has the smallest number of grain boundary fracture locations. However, even in B7 plate, the total fraction of the grain boundary fracture surface is less than 1 % of the total surface analyzed.

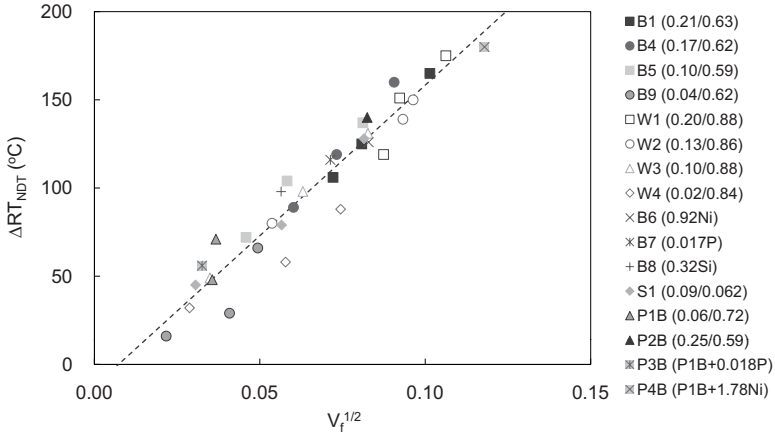


FIG. 11—Correlation between ΔRT_{NDT} and $V_f^{1/2}$.

Grain boundary chemical analyses show that the elements such as Ni, Mn, Si, Mo, and Cu are segregated at grain boundaries, but no clear enhancement in P segregation at grain boundaries with increasing fluence is observed. It should be noted that the amount of P segregation was slightly larger in B5 and B7 irradiated at lower fluxes than P1B and P3B irradiated at higher fluxes. The fact that B5 and B7 plates have larger P segregation is in good correspondence with the above grain boundary fracture measurement. These results suggest that the nonhardening embrittlement due to P segregation at grain boundaries will not be a major cause of embrittlement even at high fluxes, but further study will be necessary to verify that this is true even at lower fluxes of commercial reactors.

Correlation Between Mechanical Property and Microstructural Changes

Solute Atom Clusters and Mechanical Properties

Among the microstructural features, we first discuss about the correlation between the solute atom clusters and mechanical properties. As we can see in the comparison between Figs. 1 and 7, there is a correlation between the volume fraction of solute atom clusters and the transition temperature shifts. Figure 11 is a correlation between the ΔRT_{NDT} and the square root of the volume fraction of the solute atom clusters detected by 3DAP. A remarkably good correlation can be found between the two quantities for all the materials examined having wide range of chemistry and irradiation conditions. This is a very good first order model to connect the microstructural and mechanical property changes. When we examine the results in more detail, however, the fit of linear function to the plot in Fig. 11 gives the following equation:

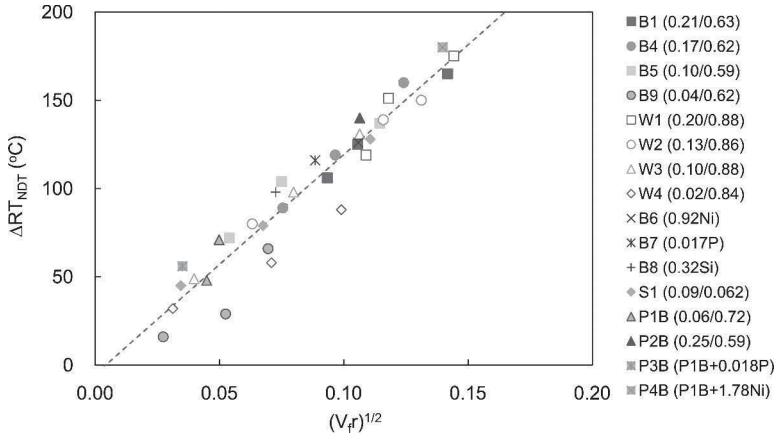


FIG. 12—Correlation between ΔRT_{NDT} and $(V_f)^{1/2}$.

$$\Delta RT_{\text{NDT}} = 1709 \times \sqrt{V_f} - 12.5, \quad R^2 = 0.926 \quad (1)$$

which does not give zero value for the constant term. Of course, since the transition temperature shift should not be necessarily zero when the volume fraction of solute atom clusters is zero, the correlation of Eq 1 is not necessarily irrational, but it will be worth doing further investigation.

As we already saw in the above results, high number densities of second phase features having small diameter and coherent atomic structure are formed in the neutron irradiated RPV steels. In such a case, a model has been proposed that correlates the increase in yield stress with the square root of the volume fraction of second order features multiplied by the radius of the features [12]. So another plot that compares the ΔRT_{NDT} with the square root of the volume fraction of solute atom clusters multiplied by the average Guinier radius of the solute atom clusters is shown in Fig. 12. Again a good linear correlation can be found in the plot, and the linear function fit is given as follows:

$$\Delta RT_{\text{NDT}} = 1244 \times \sqrt{V_f r} - 5.2 \quad R^2 = 0.924 \quad (2)$$

which has better proportionality than Eq 1.

It should be emphasized here again that these two equations work very well for all the materials, in particular P4B. As we saw in Fig. 5, the number density of P4B material was much higher compared with all the other materials. Also in Fig. 6, we saw that the diameter of P4B was the smallest compared with all the other materials. Thus, in a microstructural point of view, the response of P4B, which has much higher Ni content, is very different from those of the other materials. However when we correlate the microstructural changes with mechanical properties, the volume fraction of solute atom clusters describes the behavior of P4B material in the same manner with all the other materials. If we further look at the data point of P4B in Figs. 11 and 12, the data point of P4B in Fig. 12 is located better in the population of the other data points than

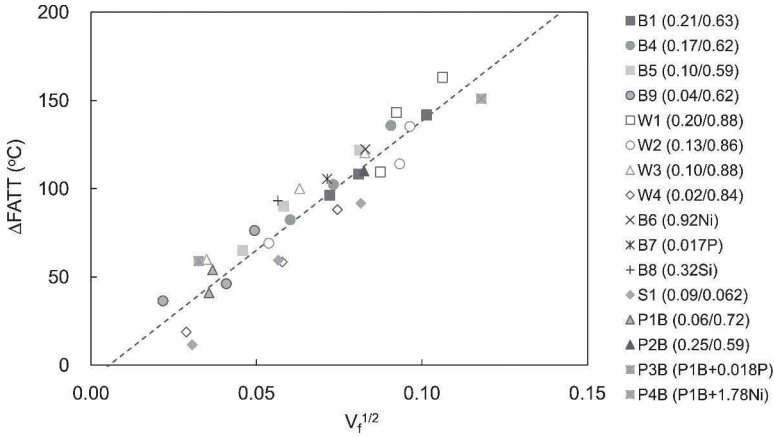


FIG. 13—Correlation between $\Delta FATT$ and $V_f^{1/2}$.

in Fig. 11. So, the above discussion suggests that the index of the square root of the volume fraction of solute atom clusters multiplied by the average Guinier radius is a better one. Nevertheless, as a first order approximation, in particular when the cluster size and number density are expected not to differ very much, the simpler index of the square root of volume fraction can be a good and useful one. It should be also pointed out here that the cluster composition looks to have very small effect on the contribution of solute atom clusters to embrittlement. For example, although we have not discussed the cluster composition in this paper, the Cu contents in the clusters change very much with the bulk Cu contents of the steels, but ΔRT_{NDT} is simply correlated with the volume fraction of the clusters and no consideration of cluster composition looks necessary. This needs further verification.

As we saw above, the index of $\Delta FATT$ can be another index of the embrittlement, in particular for the low upper shelf energy materials. Therefore, we present similar plots to Figs. 11 and 12 by changing the index of vertical axes from ΔRT_{NDT} to $\Delta FATT$ as shown in Figs. 13 and 14. The fitted linear equations are as follows:

$$\Delta FATT = 1464 \times \sqrt{V_f} - 8.0, \quad R^2 = 0.876 \tag{3}$$

$$\Delta FATT = 1073 \times \sqrt{V_f r} - 2.2, \quad R^2 = 0.885 \tag{4}$$

One can see that the fit of Eq 4 has very good proportionality, and again the data point of P4B is well described. Since the above theory using the volume fraction was developed for the estimation of increase in yield stress, it is reasonable to have a better correlation with $\Delta FATT$, which will be more directly connected to the increase in yield stress and will be able to minimize the effect of the low upper shelf energy.

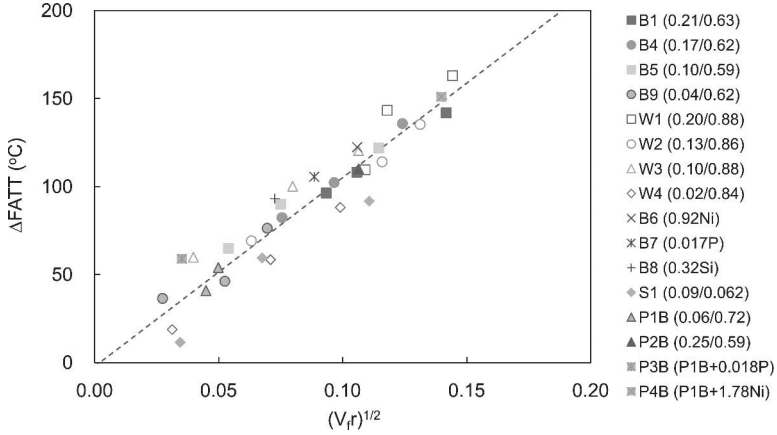


FIG. 14—Correlation between $\Delta FATT$ and $(V_f)^{1/2}$.

Dislocation Loops and Mechanical Properties

The above discussions were focused only on the correlation between the solute atom clusters and the amount of embrittlement. However, as is confirmed in the previous section, dislocation loops are formed in the neutron irradiated RPV steels, and they are highly expected to contribute to the embrittlement. This will be discussed in this section.

We have now information on the dislocation loop characteristics such as number density and size. Based on these data, the Orowan model is often used to estimate the hardening due to dislocation loops. This model tells us that the increase in yield stress, $\Delta\sigma$ (MPa), can be calculated using the number density of dislocation loops, N (m^{-3}), and the average diameter of dislocation loops, d (m), as

$$\Delta\sigma = \alpha \cdot M \cdot \mu \cdot b \cdot \sqrt{N \cdot d} \quad (5)$$

For the RPV steels, parameters for α -iron will not be bad approximations, i.e., $\alpha=0.4$, $M=2$ (bcc), $\mu=80\,000$ (MPa), and $b=0.249 \times 10^{-9}$ (m). $\Delta\sigma$ can be further converted to the transition temperature shift ΔT_{loop} by the following empirical equation:

$$\Delta T_{loop} = 0.65\Delta\sigma \quad (6)$$

The calculated values of ΔT_{loop} for the four materials, B1, S1, B9, and P1B plates, are compared with the ΔRT_{NDT} values of these materials in Fig. 15. In the B9 and P1B plates with low Cu contents, ΔRT_{NDT} and ΔT_{loop} are in almost the same magnitude, while in the Cu containing S1 and B1 plates, contributions of ΔT_{loop} are small. It should be emphasized that the absolute values of the estimated ΔT_{loop} can change due to uncertainties of the parameters used in Eqs 5 and 6. It should be also noted that due to the limitation of the spatial resolution of TEM, dislocation loops with diameters of ~ 1 nm or less cannot be detected even if they exist. Another thing that we like to point out once again

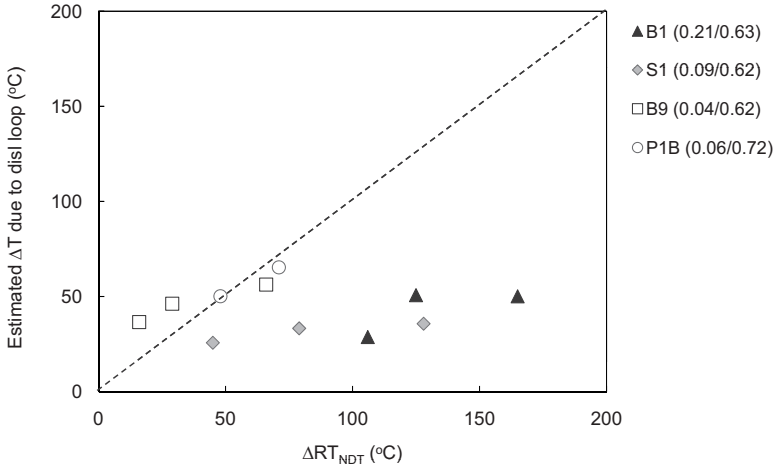


FIG. 15—Contribution of dislocation loops to transition temperature shifts.

here is that, as we see in Fig. 8, some of the dislocation loops are formed preferentially near or along pre-existing dislocation lines. This effect is not taken into consideration in the above estimates of loop contributions.

We now have measured two features, solute atom clusters and dislocation loops, that may contribute to embrittlement. In the system where we have two different obstacles having different contributions to hardening, the total hardening ($\Delta\sigma$) can be written as a square root of the sum of the two contributions, $\Delta\sigma_1$ and $\Delta\sigma_2$, squared (root-sum-square (RSS) model) [13]. The unique characteristic of this model is that the stronger contributor determines the total hardening. For example, if $\Delta\sigma_1=1$ and $\Delta\sigma_2=3$, $\Delta\sigma=(1^2+3^2)^{1/2}=10^{1/2}=3.16$ is very similar to the value of $\Delta\sigma_2$. Therefore, it is reasonable that in the Cu containing materials, where the volume fractions of solute atom clusters are large, the square root of cluster volume fraction is almost proportional to the total hardening, and thus the transition temperature shifts. On the other hand, in such materials as B9 and P1B plates, either of solute atom clusters and dislocation loops looks to describe the total shifts. When the magnitudes of the two contributors are similar, the total amount of transition temperature shift will be about 40 % larger, $(1^2+1^2)^{1/2}=1.4$, than each of the two contributions. However, since the shifts in B9 and P1B are not very large, the magnitude of 40 % difference in total shift is well within the scatter of the data, and thus each one of the two contributions can be close to the total shift. Another point that should be noted here is that the dislocation loops measured by TEM and solute atom clusters measured by 3DAP might be identical in some cases. In fact, large (~several nanometers) dislocation loops decorated by solute atoms are often observed in the 3DAP analyses, and in particular in low Cu materials, it is likely that solute atom clusters are formed by segregation to the point defect clusters. Further study using direct comparisons between the 3DAP and TEM measurements may give some insights.

Summary

Extensive microstructural analyses were performed on the RPV steels irradiated to very high fluences beyond 10^{20} n/cm², $E > 1$ MeV, at high fluxes under the two major projects, PTS and PLIM, in Japan. The steels are plates and weld metals with a wide range of chemical compositions. 3DAP analyses show that solute atom clusters are formed in all the materials analyzed regardless of the Cu impurity contents. Cluster size increases with neutron fluence, while the number density increases with fluence at low fluences, but it tends to saturate at high fluence region. Dislocation loop formation was studied using TEM observation, and we confirmed that dislocation loops are formed in these steels. P segregation on grain boundaries was studied by surface analyses as well as grain boundary chemical analyses. We found that nonhardening type embrittlement due to grain boundary fracture is not a major contributor to the embrittlement in these materials and irradiation conditions.

With respect to the correlation between microstructures and mechanical properties, we found that the volume fraction of solute atom clusters has very good correlation with the change in ΔRT_{NDT} , though the detailed characteristics of clusters such as number density, cluster size, and cluster composition depend on the environmental and metallurgical variables. Contributions of the dislocation loops to the transition temperature shifts estimated by the Orowan model show that dislocation loops may be a major contributor in low Cu materials, but in Cu containing materials the contribution is weak. RSS of the two contributions of solute atom clusters and dislocation loops seems a reasonable model to describe the ΔRT_{NDT} .

References

- [1] Japan Electric Association, "Method of Surveillance Tests for Structural Materials of Nuclear Reactors," *Japan Electric Association Code JEAC 4201-1991*, 1992, Chiyoda-ku, Tokyo, Japan.
- [2] Otaka, M. and Osaki, T., "Reduction of Upper Shelf Energy of Highly Irradiated RPV Steels," *Proceedings of the 30th MPA-Seminar*, Stuttgart, October 6–7, 2004, University of Stuttgart, Germany, 9.1.
- [3] Ishino, S., Kawakami, T., Hidaka, T., and Satoh, M., "The Effect of Chemical Composition on Irradiation Embrittlement," *Nucl. Eng. Des.*, Vol. 119, 1990, pp. 139–148.
- [4] Kelly, T. F. and Larson, D. J., "Local Electrode Atom Probes," *Mater. Charact.*, Vol. 44, 2000, pp. 59–85.
- [5] Miller, M. K., "ATOM PROBE TOMOGRAPHY Analysis at the Atomic Level," *Atom Probe Tomography*, Kluwer Academic/Plenum Publishers, New York, 2000.
- [6] Hyde, J. M. and English, C. A., "An Analysis of the Structure of Irradiation Induced Cu-Enriched Clusters in Low and High Nickel Welds," *MRS 2000 Fall Proceedings, Volume 650, Microstructural Processes in Irradiated Materials*, 2001, G. E. Lucas, L. Snead, M. A. J. Kirk, and R. G. Elliman, Eds., Materials Research Society, Warrendale, PA, R6.6.
- [7] Kirkegaard, P., Eldrup, M., Mogensen, O. E., and Pedersen, N. J., "Program System for Analyzing Positron Lifetime Spectra and Angular Correlation Curves," *Comput.*

Phys. Commun., Vol. 23, 1981, pp. 307–335.

- [8] Hawthorne, J. R., “Significance of Nickel and Copper Content to Radiation Sensitivity and Postirradiation Heat Treatment Recovery of Reactor Vessel Steels,” *ASTM Spec. Tech. Publ.*, Vol. 782, 1982, pp. 375–391.
- [9] Miller, M. K. and Burke, M. G., “Fine-Scale Microstructural Characterization of Pressure Vessel Steels and Related Materials Using APFIM,” *ASTM Spec. Tech. Publ.*, Vol. 1046, 1990, pp. 107–126.
- [10] Auger, P., Pareige, P., Akamatsu, M., and Blavette, D., “APFIM Investigation of Clustering in Neutron-Irradiated Fe-Cu Alloys and Pressure Vessel Steels,” *J. Nucl. Mater.*, Vol. 225, 1995, pp. 225–230.
- [11] Carter, R. G., Soneda, N., Dohi, K., Hyde, J. M., English, C. A., and Server, W. L., “Microstructural Characterization of Irradiated-Induced Cu-Enriched Clusters in Reactor Pressure Vessel Steels,” *J. Nucl. Mater.*, Vol. 298, 2001, pp. 211–224.
- [12] Gerold, V. and Haberkorn, H., “On the Critical Resolved Shear Stress of Solid Solutions Containing Coherent Precipitates,” *Phys. Status Solidi*, Vol. 16, 1966, pp. 675–684.
- [13] Foreman, A. J. E. and Makin, J. J., “Dislocation Movement Through Random Arrays of Obstacles,” *Can. J. Phys.*, Vol. 45, 1967, pp. 511–517.

Yutaka Nishiyama,¹ Masatake Yamaguchi,² Kunio Onizawa,¹
Akihiko Iwase,³ and Hiroshi Matsuzawa⁴

Irradiation-Induced Grain-Boundary Solute Segregation and Its Effect on Ductile-to-Brittle Transition Temperature in Reactor Pressure Vessel Steels

ABSTRACT: A study on grain-boundary segregation and embrittlement in terms of the Charpy ductile-to-brittle transition temperature (DBTT) has been performed for the neutron-irradiated A533B steels with typical contents of impurities of Japanese reactor pressure vessel ones. The neutron irradiation was conducted at 563 K to a fluence of $1.3 \times 10^{24} \text{ n/m}^2$ ($E > 1 \text{ MeV}$) using material testing reactors. The neutron irradiation induced the P and Ni segregation and the reduction in C in some cases at grain-boundaries. The increase in the P segregation at high fluence ($> 5 \times 10^{23} \text{ n/m}^2$, $E > 1 \text{ MeV}$) was less than 0.1 in monolayer coverage for the steels with the bulk content of P not exceeding 0.02 wt%. The hardening more strongly affected the DBTT shift than the P segregation for those steels. The reduction in segregated C that enhances the grain-boundary cohesion by neutron fluence is not large enough to cause the DBTT shift.

Manuscript received June 24, 2008; accepted for publication June 2, 2009; published online July 2009.

¹ Nuclear Safety Research Center, Japan Atomic Energy Agency, Shirakata-shirane 2-4, Tokai-mura, Ibaraki-ken 319-1195, Japan.

² Center for Computational Science and e-Systems, Japan Atomic Energy Agency, Shirakata-shirane 2-4, Tokai-mura, Ibaraki-ken 319-1195, Japan.

³ Dept. of Materials Science, Osaka Prefecture Univ., Gakuen-cho 1-1, Naka-ku, Sakai-shi, Osaka 599-8531, Japan.

⁴ Japan Nuclear Energy Safety Organization, 3-17-1, Toranomon-3 chyome, Minato-ku, Tokyo 105-0001, Japan.

Cite as: Nishiyama, Y., Yamaguchi, M., Onizawa, K., Iwase, A. and Matsuzawa, H., "Irradiation-Induced Grain-Boundary Solute Segregation and Its Effect on Ductile-to-Brittle Transition Temperature in Reactor Pressure Vessel Steels," *J. ASTM Intl.*, Vol. 6, No. 7. doi:10.1520/JAI101959.

Copyright © 2009 by ASTM International, 100 Barr Harbor Drive, PO Box C700, West Conshohocken, PA 19428-2959.

KEYWORDS: reactor pressure vessel, phosphorus segregation, carbon segregation, grain-boundary, neutron irradiation, embrittlement, ductile-to-brittle transition temperature (DBTT), intergranular fracture

Introduction

More than ten light water reactors (LWRs) in Japan that began to operate in the 1970s have reached over a 30-year operation. In order to ensure the integrity of aging LWRs, it is of great importance to gain a fundamental understanding of the degradation mechanism of reactor pressure vessel (RPV) A533B steels exposed to high neutron fluence and to re-evaluate an embrittlement correlation with the recent surveillance and accelerated irradiation data. A new embrittlement method has been developed for the Japanese RPV steels [1], where the cause of embrittlement is irradiation-hardening due to formation of solute-rich clusters and matrix damage in the grain matrix. One of the other possible degradation mechanisms of A533B steels neutron-irradiated at high fluence ($>5 \times 10^{23}$ n/m², $E > 1$ MeV) is intergranular embrittlement due to irradiation-induced grain-boundary segregation of impurity, commonly P. It is well known that the increase in P concentration at grain-boundaries is linearly correlated with the shift in Charpy ductile-to-brittle transition temperature (DBTT) associated with increased fraction of intergranular fracture for unirradiated steels [2]. In order to estimate when the intergranular embrittlement occurs for a long-term service of RPV, data and analysis are necessary on a dependence of P segregation on neutron fluence and the combined effect of grain-boundary P segregation and irradiation-hardening on the embrittlement [3].

In previous studies [4,5], the grain-boundary P segregation and irradiation-hardening in P-doped A533B steels irradiated mostly up to neutron fluence of 6.9×10^{23} n/m² ($E > 1$ MeV) at 563 K using material testing reactors (MTRs) were examined by a scanning Auger microprobe (SAM), a local electrode atom probe, and positron annihilation spectroscopy. The neutron irradiation facilitated the grain-boundary P segregation. The content of bulk P significantly affected irradiation-hardening due to distinct formation of P-rich precipitates or clusters stabilized by vacancies as well as the P segregation. Analyzing the correlations between the P segregation, hardening, fraction of intergranular fracture, and DBTT, it was found neutron irradiation mitigates an embrittling effect of segregated P. The Master Curve approach has been applied to study the effect of mixed cleavage/intergranular modes on the fracture toughness scatter for those irradiated P-doped A533B steels.

The present study is conducted to investigate the grain-boundary solute segregation and how the segregation and irradiation-hardening affect the embrittlement in terms of DBTT for A533 steels with typical contents of impurities in Japanese RPV ones neutron-irradiated at higher fluence than the previous study. The likelihood of intergranular embrittlement is discussed in these results.

TABLE 1—Chemical compositions (wt%) of A533B steels.

Designation	C	Si	Mn	P	S	Cu	Ni	Cr	Mo
P3B	0.19	0.22	1.44	0.018	0.006	0.06	0.57	...	0.47
B7	0.24	0.14	1.53	0.017	0.024	0.10	0.63	0.13	0.51
B5	0.24	0.14	1.52	0.009	0.020	0.10	0.59	0.13	0.51
P1B	...	0.21	...	0.008	...	0.06	0.58
PH ^a	0.18	0.25	1.47	0.057	0.009	0.12	0.65	0.13	0.51
PM ^a	0.18	0.25	1.45	0.026	0.009	0.12	0.65	0.16	0.51
PL ^a	0.18	0.22	1.41	0.013	0.003	0.01	0.65	0.16	0.51
JRQ ^b	0.18	0.24	1.42	0.017	0.004	0.14	0.84	0.12	0.51
PA ^c	0.28	0.22	1.26	0.017	0.019	0.09	0.57	0.08	0.51
PB ^c	0.26	0.25	1.49	0.013	0.011	0.17	0.54	0.09	0.49

^aReference 4.^bReference 5.^cReference 6.

Experimental Procedure

The materials used in the present study were four kinds of A533B steels commercially manufactured (designated as P3B, B7, B5, and P1B). The published data of the A533B steels [4,5] were used for a comparison. The chemical compositions of these steels are listed in Table 1.

The steels were neutron-irradiated at 563 K in a range of the neutron fluence from 3.1×10^{23} to 1.3×10^{24} n/m² ($E > 1$ MeV) using the Japan Materials Testing Reactor or Halden Reactor. The neutron fluence values of the SAM specimens are listed in Table 2.

The SAM analyses were performed to examine grain-boundary segregation for elements of interest: mainly P, C, S, Mo, Ni, and Fe. Notched plate specimens for the SAM analyses were machined from irradiated broken Charpy-V notch (CVN) ones. The SAM specimens at temperatures below 123 K were

TABLE 2—Neutron fluence for the samples of SAM analysis.

Steels	Neutron Fluence (n/m ² , $E > 1$ MeV) at 563 K
P3B	5.4×10^{23}
B7	8.6×10^{23}
B5	3.1×10^{23}
P1B	6.7×10^{23}
PH, PM, PL ^a	2.5×10^{23}
JRQ ^b	2.3×10^{23}
PA ^c	3.4×10^{23}
	3.1×10^{23}

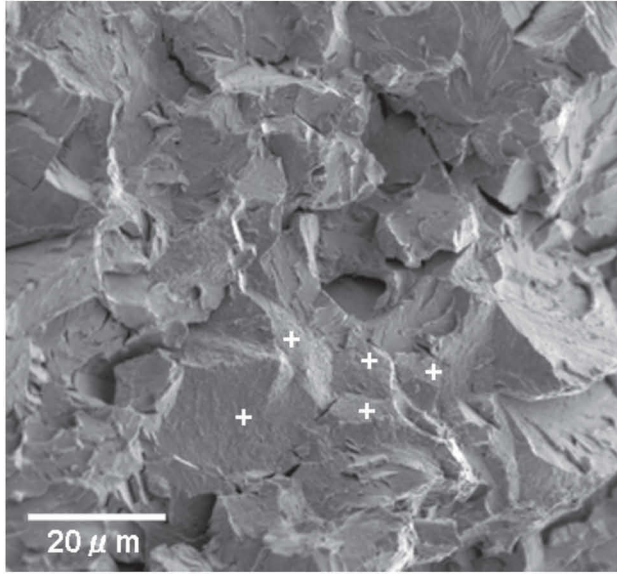
^aReference 4.^bReference 5.^cReference 6.

fractured by impact-loading in an ultra-high vacuum chamber with a pressure of $3-5 \times 10^{-8}$ Pa. The intergranular facets were identified using secondary electron images at a magnification of $\times 1000$ on fracture surfaces and analyzed with a 5 kV accelerating voltage and 100 nA beam current. The data survey was first made to identify the Auger signal and then the peak height ratio (PHR) of the first derivative Auger signals of individual elements to the Fe peak (703 eV) were measured by setting a window in a specific energy range for elements of interest [7]. The concentration of grain-boundary segregated element expressed as a monolayer coverage, where the monolayer coverage is the fraction of grain-boundary-sites occupied by the segregant, was estimated from the measured PHR based on a correction factor listed in Refs 7 and 8.

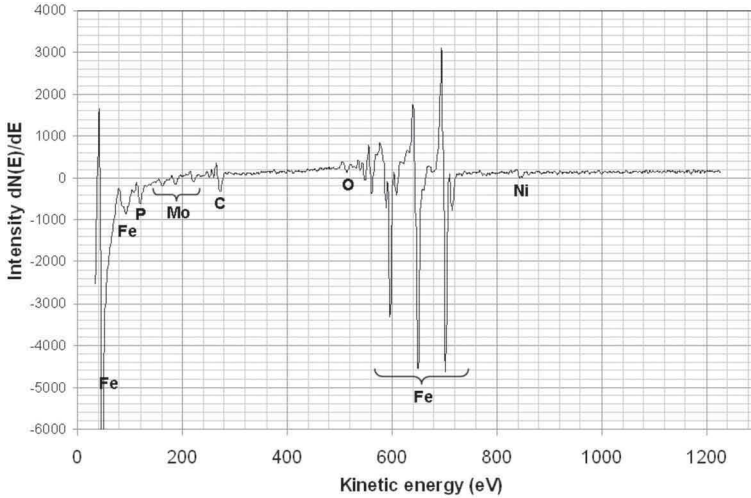
Results and Discussion

A scanning electron micrograph (SEM) of mixed intergranular/cleavage fracture surface and a typical differential Auger spectrum on an intergranular facet are shown in Fig. 1 for the P1B steel irradiated to 1.3×10^{24} n/m². Intergranular fracture is distinguished as the presence of tiny particles of grain-boundary carbides from the cleavage one. Grain-boundary enrichments of P, C, Mo, and Ni were clearly detected only on intergranular facets in both the unirradiated and irradiated steels. The Cu peak was occasionally identified on intergranular fracture surfaces. The neutron irradiation gave rise to no enrichment of other elements.

The dependence of the P segregation in monolayer coverage at grain-boundaries on the neutron fluence is shown in Fig. 2. The higher P segregation is recognized for the unirradiated steel with higher bulk content of P. The initial P segregation is determined by the conditions of post-weld heat treatment and subsequent cooling during material fabrication according to McLean's thermal equilibrium and kinetic theory [9], where the equilibrium solute segregation increases with increasing bulk solute content and decreasing temperature, and the segregation rate is controlled by solute/vacancy exchange diffusion. The P segregation is increased by irradiation for all steels. The increase in the P segregation seems to be saturated at high fluence, as seen for the P1B steel. To demonstrate clearly the effects of the bulk P content and neutron irradiation on the P segregation, the increase in the P segregation (ΔC_p^{gb}) in monolayer coverage of unirradiated and irradiated steels is plotted against the square root of the bulk P content in atomic percentage (C_p^b), together with the published data [3-6] in Fig. 3. The ΔC_p^{gb} is enhanced with increasing neutron fluence and raising $(C_p^b)^{1/2}$. It is again seen that the increase in the P segregation seems to be saturated for the steels with the bulk P content not exceeding the commercial Japanese RPV range of ~ 0.02 wt% neutron-irradiated to a fluence larger than 1×10^{24} n/m². From a post-irradiation annealing (PIA) study in various P-doped Fe alloys [10], the rate of P segregation was found to be greatly enhanced at lower PIA temperatures below 673 K. A very low activation energy estimated for the rapid P diffusion gives a clear indication that the migration of P-interstitial complexes controls the kinetics of P segregation.



(a)



(b)

FIG. 1—(a) Typical example of fracture surface observed for the PIB steel irradiated to 1.3×10^{24} n/m² ($E > 1$ MeV). Intergranular facets (+) are distinguished with tiny grain-boundary carbides from cleavage ones. (b) A differential Auger spectrum obtained on an intergranular facet.

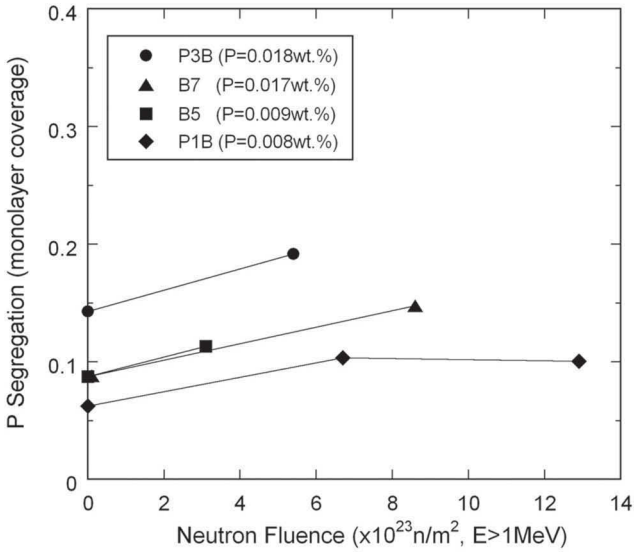


FIG. 2—Variation in grain-boundary P segregation to neutron fluence for the steels.

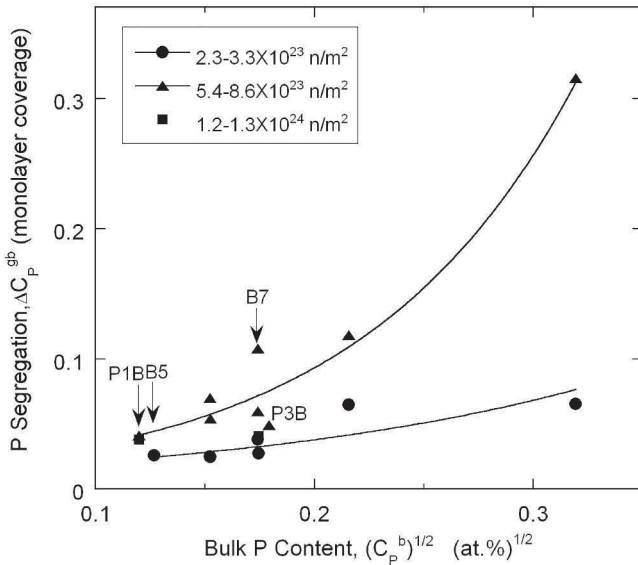


FIG. 3—Increase in grain-boundary P segregation by neutron irradiation (ΔC_p^{gb}) to square root of bulk P content $(C_p^b)^{1/2}$.

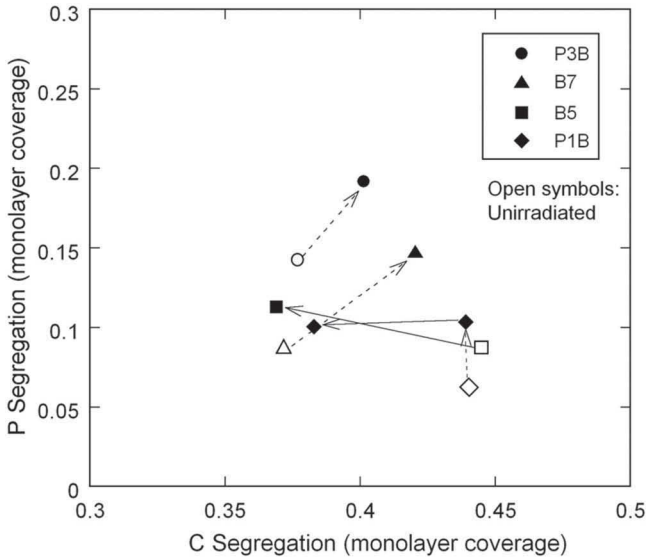


FIG. 4—Correlation between grain-boundary P and C segregation in the unirradiated and irradiated steels.

P and C that enhance the grain-boundary cohesion are known to segregate competitively to grain-boundaries during thermal aging and neutron irradiation [10]. The relationship between the grain-boundary segregated P and C is shown in Fig. 4 for the unirradiated and irradiated steels. In the previous results [5], there exist two data groups depending on the amount of grain-boundary segregated P in the same plot as Fig. 4. The segregated P and C are inversely correlated with each other for the steels with relatively high P segregation in the unirradiated condition, but the irradiation does not affect the C segregation in this group. In the steels with low P segregation, smaller C segregation was observed after neutron irradiation. The present result also suggests that the behavior of C is variable, although there is a tendency of the reduction in C segregation due to the neutron irradiation with lower initial P segregation.

For other segregated elements at grain-boundaries, Mo was almost unchanged by the irradiation. This implies that the Auger signal of Mo arises mainly from grain-boundary carbides. The dependence of segregated Ni at grain-boundaries on the neutron fluence is shown in Fig. 5. The Ni segregation increases with neutron fluence, similar to the P segregation. However, a tensile test simulation by first-principles calculations in a realistic situation using bcc Fe $\Sigma 3(111)[\bar{1}\bar{1}0]$ symmetrical tilt grain-boundary [11] has shown that the reduction in grain-boundary cohesive strength due to Ni at grain-boundaries is weak, unlike P and S [12].

The effect of irradiation-hardening in terms of the increase in the yield strength at room temperature ($\Delta\sigma_y$) on the shift in DBTT at Charpy 41J energy level (ΔT_{41J}) for the steels with different increases in irradiation-induced P seg-

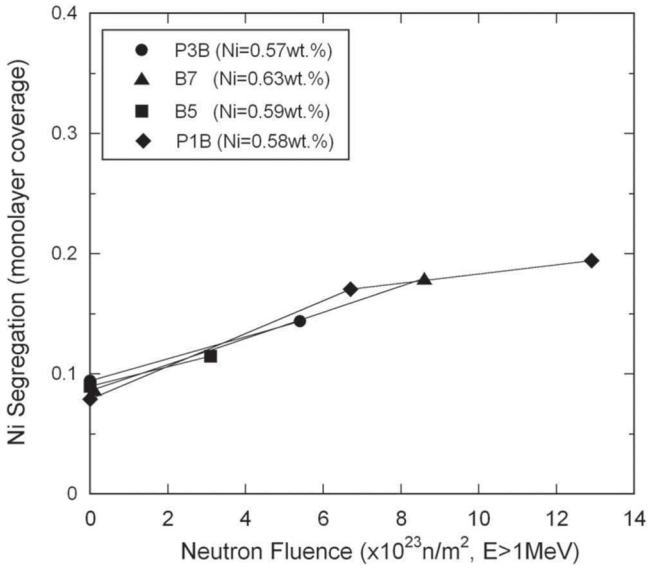


FIG. 5—Variation in grain-boundary Ni segregation to neutron fluence for the steels.

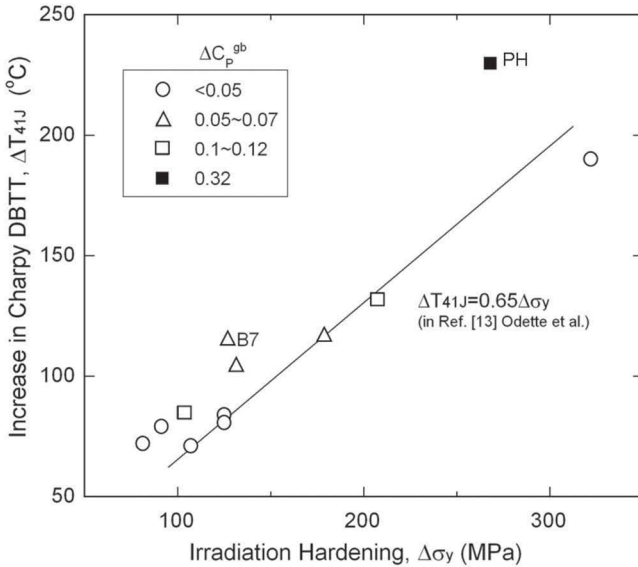


FIG. 6—Effects of irradiation-hardening in terms and increase in yield strength ($\Delta\sigma_y$) on the shifts in Charpy 41J DBTT (ΔT_{41J}) for the irradiated steels.

regation ($\Delta C_{\text{P}}^{\text{gb}}$) is shown in Fig. 6, together with the published data. Irradiation embrittlement in terms of $\Delta T_{41\text{J}}$ is often related to the irradiation-hardening ($\Delta\sigma_y$) by

$$\Delta T_{41\text{J}} = k \times \Delta\sigma_y, \quad (1)$$

where a typical value of parameter k is $0.65^\circ\text{C}/\text{MPa}$ for RPV steels [13]. This linear relation with $k=0.65$ is superimposed in the figure. When the intergranular embrittlement occurs due to the increase in P segregation induced by neutron irradiation, k becomes higher than the above value. This should be accompanied by the increase in intergranular fracture [4,5]. The B7 steel irradiated to $8.6 \times 10^{23} \text{ n/m}^2$ seems to have a higher value of k . However, the SEM observation revealed no intergranular fracture affecting the DBTT and no increase in intergranular fracture due to neutron irradiation. Only isolated intergranular fracture among the cleavage one was observed in the fracture surface of the CVN specimen fractured in the lower shelf region of the irradiated B7 steel. Additionally, it is pointed out that the reduction in grain-boundary segregated C caused by neutron irradiation as shown in Fig. 4 is not large enough to cause the DBTT shift for A533B steels unlike Fe-P-C model alloys [10,14]. On the other hand, the PH steel (■) with the highest increase in P segregation irradiated to $6.9 \times 10^{23} \text{ n/m}^2$ [5] clearly exhibits a higher value of k with an increase in the fraction of intergranular fracture of about 20 %. These indicate that if $\Delta C_{\text{P}}^{\text{gb}}$ is less than 0.12 in monolayer coverage, the irradiation-induced P segregation has little effect on the DBTT shift due to irradiation-hardening embrittlement. This is supported by the SEM observations where the fraction of intergranular fracture was almost not affected by the irradiation for other steels except for the PH steel with the highest increase in P segregation.

The likelihood of intergranular embrittlement in the irradiated RPV steels is considered. In Fig. 2, $\Delta C_{\text{P}}^{\text{gb}}$ due to neutron irradiation is less than 0.1 even at high fluence for the steels with the bulk P content not exceeding the commercial Japanese RPV range of $\sim 0.02 \text{ wt}\%$. Intergranular embrittlement would hardly occur even at high fluence as long as the flux effect on the P segregation is insignificant. However, the data in the present study were obtained by accelerated irradiation using MTRs. Data on this flux effect are very limited. A comparison of the grain-boundary P segregation by a pressurized-water reactor (PWR) surveillance and MTR irradiation to $6 \times 10^{23} \text{ n/m}^2$ has exhibited the similar magnitude of irradiation-induced P segregation [6]. Further data on surveillance samples and model predictions are crucial to examine the possibility of intergranular embrittlement.

Conclusion

The scanning Auger analysis was performed on the intergranular facets on the A533B steels irradiated to $1.3 \times 10^{24} \text{ n/m}^2$ ($E > 1 \text{ MeV}$) at 563 K using MTRs to examine the change in the concentration segregated elements due to the irradiation. The effect of irradiation-induced P segregation and hardening on the embrittlement in terms of Charpy DBTT shifts was evaluated. Results obtained in the present study are as follows:

- (1) Grain-boundary enrichment of several elements, P, C, Mo, and Ni was identified on the intergranular facets for both unirradiated and irradiated A533B steels. The neutron irradiation induced grain-boundary P and Ni segregation. The behavior of C was variable; there is a tendency of the reduction in C segregation due to the neutron irradiation with lower initial P segregation. The high neutron irradiation did not bring about grain-boundary segregation of other elements.
- (2) The dependence of P segregation on bulk P contents and neutron fluence was comprehensively determined by the present and published data. The P segregation was facilitated with bulk content of P and neutron fluence. The increase in the P segregation due to high fluence ($>5 \times 10^{23}$ n/m², $E > 1$ MeV) was less than 0.12 in monolayer coverage for the steels with the bulk content of P not exceeding the commercial Japanese RPV range of 0.02 wt%. The hardening more strongly affected the DBTT shift than the P segregation for those irradiated steels.
- (3) The likelihood of intergranular embrittlement appeared to be a little even at high fluence as far as the flux effect on the P segregation is insignificant. The importance of the data on surveillance samples was emphasized to further examine the possibility of intergranular embrittlement.

Acknowledgments

This work was carried out under a contract between the Japan Nuclear Energy Safety Organization and the Japan Atomic Energy Agency. The authors thank Mr. J. Sekino for assistance in experiment and manuscript preparation.

References

- [1] Hiranuma, H., Soneda, N., Dohi, K., Ishino, S., Dohi, N., and Ohara, H., "Mechanistic Modeling of Transition Temperature Shift of Japanese RPV Materials," *Proceedings of the 30th MPA-Seminar in Conjunction with the Ninth German-Japanese Seminar*, Stuttgart, Germany, October 2004, Stuttgart Univ., Germany, pp. 3.1–3.20.
- [2] Kimura, A., Shibata, M., Kasada, R., Hakata, H., Fujii, K., and Fukuya, K., "Grain Boundary Phosphorus Segregation and Its Influence on the Ductile Brittle Transition Temperature in Reactor Pressure Vessel Steels," *Effects of Radiation on Materials: 21st International Symposium, ASTM STP 1447*, M. L. Grossbeck, T. R. Allen, R. G. Lott, and A. S. Kumar, Eds., ASTM International, West Conshohocken, PA, 2004, pp. 565–578.
- [3] English, C. A., Ortner, S. R., Gage, G., Server, W. L., and Rosinski, S. T., "Review on Phosphorus Segregation and Intergranular Embrittlement in Reactor Pressure Vessel Steels," *Effects of Radiation on Materials: 20th International Symposium, ASTM STP 1405*, S. T. Rosinski, M. L. Grossbeck, T. R. Allen, and A. S. Kumar, Eds., ASTM International, West Conshohocken, PA, 2001, pp. 151–173.
- [4] Nishiyama, Y., Onizawa, K., and Suzuki, M., "Phosphorus Segregation and Inter-

- granular Embrittlement in Thermally Aged and Neutron Irradiated Reactor Pressure Vessel Steels," *J. ASTM Int.*, Vol. 4, No. 8, 2007, paper ID JAI100690.
- [5] Nishiyama, Y., Onizawa, K., Suzuki, M., Anderegg, J. W., Nagai, Y., Toyama, T., Hasegawa, M., and Kameda, J., "Effects of Neutron-Irradiation Induced Intergranular Phosphorus Segregation and Hardening on Embrittlement in Reactor Pressure Vessel Steels," *Acta Mater.*, Vol. 56, 2008, pp. 4510–4521.
- [6] Fukuya, K., Ohno, K., and Nakata, H., "Microstructural Evolution in Reactor Vessel Steels Under Neutron Irradiation," *Monograph No. 1 Institute of Nuclear Safety System*, Institute of Nuclear Safety System, Fukui, Japan, November, 2001.
- [7] Kameda, J. and Bevolo, A. J., "Neutron Irradiation-Induced Intergranular Solute Segregation in Iron Base Alloys," *Acta Metall.*, Vol. 37, No. 12, 1989, pp. 3283–3296.
- [8] Briggs, D. and Seah, M. P., *Practical Surface Analysis*, 2nd ed., John Wiley & Sons, Ltd, U.K., 1990.
- [9] McLean, D., *Grain Boundaries in Metals*, Clarendon Press, Oxford, U.K., 1957.
- [10] Kameda, J., Nishiyama, Y., and Bloomer, T. E., "Non-Equilibrium Intergranular Segregation and Embrittlement in Neutron-Irradiated Ferritic Alloys," *Surf. Interface Anal.*, Vol. 31, 2001, pp. 522–531.
- [11] Yamaguchi, M., Nishiyama, Y., and Kaburaki, H., "Decohesion of Iron Grain Boundary by Sulfur or Phosphorus Segregation: First-Principles Calculation," *Phys. Rev. B*, Vol. 76, 2007, pp. 035418.
- [12] Yamaguchi, M. (unpublished).
- [13] Odette, G. R., Lomborzo, P. M., and Wullaert, R. A., "Relationship Between Irradiation Hardening and Embrittlement of Pressure Vessel Steels," *Effects of Radiation on Materials: 12th International Symposium, ASTM STP 870*, F. A. Garner and J. S. Perrin, Eds., ASTM International, West Conshohocken, PA, 1985, pp. 840–860.
- [14] Jones, R. B., Cowan, J. R., Corcoran, R. C., and Walmsley, C. "Embrittlement, Hardening, and Grain Boundary Composition in an Fe-P-C alloy after Irradiation or Thermal Aging," *Effects of Radiation on Materials: 19th International Symposium, ASTM STP 1366*, M. L. Hamilton, A. S. Kumar, S. T. Rosinski, and M. L. Grossbeck, Eds., ASTM International, West Conshohocken, PA, 2000, pp. 473–491.

J. H. Lee,¹ R. Kasada,¹ H. S. Cho,¹ and A. Kimura¹

Irradiation-Induced Hardening and Embrittlement of High-Cr ODS Ferritic Steels

ABSTRACT: The dependence of irradiation temperature, neutron dose, and Cr content on irradiation hardening and embrittlement has been investigated for oxide dispersion strengthened (ODS) ferritic steels irradiated from 290 to 600°C up to the maximum neutron dose of 0.75 dpa. Irradiation hardening and embrittlement of the materials strongly depend on the irradiation temperature. While neutron dose increases from 0.01 to 0.21 dpa, the ODS steels with Al show a saturation of irradiation hardening but the no-Al ODS steel has an increase in the hardening. The higher the Cr content, the more significant the irradiation hardening and embrittlement of ODS steels irradiated below 420°C. Interestingly, the ODS ferritic steels exposed to neutrons show little change of tensile elongation, compared to 9Cr JLF-1. Furthermore the ductile-brittle transition temperature (DBTT) shift of ODS steels increases with the increasing irradiation hardening, indicating that the increase of yield strength due to radiation induced hardening increases the DBTT and thus a reduction of hardening is effective to reduce the DBTT shift.

KEYWORDS: oxide dispersion strengthened steel, neutron irradiation, irradiation hardening, irradiation embrittlement, Cr content, irradiation temperature

Introduction

In order to realize a high burn-up operation of supercritical water-cooled reactor (SCWR), sodium-cooled fast reactor (SFR), and lead bismuth-cooled fast reactor, which have been considered as a thermal and fast reactors in generation IV nuclear energy systems, respectively, candidate cladding materials must have good corrosion resistance and mechanical properties at elevated tempera-

Manuscript received June 18, 2008; accepted for publication June 8, 2009; published online July 2009.

¹ Institute of Advanced Energy, Kyoto Univ., Uji, Kyoto 611-0011, Japan.

Cite as: Lee, J. H., Kasada, R., Cho, H. S. and Kimura, A., "Irradiation-Induced Hardening and Embrittlement of High-Cr ODS Ferritic Steels," *J. ASTM Intl.*, Vol. 6, No. 8. doi:10.1520/JAI101952.

Copyright © 2009 by ASTM International, 100 Barr Harbor Drive, PO Box C700, West Conshohocken, PA 19428-2959.

TABLE 1—Chemical compositions of ODS ferritic steels and JLF-1 used in this study (in wt. %).

Materials	Chemical Composition (wt. %)											
	C	Si	Mn	Cr	Al	W	Ti	N	V	Ta	Y	Y ₂ O ₃
19Cr(K1)	0.05	0.041	0.06	18.37	<0.01	0.29	0.28	0.014	0.29	0.368
14Cr-4Al(K2)	0.04	0.033	0.06	13.64	4.12	1.65	0.28	0.009	0.30	0.381
16Cr-4Al(K3)	0.08	0.033	0.06	16.00	4.59	1.82	0.28	0.006	0.29	0.368
19Cr-4Al(K4)	0.09	0.039	0.06	18.85	4.61	1.83	0.28	0.005	0.29	0.368
22Cr-4Al(K5)	0.10	0.039	0.07	22.05	4.55	1.80	0.27	0.005	0.28	0.356
JLF-1	0.10	0.05	0.45	8.85	...	1.99	...	0.023	0.20	0.08

tures. Also, high resistance to neutron irradiation embrittlement of the claddings has been certainly required to increase an acceptability of the advanced fission reactors.

Oxide dispersion strengthened (ODS) ferritic/martensitic steels containing 9–12 wt. % chromium (Cr) have been developed for the fuel cladding material of SFR, not only because of their sufficiently high creep strength at elevated temperature, but also because they are resistant to neutron irradiation embrittlement [1–3]. However, corrosion resistance of ODS ferritic/martensitic steels is insufficient to be used as the structural materials of the fast breeder reactors and SCWR [4]. Thus, to improve the corrosion resistance at high temperatures, ODS ferritic steels with high-Cr content have been developed at Kyoto University. It was confirmed that the ODS ferritic steels with 14–22 wt. % Cr are very effective in suppressing corrosion in SCW and also have excellent mechanical properties at elevated temperatures due to the dispersion of nano-scale oxides and the very small grains [5–7]. Generally, after neutron irradiation, high-Cr content in ferritic steels leads to remarkable irradiation-induced hardening and ductility loss. However, high-Cr ODS ferritic steels showed substantial irradiation hardening accompanied by almost no loss of tensile elongation even after the irradiations at doses ranging from 0.01 to 0.75 dpa [8].

In this study, to clarify the susceptibility of high-Cr ODS steels to irradiation induced degradation, the effects of neutron dose, irradiation temperature, and Cr content on irradiation hardening and embrittlement have been investigated for several ODS ferritic steels.

Experimental

To fabricate the high-Cr ODS ferritic steels, the elemental powders were first mechanically alloyed using a high-energy ball mill with pre-alloyed Y₂O₃ powder. The mechanically alloyed powders were canned, degassed, and extruded at 1150°C to make cylindrical rods. Finally a homogenization heat treatment was performed at 1050°C for 1 h. The details about the fabrication process of ODS steels are given in Refs 9 and 10. Table 1 shows the chemical compositions of high-Cr ODS ferritic steels prepared from the manufacturing process and a reduced-activation ferritic steel, JLF-1, developed as a fusion blanket structural

material [11,12] that was selected as a reference material to the ODS ferritic steels in this experiment.

All the specimens were irradiated in the Japan Materials Testing Reactor (JMTR). As shown in Table 2, the neutron irradiations were performed at six different temperatures for several dose levels with a maximum neutron fluence of $5 \times 10^{20} \text{ n/cm}^2$ ($E > 1 \text{ MeV}$).

Tensile tests were carried out for the SS-J type miniaturized specimens of $5 \times 1.2 \times 0.25 \text{ mm}^3$, at a strain rate of $6.7 \times 10^{-4} \text{ s}^{-1}$ at room temperature. Yield strength and total elongation were determined from the recorded stress-strain curves. Charpy impact tests were performed at temperatures from -190 to 57°C with an impact velocity of 5.0 m/s . The sub-sized Charpy V-notched specimens have the following dimensions: Length=20 mm, thickness =1.5 mm, width=1.5 mm, and notch depth=0.3 mm (Fig. 1). The lower shelf energy (LSE), the upper shelf energy (USE), and the ductile-brittle transition temperature (DBTT) were calculated from transition curves obtained by fitting a hyperbolic function [Eq 1] to the data,

$$E_a = \frac{\text{USE} + \text{LSE}}{2} + \frac{\text{USE} - \text{LSE}}{2} \times \tanh\left(\frac{T - \text{DBTT}}{0.5TZW}\right) \quad (1)$$

where:

E_a = the absorbed energy,

T = the test temperature ($^\circ\text{C}$), and

TZW = the width of the temperature of ductile to brittle transition area.

Note that the tensile and Charpy impact tests were conducted in a longitudinal direction, which is parallel to the extrusion direction. Schematic drawing of the tensile and Charpy specimens showing their orientations in terms of extrusion direction is given in Fig. 1.

Results and Discussion

Irradiation Hardening

The tensile stress-strain curves of irradiated and unirradiated 16Cr4Al-ODS steel and 9Cr JLF-1 are shown in Fig. 2. In comparison to the unirradiated JLF-1, the unirradiated ODS ferritic steel has about two times higher yield strength and lower total strain. After neutron irradiation, a typical increase in yield strength and a loss of ductility are observed for 9Cr JLF-1. However, compared to JLF-1, the 16Cr4Al-ODS steel shows a little loss of ductility and a substantial irradiation hardening which tends to depend on the irradiation temperature.

The dependence of neutron dose and irradiation temperature on irradiation hardening of ODS ferritic steels is given in Fig. 3. While neutron dose increases from 0.01 to 0.21 dpa, the 19Cr-ODS steel without Al has an increase in irradiation hardening but other ODS steels with Al show a saturation of the hardening. For ODS ferritic steels irradiated to around 0.25 dpa, the increase in yield strength decreases with the increased irradiation temperature, indicating that the irradiation hardening of ODS steels is influenced by the irradiation

TABLE 2—Irradiation conditions of the JMTR ($E > 1$ MeV).

Capsule ID	Irradiation Temperature, (°C)	Irradiation Time, (h)	Irradiation Dose, (10^{20} n/cm ²) [dpa]
04M-16U	290	1403	0.09 [0.01]
05M-17U	300	2632	1.40 [0.21]
03M-69U	400	2709	2.00 [0.30]
05M-17U	420	2632	3.86 [0.58]
05M-17U	550	2632	4.94 [0.74]
03M-69U	600	2709	5.00 [0.75]

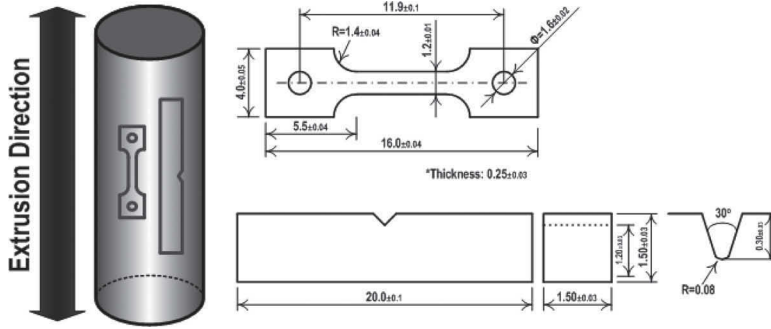


FIG. 1—The schematic drawing of the tensile and Charpy impact specimens showing their orientations in terms of extrusion direction.

temperature. Note that the ODS ferritic steels irradiated at 600°C have almost no hardening. It is suggested that irradiation damage structures created by neutrons in the ODS steels may be recovered after irradiation at 600°C.

The effect of Cr content on neutron irradiation hardening of ODS ferritic steels is shown in Fig. 4. It is interesting to note that the higher the Cr content, the more outstanding the irradiation hardening of ODS steels irradiated below 400°C. In our previous research [8], neutron irradiation characteristics of ODS ferritic steels irradiated at 290, 400, and 600°C were evaluated using the tensile experiment. The results revealed that the irradiation hardening of ODS steels irradiated at 290 and 400°C is probably due to formations of dislocation loops and Cr-rich phases, respectively. Although the transmission electron microscopy observations of the specimens irradiated at 300 and 600°C have not been completed, the irradiation hardening at 300°C is considered to also be because of the formation of dislocation loops. Note that the irradiation hardening of 19Cr4Al-ODS steels is significantly larger than that of 19Cr-ODS steels without

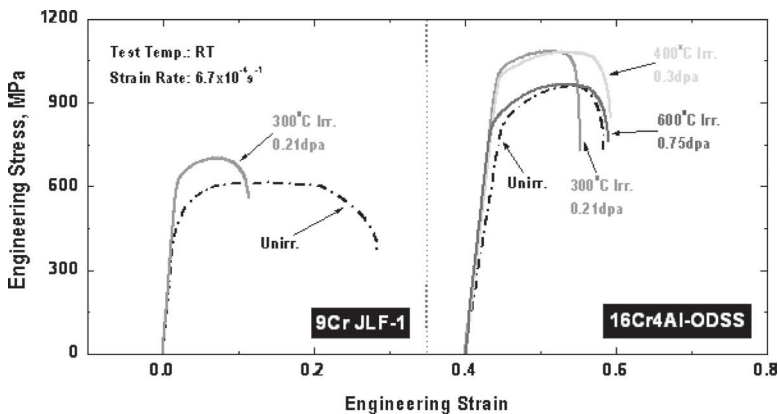


FIG. 2—The engineering tensile stress-strain curves of 9Cr JLF-1 and 16Cr4Al-ODS ferritic steel unirradiated and irradiated from 300 to 600°C up to 0.75 dpa.

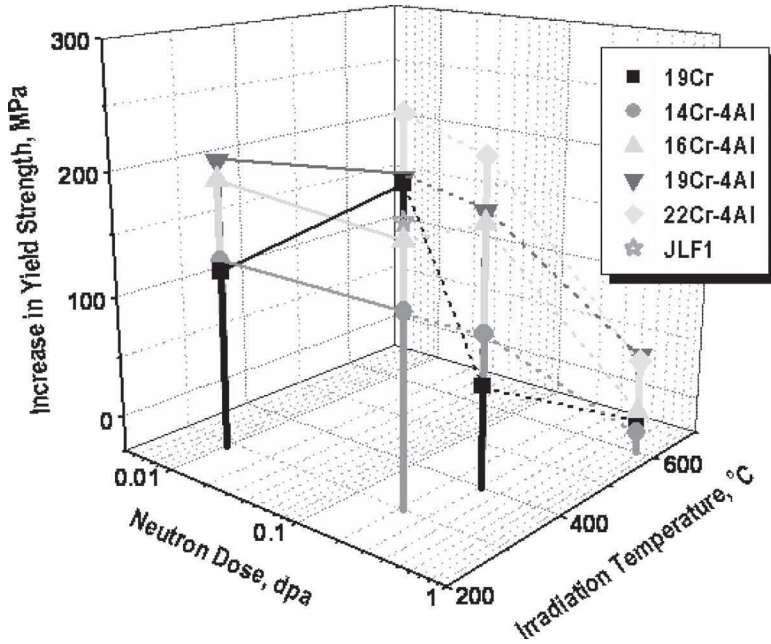


FIG. 3—The increase in yield strength as a function of neutron dose and irradiation temperature of high-Cr ODS ferritic steels and JLF-1.

Al, though the 19Cr4Al-ODS steel irradiated at 300°C has a slightly higher increase in yield strength, compared to 19Cr-ODS steel. It is deduced that during irradiation above 400°C Al addition likely accelerates the formation of Cr-rich phases. Interestingly, the 14Cr4Al-ODS steels still show a smaller irradiation hardening than 9Cr JLF-1 irradiated at 300°C. It is suggested that very small oxide particles dispersed in the matrix may act as trapping sites for irradiation-induced defects [13] and thus cause suppression of Cr diffusion or growth of Cr-rich phase even under the existence of aluminum.

Figure 5 shows the change in total elongation of the high-Cr ODS ferritic steels after exposure to various irradiation temperatures. For 19Cr-ODS steels irradiated from 300 to 600°C, the increase in total elongation is larger than that of 19Cr4Al-ODS steels. On the other hand, the 19Cr-ODS steel irradiated at 290°C has a smaller decrease in the elongation than 19Cr4Al-ODS steel. It is suggested that the addition of Al may cause an increase in loss of ductility during neutron irradiation. It is, however, remarkable that the ODS ferritic steels exposed to neutrons show little change of elongation, compared to 9Cr JLF-1 possessing a significant irradiation-induced loss of total elongation. These results may be explained in terms of acceleration of homogeneous deformation, which is caused by dense oxide particles dispersed in the material matrix, because the dispersed oxide particles likely hinder dislocation channeling induced by neutron irradiation in local regions and thus lead to the homo-

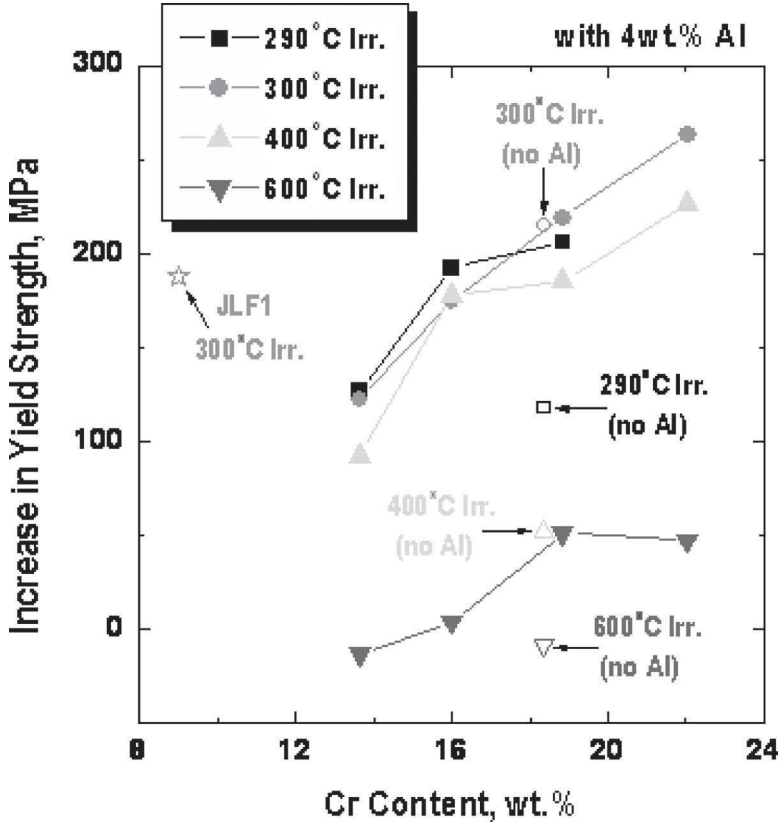


FIG. 4—The effect of Cr content on the irradiation hardening of JLF-1 irradiated at 300°C and ODS ferritic steels irradiated from 290 to 600°C.

geneous deformation continuously. Further study of the phenomenon of little ductility loss in neutron-irradiated ODS steels has been performed in our laboratory.

Irradiation Embrittlement

For high-Cr ODS steels irradiated at various temperatures, the absorbed energy at room temperature is evaluated in terms of Cr content (Fig. 6). The 14Cr4Al-ODS ferritic steels irradiated at all the temperatures are less embrittled than the other ODS steels, but the ODS steels with over 19 wt. % Cr have a serious embrittlement phenomenon below 420°C. These results indicate that the higher the Cr content, the more significant the irradiation embrittlement. Furthermore the irradiation embrittlement of ODS ferritic steels is considered to may be due to the formation of Cr-rich α' precipitates. It is also confirmed that the absorbed energy of ODS ferritic steels is lost slightly after irradiation above 550°C. Figure 7 shows the effect of Cr content on the neutron irradiation-

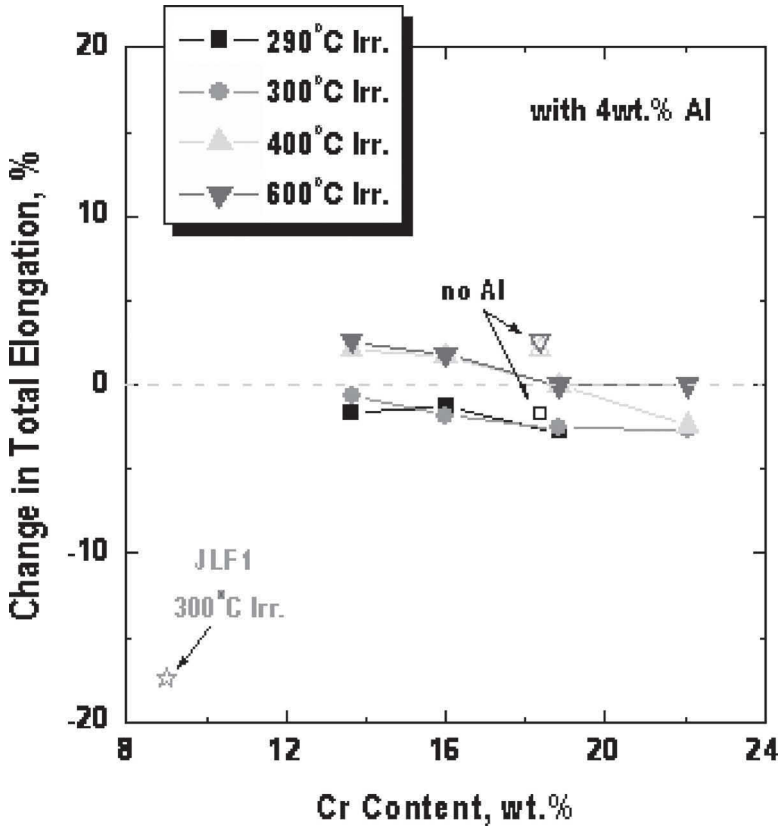


FIG. 5—The change in total elongation as a function of Cr content of JLF-1 irradiated at 300°C and ODS ferritic steels irradiated from 290 to 600°C.

induced DBTT shift of ODS ferritic steels. While the impact tests were performed at temperatures from -190 to 57°C , a critical temperature called the DBTT was not observed for the ODS steels, which are composed of over 19 wt. % Cr and irradiated below 420°C . However, the DBTT of ODS steels with 14–22 wt. % Cr is present after irradiation above 550°C . Note that the DBTT shift of 14Cr4Al-ODS steels decreases with the increased irradiation temperature. These results indicate that the DBTT shift depends on the irradiation temperature. Interestingly, after exposure to neutron irradiation above 550°C the ODS ferritic steels have a significant decrease in DBTT shift, although the DBTT shift of 14Cr4Al-ODS steels is larger than that of other ODS steels.

Correlation Between Increase in Yield Strength and DBTT Shift

Figure 8 shows the relationship between irradiation hardening and DBTT shift of high-Cr ODS ferritic steels irradiated with neutrons. For the ODS steels, the DBTT shift increases with the increasing irradiation hardening. This indicates

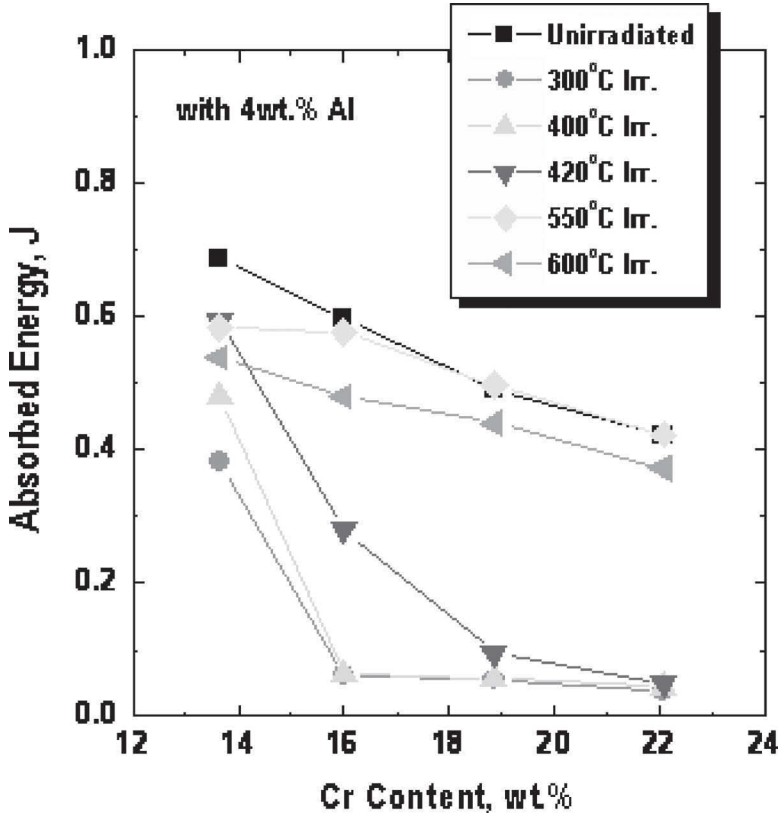


FIG. 6—The absorbed energy of the ODS ferritic steels irradiated from 300 to 600°C, evaluated at room temperature in terms of Cr content.

that the increase of yield strength due to radiation induced hardening increases the DBTT and thus a reduction of hardening is effective to reduce the DBTT shift. Also, it is suggested that the irradiation hardening and embrittlement of ODS ferritic steels are caused by the dislocation loops or Cr-rich phases induced by neutron irradiation. Note that after irradiation at 600°C to 0.75 dpa, the 14Cr4Al-ODS steel has a decrease in yield strength, though an increase in the DBTT is still present. Microstructural observation of the specimen will be conducted to understand the irradiation softening phenomenon.

Conclusions

The dependence of neutron dose, irradiation temperature, and Cr content on irradiation-induced hardening and embrittlement has been examined in the ODS ferritic steels irradiated at various temperatures (from 290 to 600°C) up to the maximum neutron dose of 0.75 dpa. The following results were obtained:

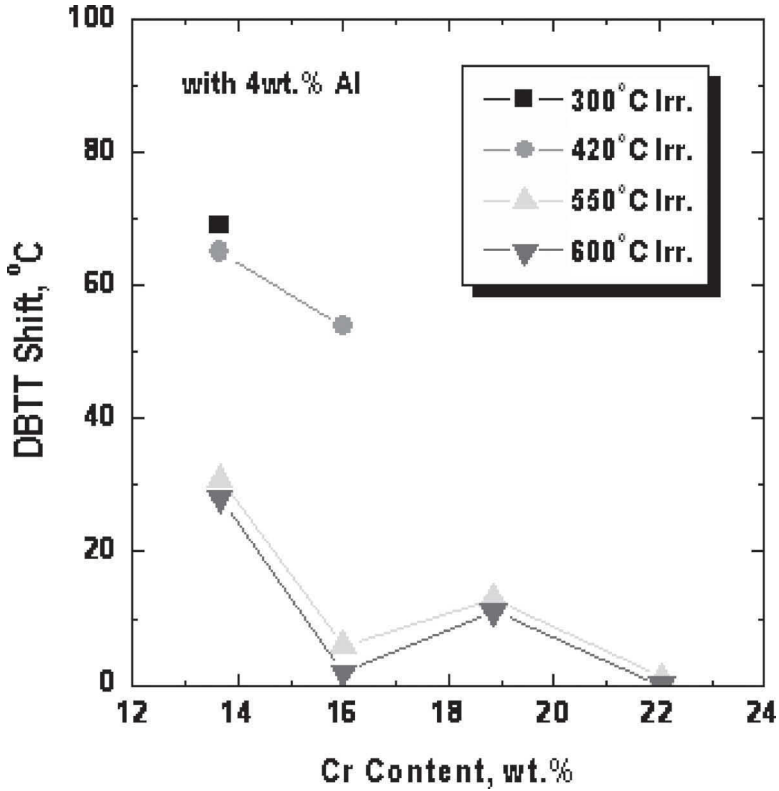


FIG. 7—The effect of Cr content on the DBTT shift of ODS ferritic steels irradiated at 300, 420, 550, and 600°C.

- (1) The irradiation hardening and embrittlement of ODS ferritic steels strongly depend on the irradiation temperature.
- (2) While neutron dose increases from 0.01 to 0.21 dpa, the ODS steels with Al show a saturation of irradiation hardening but the ODS steel without Al has an increase in the hardening.
- (3) The higher the Cr content, the more outstanding the irradiation hardening and embrittlement of ODS ferritic steels irradiated below 420°C.
- (4) Compared to 9Cr JLF-1 possessing a significant loss of total elongation, the ODS ferritic steels exposed to neutrons show little change of tensile elongation.
- (5) The DBTT shift of ODS steels increases with the increasing irradiation hardening, indicating that the increase of yield strength due to radiation induced hardening increases the DBTT and thus a reduction of hardening is effective to reduce the DBTT shift.

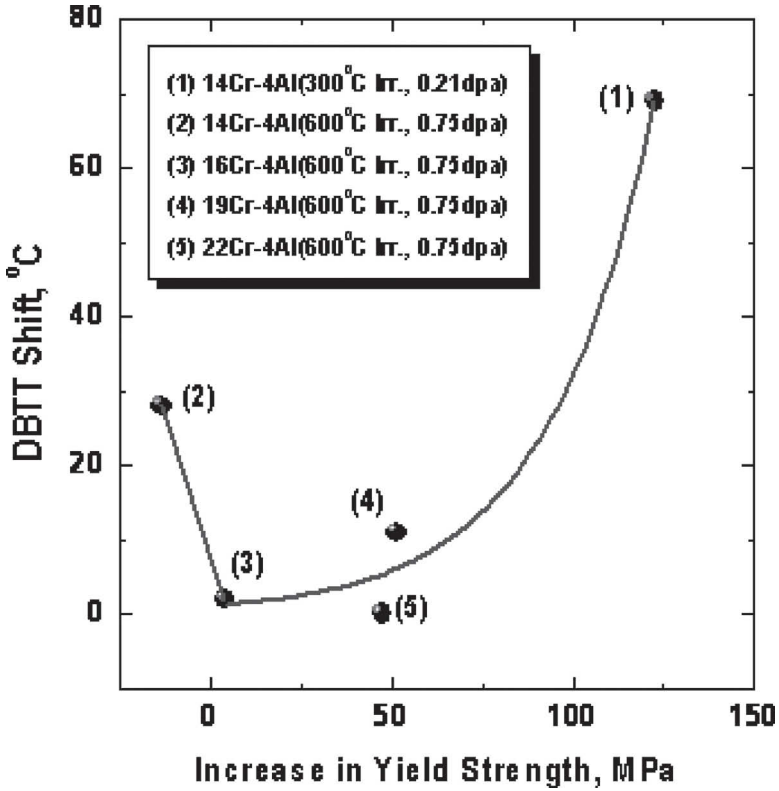


FIG. 8—The relation between increase in yield strength and DBTT shift of ODS ferritic steels irradiated with neutrons.

Acknowledgments

The work is supported by the Institute of Advanced Energy of Kyoto University, Japan.

References

- [1] Ukai, S., Nishida, T., Okada, H., Okuda, T., Fujiwara, M., and Asabe, K., "Development of Oxide Dispersion Strengthened Ferritic Steels for FBR Core Application, (I). Improvement of Mechanical Properties by Recrystallization Processing," *J. Nucl. Sci. Technol.*, Vol. 34, 1997, pp. 256–263.
- [2] Yoshitake, T., Ohmori, T., and Miyakawa, S., "Burst Properties of Irradiated Oxide Dispersion Strengthened Ferritic Steel Claddings," *J. Nucl. Mater.*, Vols. 307–311, 2002, pp. 788–792.
- [3] Yoshitake, T., Abe, Y., Akasaka, N., Ohtsuka, S., Ukai, S., and Kimura, A., "Ring-Tensile Properties of Irradiated Oxide Dispersion Strengthened Ferritic/Martensitic Steel Claddings," *J. Nucl. Mater.*, Vols. 329–333, 2004, pp. 342–346.

- [4] Cho, H. S., Kimura, A., Ukai, S., and Fujiwara, M., "Corrosion Properties of Oxide Dispersion Strengthened Steels in Super-Critical Water Environment," *J. Nucl. Mater.*, Vols. 329–333, 2004, pp. 387–391.
- [5] Cho, H. S. and Kimura, A., "Corrosion Resistance of High-Cr Oxide Dispersion Strengthened Ferritic Steels in Super-Critical Pressurized Water," *J. Nucl. Mater.*, Vols. 367–370, 2007, pp. 1180–1184.
- [6] Kasada, R., Toda, N., Yutani, K., Cho, H. S., Kishimoto, H., and Kimura, A., "Pre- and Post-Deformation Microstructures of Oxide Dispersion Strengthened Ferritic Steels," *J. Nucl. Mater.*, Vols. 367–370, 2007, pp. 222–228.
- [7] Kimura, A., Cho, H. S., Toda, N., Kasada, R., Yutani, K., Kishimoto, H., Iwata, N., Ukai, S., and Fujiwara, M., "High Burnup Fuel Cladding Materials R&D for Advanced Nuclear Systems: Nano-Sized Oxide Dispersion Strengthening Steels," *J. Nucl. Sci. Technol.*, Vol. 44(3), 2007, pp. 323–328.
- [8] Cho, H. S., Kasada, R., and Kimura, A., "Effects of Neutron Irradiation on the Tensile Properties of High-Cr Oxide Dispersion Strengthened Ferritic Steels," *J. Nucl. Mater.*, Vols. 367–370, 2007, pp. 239–243.
- [9] Ukai, S., Mizuta, S., Yoshitake, T., Okuda, T., Hagi, S., Fujiwara, M., and Kobayashi, T., "Tube Manufacturing and Characterization of Oxide Dispersion Strengthened Ferritic Steels," *J. Nucl. Mater.*, Vols. 283–287, 2000, pp. 702–706.
- [10] Iwata, N. Y., Kimura, A., Ukai, S., Fujiwara, M., and Kawashima, N., "Characterization of Raw-Powders for High-Cr Oxide Dispersion Strengthening Steels," *Proceeding of the 2005 International Congress on Advances in Nuclear Power Plants (ICAPP '05)*, Seoul, Korea, 2005, p. 5528.
- [11] Kasada, R., Ono, H., and Kimura, A., "Small Specimen Test Technique for Evaluating Fracture Toughness of Blanket Structural Materials," *Fusion Eng. Des.*, Vol. 81, 2006, pp. 981–986.
- [12] Kimura, A., Kasada, R., Kohyama, A., Tanigawa, H., Hirose, T., Shiba, K., Jitsukawa, S., Ohtsuka, S., Ukai, S., Sokolov, M. A., Klueh, R. L., Yamamoto, T., and Odette, G. R., "Recent Progress in US-Japan Collaborative Research on Ferritic Steels R&D," *J. Nucl. Mater.*, Vols. 367–370, 2007, pp. 60–67.
- [13] Pareige, P., Miller, M. K., Stoller, R. E., Hoelzer, D. T., Cadel, E., and Radiguest, B., "Stability of Nanometer-Size Oxide Clusters in Mechanically-Alloyed Steel Under Ion-Induced Displacement Cascade Damage Conditions," *J. Nucl. Mater.*, Vol. 360, 2007, pp. 136–142.

Akiyuki Takahashi,¹ Shahram Sharafat,² Koji Nagasawa,¹ and Nasr Ghoniem²

Kinetic Monte Carlo Simulation of Helium-Bubble Evolution in ODS Steels

ABSTRACT: Oxide dispersion strengthened (ODS) ferritic/martensitic steels are being developed for high temperature applications for fission reactors and future fusion devices. ODS-Eurofer97 (Fe–9CrWVTa–0.3Y₂O₃) and ODS-MA957 (Fe–14CrTiMo–0.25Y₂O₃) have shown promising high temperature mechanical properties, such as tensile strength, toughness, fatigue, and creep rupture. Recent neutron irradiation experiments with simultaneous helium implantation indicate that helium transport is favorably impacted by the nanometer-sized oxide particles, small grain sizes, and high dislocation densities of ODS steels. Simulating helium transport in ODS steels requires a three-dimensional spatially resolved model, which takes into account discrete geometric and microstructural features of the steel. We have developed such a helium transport simulation model using an event kinetic Monte Carlo (EKMC) approach called Monte Carlo simulation of helium-bubble evolution and resolutions (McHEROS). First, a spatially resolved kinetic rate theory is used to establish helium-vacancy cluster and stable helium-bubble nuclei concentrations. The maximum helium-bubble density is then used as an initial condition for randomly distributed matrix bubbles for the EKMC simulation. Migration, coalescence, and trapping of helium bubbles by oxide particles are simulated. Matrix helium bubbles that come into contact with each other are assumed to undergo instantaneous coalescence, which leads to bubble growth. However, migrating bubbles that are intercepted by oxide particles are assumed trapped but can grow through coalescing with newly arriving bubbles. The oxide particles effectively reduce the growth rate of matrix bubbles. Helium-bubble size and spatial distributions of the EKMC simulation are compared with recent experimental measurements. As part of this study, the effectiveness of the ODS microstructure on reducing helium-

Manuscript received June 23, 2008; accepted for publication October 26, 2009; published online December 2009.

¹ Tokyo Univ. of Science, 2641 Yamazaki, Noda-shi, Chiba 278-8510, Japan.

² Univ. of California—Los Angeles, Los Angeles, CA 90095-1597.

Cite as: Takahashi, A., Sharafat, S., Nagasawa, K. and Ghoniem, N., "Kinetic Monte Carlo Simulation of Helium-Bubble Evolution in ODS Steels," *J. ASTM Intl.*, Vol. 7, No. 2. doi:10.1520/JAI101971.

Copyright © 2010 by ASTM International, 100 Barr Harbor Drive, PO Box C700, West Conshohocken, PA 19428-2959.

bubble growth rates is presented by comparing EKMC simulations of steels with and without ODS particles. This first application of the McHEROS code has demonstrated the viability of the code as a tool in describing the behavior of helium-bubble transport in ODS alloys.

Introduction

The deuterium-tritium reaction in fusion devices produces high energy (14.1 MeV) neutrons, which can lead to substantial gaseous transmutations in surrounding structural materials, such as iron at a rate of ~ 10 He/dpa. Helium has a closed electronic structure and is insoluble in solid materials. As a result helium atoms tend to cluster and/or interact with defects, such as vacancies, dislocations, precipitates, or pre-existing helium bubbles. Helium clusters can migrate, coalesce, or grow by acquiring vacancies or helium atoms to form helium-filled bubbles, which have detrimental effects on structural material performance.

At high irradiation temperatures ($>0.5T_m$) tensile, creep, and fatigue properties of structural alloys are adversely affected due to the formation of helium bubbles, particularly in grain boundary regions. At low temperatures ($<0.4T_m$), the fatigue life can be reduced due to the interference of helium bubbles with plastic deformation. The dimensional integrity of structures can also be affected because of the stabilizing effect of helium on void and bubble formation and growth. Helium accelerates the onset of swelling by reducing the critical radius for bias driven bubble growth. In-depth review articles on the effects of helium on microstructural evolution have been published by numerous authors, e.g., Trinkaus [1] and Ullmaier [2].

The detrimental effects of helium can be mitigated by suppressing helium driven bubble growth by distributing the helium among a large number of cavities. Early on, Mansur et al. [3] showed that the dilution of gas among many cavities in ferritic/martensitic (FM) steels results in extreme swelling resistance. The high density of phosphide precipitates were shown to force cavities to form on precipitate/matrix interfaces, thereby forcing cavity nucleation and helium trapping on a fine scale. Cavity densities were about three orders of magnitude larger in alloys with precipitates [3].

Recently, Kurtz et al. [4] studied implanted Eurofer97 (FM steel) under neutron irradiation at 673 and 773 K using a novel He-implantation technique with controlled He-to-displacements per atom (dpa) ratios. It was shown that in Eurofer97, helium is distributed among a large density ($\sim 10^{22} \text{ m}^{-3}$) of helium bubbles, which formed preferentially at pre-existing dislocations. Similarly, using the same He-implantation technique in oxide dispersion strengthened (ODS) (MA957) steels, Yamamoto et al. [5] showed that helium bubbles form preferentially along dislocations and at the interface between matrix and nano-sized oxide precipitates in ODS (MAE967) steels. ODS alloys are produced by mechanically alloying high density ($\sim 10^{24} \text{ m}^{-3}$) nanosized oxide particles (<5 nm), such as Y-Ti-O, into steels. Irradiation up to 9 dpa damage with 380 appm He at 773 K resulted in a helium-bubble density, which was of the same order of magnitude as that of the particulate density of about $3 \times 10^{23} \text{ m}^{-3}$. The He bubbles that were trapped at the nanoscale Y-Ti-O precipitate/matrix inter-

faces had an average radius of ≤ 1 nm. The effectiveness of trapping vacancies and helium at precipitate-matrix interfaces has been reported by a number of investigators [6–8]. However, detailed energetics of the trapping mechanisms has not been published widely and is also not addressed in our simulation.

In this work, we simulate the evolution of helium bubbles in typical ODS alloys. We use the event kinetic Monte Carlo (EKMC) technique to simulate the migration and coalescence of He bubbles in a control volume with randomly distributed nanosized particles. The focus of this work is on the early development of the EKMC tool itself; hence simulation results are based solely on migration, coalescence, and consequent growth of pre-existing helium bubbles in the presence of distributed particles and nucleation, and the growth of new helium bubbles due to continuous helium implantation is not included in these simulations. We present here the first results of our EKMC simulation of helium-bubble kinetics in the presence of precipitates. The simulation results indicate that helium-bubble evolution trends in the presence of dispersed particles are reasonably described by the Monte Carlo simulation of helium-bubble evolution and resolutions (McHEROS) code.

ODS Alloys and He-Implantation Results

Due to their high swelling resistance (~ 1 vol. %/100 dpa) compared with austenitic stainless steels (~ 1 vol. %/10 dpa), FM steels are primary candidates for fission and fusion structural components. To increase the operating temperature of FM steels, several ODS FM steels are being developed for fission and fusion applications in Japan [9,10], Europe [11], and the United States [12–14]. High temperature strengthening is due to presence of high density ($\sim 10^{23}$ – 10^{24} m⁻³) nanosize (< 5 nm) oxide particles and the ensuing interlocking of fine ferrite grain structure.

ODS-Eurofer97 (Fe–9CrWVTa–0.3Y₂O₃), ODS-MA957 (Fe–14Cr–0.3Mo–1Ti–0.25Y₂O₃), and ODS-12YWT (Fe–12Cr–2.5W–0.4Ti–0.25Y₂O₃) have shown greatly improved mechanical properties, such as tensile strength, toughness, fatigue, and creep rupture of up to ~ 973 K [11,12].

The microstructural stability of mechanically alloyed (MA)/ODS Fe–14 wt % Cr–3 % W–0.4 % Ti–0.3 % Y₂O₃ ferritic alloys was recently investigated by ion irradiation [14] and by atom probe tomography [13]. Atom probe tomography revealed that the MA/ODS 14YWT ferritic alloys contain a high number density of nanometer scale titanium-, yttrium-, and oxygen-enriched nanoclusters in the as-extruded condition. These nanoclusters were found to be extremely resistant to coarsening for at least 14 500 h at temperatures of 1073 K [13] and for 3000 h at about 1273 K [15]. Ion irradiation tests of up to 150 dpa between 773 and 973 K showed that the average oxide size decreased, while the oxide density increased [14]. The decrease in oxide size was attributed to temperature and not ballistic processes.

In addition to improving high temperature mechanical properties, the ODS FM-alloys are attractive because the dispersed oxide particles benignly trap helium at particle/matrix interfaces, thereby impeding the growth of matrix and grain boundary helium bubbles.

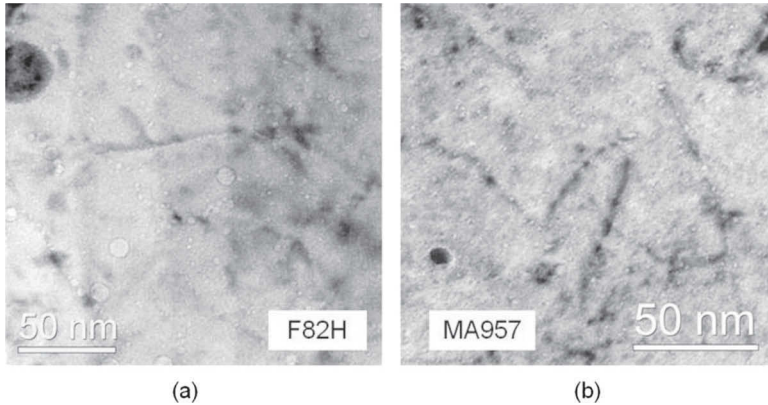


FIG. 1—TEM of cavity and bubble microstructure for (a) F82H and (b) MA957 neutron irradiated in HFIR at 773 K to about 9 dpa and 380 appm helium, indicating the much larger number density and smaller mean bubble size for the ODS-MA957 alloy.

Recent high flux isotope reactor (HFIR) neutron irradiation experiments with simultaneous helium implantation indicate that helium transport is favorably impacted by the nanometer-sized oxide particles, small grain sizes, and high dislocation densities of ODS steels [4,5,16,17]. Odette et al. [16] and Yamamoto et al. [17] showed that the number density of helium bubbles is about 1/3 lower in F82H ($\sim 1 \times 10^{23} \text{ m}^{-3}$) than in MA957 ($\sim 3 \times 10^{23} \text{ m}^{-3}$), with an average bubble radius about twice as large in F82H ($\sim 2 \text{ nm}$) than in ODS-MA957 ($\leq 1 \text{ nm}$). Figure 1 shows a comparison of the bubble and cavity microstructure of irradiated F82H and MA957.

These preliminary experiments indicate that the nanosized Y-Ti-O oxides ($\sim 10^{24} \text{ m}^{-3}$ and $\sim 5 \text{ nm}$ diameter) prevent helium from forming large matrix and grain boundary bubbles by trapping significant amount of helium at the oxide/matrix interfaces. These new findings indicate that ODS steels could potentially reduce high temperature ($\sim 997\text{--}1073 \text{ K}$) irradiation induced creep embrittlement caused primarily by the formation and growth of helium bubbles in grain boundary regions.

Simulation of He-Bubble Evolution

Traditionally, modeling of helium-bubble evolution during irradiation was based on chemical rate theory also referred to as Master Equation [18,19]. However, rate theory assumes homogenized field parameters, which makes detailed modeling of spatially dependent processes, particularly interaction of bubbles with three-dimensional (3D) geometric features, such as precipitates and grain boundaries, not practical unless these features can be represented as mean field parameters. Recently, a kinetic rate theory (KRT) based computer code called HEROS [20] was developed in an effort to simulate spatially dependent helium transport. The HEROS bubble evolution model is based on a set of simplified hierarchical kinetic rate equations, which simulate the micro-

structure evolution associated with damage production along with helium generation or implantation. The structure of the HEROS codes affords solving space-dependent and highly transient irradiation conditions along with spatial and transient bubble migration driving forces, such as temperature and stress gradients. Despite its spatially resolved approach, HEROS does not allow for detailed modeling of interactions between helium clusters or bubbles with 3D geometric features, such as precipitates in ODS alloys.

To overcome the shortcomings of the mean field approach (rate theory), the KMC simulation technique was used to model the evolution of gas bubbles in the presence of 3D geometric features. Our approach is based on the work done by Evans et al. [21], who successfully simulated the evolution of oversized bubbles in annealed helium implanted copper samples. The result is a helium-bubble evolution simulation code called McHEROS [22,23], which stands for Monte Carlo simulation of helium-bubble evolution and resolutions. The McHEROS code is capable of simulating the migration and coalescence of He bubbles including interaction with distinct geometric 3D material features.

The McHEROS code contains models for both bubble surface and volume diffusion mechanisms. Previously reported helium-bubble evolution simulations using the McHEROS code [22] have shown good agreement between calculated and experimentally measured surface pore densities and size distributions. The McHEROS code was recently used to simulate the impact of driving forces, such as stress and/or temperature gradients on helium-bubble evolution [23], and it was shown that helium-bubble migration, coalescence, and growth compared well with experimental observations [22].

Hybrid Helium Transport Model

The time evolution of helium bubbles can be categorized into incubation, nucleation, growth, and coarsening phases. During the incubation and nucleation phase, the density of stable bubble nuclei increases steadily and reaches a maximum followed by a growth and coarsening phase, during which the bubble density drops and the average bubble size increases. A schematic of the two primary phases, nucleation and growth, is shown in Fig. 2. During the growth phase, the nucleation of new bubbles is increasingly suppressed. The range and duration of the nucleation and growth phases are temperature and damage rate dependent. For 10 keV helium implantation in FeNiCr alloys, Ono et al. [24] showed that bubble evolution is dominated by growth above the implantation temperature of 873 K, while below 673 K it is predominantly nucleation driven.

The current version of the McHEROS code does not include a model for the nucleation of stable helium bubbles; thus in its present form the McHEROS code is only applicable for simulating the growth and coarsening phase of helium-bubble evolution. To resolve this shortcoming, a “hybrid helium transport” approach is used, where bubble nucleation rates are determined using the KRT based HEROS code and then used as an initial condition in the McHEROS code. Experimental investigations of helium implanted ODS alloys were recently performed at 773 K, which is at about $0.43T_m$, where T_m is melting temperature of ferritic steels [4,5]. In Fe irradiated at 773 K, the nucleation of

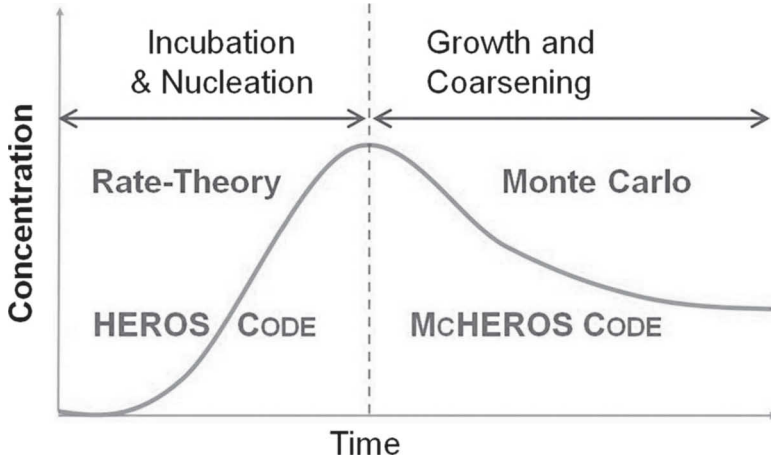


FIG. 2—Schematic of the hybrid rate theory—KMC helium transport code.

stable helium-bubble nuclei is suppressed once the bubble growth phase has started [24]; therefore the hybrid helium transport approach is considered to be a reasonable approach above 773 K. First, the nucleation of stable helium bubbles is estimated using the HEROS rate theory model, and then the McHEROS KMC code is used to simulate helium-bubble migration, coalescence, and growth in the presence of nanosized oxide particles in ODS steels.

In Fe at a temperature of about ~ 603 K ($\sim 0.3T_m$), surface diffusion and bubble diffusion coefficients of 1 nm diameter bubbles are 3.1×10^{-8} and 6.3×10^{-10} cm²/s, respectively [24]. These high diffusion coefficients indicated that above $\sim 0.3T_m$, the bubble nucleation phase more or less ends as soon as the bubbles reach critical radius for bias driven growth. Indeed, Coghlan et al. [25] showed that at 773 K, the critical radius for bias driven growth is less than a few nanometres for bubbles containing less than ~ 100 helium atoms.

For this work we thus assume that prior to the onset of the bubble coarsening phase, equal-sized helium bubbles are uniformly distributed inside the ODS matrix material. The McHEROS KMC simulation is used to simulate growth phase only, i.e., the interaction of bubbles with each other and with the dispersed oxide particles.

The McHEROS He-Bubble Evolution Code

Here we briefly outline the fundamental modeling aspects of the McHEROS EKMC code. The kinetics of bubble migration and bubble coalescence include Brownian motion and bias driven migration, such as in a stress and/or temperature gradient.

Bubble Diffusion Model

Both surface and volume diffusion of bubbles are included, in the McHEROS code, however at irradiation temperatures below $\sim 0.7T_m$, surface diffusion is the predominant diffusion mechanism given by [26]

$$D_B = \frac{3\Omega^{4/3}}{2\pi r^4} D_S \quad (1)$$

where:

D_B = bubble diffusion coefficient,

Ω = atomic volume ($\sim 1.16 \times 10^{-29} \text{ m}^3$ for Fe [27]),

r = bubble radius, and

D_S = surface diffusion coefficient defined as $D_S = D_o \exp(-E_s/kT)$, where D_o is the pre-exponential and E_s is the surface activation energy.

Stroscio et al. [28] studied the diffusion of Fe on Fe(0 0 1) surfaces and reported an activation energy $E = 0.45 \pm 0.4 \text{ eV}$ and a pre-exponential $D_o = 7.2 \times 10^{-8} \text{ m}^2 \cdot \text{s}^{-1}$. Flahive et al. [29] used Morse potential with no relaxation and showed that the activation energy for Fe is between 0.2 and 1.0 eV depending on the surface orientation.

Surface activation energies and associated pre-exponential factors for helium bubbles in FeNiCr steels were also reported by Carsughi et al. [27]. The surface activation energy was deduced from the diffusivity of pressurized ($\sim 5 \text{ GPa}$) bubbles in FeNiCr alloys and reported to be $\sim 1.9 \pm 0.4 \text{ eV}$ with pre-exponential of $\sim 1 \times 10^{-8} \text{ m}^2 \cdot \text{s}^{-1}$. The activation energy is almost a factor of 4 larger than the measured value ($E_s \sim 0.45 \text{ eV}$) reported by Stroscio et al. [28]. The reason for the large scatter in reported activation energies could be that the authors [27] failed to take into account the helium-bubble Brownian motion, which results in a mean square migration distance proportional to time. Ono et al. [24] reported the diffusivity of helium bubbles in FeNiCr alloys due to Brownian motion and deduced that an effective bubble activation energy is $\sim 2.1 \text{ eV}$, which results in a diffusion coefficient of $\sim 9.55 \times 10^{-16} \text{ cm}^2/\text{s}$ for a 1 nm diameter bubble at 773 K. The diffusivities reported by both Ono and Carsughi are of the same order of magnitude, which leads to this author deducing that the surface activation energies reported by Carsughi ($\sim 2 \text{ eV}$) are based on Brownian motion and do not represent pure surface diffusion activation energies, D_s . For the current analysis an activation energy of 0.5 eV and a pre-exponential of $5 \times 10^{-8} \text{ m}^2 \cdot \text{s}^{-1}$ are used, which result in a surface diffusion value of $D_s \sim 2.7 \times 10^{-7} \text{ cm}^2 \cdot \text{s}^{-1}$ at 773 K. The corresponding bubble diffusion coefficient (Eq 1) is ~ 5 .

Bubble Coalescence Model

To simplify computations, the McHEROS code assumes that once bubbles come within a lattice constant distance of each other or make physical contact, they will coalesce, and the new bubble will instantaneously grow to a size that is in equilibrium with the pressure based on

$$p = \frac{2\gamma}{r} \quad (2)$$

where:

p = pressure,

γ = surface energy ($\gamma \sim 2.45 \text{ J/m}^2$ for iron [29]), and

r = radius of the bubble.

Using a modified Van der Waals equation of state, the pressure in a bubble is given by

$$p = m_{\text{He}}kT / \left(\frac{4}{3}\pi r^3 - m_{\text{He}}B \right) \quad (3)$$

where:

m_{He} = number of helium atoms in the bubble,

kT = Boltzmann factor, and

B = van der Waals volume correction coefficient ($B = 1.59 \times 10^{-29}$ [30]).

The numerical condition for bubble coalescence is taken as

$$r_1 + r_2 + r_c > d_{12} \quad (4)$$

where:

r_1 and r_2 = respectively the radius of the two engaging helium bubbles,

r_c = capture radius, and

d_{12} = distance between the centers of the two bubbles.

The capture radius is conservatively taken to be equal to a lattice constant but is much larger due to the strain fields surrounding helium bubbles. The radius of the new bubble is calculated based on Eqs 2 and 3.

Evans [21] defined a temperature range between $0.4T_m$ and $0.5T_m$ at which coalesced bubbles collect sufficient number of vacancies to relieve any excess internal pressure and regain equilibrium. The recently developed helium implantation process with controlled He-to-dpa ratios [4,5] generates 4.79 MeV alpha-particles, which produce about 155 vacancies/ion in Fe. Given the large vacancy production and the high irradiation temperatures ($\sim 0.4T_m$), it is reasonable to assume that sufficient vacancies exist for coalescing bubbles to grow rapidly to equilibrate the pressure. Furthermore, the high surface diffusion value of $D_s \sim 2.7 \times 10^{-7} \text{ cm}^2 \cdot \text{s}^{-1}$ at 773 K indicates that rapid surface diffusion can occur to assist bubble growth by reshaping the coalesced bubbles into spheres.

Bubble Oxide Particle Interaction

Migrating bubbles can interact with stationary oxide particles. We assume that once a bubble comes within one lattice constant distance of an oxide particle, it is captured permanently. The captured bubble is assumed to remain "frozen" at the location of first contact and is assumed to maintain its original spherical shape; however the combined oxide-bubble complex radius increases. Figure 3 shows a schematic drawing of the bubble oxide interaction process for a first capture and for subsequent bubble entrapments. The radius of the trapped bubble increases with every new bubble capture, and the new combined oxide-multiple bubble diameter is updated using

$$x_j' = \frac{r'}{r} \cdot \frac{r(x_j - x_i)}{R + r} + \frac{Rx_j + rx_i}{R + r}$$

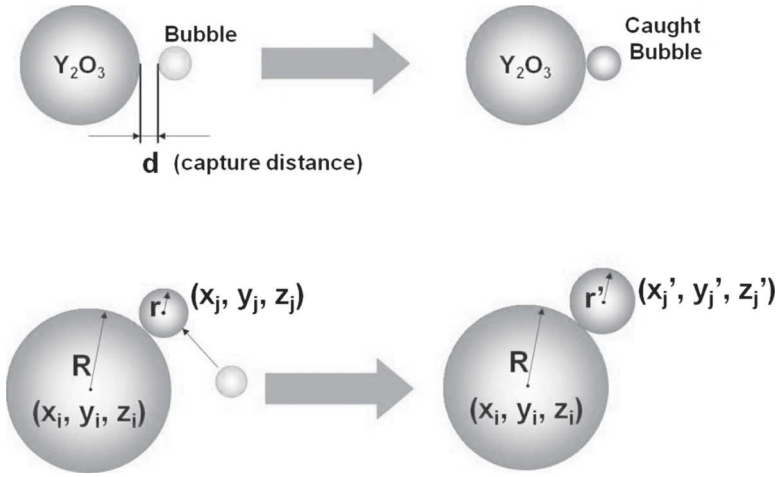


FIG. 3—Schematic of oxide-bubble interaction. Top: First bubble capture. Bottom: Subsequent bubble capture resulting in increase of combined oxide-bubble capture radius.

$$y_j' = \frac{r'}{r} \cdot \frac{r(y_j - y_i)}{R + r} + \frac{Ry_j + ry_i}{R + r}$$

$$z_j' = \frac{r'}{r} \cdot \frac{r(z_j - z_i)}{R + r} + \frac{Rz_j + rz_i}{R + r} \tag{5}$$

(see Fig. 3 for definition of terms). The new size of the oxide-bubble complex increases the effective capture radius. In this work we assume that once helium bubbles interact with precipitates, they are trapped and bound permanently on the precipitate surfaces.

McHEROS Code Algorithm

Initially, the diffusion coefficients of helium bubbles are calculated based on Eq 1. The calculated diffusion coefficients are converted into probabilities of the occurrence of the events (EKMC). The event is in this case the diffusion of a bubble within a time step Δt . The probabilities are then summed up to find the total probability of the events. The total probability is used to normalize the probability of each event. A uniformly distributed random number ranging between zero and one is generated and used to select one of the possible events. The selected event is immediately carried out. After the diffusion of the bubble, the nearest neighbor bubble or oxide particle nearest to the diffused bubble is searched for. If the distance between the diffused bubble and the nearest neighbor bubble or particle is within the capture distance (Eq 5), they are combined into one single bubble or into a frozen oxide-bubble complex. The new radius of the coalesced bubble or oxide-bubble complex is calculated, and the diffu-

sion coefficients of all helium bubbles are reevaluated. This process is repeated until all the bubbles are trapped on oxides or when a designated run time is reached and the McHEROS code terminates.

The McHEROS code time increment (Δt) between events is estimated by

$$\Delta t = \frac{-\log R}{\sum_i \nu_i} \quad (6)$$

where:

R = uniformly distributed random number ranging between zero and one and

ν_i = probability of an event.

McHEROS Simulation Results

Three sets of simulations were performed: (1) Without nanoscale oxide particles, (2) with low oxide particle densities, and (3) with a high density of particles. The high oxide density case ($\sim 3 \times 10^{23} \text{ m}^{-3}$) represents typical nanosized oxide particle densities of tested MA957 [5]. A simulation temperature of 773 K was used based on the reported experimental irradiation conditions [4,5]. Table 1 summarizes the McHEROS KMC simulation and initial conditions.

Non-Oxide Dispersion Strengthened and Low-Oxide Dispersion Strengthened Simulation Results

Figure 4 shows a sequence of snapshots of the simulation with no oxide particles (non-ODS) and a starting helium-bubble radius $r = 1 \text{ nm}$. As expected the Brownian motion results in migration of the bubbles, which coalesce into larger bubbles. At the end of the simulation ($t = 2.82 \times 10^7 \text{ s}$), the average bubble radius grew from 1, 2, and 3 nm to 9, 12, and 14 nm, respectively, for non-ODS steel. Correspondingly, for low-ODS steels the average radius of bubbles with initial radii of 1, 2, and 3 nm grew only to 2.4, 5.5, and 9.0 nm, respectively (Fig. 5).

In non-ODS steels bubbles with initial radius $r_o = 1 \text{ nm}$ experience a drop in bubble number density from an initial value of about $4.0 \times 10^{22} \text{ m}^{-3}$ (5000 bubbles) to about $5.7 \times 10^{20} \text{ m}^{-3}$ (71 bubbles) or a factor of ~ 70 decrease within $2.82 \times 10^7 \text{ s}$. However, for low-ODS steels the simulation shows a number density reduction to about $N_b \sim 4.5 \times 10^{21} \text{ m}^{-3}$, which is about a factor of ~ 9 times higher than for non-ODS steels (see Fig. 6).

The impact of slight variations of the low density of oxide particles was studied. The simulation was run for 2.55×10^{20} , 5.12×10^{20} , and $7.68 \times 10^{20} \text{ m}^{-3}$ (i.e., the density was varied by factors of 2 and 3 only). Figure 7 shows the effect of the small variation in particle density on the average bubble radius. While for the non-ODS case the average radius grew to about 12 nm, the low density particles significantly suppressed the average radius to about

TABLE 1—KMC simulation parameters and initial conditions.

	Simulation Width (nm)	Volume (nm ³)	Oxide Radius (nm)	Oxide Density (m ⁻³)	Initial Bubble Radius (nm)	Initial Bubble Density (m ⁻³)	Initial Bubble Number	Helium Conc. (appm)
No oxides	500	1	4.00×10^{22}	5000	200
					2	4.00×10^{22}	5000	800
					3	4.00×10^{22}	5000	1800
Low oxide density	500	...	28	2.56×10^{20} (three runs) ^a	1	4.00×10^{22}	5000	200
					2	4.00×10^{22}	5000	800
					3	4.00×10^{22}	5000	1800
High oxide density	250	...	5	3.00×10^{23}	0.5	3.00×10^{23}	4688	370
					1.0	7.50×10^{22}	1172	370
					1.5	3.40×10^{22}	531	370

^aThe low density case was run with particle densities of 2.56×10^{20} , 5.12×10^{20} , and 7.68×10^{20} m⁻³.

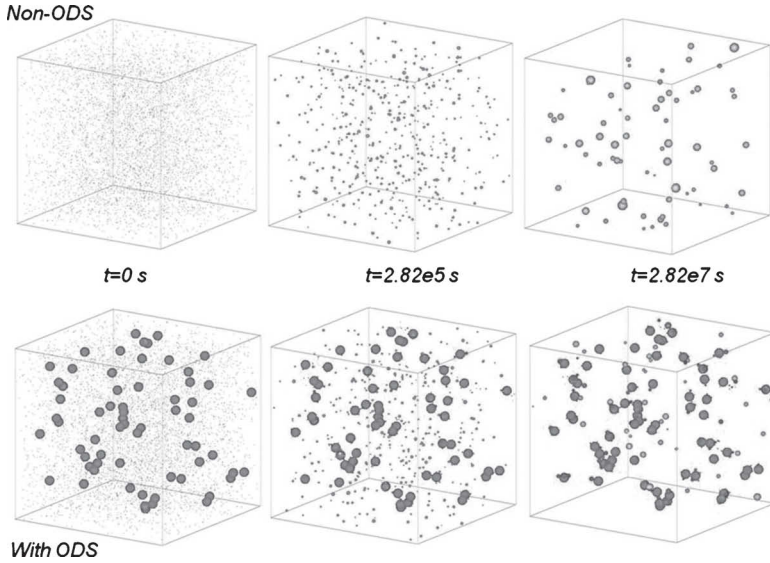


FIG. 4—Sequence of helium-bubble evolution snapshots starting with 5000 helium bubbles (200 appm) with initial radius $r_o=1$ nm inside a volume of $500 \times 500 \times 500$ nm³ of oxide particle free (top: Non-ODS) and ODS alloy (bottom) at 773 K. Note the oxide particle density is low ($\sim 5.12 \times 10^{20}$ m⁻³) and bubbles trapped by oxide particles are shown as red dots in bottom figures; the large dark dots in the bottom figures represent oxide particles; the large dots in the top figure represent helium bubbles.

6.94, 5.50, and 4.76 nm, respectively, for 2.55×10^{20} , 5.12×10^{20} , and 7.68×10^{20} m⁻³ particle densities. A factor of 3 increase in particle density reduced the average radius of bubble by a factor of about 1.5.

Simulation Results for High Oxide Particle Densities

Helium implantation experiments were performed with non-ODS and ODS-MA957 alloys, which contained a particle density of about 3.20×10^{23} m⁻³ [4,5]. Yamamoto et al. [17] neutron irradiated F82H and MA957 in HFIR at 773 K to about 9 dpa and 380 appm helium. Figure 1 shows a comparison of the bubble and cavity microstructure of irradiated F82H and MA957.

A simulation was performed using similar experimental conditions, i.e., 5 nm diameter oxide particles with a density of 3×10^{23} m⁻³ and 370 appm helium at 773 K. Figure 8 shows snapshots of initial and final bubble distributions starting with 1 nm diameter matrix bubbles (green spheres). At the end of the simulation, $t=5000$ s, all of the bubbles have been trapped by the oxide particles (red spheres), and interestingly the size of the bubbles did not change significantly. Figure 9 shows the bubble density evolution, and Fig. 10 shows the mean radius evolution as a function of simulation time for bubbles with initial diameter of 1, 2, and 3 nm and 3×10^{23} m⁻³ particle density at 773 K and 370 appm helium. The number of the 1 nm sized bubbles is reduced from

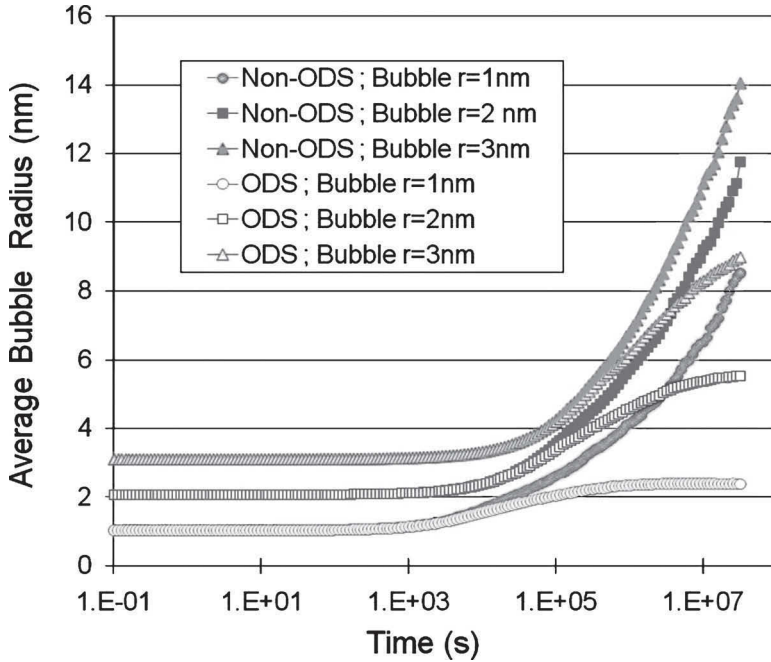


FIG. 5—Evolution of the average helium-bubble radius with and without oxide particles ($\text{ODS}=5.12 \times 10^{20} \text{ m}^{-3}$) at 773 K (filled symbols: Non-ODS; open symbols: ODS).

about 4688 ($\sim 3.75 \times 10^{22} \text{ m}^{-3}$) to about 3899 ($\sim 3.12 \times 10^{22} \text{ m}^{-3}$), while the density of the 2 and 3 nm bubbles stays almost constant. The associated mean radius remain almost unchanged for all three bubble sizes. This indicates the effectiveness of the oxide particles in interacting with the bubbles by preventing bubble growth due to migration and coalescence.

The change in the maximum bubble size varies depending on the initial average bubble diameter, as shown in Fig. 11. The ratios between final average and maximum bubble radius are about 2.3, 2, and 1.7 for initial radius $r_o = 0.5, 1, \text{ and } 1.5 \text{ nm}$, respectively. This indicates that the smaller the initial bubble size is, the more likely it is that growth through coalescence will occur.

Summary and Conclusions

The presence of stable nanosize particles within the matrix of FM steels has been shown to favorably affect helium transport. The oxide particles benignly trap the helium, thus minimizing helium-bubble growth. Recent experiments [4,5] have shown that the number density of helium bubbles ($\sim 1 \times 10^{23} \text{ m}^{-3}$) is about 1/3 lower in non-ODS F82H compared in ODS-MA957 ($\sim 3 \times 10^{23} \text{ m}^{-3}$), and the average bubble radius ($\sim 2 \text{ nm}$) is about twice as large in F82H than in ODS-MA957 ($\leq 1 \text{ nm}$).

An EKMC code has been developed, called McHEROS [22,23], to simulate

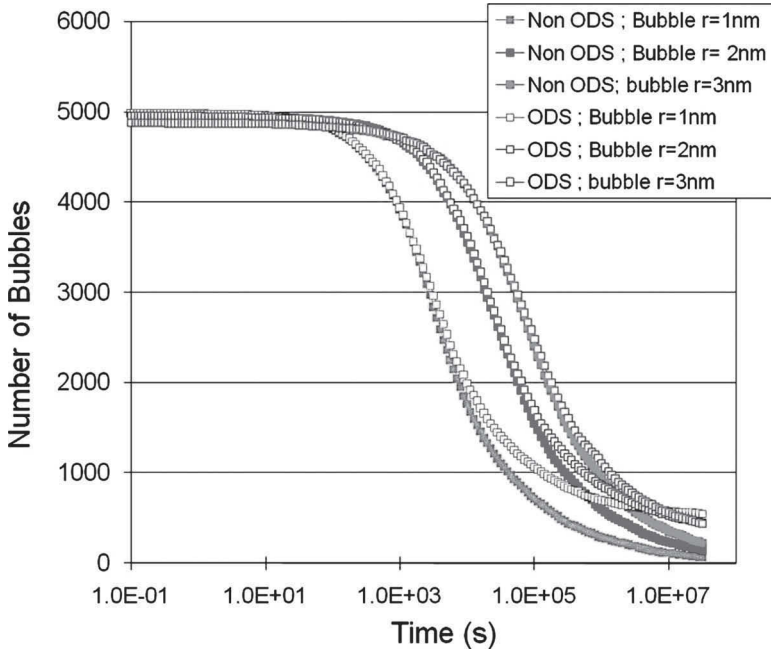


FIG. 6—Evolution of the number of helium bubbles with and without oxide particles (ODS= $5.12 \times 10^{20} \text{ m}^{-3}$) at 773 K. 5000 bubbles corresponds to a bubble density of $\sim 4.0 \times 10^{22} \text{ m}^{-3}$ (filled symbols: Non-ODS; open symbols: ODS).

the transport of helium and the evolution of bubbles. In its present development stage, the McHEROS code does not simulate bubble nucleation but uses the peak bubble density at the end of the nucleation phase as initial condition for the bubble growth phase. The bubble nucleation rate in the presence of damage is estimated using a spatially resolved KRT code called HEROS [20]. This hybrid helium transport approach has been successfully employed to model helium transport and bubble evolution of implantation experiment at elevated temperatures ($>0.4T_m$).

The McHEROS code was employed to simulate ODS-free, low, and high density ODS alloys. The simulation was run at 773 K, which is above the bias driven growth temperature for helium bubbles. At this temperature the separation of helium-bubble evolution into nucleation and growth phases has been shown to be a reasonable approximation [1,24].

To simplify the computation, it was assumed that at the start of the simulation, all helium is introduced as a random distribution of equal-sized matrix bubbles. For low density but large oxide particles ($\sim 5 \times 10^{20} \text{ m}^{-3}$ and 28 nm), it was shown that the interaction of helium bubbles with the oxides can be quite significant. The mean radius of bubbles with an initial radius of $r_o = 1 \text{ nm}$ grew to about 9 nm in the absence of oxides but only to about 2 nm in the presence of oxides. With a low density of oxide particles, the number densities of bubbles dropped from an initial value of about $4.0 \times 10^{22} \text{ m}^{-3}$ (5000

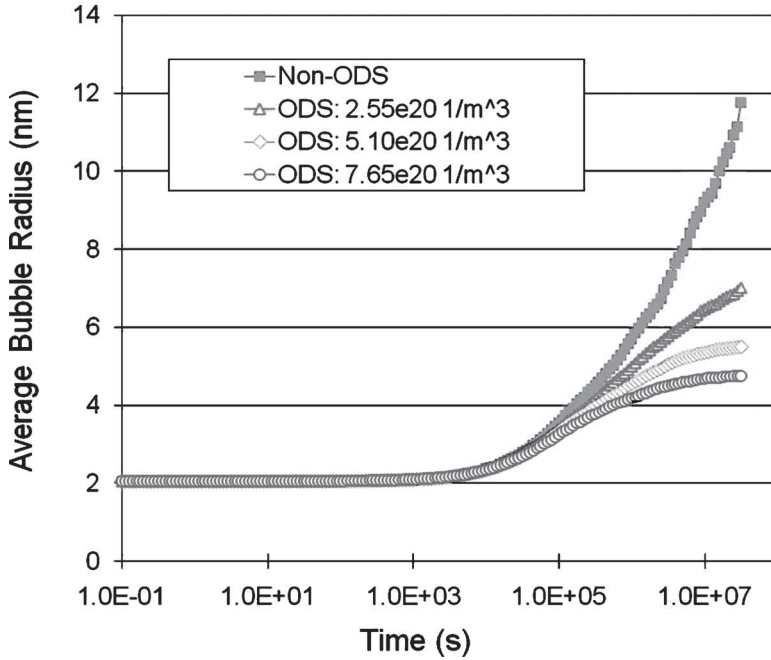


FIG. 7—Effect of oxide particle density on the evolution of the average radius of helium bubbles (initial bubble radius of $r_o=2$ nm and $T=773$ K; filled symbols: Non-ODS; and open symbols: ODS).

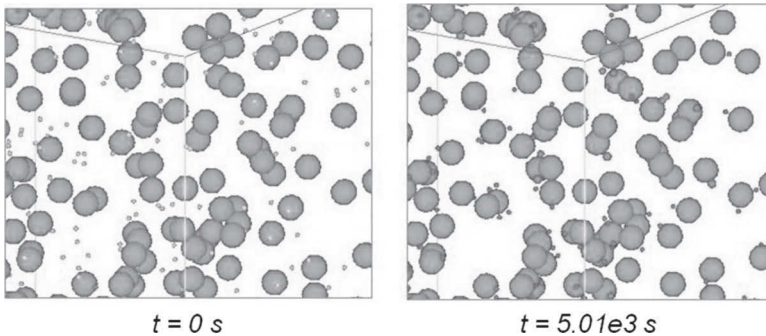


FIG. 8—KMC simulation of helium-bubble evolution and transport in high density ODS alloy ($\sim 3.2 \times 10^{23} \text{ m}^{-3}$; oxide diameter=5 nm) with initial bubble radius of $r_o=1$ nm. Note that the number density and the mean bubbles radius do not change significantly; however after about 5000 s, all the bubbles have been trapped by the oxides (left: small green (light gray) dots represent matrix bubbles; right: small red (attached to oxide particles) dots represent trapped bubbles).

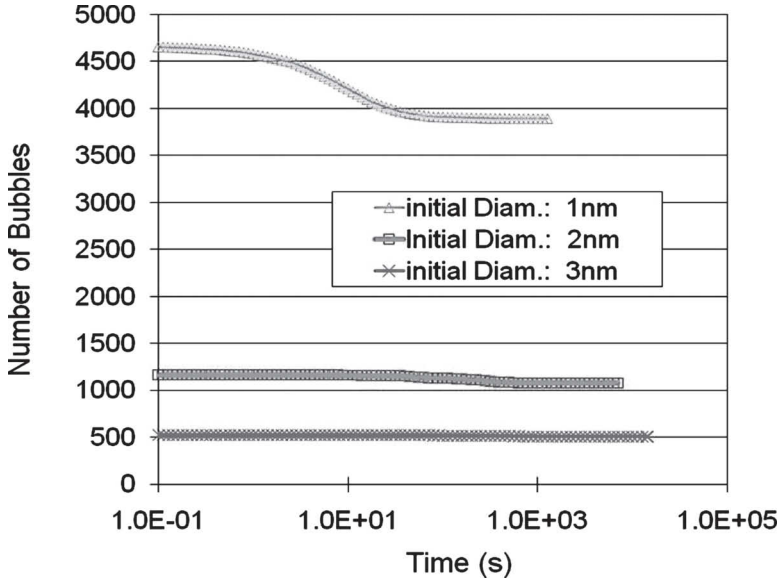


FIG. 9—Evolution of bubble densities in ODS with $\sim 3 \times 10^{23} \text{ m}^{-3}$ oxide particle density and 370 appm helium at 773 K (5000 bubbles correspond to about $4.0 \times 10^{22} \text{ m}^{-3}$).

bubbles) to about $5.7 \times 10^{20} \text{ m}^{-3}$ (71 bubbles) for $r_o = 1 \text{ nm}$ or a factor of ~ 70 decrease within about $2.82 \times 10^7 \text{ s}$ at 773 K. This significant drop in bubble density is because the low particle density is not very effective in trapping migrating helium bubbles before they get a chance to coalesce and form larger bubbles. As indicated in Fig. 6, under the same conditions the number density of bubbles in non-ODS drops significantly more compared with ODS.

The presence of a large number density ($\sim 3 \times 10^{23} \text{ m}^{-3}$) of oxide particles shows a more drastic impact on helium-bubble evolution. Three different initial bubble sizes of 1, 2, and 3 nm diameter but with the same concentration of 370 appm of helium were considered. For all three bubble sizes, the simulation showed that the oxides trap all of the bubbles within a simulation time of less than $1.4 \times 10^4 \text{ s}$ ($\sim 4 \text{ h}$) at 773 K. Furthermore, the initial number density of the 1 nm diameter bubbles was reduced only slightly from the original value of about 4×10^{22} to about $3 \times 10^{22} \text{ m}^{-3}$. The 2 and 3 nm sized bubbles showed a negligible change in their number density. Correspondingly, the mean radius of the bubbles did not change by any significant value for all three bubble sizes.

The McHEROS simulation results agree with the preliminary experimental findings, particularly the small residual mean bubble size of $\sim 1 \text{ nm}$. However, the simulated bubble number density ($\sim 3 \times 10^{22} \text{ m}^{-3}$) is about a factor of 10 smaller than reported [5]. The difference can be attributed to the fact that the simulation assumed that all the bubbles are of equal size and are all introduced into the matrix at time $t = 0 \text{ s}$. This assumption precludes the capture of small HeV clusters by oxide particles as well as the probability of initiating helium

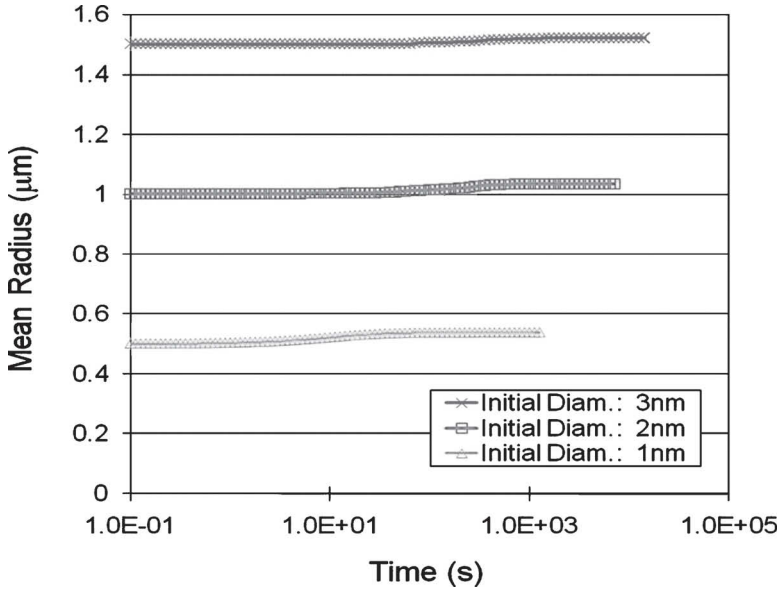


FIG. 10—Evolution of the bubble mean radius in ODS with $\sim 3 \times 10^{23} \text{ m}^{-3}$ oxide particle density and 370 appm helium at 773 K and starting radii $r_o=0.5, 1, \text{ and } 1.5 \text{ nm}$.

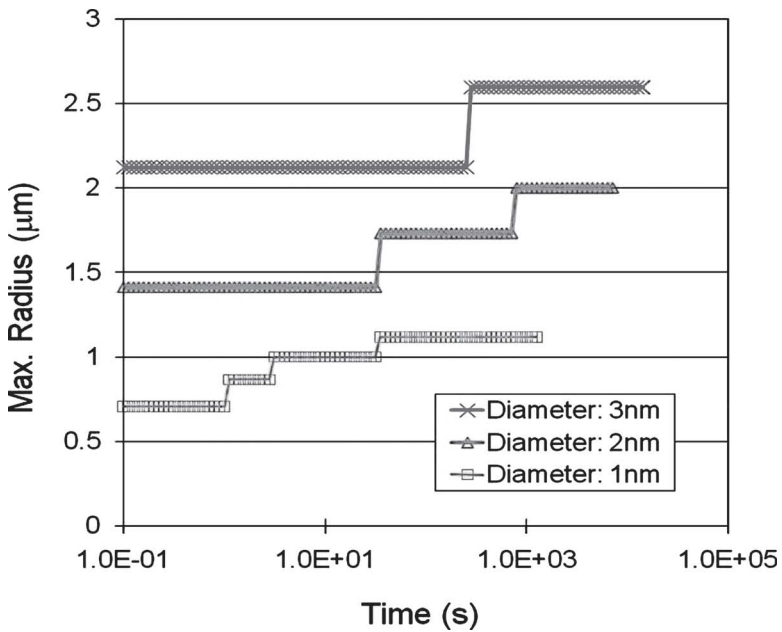


FIG. 11—Evolution of the maximum bubble radius with $\sim 3 \times 10^{23} \text{ m}^{-3}$ oxide particle density and 370 appm helium at 773 K for $r_o=0.5, 1, \text{ and } 1.5 \text{ nm}$.

bubbles at oxide/matrix interfaces; both of these processes could result in larger number densities of bubbles.

In summary, this first application of the McHEROS EKMC simulation has demonstrated the viability of the code as a tool in describing the behavior of helium-bubble transport in ODS alloys. Future, efforts are underway to model more realistic irradiation conditions, including continuous generation of helium atoms and the clustering of HeV clusters in the presence of damage.

Acknowledgments

The writers would like to thank the U.S. Department of Energy, Office of Fusion Science—Fusion Energy, for support for this work through a contract with UCLA. Also, the support of the High Average Power Laser IFE project, under which this work was initiated, is greatly appreciated.

References

- [1] Trinkaus, H. and Singh, B. N., "Helium accumulation in metals during irradiation—where do we stand?," *J. Nucl. Mater.*, Vol. 323, 2003, pp. 229–242.
- [2] Ullmaier, H. and Chen, J., "Low temperature tensile properties of steels containing high concentrations of helium," *J. Nucl. Mater.*, Vol. 318, 2003, pp. 228–233.
- [3] Mansur, L. K. and Lee, E. H., "Theoretical basis for unified analysis of experimental data and design of swelling-resistant alloys," *J. Nucl. Mater.*, Vol. 179–181, 1991, pp. 105–110.
- [4] Kurtz, R. J., Odette, G. R., Yamamoto, T., Gelles, D. S., Miao, P., and Oliver, B. M., "The transport and fate of helium in martensitic steels at fusion relevant He/dpa ratios and dpa rates," *J. Nucl. Mater.*, Vol. 367–370, 2007, pp. 417–422.
- [5] Yamamoto, T., Odette, G. R., Miao, P., Hoelzer, D. T., Bentley, J., Hashimoto, N., Tanigawa, H., and Kurtz, R. J., "The transport and fate of helium in nanostructured ferritic alloys at fusion relevant He/dpa ratios and dpa rates," *J. Nucl. Mater.*, Vol. 367–370, 2007, pp. 399–410.
- [6] de Castro, V., Leguey, T., Muñoz, A., Monge, M. A., Pareja, R., Marquis, E. A., Lozano-Perez, S., and Jenkins, M. L., "Microstructural characterization of Y₂O₃ ODS-Fe-Cr model alloys," *J. Nucl. Mater.*, Vol. 386–388, 2009, pp. 449–452.
- [7] David, C., Panigrahi, B. K., Balaji, S., Balamurugan, A. K., Nair, K. G. M., Amarendra, G., Sundar, C. S., and Raj, B., "A study of the effect of titanium on the void swelling behavior of D9 steels by ion beam simulation," *J. Nucl. Mater.*, Vol. 383, 2008, pp. 132–136.
- [8] Zhang, C. H., Jang, J., Cho, H. D., and Yang, Y. T., "Void swelling in MA956 ODS steel irradiated with 122 MeV Ne-ions at elevated temperatures," *J. Nucl. Mater.*, Vol. 386–388, 2009, pp. 457–461.
- [9] Ukai, S., Yoshitake, T., Mizuta, S., Matsudaira, Y., Hagi, S., and Kobayashi, T., "Preliminary tube manufacturing of oxide dispersion strengthened ferritic steels with recrystallized structure," *J. Nucl. Sci. Technol.*, Vol. 36(8), 1999, pp. 710–712.
- [10] Kimura, A., Cho, H.-S., Toda, N., Kasada, R., Yutani, K., Kishimoto, H., Iwata, N., Ukai, S., and Fujiwara, M., "High burnup fuel cladding materials R&D for advanced nuclear systems nano-sized oxide dispersion strengthening steels," *J. Nucl. Sci. Technol.*, Vol. 44(3), 2007, pp. 323–328.

- [11] Schaeublin, R., Leguey, T., Spätig, P., Baluc, N., and Victoria, M., "Microstructure and mechanical properties of two ODS ferritic/martensitic steels," *J. Nucl. Mater.*, Vol. 307–311, 2002, pp. 778–782.
- [12] Klueh, R. L., Shingledecker, J. P., Swindeman, R. W., and Hoelzer, D. T., "Oxide dispersion-strengthened steels: A comparison of some commercial and experimental alloys," *J. Nucl. Mater.*, Vol. 341, 2005, pp. 103–114.
- [13] Miller, M. K., Kenik, E. A., Russell, K. F., Heatherly, L., Hoelzer, D. T., and Maziasz, P. J., "Atom probe tomography of nanoscale particles in ODS ferritic alloys," *Mater. Sci. Eng., A*, Vol. 353, 2003, pp. 140–145.
- [14] Allen, T. R., Gan, J., Cole, J. I., Miller, M. K., Busby, J. T., Shutthanandan, S., and Thevuthasan, S., "Radiation response of a 9 chromium oxide dispersion strengthened steel to heavy ion irradiation," *J. Nucl. Mater.*, Vol. 375, 2008, pp. 26–37.
- [15] Miao, P., Odette, G. R., Yamamoto, T., Alinger, M., and Klingensmith, D., "Thermal stability of nano-structured ferritic alloy," *J. Nucl. Mater.*, Vol. 377, 2008, pp. 59–64.
- [16] Odette, G. R., Miao, P., Edwards, D. J., Yamamoto, T., Tanagawa, H., and Kurtz, R. J., "A comparison of cavity formation in neutron irradiated nanostructured ferritic alloys and tempered martensitic steels at high He/dpa ratio," *Trans. Am. Nucl. Soc.*, Vol. 98, 2008, pp. 1148–1150.
- [17] Yamamoto, T., Odette, G. R., Miao, P., Edwards, D. J., and Kurtz, R. J., "Helium effects on microstructural evolution in tempered martensitic steels: In situ helium implantation studies in HFIR," *J. Nucl. Mater.*, Vol. 386–388, 2009, pp. 338–341.
- [18] Kiritani, M., "Analysis of the clustering process of supersaturated lattice vacancies," *J. Phys. Soc. Jpn.*, Vol. 35, 1973, pp. 95–107.
- [19] Ghoniem, N. M. and Alhajji, J. N., "The effect of helium clustering on its transport to grain boundaries," *J. Nucl. Mater.*, Vol. 136, 1985, pp. 192–206.
- [20] Hu, Q., Sharafat, S., and Ghoniem, N. M., "Modeling space-time dependent helium bubble evolution in tungsten armor under IFE conditions," *Fusion Sci. Technol.*, Vol. 52(3), 2007, pp. 574–578.
- [21] Evans, J. H., Escobar Galindo, R., and van Veen, A., "A description of bubble growth and gas release during thermal annealing of helium implanted copper," *Nucl. Instrum. Methods Phys. Res. B*, Vol. 217, 2004, pp. 276–280.
- [22] Sharafat, S., Takahashi, A., and Ghoniem, N. M., "A description of bubble growth and gas release of helium implanted tungsten," *J. Nucl. Mater.*, Vol. 386–388, 2009, pp. 900–903.
- [23] Sharafat, S., Takahashi, A., Nagaswa, K., and Ghoniem, N. M., "A description of stress driven bubble growth of helium implanted tungsten," *J. Nucl. Mater.*, Vol. 389(2), 2009, pp. 203–212.
- [24] Ono, K., Arakawa, K., Oohashi, M., Kurata, H., Hojou, K., and Yoshida, N., "Formation and migration of helium bubbles in Fe-16Cr-17Ni austenitic alloy at high temperature," *J. Nucl. Mater.*, Vol. 283–287, 2000 210–214.
- [25] Coghlan, W. A. and Mansur, L. K., "Critical radius and critical number of gas atoms for cavities containing a van der waals gas," *J. Nucl. Mater.*, Vol. 122, 1984, pp. 495–501.
- [26] Nichols, F. A., "Kinetics of diffusional motion of pores in solids: A review," *J. Nucl. Mater.*, Vol. 30, 1969, pp. 143–165.
- [27] Carsughi, F., Ullmaier, H., Trinkaus, H., Kesternich, W., and Zell, V., "Helium bubbles in FeNiCr after post-implantation annealing," *J. Nucl. Mater.*, Vol. 212–215, 1994, pp. 336–340.
- [28] Stroschio, J. A., Pierce, D. T., and Dragoset, R. A., "Homoepitaxial growth of iron and a real space view of reflection-high-energy-electron diffraction," *Phys. Rev.*

Lett., Vol. 70, 1993, pp. 3615–3618.

- [29] Flahive, P. G., and Graham, W. R., "Pair potential calculations of single atom self-diffusion activation energies," *Surf. Sci.*, Vol. 91, 1980, pp. 449–462.
- [30] Mansur, L. K. and Coghlan, W. A., "Mechanisms of helium interaction with radiation effects in metals and alloys: A review," *J. Nucl. Mater.*, Vol. 119, 1983, pp. 1–25.

C. N. Venkiteswaran,¹ V. Karthik,¹ P. Parameswaran,¹
N. G. Muralidharan,¹ V. Anandaraj,¹ S. Saroja,² V. Venugopal,¹
M. Vijayalakshmi,¹ K. V. Kasi Viswanathan,¹ and B. Raj¹

Study of Microstructure and Property Changes in Irradiated SS316 Wrapper of Fast Breeder Test Reactor

ABSTRACT: This paper presents the results of a study on mechanical properties and microstructure in a SS316 wrapper irradiated in a 40MWt/13MWe fast breeder test reactor at Kalpakkam, India. Transmission electron microscopy (TEM) examination and mechanical property evaluation were carried out on the hexagonal wrapper subjected to different displacement damages up to a maximum of 83 dpa at an operating temperature of about 673 K. The steel irradiated to 83 dpa showed an increase in the yield strength and ultimate tensile strength, with a reduction in uniform elongation to about 8%–10% from about 20% in the unirradiated material. Density measurements on the specimen from different portions of the irradiated wrapper showed a peak volumetric swelling of about 3.5% at a damage of 83 dpa. TEM studies showed extensive void formation at 40 dpa and beyond in addition to extensive precipitation and formation of dislocation loops. The void density and size showed a progressive increase with displacement damage. The precipitates were identified to be of nickel and silicon enriched M_6C type of η phase, while radiation induced G phase was also observed at 83 dpa. The increase in strength and reduction in ductility with increase in dpa is attributed to irradiation hardening, which is supported by the increase in defect density as observed from the dislocation substructure and increase in the void density and size. The paper would discuss the degradation in mechanical property in terms of the microstructural changes.

Manuscript received June 27, 2008; accepted for publication June 2, 2009; published online July 2009.

¹ Indira Gandhi Centre For Atomic Research, Kalpakkam 603 102, India

² Indira Gandhi Centre For Atomic Research, Kalpakkam 603 102, India, (Corresponding author) e-mail: saroja@igcar.gov.in

Cite as: Venkiteswaran, C. N., Karthik, V., Parameswaran, P., Muralidharan, N. G., Anandaraj, V., Saroja, S., Venugopal, V., Vijayalakshmi, M., Viswanathan, K. V. Kasi and Raj, B., "Study of Microstructure and Property Changes in Irradiated SS316 Wrapper of Fast Breeder Test Reactor," *J. ASTM Intl.*, Vol. 6, No. 7. doi:10.1520/JAI101991.

Copyright © 2009 by ASTM International, 100 Barr Harbor Drive, PO Box C700, West Conshohocken, PA 19428-2959.

KEYWORDS: transmission electron microscopy, voids, yield strength, ultimate tensile strength, ductility, precipitates, dpa

Introduction

Successful operation of sodium cooled fast reactors depends on the performance of core structural materials namely clad and wrapper, which are subjected to intense neutron irradiation and high temperatures [1,2]. The neutron flux levels in fast breeder reactors are high (10^{15} n cm⁻² s⁻¹), which is about two orders of magnitude higher than that in thermal reactors [3]. This leads to problems such as void swelling, irradiation creep, and helium embrittlement. Deformation of various components in the fuel subassemblies may occur due to void swelling, thermal, and irradiation creep. The combination of void swelling and creep induced by internal sodium pressure can cause dilation and rounding of wrapper faces. The flux and temperature gradient in the core can lead to differential swelling resulting in bowing of the subassemblies. Interaction between wrappers due to deformation can lead to excessive loads during fuel handling. The residence time of the fuel subassembly and hence the achievable burn-up is limited either by void swelling of the hexagonal wrapper or the exhaustion of creep ductility of the clad, which in turn increases the fuel cycle cost.

Peak swelling in austenitic stainless steels takes place generally in the temperature range of 673–873 K during irradiation in fast breeder reactors, which is close to the operating temperatures of fast breeder test reactor (FBTR). Irradiation induced defect structures manifest as dimensional deformations, change in mechanical properties, and embrittlement. The defect structures evolve as a function of accumulated displacement damage and temperature of irradiation [4,5]. The formation and growth of voids and consequently the swelling is sensitive to the metallurgical variables such as chemical composition, thermo-mechanical history, and irradiation conditions such as irradiation temperature, fluence, and dose rate. Several improvements using alloying additions or modification of the metallurgical structure by cold working have been carried out. The fluence dependence of swelling can be described as a low incubation dose, a transient period with low rate of swelling followed by acceleration to a regime of near linear swelling rate. Improvement in swelling resistance is by way of enhancing the incubation and transient regimes. The steady state swelling rate is constant for most austenitic stainless steels, of the order of ~1 % per dpa, for a wide range of irradiation temperatures [6].

20 % cold worked (CW) SS316 has been used as the clad and wrapper material of FBTR. The wrapper in the core subassembly operates at relatively lower temperatures than the fuel clad. The typical operating temperatures in FBTR are in the range 623–723 K. The peak neutron dose is about 83 dpa similar to that of the clad corresponding to a fuel burn-up of 155 GWd/t. Adequate data is available in literature on radiation damage in 20 % CW austenitic stainless steels up to about 70 dpa. However, damage induced in the structural material, which is also a function of other irradiation parameters such as irradiation temperature and displacement damage rate are unique for each reactor [7]. Further, the formation of irradiation-induced or enhanced precipitation

and precipitates not encountered during thermal aging not only change the overall microstructure but also remove potentially beneficial elements from the matrix, causing degradation of properties. Hence, a detailed post irradiation examination on the irradiated clad and wrapper is essential to understand the behavior of the structural material in FBTR. The material behavior at different dpa is a very critical input to further enhance the fuel burn-up [8]. This also provides valuable data to design alloys for core components for the 500 MWE Prototype Fast Breeder Reactor presently under construction at Kalpakkam, India. An extensive structure-property study has therefore been carried out on irradiated hexagonal wrapper of FBTR fuel subassemblies, which had undergone burn-ups of 100 and 155 GWd/t. Evaluation of mechanical properties by miniature specimen mechanical testing, estimation of swelling and microstructural investigation using transmission electron microscopy was (TEM) carried out, and the results of which are presented in this paper.

Experimental Details

The wrapper material was AISI 316 stainless steel with 0.05 wt % carbon. The irradiated hexagonal wrapper of 1.0 mm thickness from FBTR fuel subassemblies corresponding to peak burn-ups of 100 and 155 GWd/t that had experienced a temperature in the range of 620–780 K were studied. The displacement damages (dpa) along the length of the fuel assembly wrapper were estimated from the flux and spectrum of FBTR using the norgett robinson torrens model. A maximum of 83 dpa was estimated at the maximum fluence location corresponding to the center of the fuel column for the 155 GWd/t subassembly. The temperatures of the wrapper along the core were calculated from the operating history of the fuel assembly and the channel temperatures estimated using the Super Energy code. The dpa and irradiation temperature profile along the core length of the 155 GWd/t burn-up FBTR fuel subassembly is shown in Fig. 1. The displacement damage rate of the different specimens examined in the present study is estimated to be in the range from 0.8×10^{-6} to 1.6×10^{-6} dpa/s.

A specially designed hollow end mill cutting machine was used for specimen extraction inside the hot cells. Specimens of 8 mm diameter and 1 mm thickness were extracted from different axial locations of irradiated wrapper, corresponding to different displacement damages. The edges and surfaces of the specimens were made uniform by grinding using abrasive papers. The specimens after decontamination were used for density measurements, mechanical testing, and microstructural examination. Each 8 mm diameter specimen had a contact β , γ dose rate of about 20 mSv/h.

Density measurements were carried out on the 8 mm diameter disk specimens subjected to different dose levels by liquid immersion technique. A precision weighing balance (accuracy of 0.001 g) with the density kit was installed inside the hot cell for estimation of volume. Analytical grade ethanol was used as the liquid medium. Mechanical properties of the irradiated hexagonal wrapper were evaluated using shear punch test at room temperatures using a lead shielded servo-hydraulic test machine. The shear punch testing is a miniature

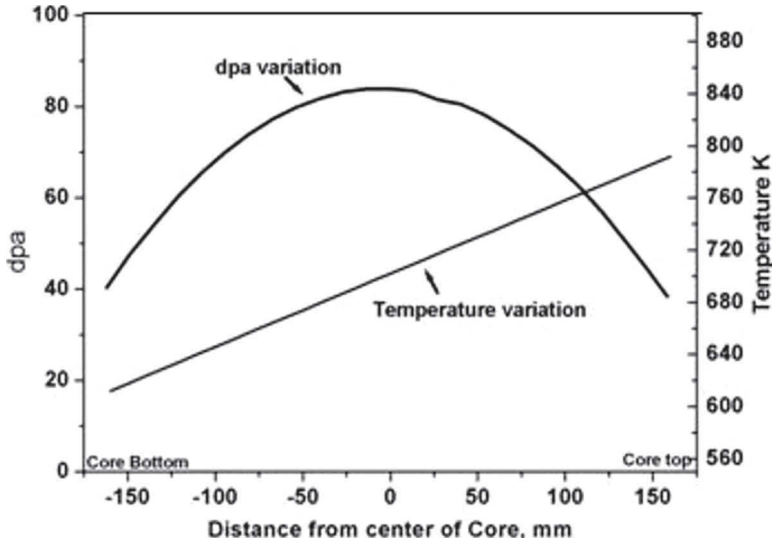


FIG. 1—Axial profile of temperature and dpa of the FBTR fuel subassembly discharged after burn-up of 155 GWd/t.

specimen testing technique, in which a cylindrical punch with a flat end is forced to punch a hole in a clamped small disk specimen [9]. The test fixture consists of a flat punch of 3 mm diameter made of hardened tool steel (RC 62) and a set of dies between which the specimen is clamped. The diameter of the receiving hole in the lower die is 3.040 mm. The deformation takes place in the radial clearance zone of 0.020 mm. This is in the same range as that used by other investigators [10]. The test technique was standardized using virgin SS316 with different cold rolled and solution annealed microstructures. By carrying out both tensile and shear punch tests on the steel with these microstructural conditions, a tensile-to-shear correlation was obtained for yield strength (YS), ultimate tensile strength (UTS), and strain hardening parameters. The details of test fixture, testing procedures, and analysis are described elsewhere [11].

The 3 mm slug resulting out of the shear punch test was used as the starting material for TEM studies. TEM specimens were prepared from different locations of hexagonal wrapper, which had undergone displacement damage from 2 to 83 dpa. Electrolytic thinning parameters of samples for TEM studies were established by adopting extensive trials on unirradiated specimens. Radiation dose rate on the thin specimen was found to be about 0.3 mSv/h. TEM on thin foils was carried out in a Philips CM200 with energy dispersive spectrometer (super ultra thin window) and DX4 analyzer using an operating voltage of 120–200 kV. Precipitates were identified by a combination of electron diffraction and energy dispersive spectroscopy (EDS) analysis. Quantification of the EDS spectra was done by the Cliff Lorimer method using K_{AB} values generated from standard samples of known chemical composition [12].

Results

Variation of Mechanical Properties with Neutron Irradiation

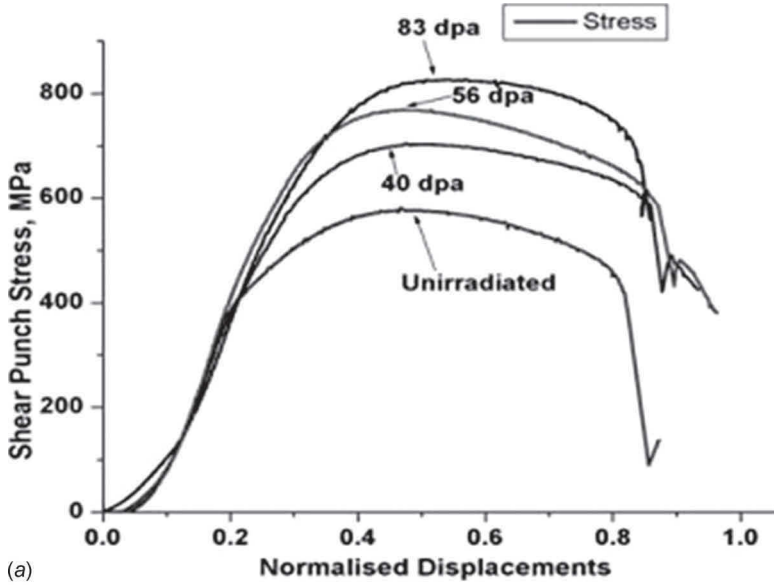
The shear punch load-displacement plot obtained for various irradiated conditions of SS316 is shown in Fig. 2(a). The linear slope, which is similar in elastic range in all the curves, suggests that there is negligible change in shear modulus due to increase in irradiation dose. The rate of work hardening is also low for the unirradiated steel and the specimen subjected to low dpa as compared to the high dpa specimen. Using the derived tensile-shear correlation, which is, similar to that reported by Hankin et al. [13], the tensile properties of irradiated SS316 wrapper were evaluated from the shear punch test parameters. The variation in properties as a function of dpa is shown in Fig. 2(b). It can be seen that there is an increase in the room temperature YS and UTS and a decrease in the percent uniform elongation with increasing dpa. The increase in UTS to 1200 MPa after 83 dpa neutron irradiation from the pre-irradiation value of 750 MPa indicates hardening behavior. The steel irradiated to 83 dpa showed a reduction in uniform elongation to about 8 %–10 % from about 20 % in the unirradiated material. It can be seen that the wrapper material possesses sufficient ductility at room temperature even after 83 dpa, which is very crucial to enhance the residence time of the fuel subassembly. The observed trends in tensile properties are in agreement with reports on SS316 subjected to neutron irradiation at low temperatures (<723 K) [14].

The volume increase ($\Delta V/V$) was estimated to be 2.3 % for 56 dpa specimen, which increased to about 3.5 % with increase in dpa to 83. The extent of volumetric swelling was found to be less in this case as compared to the data reported in the literature for material exposed to similar dpa levels [7]. This is attributed to the low irradiation temperature of about 673 K experienced by the wrapper during service in FBTR. The low swelling also shows that the material is far below the swelling limit and exhaustion of ductility. The observed trends in irradiation hardening are due to synergistic changes in the material with respect to substructure changes in and evolution of defects and secondary phases.

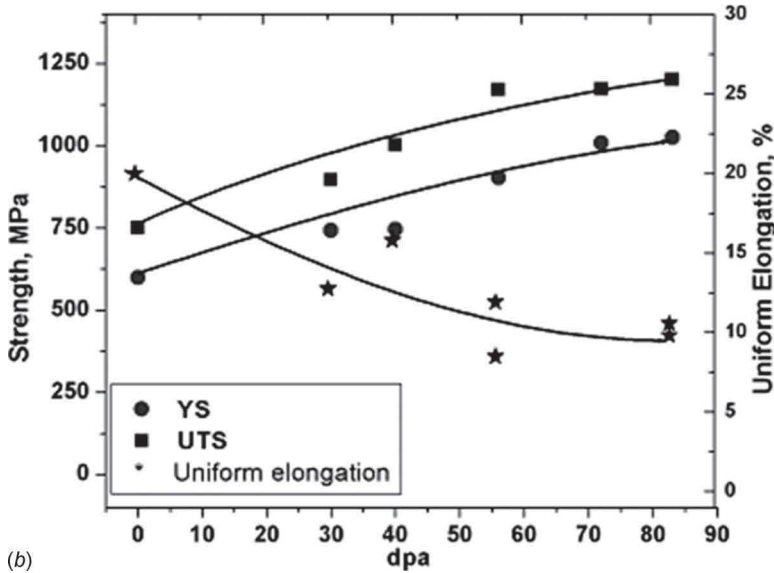
Evolution of Microstructure with Increasing dpa in 20 % CW SS316

The microstructure of the 20 % CW SS316 wrapper prior to reactor irradiation is shown in the thin foil TEM micrograph in Fig. 3. The dislocation network and slip bands, characteristic of the CW nature of the steel, can be clearly seen. No evidence for precipitates was observed in the thin foil. The microstructural changes due to neutron irradiation manifests itself as evolution of defects, voids, precipitates, and radiation induced phases, which have been studied in detail as a function of dpa. Irradiation at low doses of 1–2 dpa did not show any change in the microstructure as compared to unirradiated steel.

The TEM micrograph of the steel irradiated at 30 dpa is shown in Fig. 4. The presence of voids and defects such as dislocation loops is observed. The void sizes evaluated by image analysis procedures were in the range of 6–20 nm. The percentage swelling remained low at 30 dpa. Figure 5 shows the mi-



(a)



(b)

FIG. 2—(a) Evaluation of mechanical properties using shear punch test and (b) Variation of room temperature tensile properties with dpa in irradiated SS316.

crostructural changes at 40 dpa. A random distribution of voids is seen in Fig. 5(a), while Fig. 5(b) shows a co-development of voids and precipitates. The voids are observed to be of two types, namely precipitate attached voids and the matrix voids [15–17]. Although the voids have a wide size range (8–28 nm), it is



FIG. 3—CW structure of the unirradiated 316 stainless steel wrapper.

generally observed that the precipitate attached void has a larger size than the matrix void [18]. Examination of a large number of regions also showed the retention of CW structure and presence of dislocation loops. The TEM micrograph in Fig. 6(a) shows the presence of coarse inter and intragranular precipitates. A large number of precipitates were analyzed using a combination of diffraction and EDS analysis. The electron diffraction pattern showed the presence of cubic phase with lattice spacing that matched quite closely with $M_{23}C_6$ and M_6C type of phases. The EDS spectrum showed typical compositions of Cr ~ 30 wt %, Ni ~ 30 wt %, Mo ~ 10 wt %, Si ~ 10 wt %, and balance as Fe. This is in sharp contrast to the normalized composition of $M_{23}C_6$, which is predominantly chromium rich with higher than 60 % Cr, with a very low solubility for nickel and silicon. Using the Ni and Si content as a signature for distinction between the two phases [19], the precipitates associated with voids observed at 40 dpa in this study, are classified as M_6C type η phase. This is in agreement with literature reports where formation of radiation enhanced or modified η phase during irradiation at low temperatures (<833 K) has been observed [15,20,21]. However, the presence of $M_{23}C_6$ cannot be ruled out in the present study, which could be present at regions not associated with voids.

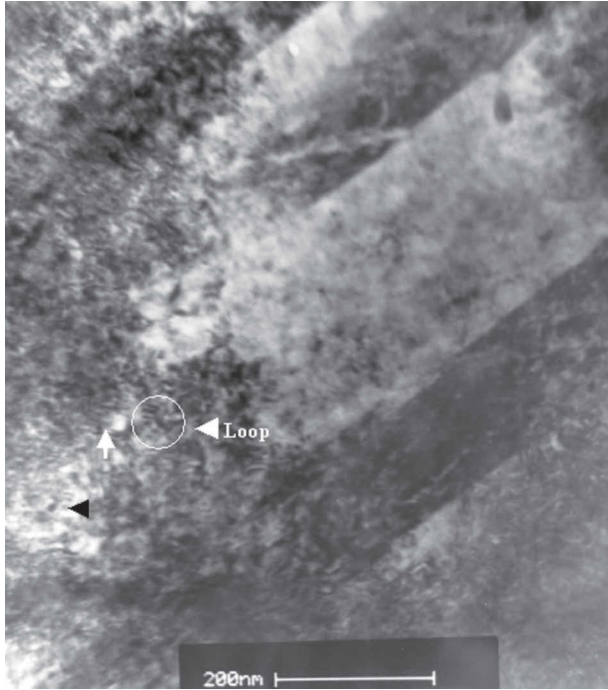


FIG. 4—Formation of voids and dislocation loops enhancing the defect density after irradiation to 30 dpa.

Increasing the irradiation dose to 83 dpa brought in several changes in the material. The retention of CW structure was unambiguously seen after 83 dpa irradiation [Fig. 7(a)]. This suggests that the temperature of operation has been low and no recrystallization has taken place. A random distribution of voids and precipitates of different sizes and morphologies was also observed [Fig.

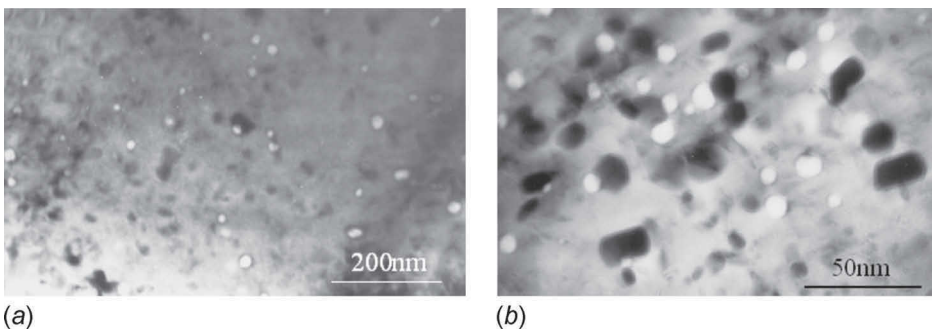


FIG. 5—A random distribution of voids in SS316 wrapper subjected to 40 dpa neutron irradiation.

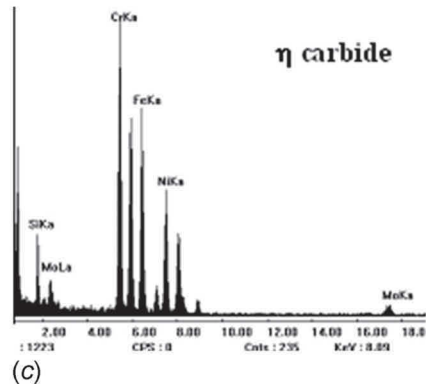
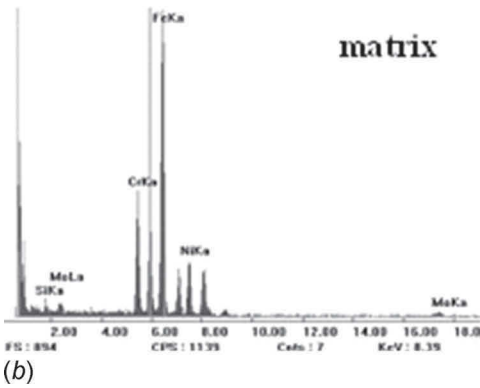
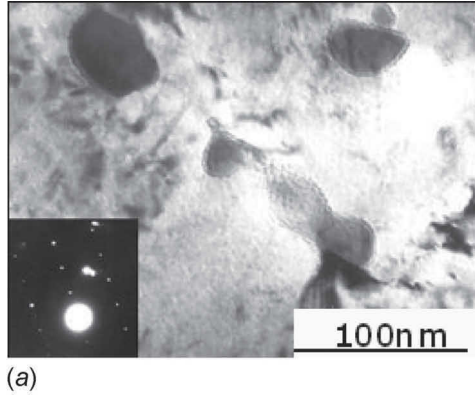


FIG. 6—(a) TEM bright field image of 40 dpa specimen showing coarse inter- and intragranular precipitates. SAD pattern in inset confirms M_6C carbides along $[611]$ zone axis. [(b) and (c)] EDS spectra from matrix and carbides clearly show the Cr and Ni rich nature of M_6C to distinguish it from $M_{23}C_6$ carbides. Segregation of Si into the precipitate as compared to matrix is also seen from the EDS spectrum.

7(b)]. The void sizes did not show much of a change. Based on a large number of measurements of void sizes from several regions, the void percentage was evaluated at different dpa, which showed an increase to only about 5.5 % at 83 dpa. It is observed that the percent swelling remains low at 30 dpa and shows an increasing trend.

Apart from the increased defect density, voids, and coarse η carbides, the specimen irradiated at 83 dpa showed additional features. The presence of fine precipitates in the size range of 10–20 nm was observed, which are shown in Figs. 8(a) and 8(b). The dark field image in Fig. 8(b) shows that these fine precipitates are associated with voids. Analysis of the diffraction pattern in Fig. 8(c) showed that these precipitates belong to the Ni and Si rich cubic G phase. The formation of radiation induced phases at higher dpa is also observed by other workers [15,20]. Due to the fine nature of the precipitates, the chemical

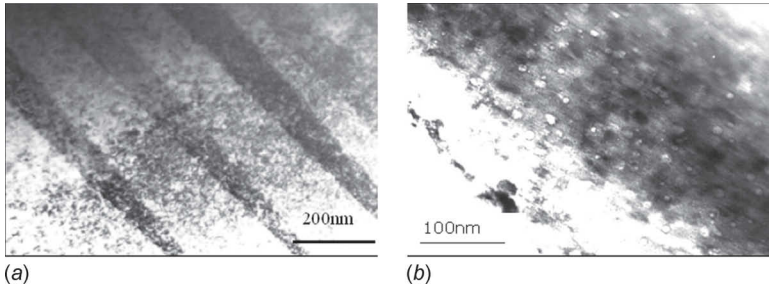


FIG. 7—(a) TEM micrograph showing retention of CW structure after 83 dpa irradiation and (b) presence of large number of voids and precipitates of different sizes.

composition could not be determined unambiguously. Further, quantitative estimation of each type of precipitate could not be carried out using the thin foil technique. The attachment of voids and precipitates can be attributed to the association of point defects with the diffusing elements, which later condense to form voids and fine precipitates. Although the presence of ordered Ni_3Si is also reported to form at low irradiation temperatures [15], no evidence could be found in the present work.

Careful examination of several regions of the specimen subjected to 83 dpa neutron irradiation showed the presence of fine twins. The bright and dark field micrographs from one such region is shown in Figs. 9(a) and 9(b). The diffraction pattern and the key are shown in Figs. 9(c) and 9(d). Analysis of the pattern showed that they are $\{111\}$ twins. It may be recalled that 3 mm diameter shear punched specimen have been used for the TEM studies, which could have given rise to the observed deformation twins.

The microstructural observations presented in this section can be summarized as increase in the defect and void density, enhanced precipitation of Ni and Si rich M_6C and formation of radiation induced G phase with increase in dpa. The absence of recrystallization further shows that irradiation hardening is pronounced rather than softening effects. This is in agreement with the observed trends in mechanical property. The low swelling of 2.5 % and 3.5 % at 56 and 83 dpa, respectively, evaluated by density measurement also supports this

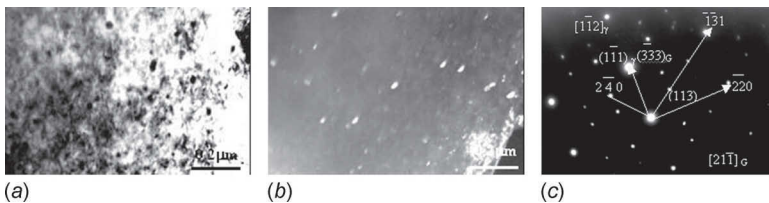


FIG. 8—[(a) and (b)] TEM bright and dark field micrographs showing the presence of fine precipitates in SS316 wrapper subjected to 83 dpa neutron irradiation and (c) SAD pattern identifying the fine precipitate as cubic G phase along $[2\bar{1}\bar{1}]$ zone axis.

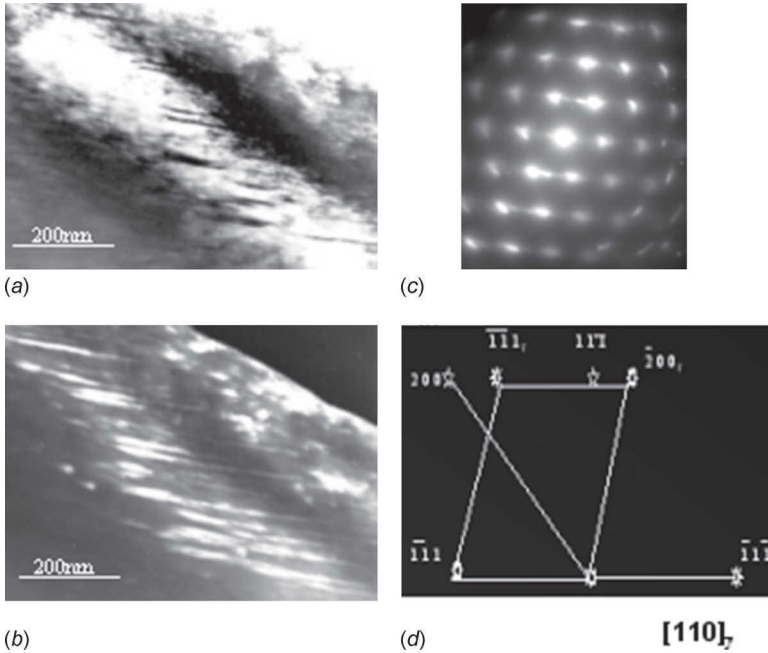


FIG. 9—TEM micrograph of SS316 wrapper subjected to 83 dpa neutron irradiation showing [(a) and (b)] bright and dark field images depicting fine deformation twins (c) SAD pattern from $[1-10]_{\gamma}$ confirming the formation of twins and (d) key for the SAD pattern in (c).

data. Further the ductility reduction is low, with a residual ductility of about 8 %, which indicates that the microstructural degradation is not severe.

Discussion

The similar slope in the stress versus displacement plot in Fig. 2 clearly demonstrated that change in irradiation dose had no effect on the shear modulus. On the other hand, the work hardening rate was low for unirradiated and low dose levels as compared to that of higher dose level. While hardening due to the generation of defects is understandable, the absence of any softening effect to offset the hardening is evident from the CW nature observed at 83 dpa and the low void density.

The precipitates most commonly encountered in SS316 is the Cr rich $M_{23}C_6$ phase, while under irradiation the formation of $M_{23}C_6$, M_6C , Laves phase (Fe and Mo), and γ' (Ni_3Si) are prevalent. The governing factor is primarily the kinetics, largely controlled by temperature, steel composition and irradiation dose. In the present study the formation of η phase can be understood as follows: The continuous production of point defects during neutron irradiation gives rise to diffusion of solute atoms either in the direction or

against that of the point defects. Several microstructural features like grain boundaries, dislocations, twin boundaries, defects, and precipitate-matrix interfaces act as sinks for point defects. They act as potential sites for segregation of solutes enhancing the local concentration of solutes. Nickel and silicon are two elements that are known to segregate under irradiation conditions. Silicon segregates due to its strong binding nature with defects, while nickel being a slow diffusing element has a tendency to remain at the sinks, while elements with higher diffusivity move away against the flow of vacancies [20,22,23]. This radiation induced segregation process causes nickel and silicon enrichment and chromium depletion (also Mo), which is reflected in the composition of the radiation modified phases and the surrounding matrix [24].

$M_{23}C_6$ is the stable carbide in austenitic stainless steels during thermal aging, with the chromium to iron ratio being strongly temperature dependent. It has been consistently observed in earlier studies [20] that $M_{23}C_6$ is predominantly Cr rich with very small amounts of Ni and Si and it remains structurally and compositionally same, irrespective of its formation by thermal aging or irradiation. Hence, it is justified to classify the Ni and Si enriched coarse precipitates observed at 40 and 83 dpa as the radiation modified or enhanced η phase.

The effect of silicon on void swelling is known to be beneficial only when it remains in solution. Segregation of Si into precipitates and the copious precipitation of nickel and silicon enriched phases could be responsible for the end of the incubation period and onset of measurable void swelling as seen in the specimen irradiated to 40 dpa [25,26]. Further the formation of Ni and Si enriched G phase at higher dose also shows the rapid removal of these beneficial elements from the matrix [20,24], resulting in a pronounced decrease in Ni content [25,26]. As voids strongly segregate nickel and with increasing fraction of voids in the microstructure, the spaces between the voids become increasingly depleted in nickel with a concomitant increase in chromium content. This could lead to decreased austenite stability, resulting in regions of ferrite or martensite. The formation of ferrite has not been observed in the present study.

Conclusions

The effect of neutron irradiation on the microstructure and mechanical properties were studied in the 20 % CW SS316 wrapper of FBTR. The main conclusions are as follows:

- The YS and UTS showed an increasing trend, while the ductility decreased with increasing dpa levels up to 83 dpa.
- Microstructural investigations revealed an increase in defect density and voids with increase in dpa. However, the percentage swelling was low ~ 5.5 % even at 83 dpa.
- Both precipitate associated voids and matrix voids were observed, with a distinct difference in the size distribution.
- Formation of radiation enhanced precipitates such as Ni and Si enriched η and radiation induced G phase was observed at higher dpa (>40 dpa).

- The mechanical property changes are consistent with the observed microstructures at different dpa.
- Volumetric swelling of wrapper was found to be low, with adequate margin in exhaustion of tensile ductility.

References

- [1] Mannan, S. L., Chetal, S. C., Baldev R., and Bhoje, S. B., "Selection of Materials for Prototype Fast Breeder Reactor," *Proceedings of Seminar on Materials R & D for PFBR*, S. L. Mannan and M. D. Matthew, Eds., IGCAR, Kalpakkam, India, 2003, pp. 9–43.
- [2] Lallement, R., Maikailoff, H., Mustellier, J. P., and Villeneuve, J., "Fast breeder reactor fuel design principles and performance," *Nucl. Energy*, Vol. 28, 1989, pp. 41–49.
- [3] Bailly, H., Menessier, D., and Prunier, C., *The Nuclear Fuel of Pressurized Water Reactors and Fast Neutron Reactors*, Lavoisier Publishing, Paris, 1999, pp. 16–36.
- [4] Garner, F. A., "Irradiation Performance of Cladding and Structural Steels in Liquid Metal Reactors," *Nuclear Materials, Part 1, Materials Science and Technology—A Comprehensive Treatment*, Vol. 10, B. R. T. Frost, Ed., VCH Publishers, New York, 1994, pp. 419–543.
- [5] Yang, W. J. S., "Precipitate Evolution in Type 316 SS Irradiated in EBR-II," *Radiation Induced Changes in Microstructure, 13th International Symposium, ASTM STP955*, F. A. Garner, N. H. Packan, and A. S. Kumar, Eds., ASTM International, West Conshohocken, PA, 1987, pp. 628–646.
- [6] Mannan, S. L. and Sivaprasad, P. V., *Encyclopedia of Materials Science and Engineering*, J. Buschow, R. W. Cahn, M. C. Flemings, B. Ilshner, E. J. Kramer, and S. Mahajan, Eds., Elsevier, New York, 2001, pp. 2857–2865.
- [7] Puigh, R. J. and Garner, F. A., "Neutron-Induced Swelling in Cold-Worked Titanium-Modified AISI 316 Alloys," *Radiation Induced Changes in Microstructure, 13th International Symposium, ASTM STP955*, F. A. Garner, N. H. Packan, and A. S. Kumar, Eds., ASTM International, West Conshohocken, PA, 1987, pp. 154–160.
- [8] Venkiteswaran, C. N., Parameswaran, P., Anandaraj, V., Karthik, V., Muralidharan, N. G., Venugopal, V., Saroja, S., Vijayalakshmi, M., Kasiviswanathan, K. V., and Baldev, R., "TEM Studies on Irradiated Wrapper of FBTR at Different Displacement Damages," *Advances in Stainless Steels*, University Press, India, 2009 (in press).
- [9] Lucas, G. E., "The development of small specimen mechanical test techniques," *J. Nucl. Mater.*, Vol. 117, 1983, pp. 327–329.
- [10] Lucas, G. E., Odette, G. R., and Shekherd, J. W., "The Use of Small-Scale Specimens for Testing Irradiated Materials," *ASTM STP888*, W. R. Corwin and G. E. Lucas, Eds., ASTM International, West Conshohocken, PA, 1986, pp. 112–140.
- [11] Karthik, V., Laha, K., Kasiviswanathan, K. V., and Baldev, R., "Determination of Mechanical Property Gradients in Heat-Affected Zones of Ferritic Steel Weldments by Shear-Punch Tests," *Small Specimen Test Techniques: Fourth Volume, ASTM STP1418*, M. A. Sokolov, J. D. Landes, and G. E. Lucas, Eds., ASTM International, West Conshohocken, PA, 2002 pp. 380–405.
- [12] Williams, D. and Carter, B., *Transmission Electron Microscopy—A Textbook for Materials Science*, Plenum Press, New York, 1996.
- [13] Hankin, G. L., Hamilton, M. B., Toloczko M. L., Garner F. A., and Faulkner R. G.,

- "Shear punch testing on ⁵⁹Ni isotopically-doped model austenitic alloys after irradiation in FFTF at different He/dpa ratios," *J. Nucl. Mater.*, Vols. 258–263, 1998, pp. 1657–1663.
- [14] Klueh, R. L., and Grassbeck, M. L., "Tensile Properties and Swelling of 20 % Cold-worked Type 316 Stainless Steel Irradiated in a High Flux Isotope Reactor (HFIR)," *12th International Symposium in Effects of Radiation on Materials, ASTM STP870*, F. A. Garner and J. S. Perrin, Eds., 1985, pp. 768–782.
- [15] Pedraza, D. F. and Maziasz, P. J., "Void—Precipitate Association During Neutron Irradiation of Stainless Steel," *13th International Symposium (Part I), Radiation Induced Changes in Microstructure: ASTM STP955*, F. A. Garner, N. H. Packan, and A. S. Kumar, Eds., ASTM International, West Conshohocken, PA, 1987, pp. 161–194.
- [16] Maziasz, P. J., "Some effects of increased helium content on void formation and solute segregation in neutron irradiated type 316 stainless steel," *J. Nucl. Mater.*, Vols. 108–109, 1982, pp. 359–384.
- [17] Lee, E. H., Maziasz, P. J., and Rowcliffe, A. F., "The Structure and Composition of Phases Occurring in Austenitic Stainless Steels in Thermal and Irradiation Environments," *Conference Proceedings of Phase Stability During Irradiation*, J. R. Holland, L. K. Mansur, and D. I. Potter, Eds., The Metallurgical Society of AIME, Warrendale, PA, 1981, pp. 257–270.
- [18] Ukai, S., Akasaka, N., Hattori, K., and Onose, S., "The Effects of Phase Stability on Void Swelling in P, Ti Modified 316 Stainless Steels During Neutron Irradiation," *Effects of Radiation on Materials: 18th International Symposium, ASTM STP1325*, R. K. Nanstad, M. L. Hamilton, F. A. Garner, and A. S. Kumar, Eds., ASTM International, West Conshohocken, PA, 1999, pp. 808–821.
- [19] Maziasz, P. J. and Odette, G. R. "Wide Area Beam Averaged AEM of Precipitate Particles Extracted on Replicas from Type 316 Stainless Steel," *Proceedings of the 41st Annual EMSA Meeting*, G. W. Bailey, Ed., San Francisco Press, Inc., San Francisco, CA, 1983, pp. 198–199.
- [20] Williams, T. M., "Stainless Steels 84," *International Conference Held at Chalmers University, Sweden*, The Institute of Metals London, London, UK, 1985, pp. 403–412.
- [21] Da Casa, C., Nileswhar, V. B., and Melford, D. A., "M₂₃C₆ precipitation in unstabilized stainless steel," *J. Iron Steel Inst., London*, Vol. 207, 1969, pp. 1325–1332.
- [22] Lam, N. Q. and Okamoto, P. R., "Solute segregation and precipitation under heavy-ion bombardment," *J. Nucl. Mater.*, Vol. 78, 1978, pp. 408–418.
- [23] Johnson, W. G., Morris, W. G., and Turkalo, A. M., "Radiation Effects in Breeder Reactor Structural Materials," *Metallurgical Society, AIME*, New York, 1977, pp. 421–430.
- [24] Hamilton, M. L., Yang, W. J. S., and Garner, F. A., "Mechanical Properties and Fracture Behaviour of 20 % Cold-Worked 316 Stainless Steel Irradiated to Very High Neutron Exposures," *Influence of Radiation in Material Properties: 13th International Symposium (Part II), ASTM STP956*, F. A. Garner, C. H. Henager, Jr., and N. Igata, Eds., ASTM International, West Conshohocken, PA, 1987, pp. 245–270.
- [25] Garner, F. A. and Wolfer, W. G., "Factors which determine the swelling behavior of austenitic stainless steels," *J. Nucl. Mater.*, Vol. 122, 1984, pp. 201–206.
- [26] Esmailzadeh, B., Kumar, A. S., and Garner, F. A., "The influence of silicon on void nucleation in irradiated alloys," *J. Nucl. Mater.*, Vols. 133–134, 1985, pp. 590–593.

M. N. Gusev,¹ O. P. Maksimkin,¹ I. S. Osipov,¹
N. S. Silniagina,¹ and F. A. Garner²

Unusual Enhancement of Ductility Observed During Evolution of a “Deformation Wave” in 12Cr18Ni10Ti Stainless Steel Irradiated in BN-350

ABSTRACT: Whereas most previous irradiation studies conducted at lower neutron exposures in the range 100–400°C have consistently produced strengthening and strongly reduced ductility in stainless steels, it now appears possible that higher exposures may lead to a reversal in ductility loss for some steels. A new radiation-induced phenomenon has been observed in 12Cr18Ni10Ti stainless steel irradiated to 26 and 55 dpa. It involves “a moving wave of plastic deformation” at 20 and 60°C that produces “anomalously” high values of engineering ductility, especially when compared to deformation occurring at lower neutron exposures. Due to the concentrated deformation occurring at the wave front, the wave moves much faster than the mechanically applied strain rate. However, when strained at 120°C the moving wave is not observed, indicating that the phenomenon operates at lower test temperatures. Using the technique of digital optical extensometry, the “true stress–true strain” curves were obtained. It appears that the moving wave of plastic deformation occurs as a result of an increase in the strain hardening rate, $d\sigma/d\varepsilon(\varepsilon)$. The increase in strain hardening is thought to arise from an irradiation-induced increase in the propensity of the $\gamma \rightarrow \alpha$ martensitic transformation.

KEYWORDS: deformation wave, 12Cr18Ni10Ti stainless steel, high damage dose, martensite

Manuscript received August 6, 2008; accepted for publication June 2, 2009; published online August 2009.

¹ Institute of Nuclear Physics, Almaty 050032, Kazakhstan.

² Pacific Northwest National Laboratory, Richland, WA 99352.

Cite as: Gusev, M. N., Maksimkin, O. P., Osipov, I. S., Silniagina, N. S. and Garner, F. A., “Unusual Enhancement of Ductility Observed During Evolution of a “Deformation Wave” in 12Cr18Ni10Ti Stainless Steel Irradiated in BN-350,” *J. ASTM Intl.*, Vol. 6, No. 7. doi:10.1520/JAI102062.

Copyright © 2009 by ASTM International, 100 Barr Harbor Drive, PO Box C700, West Conshohocken, PA 19428-2959.

Introduction

It is generally accepted that irradiation of stainless steels at temperatures of 100–400 °C leads to a rapid increase in strength and to a concurrent reduction in both uniform and total elongation during deformation, a behavior that is clearly seen in “engineering” stress-strain curves and that is almost always associated with early flow localization leading to necking [1,2].

Using a technique called “digital marker extensometry,” however, we have shown recently that the stress-strain deformation characteristics (true stress–true deformation) continue unchanged in the necking region even though the remainder of the specimen no longer participates in the deformation process [3,4]. This extensometer techniques involves marking the surface of the specimen with small dots and recording both the macroscopic and local deformation with a video camera during the tensile test.

Another well-accepted perception is that continued neutron exposure quickly leads to a saturation in mechanical properties that remains unchanged until significant void swelling is attained [5–9]. It now appears that this perception must be at least partially modified for relatively low irradiation temperature and very high fluence exposure, especially for steels prone to martensite instability. In this paper we demonstrate that the anticipated trend toward reduced elongation with increasing exposure is reversed at relatively high neutron dose (26–55 dpa).

This study addresses this new phenomenon of increased ductility primarily on a general scientific level, but it is also being studied for possible application to evaluation of possible relevance to plant life extension of pressurized water reactors. The baffle-former assembly that surrounds a pressurized water reactor (PWR) core is constructed from similar low-nickel steels irradiated at temperatures and neutron exposures comparable to those of this study. The recovery of ductility at higher doses may allow less conservatism in evaluation of component lifetime and may allow more aggressive handling at low temperatures characteristic of zero power after shutdown.

Experimental Details

A hexagonal wrapper constructed from 12Cr18Ni10Ti steel (nominal chemical composition, wt %: 0.10%–0.12%C, 17.5%–19%Cr, 9%–10.5%Ni, 0.5%Ti) was removed from two spent fuel assemblies designated CC-19 and H-42 after irradiation in the reflector region of the BN-350 fast reactor. The wrapper walls were 2 mm thick with face-to-face distance of 96 mm. The wrapper was annealed at 1050 °C for 30 min and formed with a final cold deformation of 15%–20%, followed by annealing at 800 °C for 1 h. The irradiation conditions of the examined regions are shown in Table 1.

Cross sections of 10 mm height were cut at various elevations between +500 and –160 mm measured relative to the core center-plane. From these sections the flat rectangular specimens with dimensions 20 mm in length, 2 mm in width, and 0.3 mm in thickness were mechanically produced. Subsequently, mini-tensile specimens with gauge length of 7–10 mm, width 2 mm, and thickness 0.3 mm were produced by mechanical grinding and electrolytic

TABLE 1—Position and irradiation conditions of investigated samples.

Assembly	Distance from the Center of the Core, mm	Irradiation Temperature, °C	Dose, dpa
H-42	-300	290	13
CC-19	+500	423	26
CC-19	-160	310	55

polishing to achieve the desired dimensions and surface quality.

Pneumatic grips were used for holding the specimen in an Instron-1195 tensile machine. Uniaxial tensile tests on both unirradiated and irradiated specimens were performed at strain rates of 8.3×10^{-3} , 8.3×10^{-4} , and $8.3 \times 10^{-5} \text{ s}^{-1}$. Most samples were tested at 20°C , but some experiments were conducted at elevated temperatures (up to 120°C).

A technique called "digital marker extensometry" was used which incorporates digital photo or video recording of the specimen during deformation. The surface of the specimen was marked with small ($\sim 0.3 \text{ mm}$) dots of dye in order to track the deformation on a local level. This technique was described in an earlier report and is especially useful in observing highly irradiated miniature specimens subject to intense flow-localization [3,4]. Application of this technique makes it possible to obtain the true stress-true strain behavior for a miniature specimen, as well as to identify the localized deformation region and to trace its evolving geometry during continuous deformation.

The first observation of the moving wave phenomenon was reported recently [10]. This current paper reports on a wider variety of tests conducted to examine this newly discovered deformation mode.

Results

The measured values of strength and ductility are shown in Table 2 for different test temperatures and applied strain rate. The data for strength agree well with

TABLE 2—Mechanical properties of investigated samples.

Assembly Level, mm	Dose, dpa	Test Temperature, °C	Strain Rate, s^{-1}	σ_{02} , MPa	σ_B , MPa	ϵ_u , %	ϵ_T , %	Presence of wave
H-42	13	20	8.3×10^{-4}	860	1060	<2	6-7	No
CC-19 +500	26	20	8.3×10^{-4}	780	930	18	18.5	Yes
CC-19 +500	26	20	8.3×10^{-3}	800	1030	48	48	Yes ^a
CC-19 +500	26	20	8.3×10^{-5}	790	950	21	21.5	Yes
CC-19 -160	55	20	8.3×10^{-4}	960	1070	20	22	Yes
CC-19 +500	26	60	8.3×10^{-4}	740	850	40	43	Yes ^a
CC-19 -160	55	120	8.3×10^{-4}	940	980	~ 1	<4	No

^aSamples having two deformation waves are marked with a star.

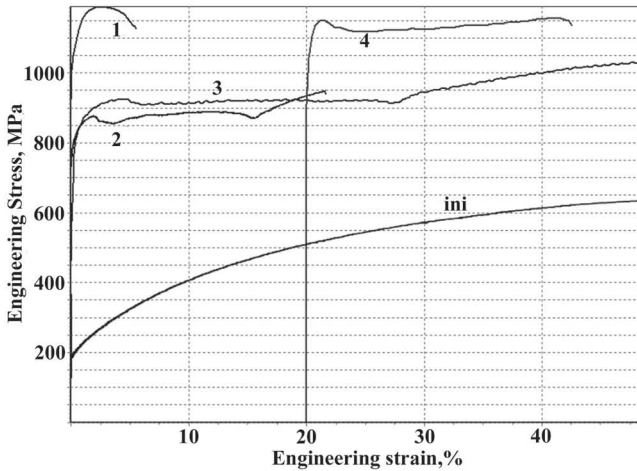


FIG. 1—Engineering curves for irradiated samples tested at 20°C (curve 1, 13.2 dpa; curves 2 and 3, 26 dpa; curve 4, 55 dpa (this curve was shifted to the right to avoid overlap). Curves 2 and 3 are at the same material and irradiation conditions, with curve 2 showing a single-wave case, and curve 3 showing a double-wave case (see comments in text). The curve designated “ini” is derived from an unirradiated specimen.

most data found in the literature. The observed plasticity in the H-42 assembly (13 dpa) also agrees well with typical literature values.

In Fig. 1 the engineering diagrams of four irradiated specimens are shown. The unirradiated steel is characterized by high ductility and high ability to strain harden with the ultimate stress σ_B significantly greater than the yield stress $\sigma_{0.2}$. Following irradiation to ~ 13 dpa at 290°C the yield stress of samples made from assembly H-42 strongly increases and a neck develops just after reaching the yield point. The uniform elongation ϵ_u is very small ($< 2\%$) and the total ductility ϵ_T falls to 6%–7%.

Based on current perceptions of saturation, one would expect that steel irradiated up to 55 dpa would achieve deformations $< 6\%$ – 7% , even in the absence of void swelling. However, ductility levels of 19%–48% were achieved in specimens tested at 20–60°C. This result was confirmed by other tests to be typical and not an anomaly. Note that after a small decrease in strength after yielding (see picture 1, curves 2–4) there is an extended plateau without significant increase in load. When tested at 120°C, however, the ductility fell to $< 4\%$ and no moving wave was observed. Over the range tested there does not seem to be any significant influence of strain rate (see Table 2, CC-19 assembly, +500 level).

As shown in Fig. 2, a series of freeze-frame video images taken during tensile testing at 20°C of a 55 dpa sample shows that localized deformation initially forms near the upper gripper position, most likely due to the stress concentration and triaxiality induced by the gripper. However, in contrast to irradiation to lower doses, a stable immobile neck did not develop at either 26

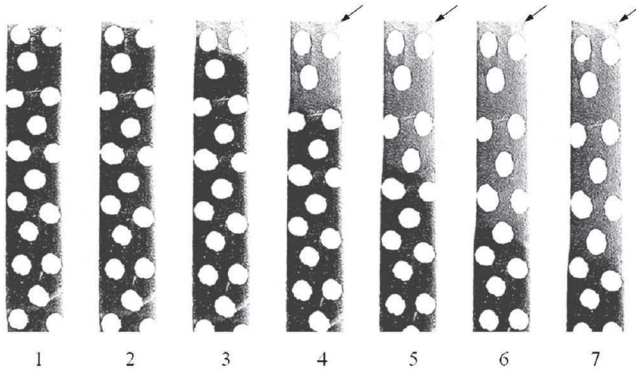


FIG. 2—Freeze frame images taken during deformation at 20°C of a specimen irradiated to 55 dpa. Photographs have been digitally processed to increase the contrast. The boundary between the lighter distorted and darker undistorted areas moves downward with time. Elongated dots behind the boundary also show the local distortion. Arrows on photos 4 to 7 show the second later-developing and immobile neck.

or 55 dpa. The localized deformation band instead progressively extended its lower boundary, producing a moving deformation front (deformation wave) that moved down the specimen. The wave moved along $\sim 2/3$ of the specimen length producing total engineering deformation on the order of 20%. All of the deformation at a given instant appeared to occur at the wave front with material behind or in front of the wave essentially not participating in the deformation process.

Due to the concentrated deformation occurring at the wave front, the wave moves much faster than the mechanically applied strain rate. For example, in the 55 dpa specimen tested at 20°C, the wave front moved at ~ 0.04 mm/s while the applied strain rate was only 0.008 mm/s.

In some cases two deformation waves occurred on a specimen, as illustrated in Fig. 3. These waves started near each grip and progressed in opposite directions. Usually the second wave begins just after the first wave stops. There was one example, however, where simultaneous movement of two waves was

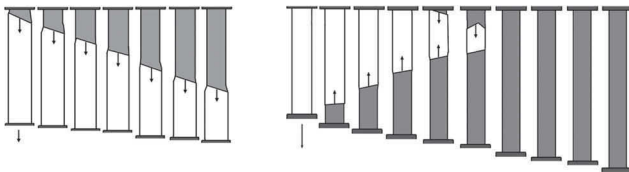


FIG. 3—Schematic illustrations of deformation waves for single-wave (left) and double-wave (right) cases. A typical single wave starts moving from one grip and stops about $2/3$ of sample length in both cases. Shortly after the first wave stops the second wave starts from the other grip. In the two-wave case there is no undeformed space remaining on the specimen.

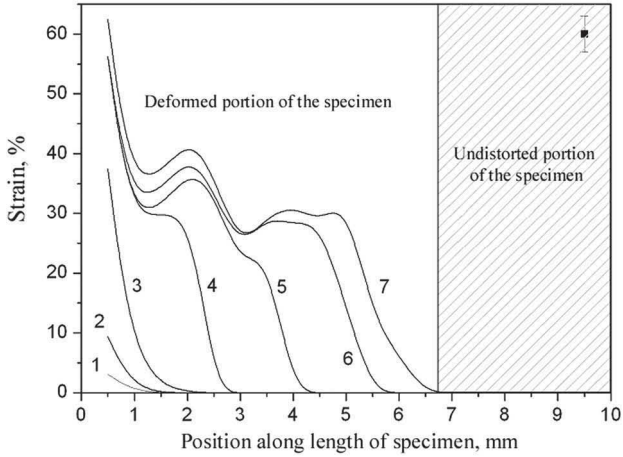


FIG. 4—Distribution of local deformation along the length of the specimen irradiated to 55 dpa at various stages of the experiment.

observed. Two waves produced the highest total engineering deformation of 40 %–48 %. In no case was the second wave observed to pass through the terminal position of the first wave.

Figure 4 shows the distribution of local deformation over length of a 55 dpa specimen as the test progressed. An abrupt increase in local deformation from zero up to 30 %–35 % was observed at the moment the deformation front passes. Failure with local deformation exceeding 60 % occurred very near to the original place where the deformation wave appeared.

The local strain observed in the case of two waves meeting is the same as for other parts of specimen, indicating that additional strain did not arise from passage of the second wave through the region traversed by the first wave. Close examination of the video sequences showed that cross-passing of two waves was never detected during the experiment.

Discussion

The condition for occurrence and development of localized deformation of the neck is [8,9]

$$d\sigma/d\varepsilon \leq \sigma, \quad (1)$$

which can be rewritten in more convenient form:

$$d\sigma/d\varepsilon - \sigma \leq 0. \quad (2)$$

One can show that localization of deformation in compliance with a given condition starts at the moment when local strain hardening can no longer compensate for geometrical “softening” which occurs as a result of a decrease in the specimen cross section.

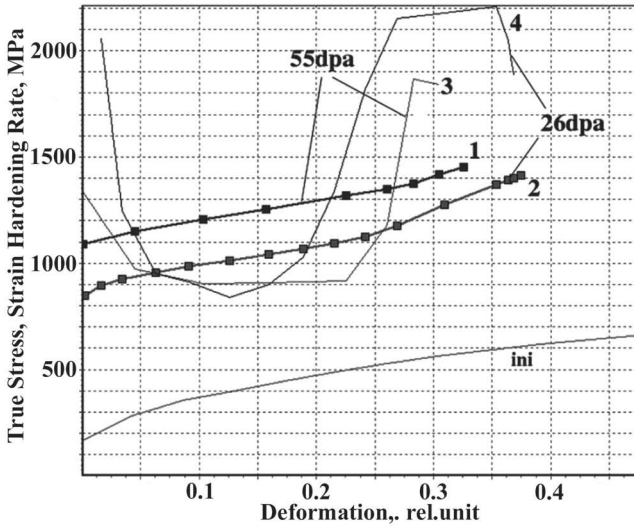


FIG. 5—Curves of σ - ϵ (1, 2, ini) and $d\sigma/d\epsilon$ - ϵ (3, 4) for unirradiated 12Cr8Ni10Ti specimen (ini) and also for 26 dpa (2, 4) and 55 dpa (1,3) specimens. The dimensions and scale for the $d\sigma/d\epsilon$ - ϵ curves are the same as for the σ - ϵ curves.

It was earlier shown by Byun et al. [11] that for Cr-Ni steels the localized deformation occurs at a stress value $\sigma_L \sim 900$ MPa and this value only weakly depends on damage dose. For some samples investigated in this study the yield stress exceeds 900 MPa ($\sigma_{02} > \sigma_L$), so localization of deformation occurs immediately after the yield stress is reached.

It is clear that for cessation of local neck formation and displacement of the deformation into neighboring, less deformed space, the law which governs hardening must be altered, i.e., it is necessary that relation 2, on achieving a certain extent of deformation, becomes invalid. As a rule this does not happen in either unirradiated or neutron-irradiated pure metals, where $d\sigma/d\epsilon$ always decreases as the strain increases (see unirradiated pure metals labeled ini in Fig. 5). If Luders bands are formed, as observed in pure iron, then an exception to this situation occurs.

Figure 5 presents “stress-deformation” curves obtained using the marker extensometry technique. Almost immediately on reaching the yield point, $d\sigma/d\epsilon$ - ϵ reduces to negative values, and the neck develops. However, in contrast to other materials we have studied, at local deformations of $\sim 25\%$ – 30% a smooth upward trend is observed in the “ σ - ϵ ” curve. As $d\sigma/d\epsilon$ increases the value of $d\sigma/d\epsilon$ - ϵ becomes positive, indicating that strain hardening rate is increasing strongly.

Apparently it is the increase in $d\sigma/d\epsilon$ that leads to suppression of development of a local neck, thereby displacing the deformation source to neighboring, undeformed space, generating the deformation wave. We consider it to be very significant that the second late-forming deformation band could not move

through the previously deformed region. It is also significant that at the front of the wave local deformations are very large at $>30\%$.

One potential source of the wave phenomenon is the $\gamma \rightarrow \alpha$ martensitic transformation. This low-nickel steel is known to be very sensitive to strain-induced α -martensite formation, especially during room temperature deformation, and to increase in propensity toward martensite with radiation-induced hardening and radiation-induced segregation [12,13]. The fact that this behavior occurs at higher exposures but not at lower doses where saturation of strength had already occurred may reflect some second-order effect such as the progressive transmutation-induced loss of Mn or build-up of V [14], or the progressive radiation-induced segregation of some other chemical elements. Nickel, in particular is known to segregate at microstructural sinks and chromium migrates away from these same sinks.

Increases in deformation speed from 8.3×10^{-5} to $8.3 \times 10^{-3} \text{ s}^{-1}$ (i.e., two orders of magnitude) might be expected to influence the formation of a deformation wave via strain-induced temperature increases, especially if a martensite transformation is occurring, a process known to be temperature-sensitive. However, such an effect was not observed in this rather limited series of tests. It is significant, however, that at $8.3 \times 10^{-4} \text{ s}^{-1}$ an increase in test temperature from 60 to 120°C led to a cessation of wave behavior. This might suggest that the double wave case might be controlled by parameters such as the temperature of the test as well as the applied strain rate. A larger number of specimens will be tested in later studies to address this possibility.

Similar deformation behavior involving an increase in strain hardening rate has been observed in this same steel in the unirradiated condition during deformation at cryogenic temperatures [15]. Intense martensitic transformation was cited as the cause, but the digital marker extensometry technique (or other vision system) was not used so it is not certain whether a deformation wave was associated with this behavior.

The possibility exists that this phenomenon may have been observed but not fully appreciated in an earlier study by Lapin and co-workers on this same steel when it was tested at 20°C after irradiation at $100\text{--}300^\circ\text{C}$ [16]. They observed a tendency for elongation to exhibit a minimum at relatively low dpa levels and then tend to increase at higher dose. There were no observations made of the mode of elongation or details of the specimen post-tensile morphology, however.

This study has focused on this new phenomenon of increased ductility primarily on a general scientific level, but it is also may be relevant for possible application to evaluation of relevance to plant life extension of Western pressurized water reactors. The baffle-former assembly that surrounds a PWR core is constructed from similar low-nickel steels irradiated at temperatures and neutron exposures comparable to those of this study. The recovery of ductility at higher doses may allow less conservatism in evaluation of component lifetime and may allow more aggressive handling at low temperatures characteristic of zero power after shutdown.

Conclusion

A new radiation-induced phenomenon has been observed in steel 12Cr18Ni10Ti irradiated to 26 and 55 dpa. It involves a moving wave of plastic deformation at 20–60°C that produces anomalously high values of engineering ductility, especially when compared to deformation occurring at lower neutron exposures or for more stable steels. Using the technique of digital extensometry the true stress–true strain curves were obtained. It appears that the moving wave of plastic deformation occurs as a result of an increase in the strain hardening rate, $d\sigma/d\varepsilon(\varepsilon)$. The increase in strain hardening is thought to arise from an irradiation-induced increase in the propensity of the $\gamma \rightarrow \alpha$ martensitic transformation.

Acknowledgments

The Kazakh portion of this work was supported by the Ministry of Energy and Mineral Resources of the Republic of Kazakhstan. The U.S. portion was sponsored by the Office of Fusion Energy Sciences, U.S. Department of Energy under Contract No. DE-AC06-76RLO at Pacific Northwest National Laboratory.

References

- [1] Was, G., *Fundamentals of Radiation Materials Science*, Springer, New York, 2007.
- [2] Voyevodin, V. N. and Neklyudov, I. M., *Evolution of the Structure Phase State and Radiation Resistance of Structural Materials*, Naukova Dumka, Kiev, 2006.
- [3] Maksimkin, O. P., Gusev, M. N., and Osipov, I. S., “Deformation Extensometry during Mechanical Tests of Highly Radioactive Metal and Alloy Specimens,” *Information News of the National Nuclear Center of the Republic of Kazakhstan*, 2005, issue 1, pp. 46–52.
- [4] Gusev, M. N., Maksimkin, O. P., Osipov, I. S., and Garner, F. A., “Application of Digital Marker Extensometry to Determine the True Stress-Strain Behavior of Irradiated Metals and Alloys,” *Proceedings of Fifth International Symposium on Small Specimen Test Technology, STP 1502*, ASTM International, West Conshohocken, PA.
- [5] Garner, F. A., Hamilton, M. L., Panayotou, N. F., and Johnson, G. D., “The Microstructural Origins of Yield Strength Changes in AISI 316 during Fission or Fusion Irradiation,” *J. Nucl. Mater.*, Vols. 103–104, 1981, pp. 803–808.
- [6] Garner, F. A., “Irradiation Performance of Cladding and Structural Steels in Liquid Metal Reactors,” *Materials Science and Technology: A Comprehensive Treatment*, Vol. 10A, VCH Verlagsgesellschaft mbH, Weinheim, Federal Republic of Germany, 1994, Chap. 6, pp. 419–543.
- [7] Hamilton, M. L., Huang, F. H., Yang, W. J. S., and Garner, F. A., “Mechanical Properties and Fracture Behavior of 20 % Cold-Worked 316 Stainless Steel Irradiated to Very High Exposures,” *Effects of Radiation on Materials: Thirteenth International Symposium (Part II) Influence of Radiation on Material Properties*, ASTM STP 956, F. A. Garner, N. Igata, and C. H. Henager, Jr., Eds., ASTM International, Philadelphia, PA, 1987, pp. 245–270.
- [8] Parshin, A. M., “Structure Resistibility and Radiation Damage in Corrosion-

- resistant Steels and Alloys," *Chelyabinsk, Metallurgy*, Chelyabinsk Department of Metallurgy, Chelyabinsk, 1988, p. 656 (in Russian).
- [9] Barabash, V., The ITER International Team, Peacock, A., Fabritsiev, S., Kalinin, G., Zinkle, S., Rowcliffe, A., Rensman, J.-W., Tavassoli, A. A., Marmy, P., Karditsas, P. J., Gillemot, F., and Akiba, M., "Materials Challenges for ITER—Current Status and Future Activities," *J. Nucl. Mater.*, Vols. 367–370, 2007, pp. 21–32.
- [10] Gusev, M. N., Maksimkin, O. P., Osipov, I. S., and Garner, F. A. "Anomalously Large Deformation of 12Cr18Ni10Ti Austenitic Steel Irradiated to 55 dpa at 310°C in the BN-350 Reactor," *J. Nucl. Mater.*, Vol. 386–388 (2009), pp. 273–276.
- [11] Byun, T. S., Hashimoto, N., and Farrell, K., "Deformation Mode Map of Irradiated 316 Stainless Steel in True Stress–Dose Space," *J. Nucl. Mater.*, Vol. 351, 2006, pp. 303–315.
- [12] Maksimkin, O. P. and Kadyrzhanov, K. K. "Martensitic Transformations in Neutron Irradiated and Helium Implanted Stainless Steels," *21st International Symposium on Effects of Radiation on Materials, ASTM STP1447*, 2004, ASTM International, West Conshohocken, PA, pp.105–118.
- [13] Nagy, E., Mertinger, V., Tranta, F., and Sólyom, J., "Deformation Induced Martensitic Transformation in Stainless Steels," *Mater. Sci. Eng., A*, Vol. 378, 2004, pp. 308–313.
- [14] Bates, J. F., Garner, F. A., and Mann, F. M., "The Effects of Solid Transmutation Products on Swelling in AISI 316 Stainless Steel," *J. Nucl. Mater.*, Vol. 103–104, 1981, p. 999.
- [15] Byun, T. S., Hashimoto, N., and Farrell, K., "Temperature Dependence of Strain Hardening and Plastic Instability Behavior in Austenitic Stainless Steels," *Acta Mater.*, Vol. 52, 2004, pp. 3889–3899.
- [16] Lapin, A. N., Nikolaev, V. A., and Razov, I. A., *Fiz. Khim. Obrab. Mater.*, Vol. 1, 1970, pp. 9–12.

K. Kondo,¹ Y. Miwa,¹ T. Tsukada,¹ S. Yamashita,² and
K. Nishinoiri²

Interrelationship between True Stress–True Strain Behavior and Deformation Microstructure in the Plastic Deformation of Neutron-Irradiated or Work-Hardened Austenitic Stainless Steel

ABSTRACT: True stress–true strain relation and deformation microstructure have been examined for high purity Fe-18Cr-12Ni alloy and its alloys doped with 0.7 wt % Si or 0.09 wt % C. In high purity alloy and C-doped alloy irradiated at 240°C up to 3 dpa, the work hardening rate is equivalent to that in unirradiated alloys. These alloys show dislocation channel structure after irradiation and deformation. In irradiated Si-doped alloy, however, the work hardening rate is different from that in unirradiated alloys. This alloy shows fully developed dislocation cell structure after deformation, as seen in unirradiated deformed stainless steels. The cell structure in irradiated Si-doped alloy was much smaller than that in unirradiated Si-doped alloy and in type 316L stainless steel. One of the factors affecting the change in the work hardening rate of irradiated austenitic stainless steel at 240°C is strong obstacles such as γ precipitate that acts as dislocation pinning and dislocation loops such as Frank loops that do not act as obstacles.

Manuscript received February 2, 2009; accepted for publication October 1, 2009; published online November 2009.

¹ Research Group for Corrosion Damage Mechanism, Nuclear Science and Engineering Directorate, Japan Atomic Energy Agency, 2–4 Shirakata-Shirane, Tokai-mura, Ibaraki-ken 319-1195, Japan.

² Materials Monitoring Section, Fuels and Materials Department, Oarai Research and Development Center, Japan Atomic Energy Agency, 2–4 Shirakata-Shirane, Tokai-mura, Ibaraki-ken 319-1195, Japan.

Cite as: Kondo, K., Miwa, Y., Tsukada, T., Yamashita, S. and Nishinoiri, K., “Interrelationship between True Stress–True Strain Behavior and Deformation Microstructure in the Plastic Deformation of Neutron-Irradiated or Work-Hardened Austenitic Stainless Steel,” *J. ASTM Intl.*, Vol. 7, No. 1. doi:10.1520/JAI102358.

Copyright © 2010 by ASTM International, 100 Barr Harbor Drive, PO Box C700, West Conshohocken, PA 19428-2959.

KEYWORDS: austenitic stainless steel, neutron irradiation, plastic deformation, dislocation channel, dislocation cell, true stress–true strain relation, work hardening rate

Introduction

In aged light water reactors, the in-reactor materials lose ductility due to radiation hardening. Radiation hardening may also affect irradiation-assisted stress corrosion cracking. It is reported that the radiation hardening is caused by the formation of Frank loops, and the loss of ductility including a decrease in the work hardening rate is affected by dislocation channeling [1–4]. However, only a limited number of studies have been conducted on the relationship between true stress–true strain relation and the plastic deformation microstructure in the neutron-irradiated stainless steels (SSs). This study compares their relationship by using neutron-irradiated stainless steels that have different microstructures.

Experimental Details

Samples

High Purity 304 and Its Alloys Doped with Carbon or Silicon [5,6]—High purity Fe-18Cr-12Ni alloy (hereafter HP304) and its alloys with addition of C or Si (hereafter HP304/C and HP304/Si, respectively) were used for irradiation experiments. Table 1 shows chemical compositions of these alloys. Solution anneal condition for HP304 and HP304/Si was at 975°C for 0.5 h and 1050°C for 0.5 h for HP304/C. A round bar type tensile specimen and a sheet type miniature tensile specimen (type SS-3) were fabricated from plates of these alloys, and the longitudinal direction of these specimens was parallel to the rolling direction of the plates. The gauge dimensions of the round bar type specimens were 24 mm in length and 4 mm in diameter. Neutron irradiation experiment was conducted at about 240°C to dose levels ranging from 1 to 5.5 dpa in the Japan Research Reactor No. 3. Authors reported that these alloys showed different engineering stress-strain curves and microstructures, especially for Frank loops development [5,6]. Table 2 summarizes the average diameter and the number density of Frank loops in each material after 1 dpa irradiation. Solute addition to HP304 resulted in the variation in the microstructural character after the neutron irradiation.

TABLE 1—*Chemical compositions of high purity alloys and type 316 stainless steel.*

Alloy	C	Si	Mn	P	S	Ni	Cr	Mo	N	Fe
HP304	0.003	0.01	1.36	0.001	0.0014	12.27	18.17		0.0014	Bal.
HP304/C	0.098	0.03	1.39	0.001	0.0020	12.50	18.30		0.0016	Bal.
HP304/Si	0.003	0.69	1.36	0.001	0.0014	12.24	18.01		0.0014	Bal.
316SS	0.05	0.56	0.83	0.028	0.001	10.09	16.20	2.09		Bal.

TABLE 2—Frank loops distribution in 1 dpa irradiated specimen.

	Ave. Diameter (nm)	Number Density (m ⁻³)	Distribution
HP304	11	6.6×10^{22}	Uniform
HP304/C	7	1.4×10^{23}	Uniform
HP304/Si	~5	$<1 \times 10^{22}$	Only near dislocation lines

Unirradiated Work-Hardened Type 316 SS—In order to compare plastic deformation behavior in unirradiated work-hardened austenitic stainless steel, type 316 stainless steel was used. The compositions are also listed in Table 1. The plate of the steel was solution annealed at 1100°C for 0.5 h; then the plate was heat treated at 650°C for 100 h. The plate was warm-rolled at about 350°C for reduction in thickness ranging from 10 % to 50 %. The round bar type tensile specimens were prepared from the warm-rolled plate. The longitudinal direction of the specimens is parallel to the rolling direction.

Tensile Test and Microstructural Observation

Tensile tests were conducted on both neutron-irradiated and warm-rolled specimens at 289–300°C with a strain rate of $\sim 1.0 \times 10^{-4}$ /s in air or vacuum conditions. The obtained engineering stress-strain curves before the occurrence of plastic instability were converted to calculated true stress-strain curves by the following equations:

$$\sigma_{\text{true}} = \sigma_{\text{engineering}}(1 + \varepsilon_{\text{engineering}}) \quad (1)$$

$$\varepsilon_{\text{true}} = \ln(1 + \varepsilon_{\text{engineering}}) \quad (2)$$

The work hardening rate, n , was approximated by the following equation [7]:

$$\sigma_{\text{true}} = f(\varepsilon_{\text{true}}) = A(\varepsilon_0 + \varepsilon_{\text{true}})^n \quad (3)$$

Microstructural observation was carried out using transmission electron microscopy (TEM) operated at 400 and 200 kV. Figure 1 shows the schematic illustration of TEM specimens sampling. Samples were taken from the uniformly elongated part of tensile tested specimens. In this sample, the microstructure just before plastic instability is observed, and the main stress direction is perpendicular to observed planes.

Result

Neutron Irradiated Alloys

Tensile Property—Figure 2(a)–2(c) shows the engineering stress-strain curves of neutron-irradiated HP304, HP304/C, and HP304/Si, respectively. Overall, after the neutron irradiation, the increase in yield stress and the loss of ductility were observed. The work hardening ability in engineering stress-strain

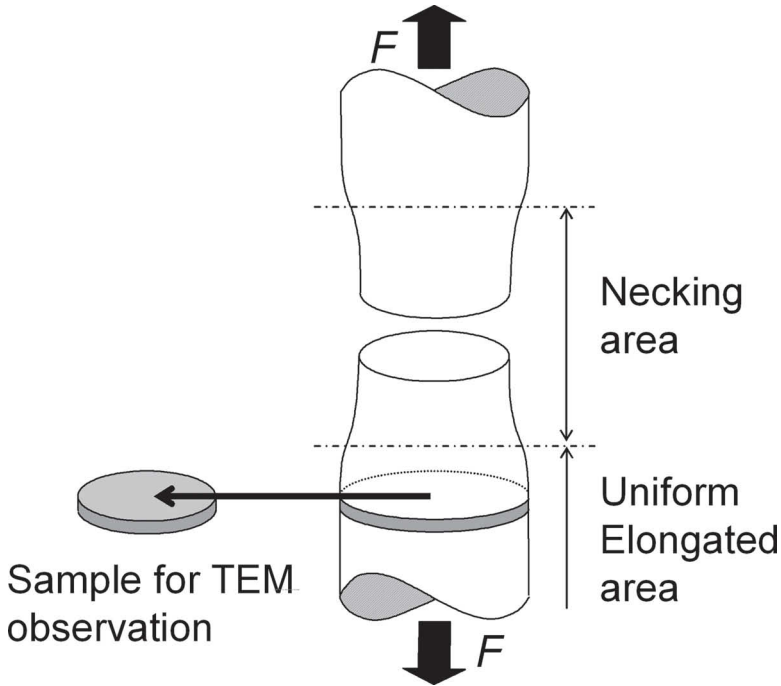
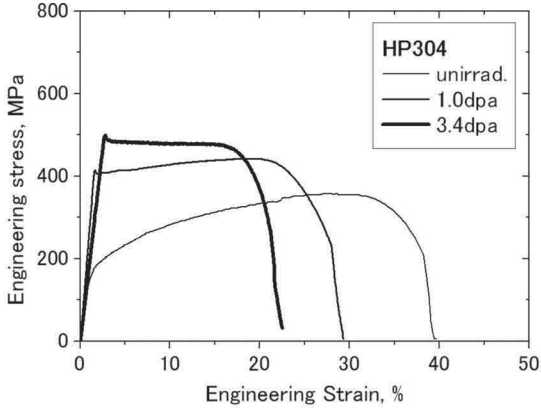


FIG. 1—Schematic illustration of TEM specimens sampling.

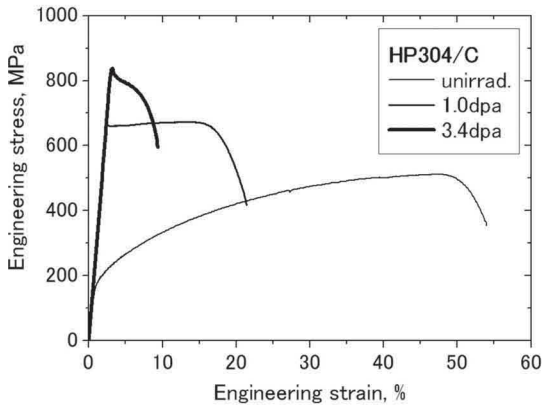
relationship decreased with increasing dose level. The addition of C or Si to HP304 results in the acceleration and suppression of radiation hardening, respectively. Much hardened specimen such as HP304/C irradiated 3.4 dpa shows plastic instability just after yielding [5,6].

Figures 3–5 show calculated true stress-strain curves for neutron-irradiated HP304, HP304/C, and HP304/Si, respectively. By shifting the true stress-strain curves to the horizontal axis by the equivalent strain account for the radiation hardening (Figs. 3(b)), the curves of HP304 and HP304/C are superimposed well in the uniform elongation range [7]. This means that work hardening rate is not changed before and after irradiation. In HP304/Si, however, the shifted curves were not superimposed on the curve of unirradiated one. Figure 6 shows the work hardening coefficient of HP304 and HP304/Si calculated using the correlation between true stress and equivalent true strain. The work hardening rate of neutron-irradiated HP304/Si became higher than that in unirradiated one, while that of HP304 was not changed drastically after neutron irradiation.

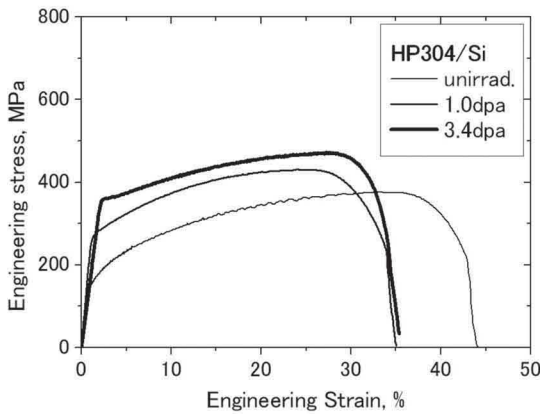
Deformation Microstructure—Figure 7(a) shows the typical deformation microstructure in HP304 specimen irradiated to 1 dpa. Only dislocation channeling was observed. Average space between channels was 690 ± 210 nm. As shown in Fig. 7(b), channel widening was observed at some intersections of channel and twin. Figure 7(c) shows the grain boundary (GB) steps at the intersection of twin and the GB, and the maximum step height was about 150



(a) HP304

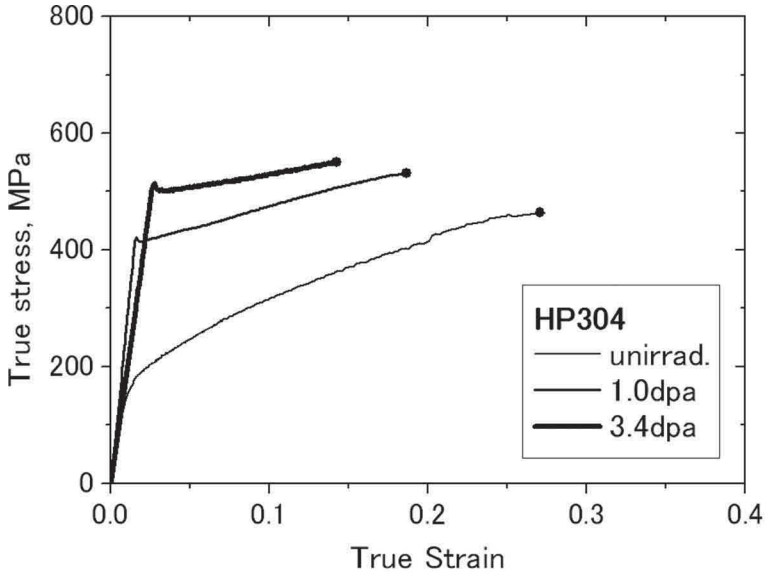


(b) HP304/C

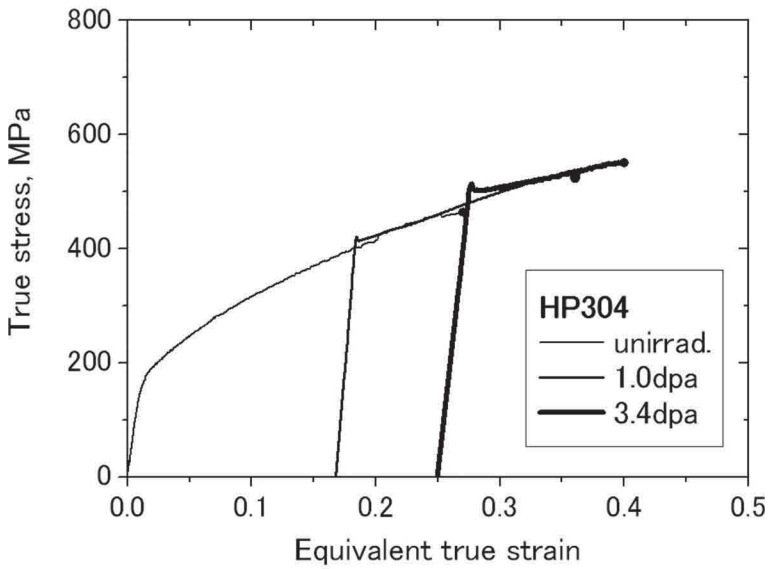


(c) HP304/Si

FIG. 2—Engineering stress-strain curves for neutron-irradiated HP304 series.

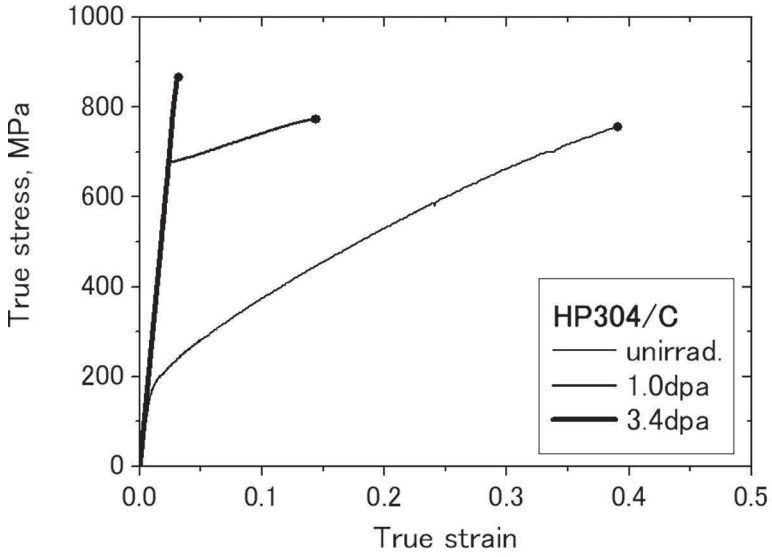


(a) calculated curves

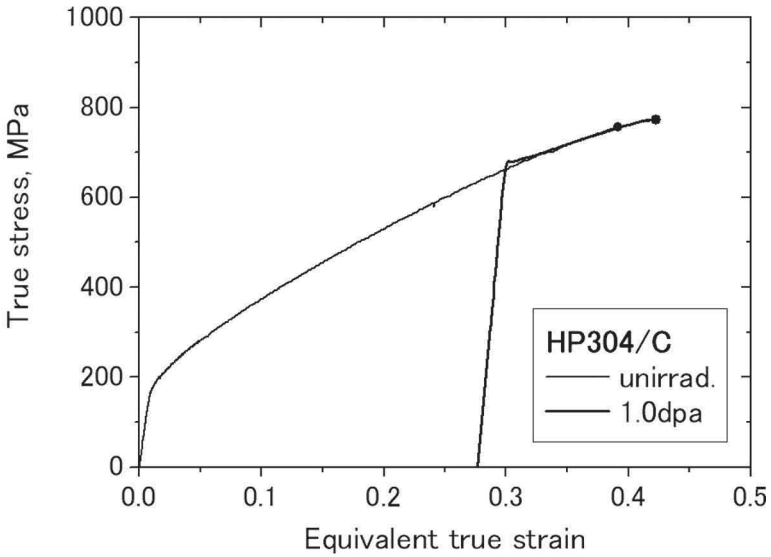


(b) calculated and shifted curves

FIG. 3—Calculated true stress-strain relations for neutron-irradiated HP304.

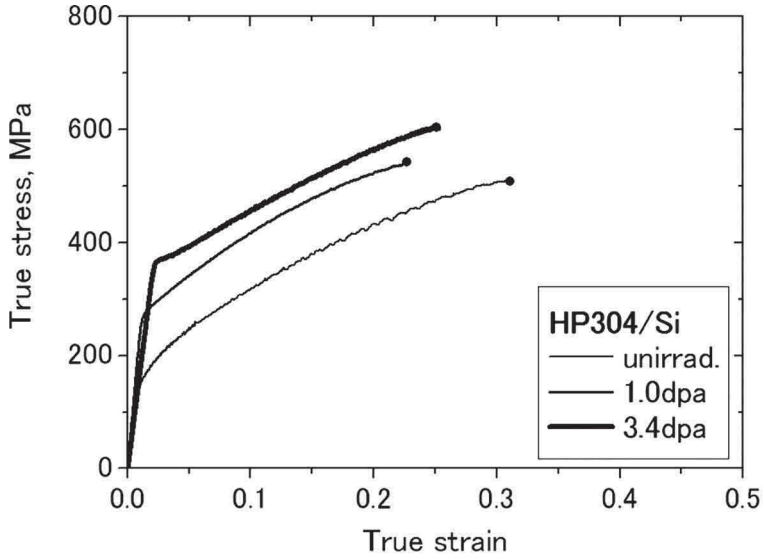


(a) calculated curves

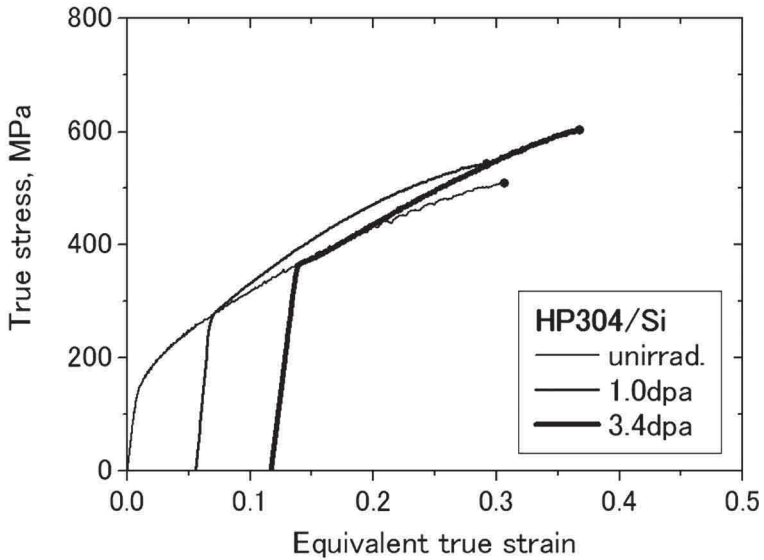


(b) calculated and shifted curves

FIG. 4—Calculated true stress-strain relations for neutron-irradiated HP304/C.



(a) calculated curves



(b) calculated and shifted curves

FIG. 5—Calculated true stress-strain relations for neutron-irradiated HP304/Si.

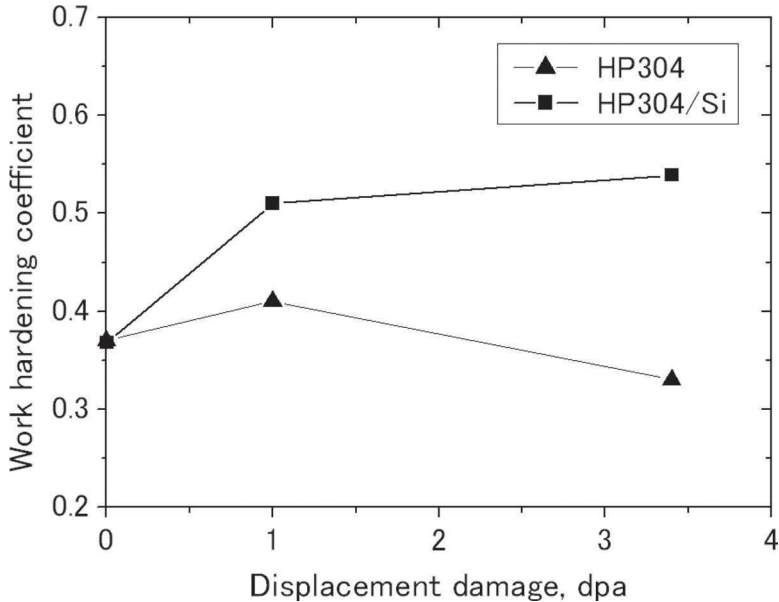


FIG. 6—Work hardening coefficient in HP304 and HP304/Si.

nm. However, such a large GB deformation was not observed frequently. In most cases, GBs were slightly deformed, and average step was about 20 nm, as shown in Fig. 7(d) at these intersections. Furthermore, neither the pileup of dislocations nor the expansion channels were observed at these intersections. Radiation induced precipitation was not confirmed in 1 dpa irradiated HP304. True strain before necking in this specimen was 0.19, and from these results it is suggested that such a large deformation was induced mainly by the dislocation channeling.

Figure 8(a) shows the deformation microstructure of 1 dpa irradiated HP304/C. Dislocation channels were frequently observed as seen in HP304. Average spacing was 1900 ± 470 nm, which was wider than that in HP304. Dislocation pileup was not observed at the intersection of the GB and the channel because it propagated into the next grain (but a few dislocations could be observed by GB). Figure 8(b) shows the widening of the dislocation channel at the intersection of dislocation channels [8]. Comparing the diffraction pattern from the widened channel and matrix, it was revealed that the diffraction pattern from widened channel rotated in $\sim 4^\circ$, and s and g conditions for expanded channel are different from those in matrix. Contrast of areas across the dislocation channel was different so that the misorientation due to lattice rotation was introduced by dislocation channeling. Dislocations were not observed in the expanded channel. Figure 8(c) shows the intersection of a GB and a dislocation channel. At the intersection, the slight deformation of the GB was observed. In this micrograph, radiation defects were not observed near the GB. Following the tilting the foil slightly, however, the contrast of radiation defect was able to be observed in that region (Fig. 8(d)). In Fig. 8(c), radiation defects

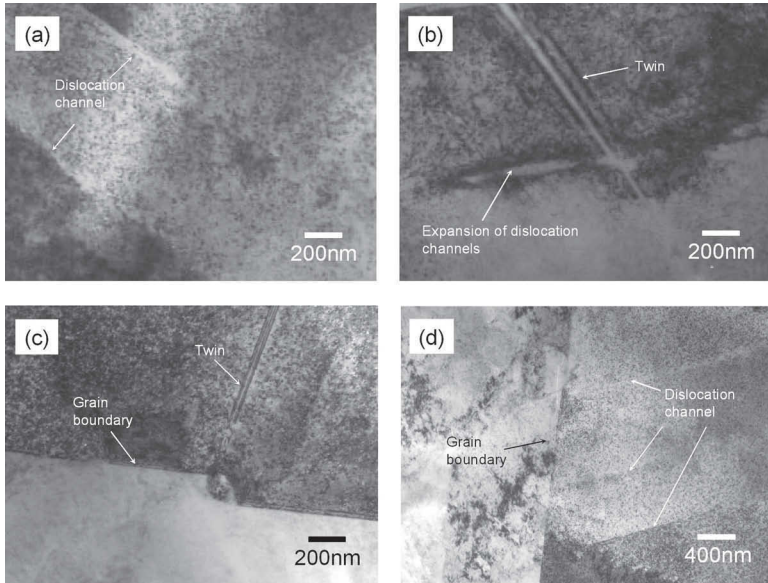


FIG. 7—Deformation microstructure in neutron-irradiated HP304 (1dpa irradiation): (a) Dislocation channels, (b) expansion of dislocation channel, (c) GB step, and (d) slight deformation of GB at the intersection of a GB and dislocation channel.

near the GB could be out of contrast by varying the deviation parameter due to the stain accumulation, not by the expansion of dislocation channel. Such a microstructure was often observed in neutron-irradiated HP304/C rather than in HP304. Because the number density of dislocation channel was small in HP304/C, the concentration of the dislocation glide occurred and resulted in a large strain at GBs.

The deformation microstructure of HP304/Si specimen neutron irradiated to 1 dpa was different from those of HP304 and HP304/C, as shown in Fig. 9. Planner type dislocations and dislocation cell structure were observed after deformation to 0.24. The average cell diameter was about 130 nm. No dislocation channel was observed in this specimen. In order to confirm the difference in the deformation microstructure between unirradiated and irradiated HP304/Si, the microstructural observation on unirradiated HP304/Si with engineering strain of 30 % was also conducted. Figure 9(c) shows the deformation microstructure of unirradiated HP304/Si, and the dominant deformation microstructure in unirradiated specimens is the dislocation cell structure with average cell diameter of 380 nm. The average cell diameter in unirradiated HP304/Si is larger than that in 1 dpa neutron-irradiated specimen. Furthermore, irradiated HP304/Si showed a characteristic microstructure different from that in HP304 and HP304/C. Figure 9(d) shows the microstructure of 5.5 dpa neutron-irradiated HP304/Si before tensile test. A few fine precipitates were observed in this specimen.

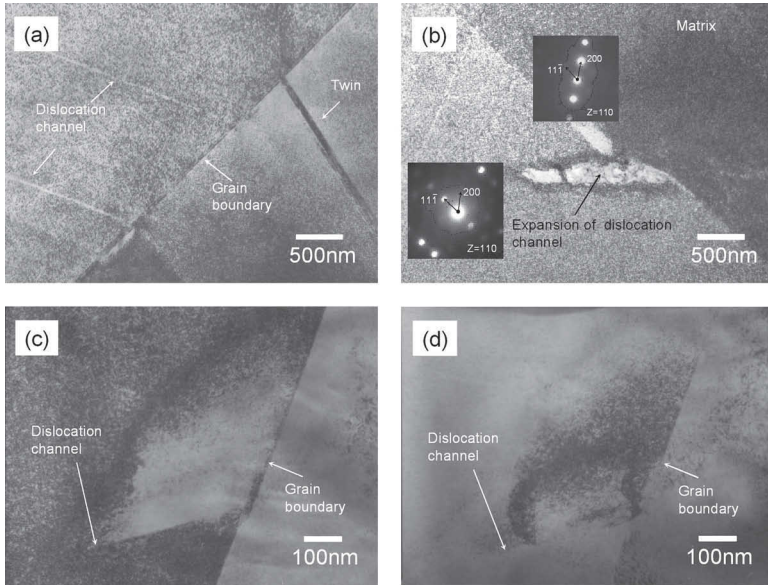


FIG. 8—Deformation microstructure in neutron-irradiated HP304/C (1 dpa irradiation): (a) Dislocation channels, (b) expansion of dislocation channel and diffraction pattern, and [(c) and (d)] intersection of a GB and dislocation channel.

Unirradiated Work-Hardened Type 316 Stainless Steel

Tensile Property—Figure 10 shows the engineering stress-strain curves for unirradiated warm-rolled 316 SSs. Increase in yield strength and loss of ductility were observed in highly reduced specimens. Specimens with reduction below 20 % exhibited the uniform elongation, and plastic instability occurred immediately after yielding in the specimen reduced over 30 %. This behavior is similar to that of neutron-irradiated alloys.

Calculated true stress-strain curves before plastic instability were shown in Fig. 11. Uniform elongation was observed in specimens with thickness reductions of 10 % and 20 %. The shifting was adapted to these specimens. All the true stress-strain curves were superimposed well so that this indicated that the work hardening coefficient was not changed by mechanical hardening. This behavior was well known as the concept of Swift type constitutive equation [5].

Deformation Microstructure—Figure 12 shows the microstructure before and after tensile tests. In the case of the specimen with reduction of 0 % (not work hardened), dislocation lines were observed in the matrix before tensile test, and dislocation cell structure after tensile deformation just before plastic instability. The cell was elongated like an ellipsoid. In the case of other specimens (with reductions of 10–50 %), dislocations cell structure has formed during warm-rolling, and the initial size of shorter diameter of cell structure was not changed after tensile test (Fig. 13).

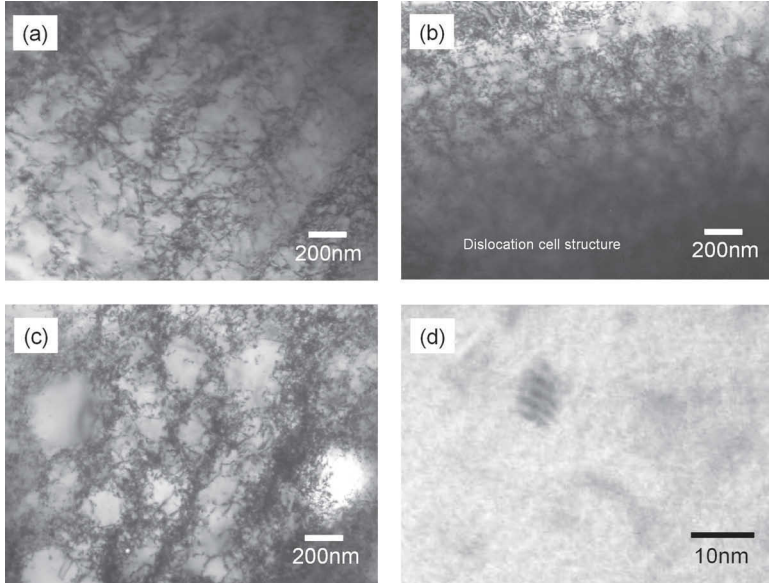


FIG. 9—Microstructure in HP304/Si. (a) and (b) show the deformation microstructure in 1 dpa irradiated specimen, (c) the deformation microstructure in unirradiated specimen, and (d) the microstructure after 5.5 dpa irradiation.

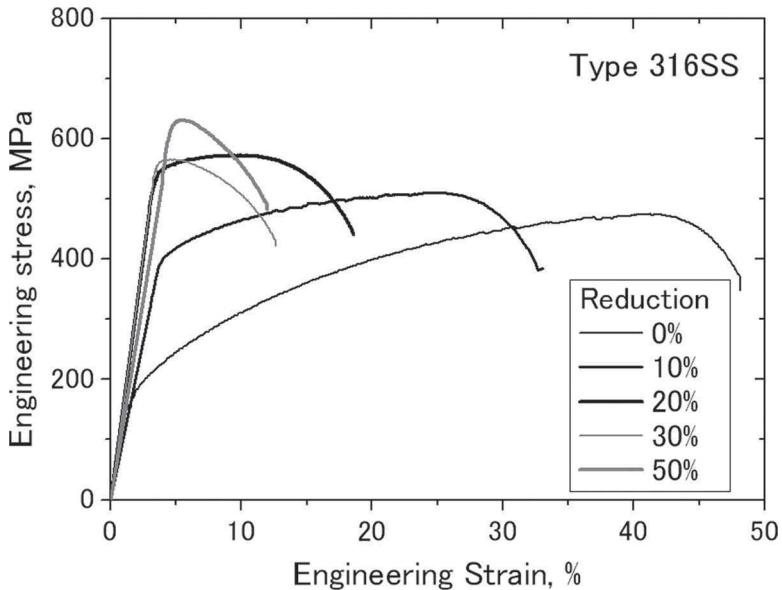
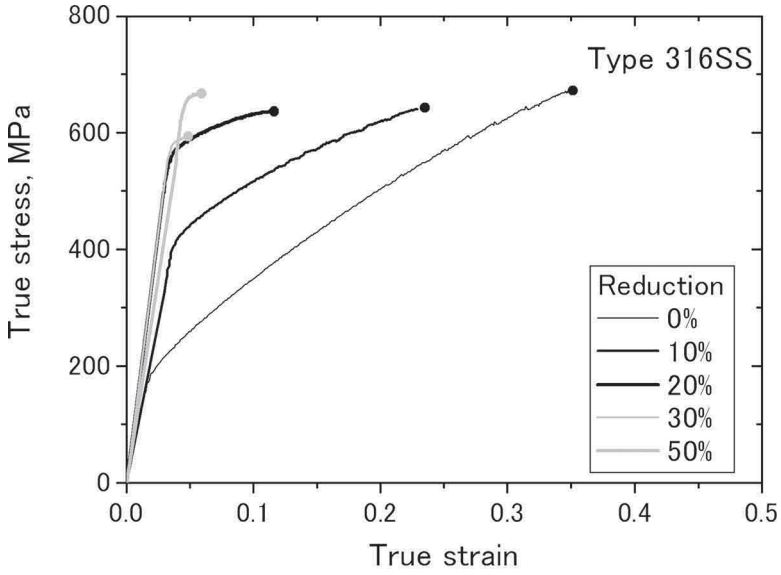
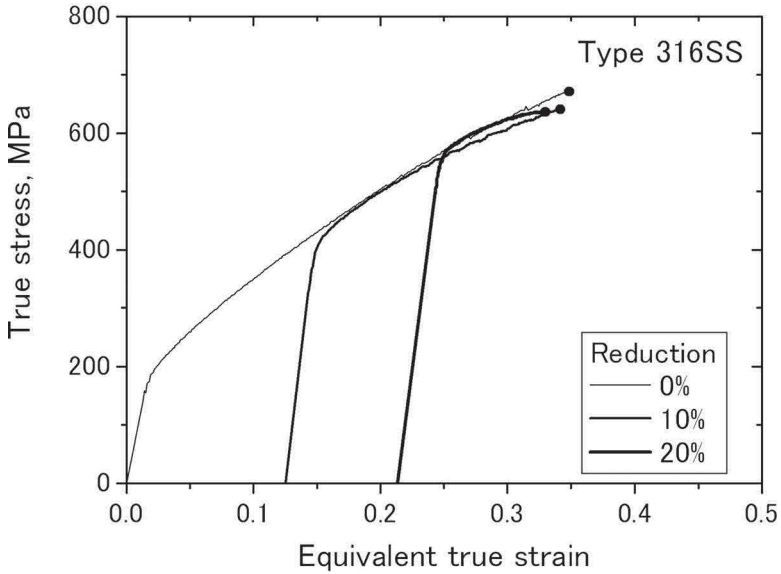


FIG. 10—Engineering stress-strain curves for unirradiated work-hardened type 316SS.



(a) calculated curves



(b) calculated and shifted curves

FIG. 11—Calculated true stress-strain curves for unirradiated work-hardened type 316SS.

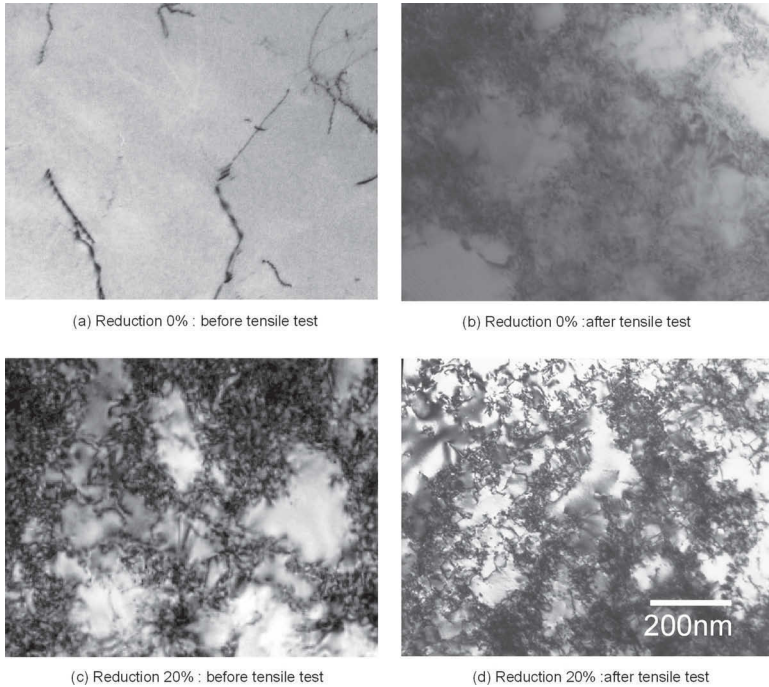


FIG. 12—*Deformation microstructure in unirradiated warm-rolled type 316SS.*

Discussion

The plastic instability just after yielding was observed in highly irradiated HP304/C materials (Fig. 2(c)). This behavior was also observed in unirradiated highly deformed type 316 stainless steel (Fig. 10). Yield drop was observed in HP304 and HP304/C after 1 dpa irradiation. The yield drop may not be affected by carbon content because the carbon content of HP304/Si, which did not show the yield drop even after 304 dpa irradiation, is the same as that of HP304. In HP304/Si, black dots and Frank loops were observed uniformly and locally near dislocation lines (Table 2), respectively. After 5.5 dpa irradiation, the yield drop was observed in all alloys [6]. On the other hand, the yield drop was not observed in the unirradiated work-hardened type 316 stainless steel. Therefore it is believed that uniformly distributed Frank loops affected the yield drop.

The work hardening coefficient in calculated true stress-strain curve was not changed in HP304 and HP304/C after irradiation up to 3.4 dpa (Figs. 3 and 4). Similar results were observed in neutron-irradiated iron [9] type 316L stainless steel irradiated by neutron to 1 dpa at 200°C [10] and EC316LN stainless steel after spallation irradiation [11]. Formation of Frank loops did not lead to the change in work hardening rate. The dominant plastic deformation mode in the irradiated HP304 and HP304/C was dislocation channeling (Figs. 7 and 8), though the average spacing between channels was different among them. The change in the deformation mode from dislocation cell structure to the disloca-

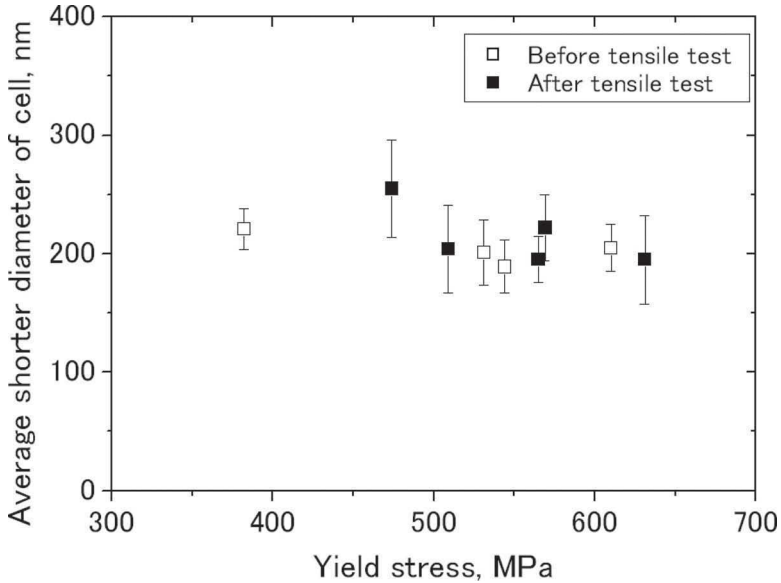


FIG. 13—Dislocation cell size of type 316 stainless steel with various yield stresses.

tion channeling does not give rise to the change in work hardening rate. In the irradiated materials, Frank loops and defect clusters act as barriers to dislocation glide and result in increased yield stress. But once dislocation channels were formed, as shown in Figs. 7 and 8, the glide of dislocations is restricted in the defect free channels during the plastic deformation even in the heavily irradiated materials. Therefore, the friction to the dislocation motion during the plastic deformation arises by interaction with dislocation lines rather than with Frank loops and defect clusters, as shown in Fig. 14(a).

Work-hardened type 316SS specimens did not cause change in their work hardening coefficient. The deformation microstructure of work-hardened specimen was the dislocation cell structure at any reduction level, and no correlation was observed between the average shorter diameter of cell and the yield strength of materials (Fig. 13). Dislocations can glide between cell walls where dislocation-dislocation interaction occurs during the plastic deformation, as shown in Fig. 14(b). This dislocation glide mechanism is similar to that in HP304 and HP304/C. In both irradiated alloys, dislocations glide through space where only dislocations such as lines and loops exist. It is concluded that there is little change in work hardening rate between irradiated and work-hardened stainless steels when the moving dislocation lines interact with only other dislocations during the plastic deformation.

On the other hand, neutron-irradiated HP304/Si showed the increase in the work hardening rate after irradiation. Engineering strain just before the onset of plastic instability was about 27 % in the specimens irradiated to 1 dpa (Fig. 2(c)), and the dominant deformation microstructure was the dislocation cell structure (Fig. 9(c)). As mentioned previously, radiation induced precipitates

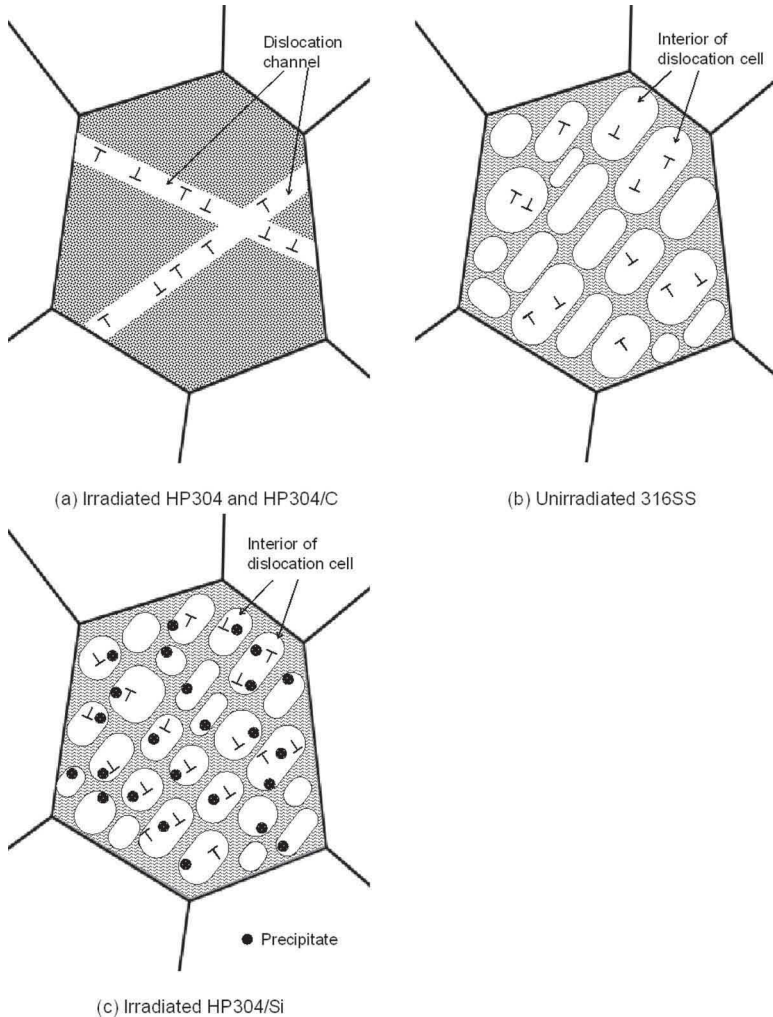


FIG. 14—Schematic of dislocation mobile part during plastic deformation: (a) Neutron irradiated HP304 and HP304/C, (b) unirradiated 316SS, and (c) irradiated HP304/Si.

were observed in HP304/Si after 5.5 dpa irradiation (Fig. 9(d)), and the dislocation cell diameter of irradiated specimen was smaller than that of unirradiated specimen. If small precipitate, which had not been observed by TEM, would nucleate uniformly with high density after irradiation to 1 dpa, then it could become a stronger obstacle to pin dislocation lines (Fig. 14(c)). The mobile distance of a dislocation at a certain external stress was restricted due to such precipitates. Consequently, the average dimension of cell in irradiated HP304/Si becomes smaller than that in unirradiated HP304/Si.

It is concluded from this study that the Frank loops and dislocation channeling do not affect the work hardening rate. Only strong precipitates affect the

rate. This means that the concept of Swift's constitutive equation is adaptable to irradiated stainless steels if the strong precipitate does not nucleate during irradiation. Then the constitutive equation of irradiated stainless steels before occurrence of plastic instability is expressed by following equation:

$$\sigma_{\text{true}} = f(\varepsilon_{\text{true}} + \varepsilon_{\text{irrad}}, n) = A(\varepsilon_{\text{true}} + \varepsilon_{\text{equi}})^n \quad (4)$$

where:

$\varepsilon_{\text{equi}}$ = equivalent strain to compensate the increase of yield strength in irradiated and work-hardened stainless steels.

This relationship was also observed in the data of work-hardened or irradiated stainless steels [12].

Conclusion

- (1) HP304 and HP304/C hardened by neutron irradiation and type 316 SS work hardened by warm-rolling show that the work hardening rate was not changed after hardening process.
- (2) In the irradiated HP304 and HP304/C, dislocation channel was dominant glide path of dislocation lines. The channels had no or less Frank loops; therefore in the channel, friction to dislocation motion arises by the interaction with other dislocation lines.
- (3) The similar interaction of dislocations occurs in the defect free cell interior in unirradiated mechanically hardened materials.
- (4) When other obstacles such as precipitates were formed like irradiated HP304/Si, friction to dislocation motion increased and resulted in the change in work hardening rate.
- (5) It is concluded that the work hardening behavior was affected by radiation induced precipitations, not by the dislocation channeling, and that work hardening mechanism in irradiated materials is the same as that in unirradiated SSs. Therefore, it could be possible to predict the work hardening capacity of irradiated materials by means of the evaluation of the mechanical property of materials with the same level of yield stress as irradiated materials.

References

- [1] Lucas, G. E., "The Evolution of Mechanical Property Change in Irradiated Austenitic Stainless Steels," *J. Nucl. Mater.*, Vol. 206, 1993, pp. 287-305.
- [2] Pawel, J. E., Rowcliffe, A. F., Alexander, D. J., Grossbeck, M. L., and Shiba, K., "Effects of Low Temperature Neutron Irradiation on Deformation Behavior of Austenitic Stainless Steels," *J. Nucl. Mater.*, Vol. 233-237, 1996, pp. 202-206.
- [3] Horsten, M. G. and De Vires, M. I., "Irradiation Hardening and Loss of Ductility of Type 315L(N) Stainless Steel Plate Material due to Neutron-Irradiation," *Effects of Radiation on Materials: 17th International Symposium, ASTM STP 1270*, Sun Valley, Idaho, 1996, D. S. Gelles, R. K. Nanstad, A. S. Kumar, and E. A. Little, Eds., ASTM International, West Conshohocken, PA, pp. 919-931.
- [4] Cole, J. I. and Bruemmer, S. M., "Post-Irradiation Deformation Characteristics of

- Heavy-Ion Irradiated 304L SS," *J. Nucl. Mater.*, Vol. 225, 1995, pp. 53–58.
- [5] Tsukada, T., Miwa, Y., Nakajima, H., and Kondo, T., "Effects of Minor Elements on IASCC of Type 316 Model Stainless Steel," *Eighth International Symposium on Environmental Degradation of Materials in Nuclear Power Systems—Water Reactors*, Amelia Island, Florida, 1997, American Nuclear Society, IL, pp. 795–811.
- [6] Nakano, J., Miwa, Y., Kohya, T., and Tsukada, T., "Effects of Silicon, Carbon, and Molybdenum Additions on IASCC of Neutron Irradiated Austenitic Stainless Steels," *J. Nucl. Mater.*, Vol. 329–333, 2004, pp. 643–647.
- [7] Jitsukawa, S., Grossbeck, M. L., and Hishinuma, A., "Stress-Strain Relations of Irradiated Stainless Steels Below 673 K," *J. Nucl. Mater.*, Vol. 191–194, 1992, pp. 790–794.
- [8] Jiao, Z., Busby, J. T., and Was, G. S., "Deformation Microstructure of Proton-Irradiated Stainless Steels," *J. Nucl. Mater.*, Vol. 361, 2007, pp. 218–227.
- [9] Ohr, S. M., "Work Hardening Characteristics of Neutron Irradiated Iron," *Scr. Metall.*, Vol. 2, 1968, pp. 213–216.
- [10] Byun, T. S. and Farrell, K., *Acta Mater.*, Vol. 52, 2004, pp. 1597–1608.
- [11] Miwa, Y., Tsukada, T., and Jitsukawa, S., "Plastic Deformation Behavior of Type 316LN Stainless Steel in Non-Irradiated, Thermally Sensitized Condition or in Irradiated Condition," *Proceedings of 12th International Conference on Environmental Degradation of Materials in Nuclear Power System—Water Reactors*, Warrendale, Pennsylvania, 2005, American Nuclear Society, IL, pp. 311–317.
- [12] Nelson, D. V., "An Approach to Development of Structural Design Criteria for Highly Irradiated Core Components," *Proceedings of Third International Conference on Mechanical Behaviour of Materials*, Cambridge, England, 1979, Pergamon Press, Oxford, pp. 355–363.

D. A. Toktogulova,¹ M. N. Gusev,¹ O. P. Maksimkin,¹ and
F. A. Garner²

Influence of Neutron Irradiation on Energy Accumulation and Dissipation during Plastic Flow and Hardening of Metallic Polycrystals

ABSTRACT: Deformation-calorimetric experiments have been performed on specimens of Armco iron, pure nickel, and two austenitic chromium-nickel alloys: 12Cr18Ni10Ti and 03Cr20Ni45Mo4Nb, each tested in both unirradiated and irradiated conditions. It has been shown that for neutron-irradiated 12Cr18Ni10Ti stainless steel and also for nickel and Armco iron, the latent energy (E_s) versus σ curves shift towards lower values of E_s , and these curves progressively lose their parabolic appearance that is typical for unirradiated metals and alloys. It has also been shown experimentally that “excess heat” is measured when stored energy associated with radiation-produced defect agglomerates is released during their annihilation in formation of defect-free channels. In effect more energy is released than the mechanical energy supplied externally to cause deformation of the specimen. When post-irradiation annealing is used to reduce the concentration of defect agglomerates, the excess energy phenomenon disappears.

KEYWORDS: neutron irradiation, energy balance, latent energy, excess heat, post-irradiation annealing

Introduction

During plastic flow of metallic polycrystals the applied mechanical energy dissipates as heat or via acoustic and electromagnetic emission but can partially

Manuscript received October 13, 2008; accepted for publication October 1, 2009; published online January 2010.

¹ The Institute of Nuclear Physics, NNC RK, 050032 Almaty, Kazakhstan.

² Pacific Northwest National Laboratory, Richland, WA 99354.

Cite as: Toktogulova, D. A., Gusev, M. N., Maksimkin, O. P. and Garner, F. A., “Influence of Neutron Irradiation on Energy Accumulation and Dissipation during Plastic Flow and Hardening of Metallic Polycrystals,” *J. ASTM Intl.*, Vol. 7, No. 1. doi:10.1520/JAI102175.

Copyright © 2010 by ASTM International, 100 Barr Harbor Drive, PO Box C700, West Conshohocken, PA 19428-2959.

accumulate via formation of crystalline defects. The energy accumulated in the material as defects is defined as stored or “latent” energy E_s [1,2]. Irradiation of metals by high-energy particles creates such defects, leading to an increase in the latent energy.

It is known that plastic flow may be accompanied by annihilation of some portion of radiation-induced defects, often resulting in formation of defect-free dislocation channels [3]. Defect-free dislocation channels are found in some irradiated materials after plastic strain of 1–5 %, and then, as deformation increases, their presence can be masked by newly developed dislocation structures. There is no reason, however, to expect that interaction between dislocations and radiation defects, and subsequent annihilation of the defects, becomes weaker with increasing deformation. Deformation-stimulated annihilation of radiation defects may significantly influence the energy dissipation processes accompanying plastic deformation. However, there has previously been no thorough consideration of this question addressed in the scientific literature although the subject is of undoubted scientific and practical interest. To address this subject this paper presents results of experimental studies of the processes responsible for energy accumulation and dissipation in a number of neutron-irradiated polycrystalline metals.

Experimental Techniques and Materials

The following materials have been studied: Armco iron (99.77 wt % Fe after annealing at 1223 K for 30 min), pure nickel (99.98 wt % Ni after annealing at 1223 K for 30 min), and two stainless austenitic chromium-nickel alloys designated 12Cr18Ni10Ti and 03Cr20Ni45Mo4Nb after annealing of each alloy at 1323 K for 30 min.

Flat tensile specimens (gauge dimensions of $10 \times 3.5 \times 0.3$ mm³) were irradiated in the WWR-K (Russian acronym for water-moderated, water-cooled reactor in Kazakhstan) reactor at temperatures of 293–330 K to exposures ranging from 2×10^{18} to 2×10^{20} n/cm² ($E > 0.1$ MeV), producing 0.0014–0.14 displacements per atom (dpa) in pure iron. Uniaxial tension tests were performed inside a specially designed microcalorimeter facility [4], which uses a standard differential microcalorimeter designated *Calvet*, produced by the French firm “Setaram.” The calorimeter sensitivity is $\pm 10^{-7}$ Wt, whereas typical values of heat dissipated by deformed specimens in this study range from $\sim 10^{-4}$ to $\sim 10^{-2}$ Wt.

Both neutron-irradiated and unirradiated specimens were deformed at room temperature with strain rates ranging from 5.5×10^{-4} to 8.3×10^{-4} s⁻¹ (0.33–0.5 mm/min). Each tensile test yielded a load-extension diagram and a thermogram (heat release intensity versus time). In addition to standard mechanical properties (yield strength $\sigma_{0.2}$ and ultimate tensile strength σ_{UTS} , uniform elongation ε_u , and total elongation ε_{tot}), the following integral energy parameters were determined: The specific work, A , spent to deform the specimen (in MJ/m³), and the energy released, Q , as a result of deformation.

The latent energy accumulated in the material is $E_s = A - Q$, and the relative latent energy is $P = E_s/A$. Using techniques described in Ref 4 and procedures of

TABLE 1—Mechanical characteristics of the steel 12Cr18Ni10Ti following neutron irradiation.

Fluence, n/cm ²	$\sigma_{0.2}$, MPa	σ_{ult} , MPa	ϵ_u , %	ϵ_{tot} , %
0	180	640	63	70
5×10^{18}	420	700	44	60
1.4×10^{19}	450	690	49	57
1.3×10^{20}	560	710	41	51

“thermogram reconstruction” [5,6], the quantities of A , Q , and E_s were calculated as functions of the amount of deformation. Additionally, $E_s(\sigma)$ curves were constructed, where σ is the “true” flow stress.

As a result of series of calibration experiments, it was determined that estimated inaccuracies are <3 % for A , <5 % for Q , and 20–30 % for E_s . Microstructures of the irradiated and deformed specimens were studied using a JEM-100CX transmission electron microscope and a Neophot-2 optical microscope.

Experimental Results and Discussion

Steel 12Cr18Ni10Ti

Table 1 presents the mechanical characteristics of 12Cr18Ni10Ti steel as a function of exposure dose as calculated from deformation diagrams (see Fig. 1(a)). The exposures are relatively low, ranging from 0.004 to 0.09 dpa (where 10^{22} n/cm² with energies $E > 0.1$ MeV produce ~ 7 dpa in pure iron). It can be seen from $\sigma_{0.2}$ and σ_{ult} values that the unirradiated steel experiences significant hardening during deformation. As the neutron exposure increases, the strength increases and the ductility decreases. Note that following irradiation the yield strength increases more rapidly than the ultimate tensile strength with increasing neutron dose.

Values of energy characteristics of the deformed steel specimens, presented in Table 2, show that as the neutron fluence increases, the energy needed to deform a specimen up to failure decreases. The latent energy E_s also decreases with increasing dose, whereas the value of dissipated heat Q increases.

The following peculiarity of the latent energy is of special interest. Note that at 1.3×10^{20} n/cm², the value of E_s is essentially zero, implying that the alloy under deformation dissipates all energy being input from outside the system. This appears to disagree with the fact that alloy has hardened as shown in all curves in Fig. 1(a) where an increase in the flow stress was observed and, hence, the deformed alloy must have absorbed energy.

Earlier we showed [7,8] that for both unirradiated and neutron-irradiated steel 12Cr18Ni10Ti up to 5×10^{18} n/cm², the relationship between the energy accumulated in a material and the plastic flow stress can be described by an expression $E_s = E_0 + k \cdot \sigma^2$, where E_0 is a factor that characterizes the polycrys-

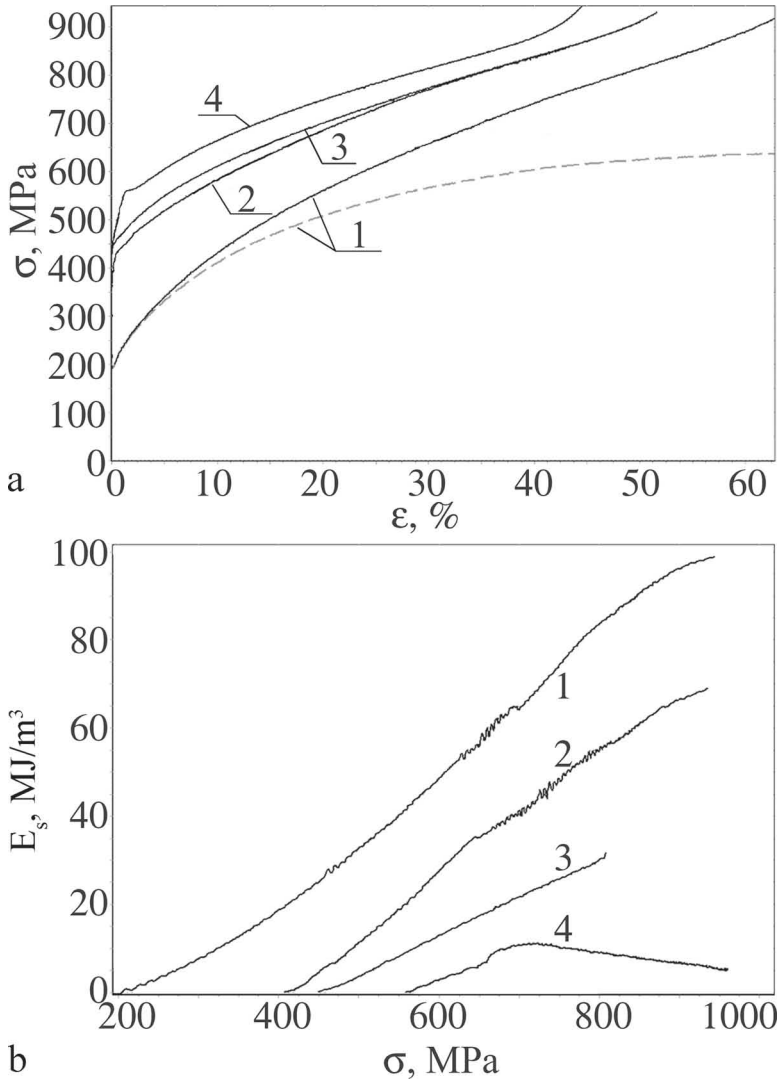


FIG. 1—(a) Measured engineering stress-strain curves ((1), dotted line) and the derived true stress-true strain curves (solid lines). (b) Latent energy versus applied stress during deformation of 12Cr18Ni10Ti steel. The various curves represent conditions of (1) unirradiated, (2) 5×10^{18} n/cm², (3) 1.4×10^{19} n/cm², and (4) 1.3×10^{20} n/cm².

talline internal energy describing the structure state prior to deformation and k is a factor dependent on the lattice parameter, temperature, stacking fault energy, etc.

As a result of irradiation to a fluence of 5×10^{18} n/cm², a shift in the “ E_s - σ ” curve is observed towards smaller E_s values by ~ 20 MJ/m³. However,

TABLE 2—Energy characteristics of plastic yield in steel 12Cr18Ni10Ti following irradiation.

Fluence, n/cm ²	A, MJ/m ³	Q, MJ/m ³	E _s , MJ/m ³	P = E _s /A
0	410	310	100	0.24
5 × 10 ¹⁸	400	340	75	0.18
1.4 × 10 ¹⁹	380	337	43	0.11
1.3 × 10 ²⁰	347	347	0–4	0.01

the general appearance of the dependence is left unchanged (see Fig. 1(b)). One might expect that the quadratic dependence observed at 5×10^{18} n/cm² before necking would be conserved but shifted towards smaller values of E_s . However, it was found that at 1.4×10^{19} n/cm², the appearance of the $E_s(\sigma)$ curve (Fig. 1, curve (3)) changed significantly, even though there was an insignificant increment in the yield stress. The parabolic shape was lost, with the curve degenerating to a straight line. The deformation hardening and growth of σ were accompanied by a significantly smaller increment in E_s .

At 1.3×10^{20} n/cm² a peak $E_s(\sigma)$ is reached at $\sigma \sim 720$ MPa, and one can see a decrease in the accumulated energy with increasing stress (see Fig. 1, curve (4)), rather than an increase. Such behavior is not observed in the annealed unirradiated state and must represent some characteristic of the irradiated state. A similar effect has been previously observed where a decrease in E_s with increasing deformation was associated with formation of micro-cracks just prior to failure [9]. In our case, measurements of specimen density (with accuracy of $\sim 0.5\text{--}0.7\%$) have not found any significant differences between initial and deformed specimens. Therefore we consider it safe to assume that such “abnormal” behavior of E_s has nothing in common with crack formation.

Karlsen and Onchi [3] showed that in a closely related steel (AISI 304) irradiated to $\sim 10^{20}$ n/cm² and then deformed by 5–10%, “defect-free channels” are formed that are free of observable radiation defects. It is commonly believed that radiation-induced defects disappear due to interaction with dislocations.

In this example, the atypical behavior of the $E_s(\sigma)$ curve is probably a result of “sweeping out” a portion of the radiation-induced defects. It should be stressed that the specimens we have studied are irradiated at $<60^\circ\text{C}$, where “black-dots” of very small size dominate [10]. That fact that such behavior is so pronounced for a steel irradiated to 10^{20} n/cm² indicates that the behavior in other lower fluence cases will also be similar.

Another potential source of excess heat is the deformation-induced martensitic $\gamma \rightarrow \alpha$ transformation [11]. For instance, in deformed crystals of ZnS this transformation is responsible for occurrence of the relationship $Q \gg A$ [12]. However, for irradiated steel 12Cr18Ni10Ti, there is no published quantitative data on the thermal effect of the $\gamma \rightarrow \alpha'$ transformation.

Alloy 03Cr20Ni45Mo4Nb

Figure 2(a) shows the conventional engineering stress-strain curves for alloy 03Cr20Ni45Mo4Nb. Table 3 presents the measured energy and mechanical

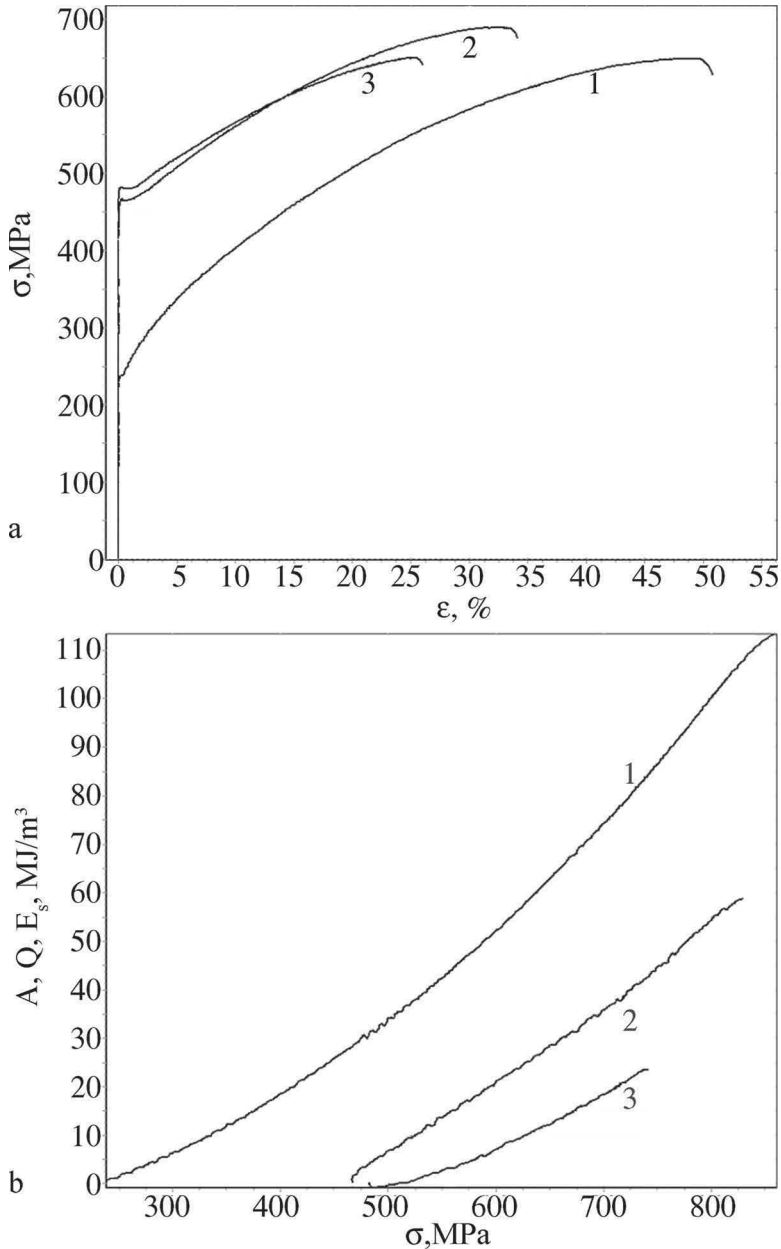


FIG. 2—(a) Engineering diagrams of 03Cr20Ni45Mo4Nb. (b) E_s versus σ curves for alloy 03Cr20Ni45Mo4Nb in the following conditions: (1) unirradiated, (2) $1.4 \times 10^{19} \text{ n/cm}^2$, and (3) $1.3 \times 10^{20} \text{ n/cm}^2$. The departure from quadratic behavior towards the end of curve (1) reflects the development of a neck.

TABLE 3—The energy and mechanical characteristics of 03Cr20Ni45Mo4Nb.

Fluence, n/cm ²	$\sigma_{0.2}$, MPa	σ_{uts} , MPa	ϵ_u , %	ϵ_{tot} , %	A , MJ/m ³	Q , MJ/m ³	E_s , MJ/m ³	$P = E_s/A$
0	238	649	49	51	282	169	113	0.4
1.4×10^{19}	465	689	32	34	209	149	60	0.3
1.3×10^{20}	482	650	25	26	155	131	24	0.15

characteristics versus neutron fluence for this high-nickel alloy, while Fig. 3(b) shows the “ E_s versus σ ” curves. In this alloy radiation hardening shifts the E_s versus σ curves towards smaller values of E_s but preserves the parabolic appearance of the curves. This implies that in this high-nickel-content alloy, in contrast to 12Cr18Ni10Ti, neither abnormal heat release nor variation in E_s occurs over this dose range.

Nickel

Nickel deformed in the unirradiated state is characterized by comparatively low strength, high ductility, and considerable deformation strengthening. Figure 3 presents engineering stress-strain curves and the curves of A , Q , and E_s versus ϵ for both unirradiated and neutron-irradiated nickel. Table 4 presents the measured energy and mechanical property characteristics and shows that nickel increases in strength as a result of neutron irradiation, whereas its ductility has decreased by a factor of ~ 1.5 . Also the values of A and Q have decreased, whereas the value of E_s has become negative. This implies that irradiated material dissipates considerably larger energy during deformation than the mechanical energy transferred from outside.

Such a result is quite unexpected because as shown in Fig. 3, nickel is characterized by significant deformation hardening after its irradiation to 1.4×10^{19} n/cm². In Ref 13 we showed that irradiation does not change the character of “true stress–true strain” curves, which thoroughly describe deformation strengthening. The potential effect of “defect sweeping,” recorded as an excess heat release, has not led to a reduction in the intensity of deformation strengthening. Therefore we assume that excess heat release is caused by annihilation of defects, mainly of a type that weakly affects the flow stress.

Armco iron

Figure 4 shows typical engineering stress-strain curves along with the corresponding thermograms obtained for this rather pure iron. Table 5 presents the mechanical and energy characteristics obtained. One may see that neutron irradiation of Armco iron has led to considerable increase in the material strength and strong reduction of its ductility. The appearance of the engineering stress-strain curves has also noticeably changed. For instance, deformation hardening at 1.4×10^{19} n/cm² is absent, the ultimate stress coincides with the yield stress, and the value of ϵ_u determined from the diagram is zero. Thus there is plastic strain without uniform deformation occurring.

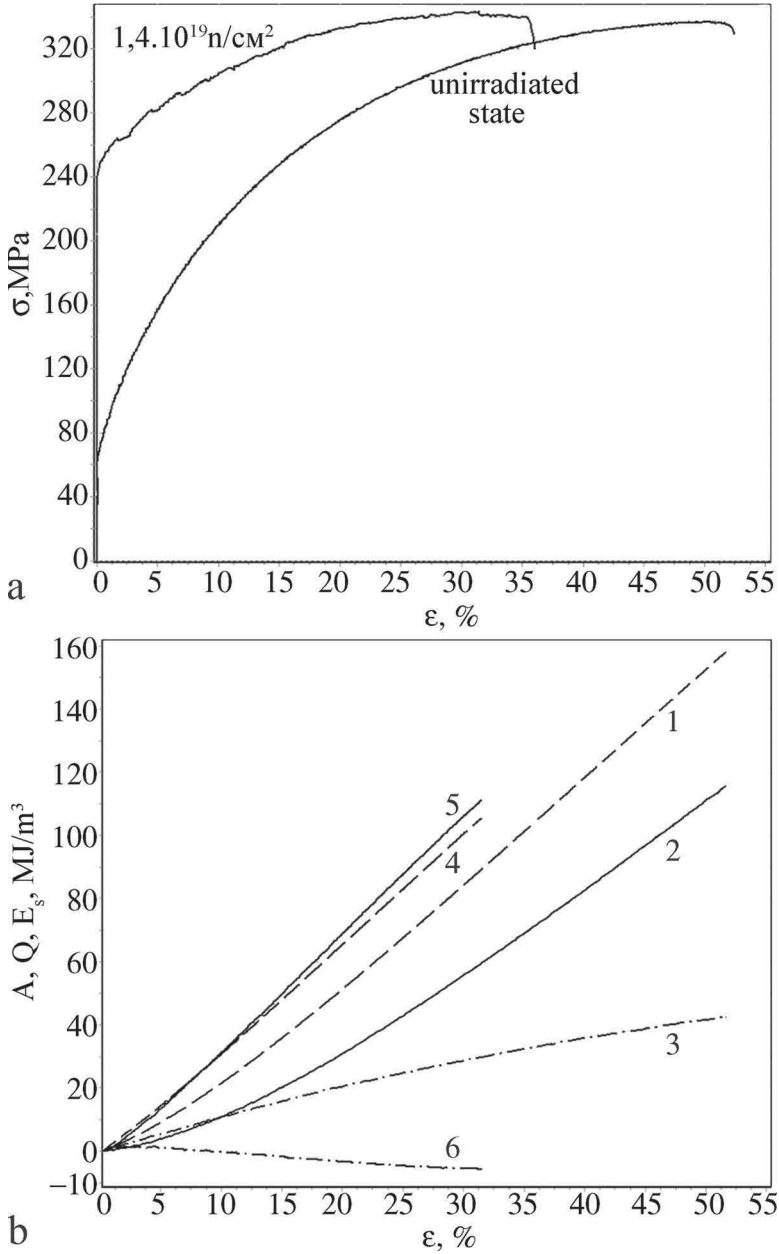


FIG. 3—(a) Engineering diagrams and (b) deformation dependencies energy characteristics of nickel: (1), (2), and (3) for the unirradiated state and (4), (5), and (6) for the neutron-irradiated material at $1.4 \times 10^{19} \text{ n/cm}^2$. (1) and (4)— $A(\epsilon)$; (2) and (5)— $Q(\epsilon)$; and (3) and (6)— $E_s(\epsilon)$.

TABLE 4—Energy and mechanical characteristics of nickel.

State	$\sigma_{0.2}$, MPa	σ_{uts} , MPa	ϵ_u , %	ϵ_{tot} , %	A , MJ/m ³	Q , MJ/m ³	E_s , MJ/m ³
Unirradiated	50	315	50	52	147	139	8
Irradiated, 1.4×10^{19} n/cm ²	225	350	27	33	105	111	-6

It should be noted that metallographic studies at 1.4×10^{19} n/cm² showed that the plastic strain usually develops via formation of a single deformation band located at an angle with respect to the load axis (see Fig. 5). In some rare cases, two intersecting bands were observed. Outside the deformation bands the measured microhardness ($H_{\mu}=200$ kg/mm²) is essentially unchanged from the pre-deformed value, indicating the absence of plastic strain. Within the band the microhardness has increased sharply, reaching 310 kg/mm². An increase in microhardness signifies deformation hardening of the material within the band.

Figure 5 shows the surface of the deformed specimen of Armco iron irradiated to 1.4×10^{19} n/cm². It is seen that on the specimen surface, deformation relief is present within the deformation band, comprised of a group of parallel slip bands that are 20–40 μm long, located at a distance of $\sim 1-1.5$ μm from each other (see Fig. 5(a)). Local macro-deformation of material in the deformation band reaches 30–50 % [14]. Outside the band of maximal deformation, deformation relief on the surface is not generally seen although isolated parallel bands are observed (see Fig. 5(b)) that are probably traces of microplastic deformation. Most probably groups of parallel bands in a region of localized deformation are formed as the dislocations move in defect-free channels that intersect the surface [15].

The specific values of A , Q , and E_s , presented in Table 5, reduce in value as fluence increases. When 1.4×10^{19} n/cm² is reached, the value of the energy accumulated in the material is becoming negative, i.e., the value of Q is getting much higher than the value of the deformation work A . If it is assumed that this effect is related to irradiation, then one may expect that quite different behavior after annealing of radiation defects prior to deformation. Therefore tests were performed in which the specimens were annealed after irradiation.

Effect of Post-Irradiation Annealing on Kinetics of Heat Release during Deformation of Iron

In Fig. 6 the engineering stress-strain curves are presented for Armco iron irradiated to 1.4×10^{19} n/cm² after different postradiation 1 h annealing temperatures. Table 6 presents values of strength and ductility, as well as the integral quantities A , Q , and E_s .

Note that annealing at 573 K leads to occurrence of a yield plateau, at 673 K, signifying recovery of mechanical properties. Following Larikov's data [16], annealing of radiation-induced vacancies takes place in bcc metals at annealing temperature of $0.3T_{\text{melting}}$, which is 600 K for iron.

According to the results presented in Table 6, it is clear that in general case

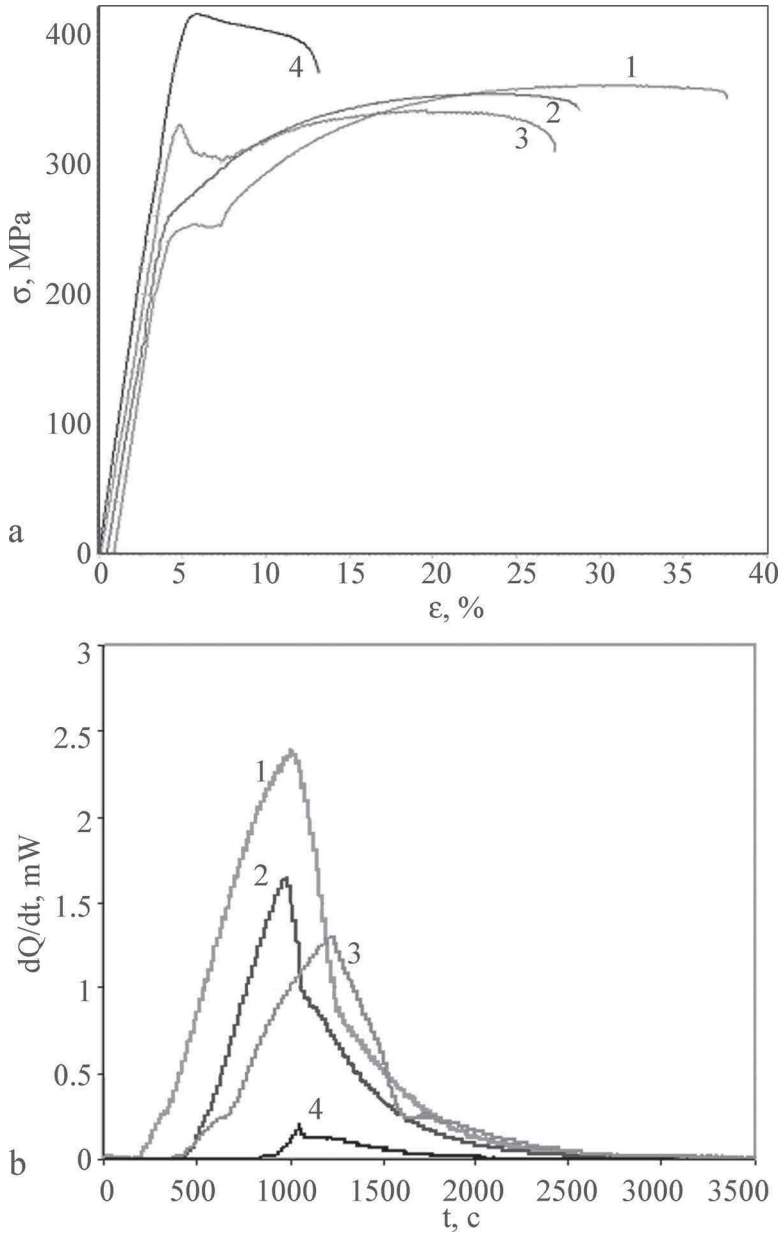


FIG. 4—(a) Engineering diagrams and (b) thermograms for Armco iron: (1) unirradiated, (2) 2×10^{18} n/cm², (3) 5×10^{18} n/cm², and (4) 1.4×10^{19} n/cm².

TABLE 5—Mechanical and energy characteristics of Armco iron.

Fluence, n/cm ²	$\sigma_{0.2}$, MPa	σ_{uts} , MPa	ϵ_{μ} , %	ϵ_{tot} , %	A, MJ/m ³	Q, MJ/m ³	E_s , J/m ³
0	253	360	26	32	95	87	8
2×10^{18}	276	355	21	29	79	74	5
5×10^{18}	317	340	15	24	72	69	3
1.4×10^{19}	418	9	30	38	-8

annealing has led to an increase in the energy accumulated under deformation. At the initial deformation stage, the growth of E_s is related to intense dislocation multiplication. As most of the point defects have disappeared during annealing, excess heat release is not observed in the annealed iron. Thus, it appears that “abnormal heat release” in deformed Armco iron is associated with sweeping out of point defects produced during irradiation.

Discussion

The results of these deformation-calorimetric experiments show that deformation of irradiated materials in some cases can be accompanied by dissipated heat Q that is in excess of the work A supplied from outside of the system. This effect arises after a certain fluence threshold. This effect was observed in this work in pure iron, pure nickel, 12Cr18Ni10Ti steel, and earlier work in copper [17]. The effect is postulated to arise as a consequence of sweeping out of radiation-induced defects, namely, vacancies, interstitials, and their complexes, as a result of their interactions with moving dislocations.

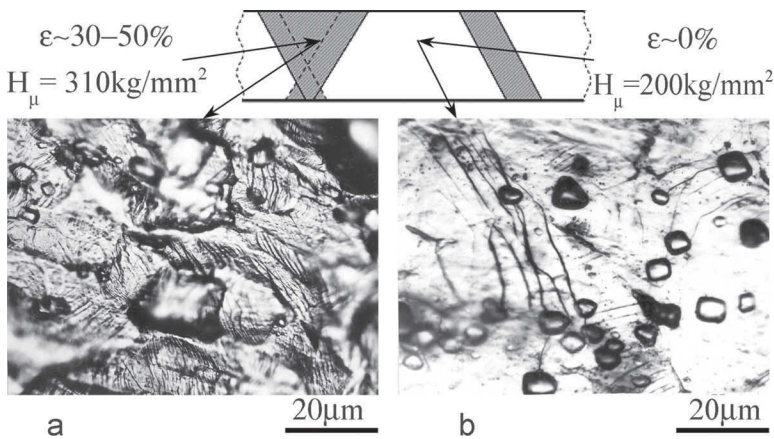


FIG. 5—Deformation relief observed on the surface of an Armco iron specimen irradiated to 1.4×10^{19} n/cm²: (a) Inside deformation band and (b) outside of deformation band.

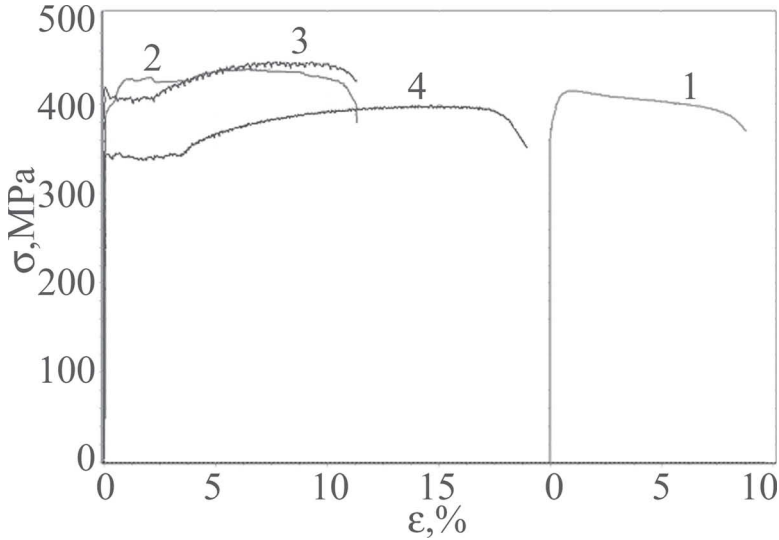


FIG. 6—Stress-strain curves for Armco iron irradiated to 1.4×10^{19} n/cm² for various post-irradiation annealing temperatures: (1) 293 K, (2) 473 K, (3) 573 K, and (4) 673 K.

Earlier we showed [5] that small agglomerates of radiation-induced defects were observed in Armco iron directly after irradiation to 1.4×10^{19} n/cm². During plastic flow in Armco iron a band of maximum deformation develops that is completely free of these small agglomerates. The removal of both the defect and its inherent stored energy by sweeping out provides the source of the excess heat release. This assumption is supported by results of our annealing experiments. It is known that annealing of most pure metals within the temperature range 250–400°C usually leads to recovery of physical-mechanical properties (σ_T , σ_B , and ϵ) [17].

According to Ref 18, the densities of other microstructural components are changed in course of annealing following irradiation. Examples are radiation-enhanced precipitate phases, as well as the density of dislocations and dislocation loops. In stainless steels especially, the evolution of such components will undoubtedly have some impact on the thermal release properties. The questions of what portion of the latent energy arises from radiation-induced defects

TABLE 6—Effect of the post-irradiation annealing temperature on the mechanical and energy characteristics of Armco iron irradiated to 1.4×10^{19} n/cm².

$T_{\text{annealing}}$, K	$\sigma_{0.2}$, MPa	σ_{uts} , MPa	$\epsilon_{u'}$, %	ϵ_{tot} , %	A , MJ/m ³	Q , MJ/m ³	E_s , MJ/m ³
293	418	8.8	30	38	-8
473	426	440	7.3	11	49	42	7
573	407	447	8.7	11.3	44	44	0
673	340	400	15.4	19	68	39	29

(E_s^{irr}) and how it depends on irradiation temperature are rather interesting, but unfortunately these questions have not been sufficiently addressed in the scientific literature. In Ref 19 a value of $E_s^{\text{irr}} = 7 \text{ MJ/m}^3$ was found with the use of a differential scanning calorimeter for copper subject to post-irradiation annealing. In order of magnitude, this value is comparable with values of heat release we measured for iron and nickel at 16 and 14 MJ/m^3 , respectively.

For 12Cr18Ni10Ti steel the measured value of excess heat release is significantly higher however. It is probable that metastability of the steel during deformation is one of the reasons, especially the formation of α martensite, leading to another contribution to excess thermal energy release. It is known that following irradiation α -martensite produced by deformation is strongly increased in this steel [20].

Conclusions

Deformation-calorimetric experiments have been performed on specimens of Armco iron, pure nickel, and two austenitic chromium-nickel alloys: 12Cr18Ni10Ti and 03Cr20Ni45Mo4Nb, each tested in both unirradiated and irradiated conditions. It has been shown that for neutron-irradiated steel 12Cr18Ni10Ti and for pure nickel and pure iron the E_s versus σ curves shift towards lower values of E_s , and these curves progressively lose their parabolic appearance that is typical for unirradiated metals and alloys.

It has been shown experimentally that “excess heat” is measured when stored energy associated with radiation-produced defect agglomerates is released during their annihilation in formation of defect-free channels. In effect more energy is released than the mechanical energy supplied externally to cause deformation of the specimen. When post-irradiation annealing is used to reduce the concentration of defect agglomerates, the excess energy phenomenon disappears.

References

- [1] Bolshanina, M. A. and Panin, V. A., “Latent Energy of Deformation” *Researches on Solid-State Physics*, Academy of Science, Kazakhstan, Moscow, 1957. pp. 193–233.
- [2] Wolfenden, A. and Appleton, A. S., “The energy stored during the low-temperature deformation of copper and aluminum single crystals,” *Acta Metall.*, Vol. 16, 1968, pp. 915–925.
- [3] Karlson, W. and Onchi, T., *Proceedings of the Annual Meeting of Intergranular Cracking—Environmentally Assisted Corrosion (ICG-EAC)*, Charleston, SC, May 14–19, 2006.
- [4] Maksimkin, O. P. and Gusev, M. N., “Technique and Installation for Studying of Thermal Emission and Accumulation of Energy in the Course of Deformation of Irradiated Metal Materials,” (in Russian), *Bulletin National Nuclear Center No. 4*, Institute of Nuclear Physics of Kazakhstan, 2000, pp. 69–75, <http://www.nnc.kz/ru/publications/vestnik/bulletin-archive.html> (Last accessed December 2009).
- [5] Astafiev, I. V. and Maksimkin, O. P., *Industrial Laboratory*, Vol. 46, 1994, pp. 44–46.
- [6] Shenogin, S. V., Höhne, G. W. H., and Oleinik, E. F., “Thermodynamics of the

- Pre-Yield Deformation Behavior of Glassy Polymers: Measurements with New Deformation Calorimeter,” *Thermochim. Acta*, Vol. 391, 2002, pp. 13–23.
- [7] Maksimkin, O. P. and Gusev, M. N., “Changes of Stress and Latent Energy on Deformation of Stainless Steel 12Cr18Ni10Ti Irradiated with Neutrons,” (in Russian), *Letter in JTP*, Vol. 29, No. 3, 2003, pp. 1–12.
- [8] Maksimkin, O. P. and Gusev, M. N., “Influence of Reactor and Cyclotron Irradiation on Energy Transformation During Plastic Strain of Metal Materials,” *Effects of Radiation on Materials: 20th International Symposium, ASTM STP 1405*, June 4–8, 2000, Williamsburg, ASTM, West Conshohocken, PA, 2001, pp. 813–824.
- [9] Samsonik, A. L. and Sirenko, G. A., “Energy Absorption during Deformation of Yttrium and Zirconium,” (in Russian), *Metallophysics*, Vol. 4, No. 10, 1982, pp. 112–114.
- [10] Neustroev, V. S., 2006, Ph.D. thesis, Moscow Physical Engineering Institute, Moscow, Russia.
- [11] Astafiev, I. V. and Maksimkin, O. P., “Calorimetric Studies of the $\gamma \rightarrow \alpha$ Transformations upon Deformation of Irradiated Steel 12Cr18Ni10Ti,” (in Russian), *Phys. Met. Metallogr.*, Vol. 177, No. 3, 1994, pp. 166–168.
- [12] Gurov, A. F., Kulakov, M. P., Polovov, V. M., and Shmurak, S. Z., “Abnormal Correlation between Supplied Work and Dissipated Heat during Plastic Deformation of ZnS Crystals,” (in Russian), *Phys. Stat. Sol.*, Vol. 18, No. 12, 1976, pp. 3706–3708.0002-7820
- [13] Gusev, M. N. and Maksimkin, O. P., *Proceedings of ICNRP-05*, Almaty, Kazakhstan, September 26–29, 2005, Institute of Nuclear Physics, Almaty, Kazakhstan, Vol. 2, pp. 359–367.
- [14] Maksimkin, O. P. and Gusev, M. N., Tsai, K. V., Toktogulova, D. A., and Osipov, I. S., “Features of Plastic Deformation of ARMCO Iron Irradiated by Neutrons,” (in Russian), *Bulletin National Nuclear Center of Kazakhstan No. 1*, Almaty, Kazakhstan, 2006, pp. 39–46.
- [15] Edwards, D. J. and Singh, B. N., “Evolution of Cleared Channels in Neutron-Irradiated Pure Copper as a Function of Tensile Strain,” *J. Nucl. Mater.*, Vol. 329–333, 2004, pp. 1072–1077.
- [16] Larikov, L. N., *Radiation Defects in Metals*, Science, Almaty, Kazakhstan, 1981, pp. 87–100.
- [17] Nikolaev, V. A., “Irradiation Embrittlement of Metals and Alloys,” *Radiation Defects in Metal Crystals*, Science, Almaty, Kazakhstan, 1978, pp. 158–176.
- [18] Neustroev, V. S., *Proceedings of the Third Radiation Material Science Conference*, September 21–25, 1994, RIAR, Dimitrovgrad, Russia, 1994, Vol. 2, pp. 31–55.
- [19] Pedchenko, K. S. and Karasev, V. S., “Latent Energy in Metals Irradiated by Neutrons,” (in Russian), *Physicochemical Mechanics of Materials*, Vol. 4, No. 4, 1968, pp. 453–458.0002-7820
- [20] Maksimkin, O. P., 1996, Ph.D. thesis, The Institute of Nuclear Physics, Almaty, Kazakhstan.

Timothy J. Lampman,¹ Adrian Popescu,¹ and
Jose Freire-Canosa²

Comparison of CANDU Fuel Bundle Finite Element Model with Unirradiated Mechanical Load Experiments

ABSTRACT: A requirement of spent nuclear fuel is to maintain its structural integrity at all times to enable its safe and efficient handling during storage, transportation, and placement in a deep geological repository. In Canada, commercial spent fuel is currently stored in light water pools for about ten years before being transferred to dry storage where storage may extend up to 100 years. Investigations on the fuel structural integrity evolution during dry storage are being performed for spent CANDU fuel bundles. A CANDU nuclear fuel bundle is a cylindrical assembly approximately 0.1 m in diameter and 0.5 m in length made of 28 or 37 fuel elements held together by welding two endplates at both ends. The welds have a circular notch of less than 10 μm diameter. Significant hydraulic, mechanical, and thermal loads during bundle irradiation in the reactor may lead to bundle deformation, which when coupled with the sharp weld notch can result in significant stress enhancement at the notch tip and possibly activate delayed hydride cracking (DHC) during dry storage. To better understand the stress levels in CANDU fuel during dry storage, a finite element model of CANDU fuel bundles is under development. The stress distribution in the bundle and the stress intensity factor at each weld notch can be evaluated by the model for the spent fuel geometry and dry storage conditions. This paper discusses the agreement

Manuscript received June 25, 2008; accepted for publication January 17, 2009; published online February 2009.

¹ AMEC NSS, 700 University Avenue, 4th Floor, Toronto, Ontario, Canada, M5G 1X6, timothy.lampman@amec.com

² Nuclear Waste Management Organization, 22 St. Clair Ave. East, Sixth Floor, Toronto, Ontario, Canada, M4T 2S3.

Cite as: Lampman, T. J., Popescu, A. and Freire-Canosa, J., "Comparison of CANDU Fuel Bundle Finite Element Model with Unirradiated Mechanical Load Experiments," *J. ASTM Intl.*, Vol. 6, No. 3. doi:10.1520/JAI101985.

Copyright © 2009 by ASTM International, 100 Barr Harbor Drive, PO Box C700, West Conshohocken, PA 19428-2959.

between the finite element model and validation experiments using unirradiated 28-element CANDU fuel bundles tested in the elastic and plastic regime.

KEYWORDS: finite element modeling, CANDU fuel, spent fuel storage

Introduction

The CANDU reactor is a pressurized heavy water reactor consisting of half-metre length, natural UO_2 fuel bundles loaded into pressurized fuel channels, which are fueled during full power operations. Typically, a fuel bundle resides in the reactor core for approximately one year before it is discharged to a light water storage pool. After a minimum underwater storage period of ten years, the fuel is loaded into dry storage canisters where they may remain up to 100 years before placement in a deep geological repository. Until placement into the repository, it is essential that the fuel maintains its structural integrity at all times to allow for safe handling during transfer between the different storage stages.

While in the reactor, the fuel bundle is impacted by complex processes affecting its material properties. Irradiation effects and both thermal and mechanical stresses lead to changes in the fuel bundle material properties and residual stresses or deformations. Post in-reactor handling also contributes to additional loads that have the potential to impact the fuel bundle integrity. Post-discharge visual and destructive examinations of the fuel bundles show that they are structurally sound and meet the expected operational performance requirements for in-core residence.

During underwater storage, temperatures of storage are benign and maintained in the 20–30°C range with waterpool chemistry conditions well within prescribed limits. Early studies with commercial fuel have indicated that storage of CANDU spent fuel under water storage is warranted for periods of at least 50 years, and could possibly be extended to 100 years without significant observable changes to the fuel structural integrity.

Following wet storage, the fuel is stored dry in air or helium in concrete canisters or CANSTOR Convection vaults at temperatures that are considerably higher than those of storage in water. Temperatures in dry storage are in the range of 100–170°C depending on the storage method, the storage medium, and the age of the fuel. The higher temperature has an impact on the solubility of hydrides present in the fuel elements' cladding after in-reactor service and may lead to redistribution of precipitated hydrogen and deuterium in the clad. The weld regions of the fuel bundles are particularly vulnerable because the weld morphology generally presents a 10 μm notch that may act as an initiating crack for delayed hydride cracking (DHC).

To understand if DHC could be present during the dry storage period, a finite element model of the CANDU fuel bundles is being developed. The model includes the fuel bundle structural material, the natural UO_2 pellets in each element, and contacts between pellets and clad and adjacent elements. The current model is only capable of evaluating the response of an unirradiated CANDU fuel bundle to externally applied mechanical loads. The stress distribu-



FIG. 1—28-Element fuel bundle irradiated at Pickering NGS.

tions and deformation throughout the entire bundle under different loading conditions can be calculated. A submodel of the endcap-to-endplate weld region has also been developed to evaluate stress intensity factors at the weld notches. Future development of this model to account for irradiated fuel bundles will be performed to assess the stress distributions in dry-stored spent CANDU fuel and the potential for DHC.

CANDU Fuel Design

Typical CANDU fuel has 28 or 37 fuel elements depending on the reactor design. In this paper, focus will be given to the 28-element CANDU fuel bundle currently in use at the Pickering Nuclear Power Plant in Ontario, Canada.

CANDU fuel is a small size cylindrical array of fuel elements that are held together by endplates, as shown in Fig. 1. The size of the array is roughly 10 cm in diameter by 50 cm long weighing about 25 kg. The fuel elements, shown in Fig. 2, are small round tubes of a neutron-transparent zirconium alloy capped at either end and containing the UO_2 fuel in the form of solid cylindrical pellets about 1.5 cm long. The fuel pellets are stacked in the fuel element and are specifically designed to provide volumetric space to accommodate fission gases generated during their irradiation in the reactor. The array of fuel elements is held together by resistance welding the endcaps of the elements to the end-

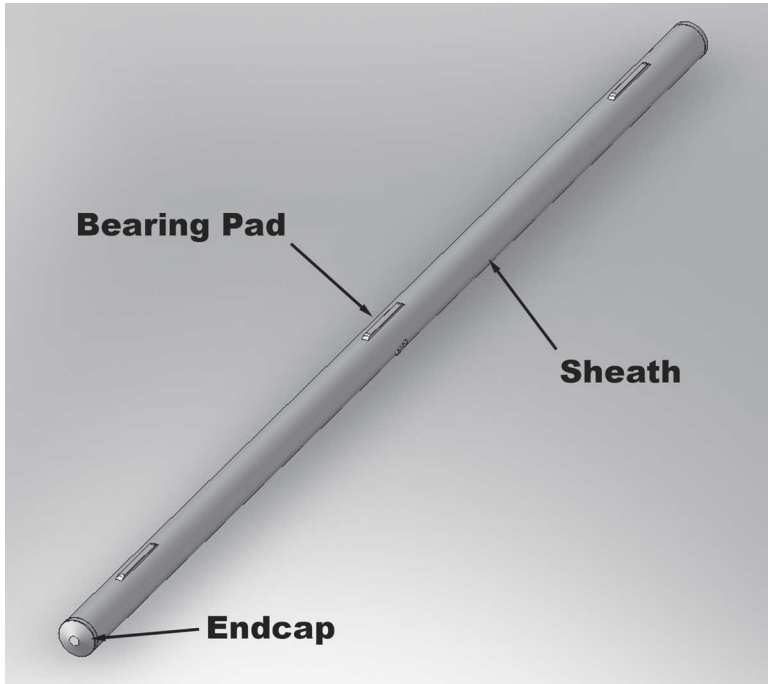


FIG. 2—28-Element fuel element design.

plates. The endplates are designed to maintain the fuel elements array in place and to allow for fluid flow of the reactor coolant along the fuel bundle axis while being irradiated in the reactor.

Commercial CANDU fuel bundles are manufactured from Zircaloy-4 and the UO_2 pellets are sintered ceramics. The fuel elements are made of a Zircaloy-4 fuel cladding, commonly called the sheath, rolled as a cylindrical tube, and closed off at either end by welded endcaps. The endcaps are machined from Zircaloy-4 barstock. Prior to seal welding with the endcaps, the UO_2 fuel pellets are loaded into the fuel sheath. The ceramic pellets are machined to tight tolerances because the gap between the pellet and the sheath is approximately 0.05 mm.

The fuel sheath can withstand stresses from pellet expansion and coolant pressure during in-reactor operation. In the reactor, the fuel bundles absorb hydrogen and deuterium from the coolant to concentrations typically in the range of 40–120 ppm hydrogen equivalent. The Zircaloy-4 texture used in the CANDU fuel bundle elements promotes precipitation of the absorbed hydrogen in the form of hydride platelets in a circumferential direction in the elements rather than radially to minimize the effect that hydride fracturing has on the material fracture toughness. This also improves the sheath's resistance to DHC.

Bearing pads and spacer pads are attached to the fuel elements. Both bearing pads and spacer pads are punched out from Zircaloy-4 sheets and beryllium brazed to the fuel element sheath at designated locations as demanded by the

TABLE 1—*Element CANDU Fuel Bundle Dimensions.*

Bundle Components	Nominal Model Dimensions
<i>Bundle Overall Dimensions</i>	
Bundle Length (mm)	495.3
Bundle Diameter (mm)	102.5
<i>Fuel Element</i>	
Outside Diameter (mm)	15.25
Sheath Thickness (mm)	0.4
<i>Bearing Pads</i>	
Width (mm)	2.54
Height (mm)	1.2
<i>Spacer Pads</i>	
Length (mm)	8.25
Width (mm)	2.29
<i>Endplates</i>	
Radius (mm)	44.2
Thickness (mm)	1.5
<i>Fuel Pellets</i>	
Density (Mg/m ³)	10.65
Diameter (mm)	14.3
Diameter Clearance (mm)	0.08
Length/Diameter ratio	1.0

fuel bundle design. The bearing pads maintain fuel sheath clearances with the channel pressure tube to allow for good coolant flow and heat transfer. The spacer pads are located at strategic locations in the elements to maintain clearances between adjacent fuel elements to allow for sufficient coolant flow and heat transfer.

The nominal dimensions included in the 28-element CANDU fuel bundle model are summarized in Table 1. It will be noted that the thickness of the fuel sheath is approximately 0.5 mm and is thinner than fuel element cladding used with other types of commercial reactors.

Development of the CANDU Bundle Stress Model

The primary purpose of modeling the CANDU fuel bundle is to determine the stresses throughout the fuel bundle. The thermal-mechanical loads experienced by the fuel bundle in-reactor lead to bundle permanent deformation, and the deformations lead in turn to residual stresses. The development of a stress model for the CANDU bundle enhances our knowledge of bundle behavior. Also, the stress model allows prediction of the stresses in the bundle in any location thus allowing prediction of its behavior in the long-term. Consequently, this knowledge facilitates the design of long-term storage and handling

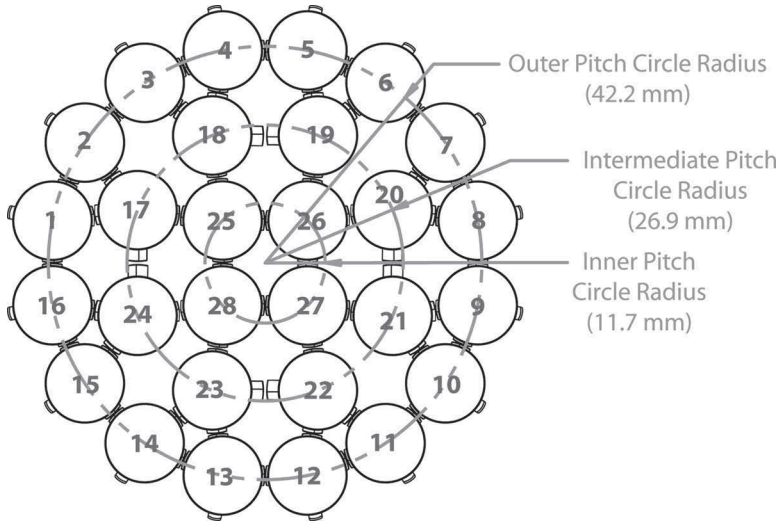


FIG. 3—Fuel element arrangement and numbering for 28-element bundle.

facilities, as well as the implementation of measures to mitigate the exposure of the bundle to conditions that could lead to its deterioration.

For this purpose, a finite-element model (FEM) using the ANSYS version 10 code to describe typical CANDU fuel bundles was developed. During dry storage, applied stress levels in the bundles are expected to be relatively small and all deformation will be elastic. However, permanent deformations of the irradiated fuel bundles are to be expected and are mainly induced by the high operating temperature combined with the mechanical and hydraulic forces. This could affect the residual stresses in the bundles, hence the need to also include in the model nonlinearities, both material (plastic deformation) and geometric (contacts between adjacent elements).

There is a high degree of symmetry around the bundle longitudinal central axis but depending on the bundle type, this symmetry can be complex and result in challenging the development of the FEM. In the case of the 28-element fuel bundle, there are three concentric rings of fuel elements known as the inner, center, and outer rings. The distribution of the fuel elements is shown in Fig. 3 along with the fuel element numbering scheme. It will be noted that the inner rings consist of four fuel elements, followed by the center ring with eight and the outer ring with 16 elements. Both center and outer rings have two types of elements which are mirror images of each other with the difference due to the location of the spacer pads. The inner ring is composed of four identical fuel elements. Similarly, the endplate is symmetrical as shown in Fig. 4.

Due to the complex geometry of the fuel bundles, and the requirement that variations in the initial (post-discharge) model geometry be examined, the model was created using a series of ANSYS Parametric Design Language (APDL) input scripts. The models have been built using a top-down approach where a solid model is created first and subsequently meshed.

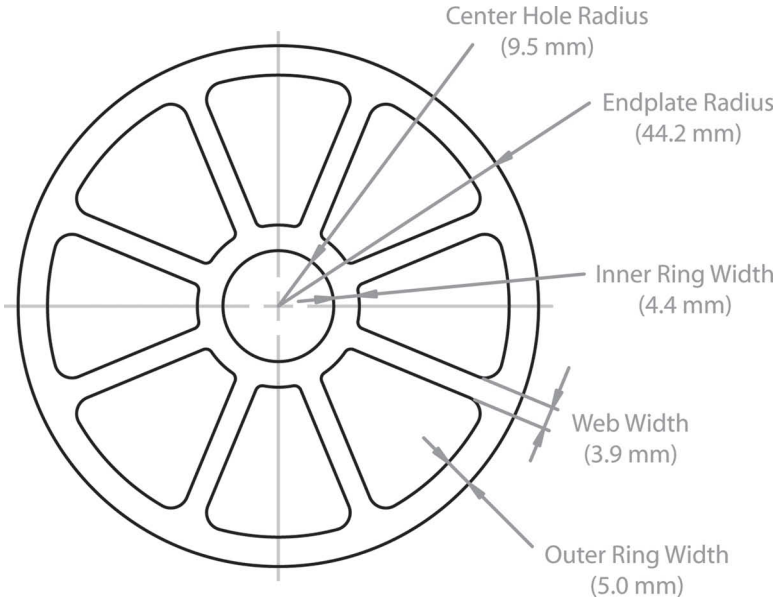


FIG. 4—Geometry and dimensions of 28-element endplate.

After irradiation, the bundle geometry will be slightly different than its nominal dimensions. The most obvious and important changes are due to deformation of the endplates and bowing of the elements. Deformation of the endplate has not been addressed in the current model but bowing of the elements has been included. The deformation of each element at the center of the bundle can be input into the model. This is fully parametric for all 28 elements.

Finite Element Model for the CANDU Bundle Stress Model Components

A solid geometric model of the fuel bundle was first conceptualized from a typical 28-element commercial CANDU fuel and then the finite element mesh was developed over this solid model. The size of the finite element fuel bundle model is on the order of 100 000 elements. Linear finite elements have been used throughout the model development so simulation results are achieved on a reasonable timeframe.

In developing a solid geometric model for the fuel bundle, the bundle was disassembled into its main components: mainly the fuel elements, endcaps, endplates, bearing pads, and spacer pads. The following sections discuss the finite element modeling of the element components and material properties in more detail.

Fuel Bundle Material Properties

Temperature dependent material properties for both the Zircaloy-4 and the UO_2 ceramic pellets were obtained from the MATPRO material property library

[1]. Material properties relevant to the modeling included for Zircaloy-4: elastic modulus, stress-strain curves, and density of the material, and for UO_2 : its density and elastic modulus. The relevant data is detailed in Tables 2 and 3. The material properties are also dependent on the effects of irradiation and the cold work of the material. For CANDU fuel, the Zircaloy sheath has about 15 % cold work and the fuel is exposed to a neutron fluence of about 10^{25} n/m² while in the reactor. The elastic modulus is dependent on temperature but for the purposes of the modeling, the fuel bundle was assumed to be at room temperature (25 °C)

Material properties for weld affected areas such as the endcap/endplate welds and weld heat affected zones of spacer pads and bearing pads to the sheath are not known. However, it was assumed that their properties are well represented by those of Zircaloy-4.

Fuel Elements

Solid models were first developed for the fuel elements. All fuel elements are essentially identical except for the minor variations introduced by the location of the bearing pads and spacer pads. In modeling the fuel elements, two models were created: one consisting of empty fuel elements without the UO_2 pellets (hollow model) and one using fuel elements fully loaded with pellets (segmented model). In creating the fuel element models, the pellets are created and meshed, then the fuel sheath, and finally the endcaps. All contacts between pellets and sheath are finally meshed on the surfaces.

To account for the deformation of fuel elements during their in-reactor service life, the axis deformation for the fuel element is defined along its central axis. The deformation is introduced as a 3-D curve of sinusoidal shape similar to a half-sine wave fixed at the endcap-to-endplate welds and with the maximum displacement at the center of the fuel element.

In the model with pellets, the pellets are extruded from their cross section. The pellet-to-pellet and the pellet-to-endsheath contacts are also created. The fuel element sheath cross section is then extruded along the element axis and the sheath-to-pellet contacts are created. In the model without fuel pellets, the sheath of the element is created without the fuel pellets. However, for the hollow model, the density of the Zircaloy-4 was combined with the density of the UO_2 pellets to take into account their weight while modeling the elements as empty shells without fuel pellets.

From the perspective of the parameterized model, dimensional changes are incorporated into the parameters. In total, there are five 28-element types that are distinguished by appendage arrangements. Since the appendages are extruded from the sheath, there are five sheath types that are modeled.

In completing the solid model for the fuel element, the solid is divided into smaller areas joined at the edges in order to provide the location for the extrusion of the appendages (bearing pads and spacer pads). After the solid is created, the areas are meshed using 4-node, linear shell elements. The resulting element mesh contains typically over 1500 finite elements and over 1600 nodes. The other four fuel element types will be slightly different due to the position of the appendages but design and mesh elements and nodes are quite similar.

TABLE 2—*Sheath material properties.*

Zircaloy-4 Properties	
Elastic Modulus of Elasticity	$E = \frac{1.088 \times 10^{11} - 5.475 \times 10^7 \times T + K_2}{K_3},$ <p>where</p> $K_2 = -2.6 \times 10^{10}C \text{ and } K_3 = 0.88 + 0.12e^{-\phi 10^{-25}}.$ <p>C is the cold work (ratio of areas) and Φ is the high energy neutron fluence in n/m^2. For CANDU fuel, Φ is of the order of 10^{25} n/m^2, and Zircaloy-4 has about 15 % cold work.</p>
Stress-Strain Curves	<p>For the elastic regime, $\sigma = E\varepsilon$, where σ is true stress and ε is true strain.</p> <p>For the plastic regime, $\sigma = K\varepsilon^n$, where K is the strength coefficient and n is the strain hardening coefficient. For this model, K is given for the temperature range of 300–600 K as follows:</p> $K = A(1.17628 \times 10^9 + 4.54859 \times 10^5 T - 3.28185 \times 10^3 T^2 + 1.72752 T^3),$ <p>where A is a correction for cold work and irradiation given by:</p> $A = 1 + 0.546C + 9.76 \times 10^{-27} \phi,$ <p>where Φ is the neutron fluence (n/m^2).</p> <p>Assuming the strain does not exceed 5 %, the strain hardening coefficient, n, is given by:</p> $n = B(-9.49 \times 10^{-2} + 1.165 \times 10^{-3} T - 1.992 \times 10^{-6} T^2 + 9.588 \times 10^{-10} T^3),$ <p>where B is a correction factor due to cold work and irradiation given by:</p>

TABLE 2— (Continued.)

Zircaloy-4 Properties	
	$B = 0.17 \times e^{-\phi^{1/3}/(3.73 \times 10^7 + 2 \times 10^8 C)} (0.153 - 0.0916C + 0.299C^2 + 0.847e^{-39.2C})$.
Yield Stress and Yield Strain	$\sigma_Y = \left(\frac{K}{E}\right)^{1/(1-n)}$ and $\varepsilon_Y = \left(\frac{K}{E^n}\right)^{1/(1-n)}$, respectively.
Density	6.55 g/cm ³ , assumed independent of temperature.

Endcaps

The endcaps are modeled as solid entities using 8-node, linear brick finite elements. The normal-density Zircaloy-4 material properties are applied to the elements. To improve the control over the meshing of the endcaps, a cross section was created first and meshed. This meshed area was then revolved around the endcap axis to form the solid model and volume mesh.

Figure 5 illustrates the cross sections and area meshes used for the 28-element endcaps. There are two important things to note from the cross sections: the endcap model also includes a section of the endplate and sheath, and the interior of the endcap has been simplified from the endcap design by removing material that is superfluous to the modeling and does not contribute to

TABLE 3—Pellet material properties.

UO ₂ Properties	
Elastic Modulus	$E_S = 22.32 \times 10^{11} - 56.3 \times 10^{11} P$ with an error of $\pm 0.6 \times 10^{11}$.
	E_S is given in Pascals and P is the fuel porosity defined in relation to the theoretical density of UO ₂ such that,
	$P = 1 - \frac{\rho}{\rho_t}$
	where ρ is the density of the fuel and ρ_t is the theoretical density of UO ₂ (10.98 g/cm ³).
Poisson's Ratio	0.316
Density	10.98 g/cm ³

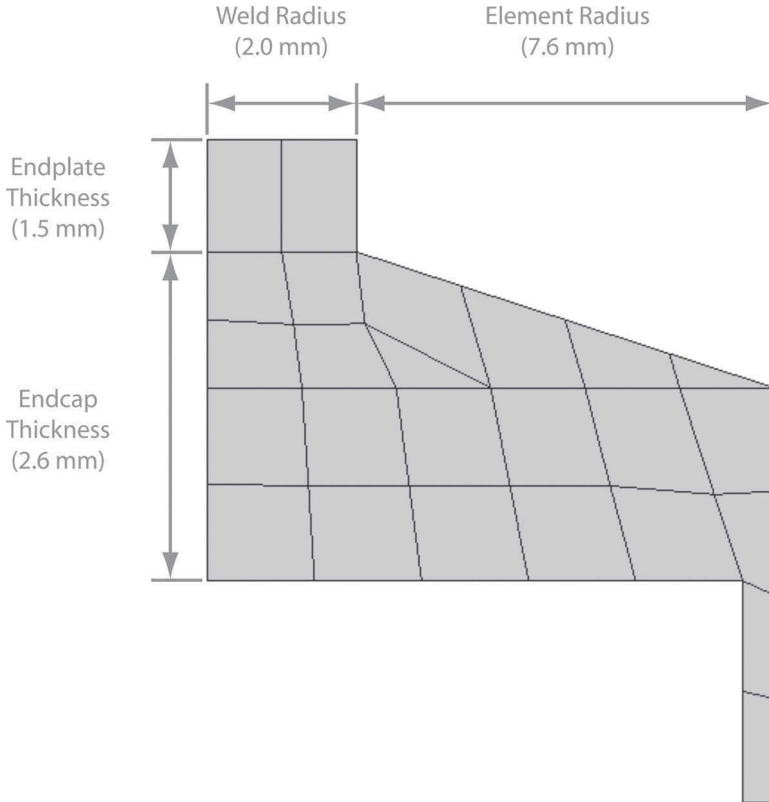


FIG. 5—Endcap radial cross section with basic dimensions and FE mesh.

the mechanical strength of the endcap. The number of finite elements and nodes for the 28-element endcap model are 400 and 502, respectively.

The reason that the endplate and sheath material was added to the endcap model was to ease mating of adjacent components as the bundle is assembled. In mating the endplates to the endcaps, there is a complication since the symmetries, or coordinate systems, are different. The endplate has a cylindrical symmetry centered on the bundle axis, whereas the cylindrical symmetry of the endcap is centered on each element axis. Aligning nodes for each meshed body (endplate and endcap) is problematic. Contact modeling could be used to “connect” the two meshes, but the preferable approach is to have one solid continuous volume mesh for the endplates and endcaps. Therefore, a cylindrical cut was made through the endplate at each element location (see Fig. 6) and the “endplate cylinder” part of the endcap model fits in place. Fine control of the mesh at these locations allows for a continuous volume mesh between the endplates and endcaps. The endplates were meshed using 8-node, linear brick elements and they are compatible with the elements used for the endplates.

The reason for incorporating a portion of the sheath to the endcap model is slightly different than the endplate since the axis of symmetry is identical.

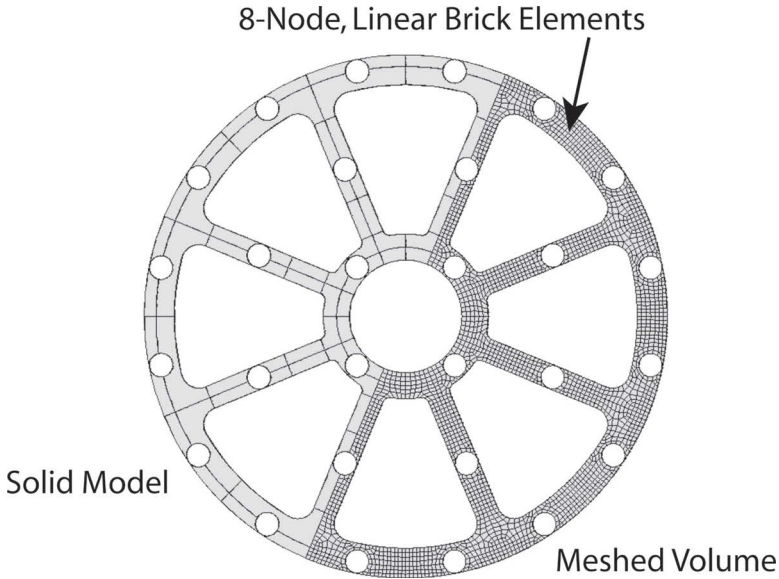


FIG. 6—28-Element fuel bundle endplate model.

However, since the sheath is modeled using shells and the endcaps are solids, some form of coupling is required. Simple nodal merging or coupling is not sufficient since shell elements contain rotational and translational degrees of freedom (DOF) but 3-D finite elements do not contain rotational DOF. Therefore, a mechanism to couple the shell elements rotational DOF to the bricks translational DOF is required. This coupling is facilitated in ANSYS by creating a bonded contact/target pair and applying the solid-to-solid multipoint constraint (MPC) algorithm to this contact pair. A section of the sheath was added to the solid endcap model so this coupling would be made away from the sheath-endcap interface.

A 3-D representation of the solid-shell coupling is shown in Fig. 7. Details of the endcap/endplate assembly are shown in Fig. 8. The sensitivity of the model to mesh density was examined in the endcap regions shown in Figs. 5–8. Increased density in the sheath, endcap, and endplate showed minimal variation in calculated nodal displacement and stress values.

Fuel Pellets

The fuel pellets are modeled as cylinders and the chamfers and dishing at the ends have been neglected. The fuel pellets are made of 8-node, linear brick elements.

Pellets are packed into a fuel element with the pellet axis aligned with the element axis. The exact number of pellets in an element is proprietary information, but based on general pellet dimensions, it is estimated that about 30 pellets form the *pellet stack* inside the element. The pellet stack is modeled inside the sheath with a gap between each pellet the same width as the gap between

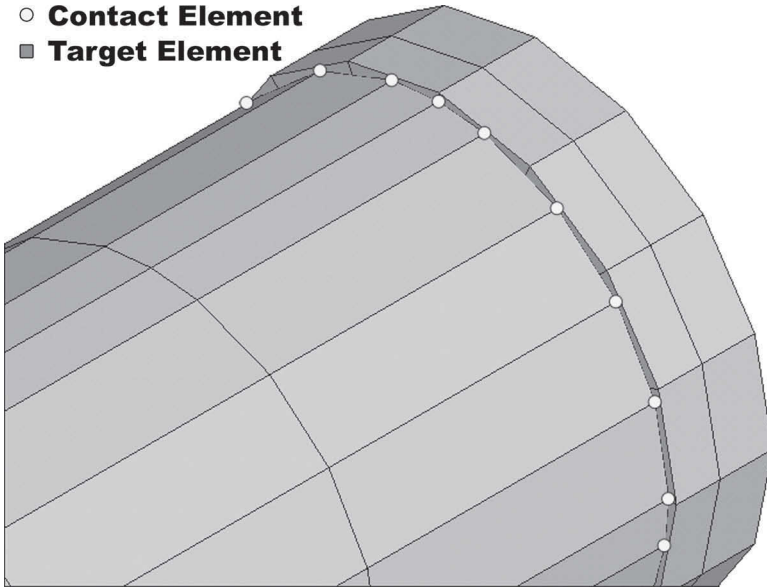


FIG. 7—Multipoint constraint contact elements coupling the sheath to the endcap.

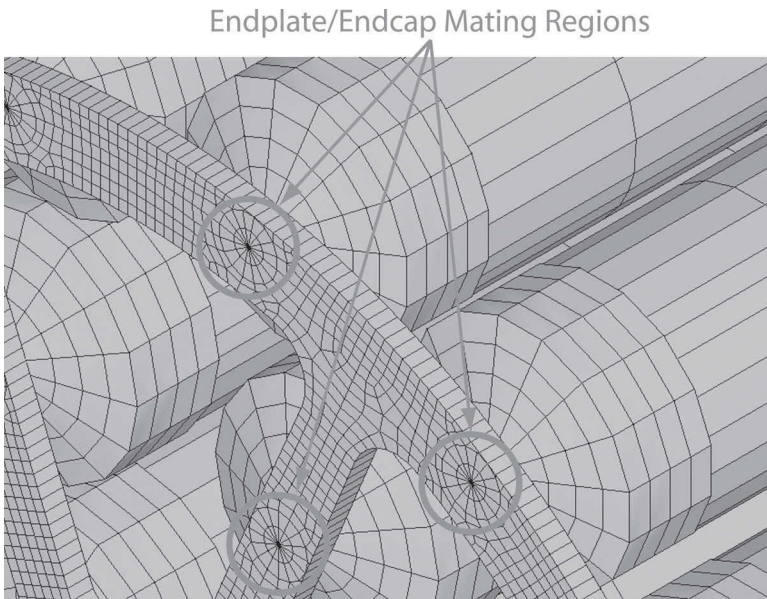


FIG. 8—Detail of bundle mesh with mating between the endplate and endcaps.

8-Node, Linear Brick Elements

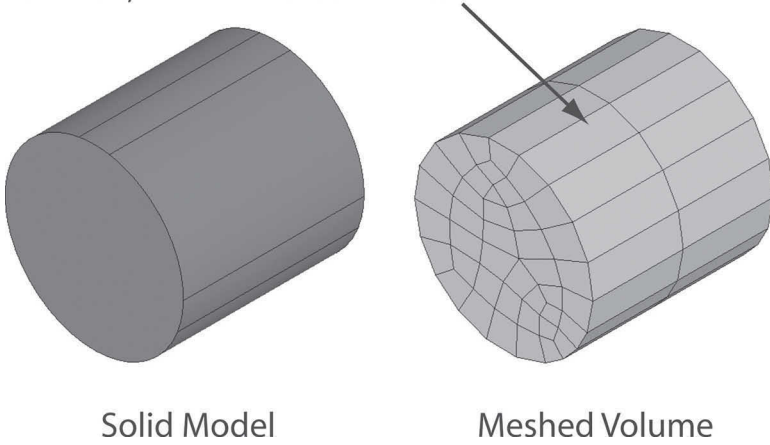


FIG. 9—Finite element fuel pellet model.

the pellet and the sheath. The pellets are also created by extrusion along the element axis in a similar manner to the creation of the sheath.

The solid model and finite element model of the fuel pellet and pellet stack are illustrated in Fig. 9. The entire surface of each pellet is meshed with surface contact elements. The surrounding sheath and endcap surfaces are meshed with target elements. These elements are used to constrain the pellets within the element. The contacts of each pellet with adjacent pellets are also modeled. These contacts transfer loads between adjacent pellets. Static analysis in ANSYS of these open contacts results in rigid body motion errors for the pellets and any solution with the model is extremely divergent.

To prevent rigid body motion until sufficient support of the pellets is maintained by the contact, “truss” elements have been used. These elements have an elastic modulus that is approximately 1 % of the Zircaloy-4 modulus and the density of the elements has been set to zero. The elements provide no mass to the model, but the string will be slightly supported at the endcaps. However, during solution with ANSYS, the truss elements can be eliminated after sufficient contact of the pellet with the sheath has occurred.

Appendages

The bearing pads and spacer pads are created in the model by extruding their cross-sectional area on the sheath to the desired height. The volume mesh is similarly created by extruding the area mesh on the sheath to form the volume mesh. Using this approach results in several differences between real bundles and the model. First, the bearing pad ramp is not present on either end of the pad. The length and width of the contact part of the bearing pad is sufficiently larger than the ramps suggesting that modeling of the ramp will have little impact on the stiffness of the element. The radius of curvature for the bearing pad surfaces is different, but this is not expected to have any real effect on the

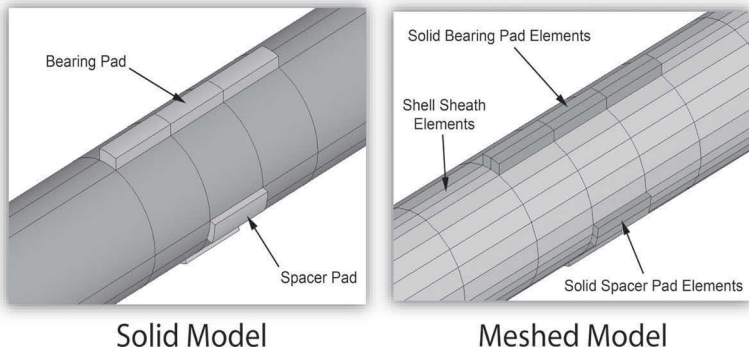


FIG. 10—Solid model and meshed volumes for bearing pads and spacer pads.

bundle model (see Fig. 10). The 15° angle of the spacer pads long axis with the element axis is not included in the model. The primary purpose of modeling the spacer pads is to account for interactions between adjacent elements. It is not expected that the angle of the spacer pads will affect this interaction.

The technique used to model the appendages does introduce a very small extra stiffness to the elements. The sheath model areas and elements are located at the half-thickness of the sheath and the appendages are extruded from the sheath area. The sheath half-thickness is added to the extrusion so the appendage surfaces are in the right position. The material in the region where the extruded appendage overlaps the sheath volume has been accounted for twice: once by the thickness parameter in the shell elements and once by the volume mesh of the appendage. This will add an extra stiffness to the element. However, the thickness of this region is only half the sheath thickness (~ 0.2 mm) and the effect is expected to be very negligible.

Experimental Testing

Experimental Setup

Experiments were done to validate the results of the modeling and to test how well the model predicted actual bundle behavior. For this purpose a test apparatus was designed and built with the testing done at Stern Laboratories Inc.³ Figure 11 illustrates the experimental setup and test apparatus. The apparatus is designed for fixed-displacement tests where the displacement is applied via a mechanical “clamping fixture,” which is in contact with the bundle. A threaded rod with a nut is used to control the displacement of the clamping fixture, thus applying a load to the bundle. The bundle can be constrained during the tests by either the endplate plugs or the semi-circular supports, as appropriate. De-

³Stern Laboratories Inc. 1590 Burlington Street East. Hamilton, Ontario, Canada L8H 3L3

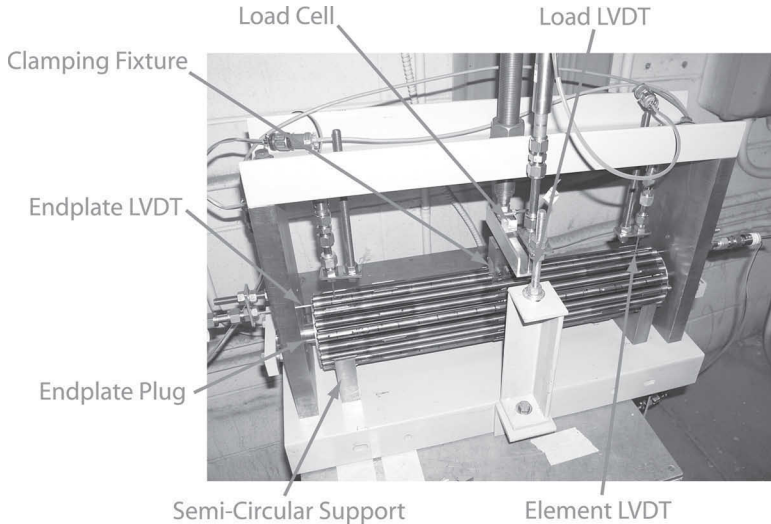


FIG. 11—Stern Laboratories fuel bundle mechanical test apparatus.

formation of the bundle is measured with linear variance differential transducers (LVDTs) during the test at five locations: one where the force is applied (the force is measured by a load cell), two along the length of element, and two on the endplates at each end of the bundle.

Types of Tests

A series of three element pull tests were performed with unirradiated 28-element General Electric CANDU fuel bundles. Loads applied to the bundles tested bundle behavior in both the elastic and plastic regimes. The pull test involved pulling a single element at its midpoint in a radial direction away from the bundle central axis while constraining the bundle endplate. Both the displacement and load at the point where the load is applied is recorded. Displacement measurements were also made at other locations in the fuel element near the endplates (Table 4) and at the endplates.

Two other types of tests are also being investigated: element push test

TABLE 4—Experimental testing LVDT locations for 28-element CANDU fuel bundles.

Test Number	Bundle Serial Identification Number	Element Identification Number for Element Pulled	Load LVDT	Left LVDT Location in mm from Left Endplate	Right LVDT Location in mm from Right Endplate
13	N85917C	1	On center	30	37
14	N85917C	4	On center	30	37
15	N85917C	7	On center	30	37

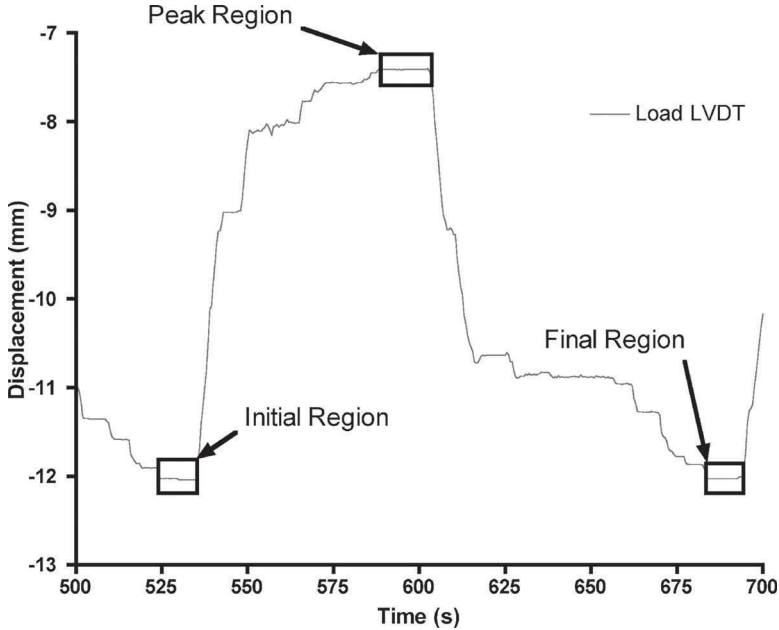


FIG. 12—LVDT signal during load cycle illustrating analysis regions.

where the outer bearing pad of an element is pushed radially inward into the bundle, and a center load test which involves pushing the entire bundle at its center and measuring its displacement.

Test Procedure

The test procedure involved loading the bundle into the apparatus, applying the bundle constraints, attaching clamping fixture and LVDTs, and cycling the applied displacement to the bundle while measuring deformations and applied load at the load cell. The test initially started with zero displacement corresponding to zero applied load. The displacement was then increased until the load cell measured the maximum load for that cycle. The displacement was then decreased until the applied load was zero. The loading cycle was repeated with an increasing maximum load until permanent deformation was observed.

The experimental data were analyzed to determine the maximum displacement and permanent displacement of each LVDT for the load cycles. The maximum displacements were determined by subtracting the initial load cycle displacement from the peak load cycle displacement. The permanent displacements were determined by subtracting the initial load cycle displacement from the final load cycle displacement. This is shown graphically in Fig. 12. The same procedure was performed with the load cell signal to determine the maximum load.

It was observed during the analysis that at the higher loads, the load signal decays with time in an exponential manner. This would appear to indicate that

load relaxation is occurring and the test results at higher loads might not represent steady-state loads. In order to best approximate the steady-state load, the maximum load was determined using a small section of the signals near the end of the load cycle peak when the load stabilized and remained unchanged with time.

The uncertainty in the experimental data was estimated by evaluating the test results for identical test types. A cubic polynomial was fit to the data and the variance between the polynomial and the experimental data was determined. The uncertainty for the experiment type is twice the standard deviation of the fit. The polynomial was also extrapolated to zero load to determine the offset, or bias, of the experimental data.

Bundle Stress Model Simulations and Mechanical Tests Results

Simulations of the mechanical tests were performed in ANSYS with the 28-element element fuel bundle models. Constraints were applied to the bundle model to represent the experimental constraints as best as possible. The displacement of nodes nearest to the LVDT locations was used to simulate the LVDT measurements. A series of ten load cycles were simulated instead of the number of cycles used for each test. This minimized the time required to run simulations while still providing sufficient information to compare with the experimental results. The static solver was used for the simulations, which means that the modeled results all represent steady-state loads and displacements.

The pull tests were simulated in ANSYS by fixing the interior faces of the endplate inner ring. The total force was applied to the sheath nodes which were on the inside of the element along the length of the bearing pad. LVDT measurements were simulated using nodal displacements for the nodes closest to the LVDT position. For all the pull test simulations, partial bundle models were used. The partial models only included elements in the vicinity of the test element, which reduced the model size and the solution time. A comparison of results from sample pull tests using the partial model and a full bundle model was made and this analysis showed that all results agreed to within 0.01 %. This is sufficient agreement for the present purposes.

In total, three pull tests were performed on the 28-element bundle with load cycles increasing by either 25 N or 50 N up to a maximum force of about 400 N. Typical results for the 28-element bundle are shown in Figs. 13–18. The applied load is plotted against the maximum displacement measured for each of the LVDTs. The plotted simulation results also include simulation results from the hollow element bundle stress model along with the segmented pellet model to indicate to what extent pellets effects are important.

The simulation model over predicts the observed displacements by about 20 % at the center of the pulled element (Fig. 13), and, by about 25 % at the location of the left LVDT (30 mm from the left endplate: Fig. 14). However, displacements 37 mm from the right endplate (Fig. 15) are about twice as large as those found experimentally. Additionally, the simulation results from the hollow bundle model predict the bundle should behave elastically for the whole

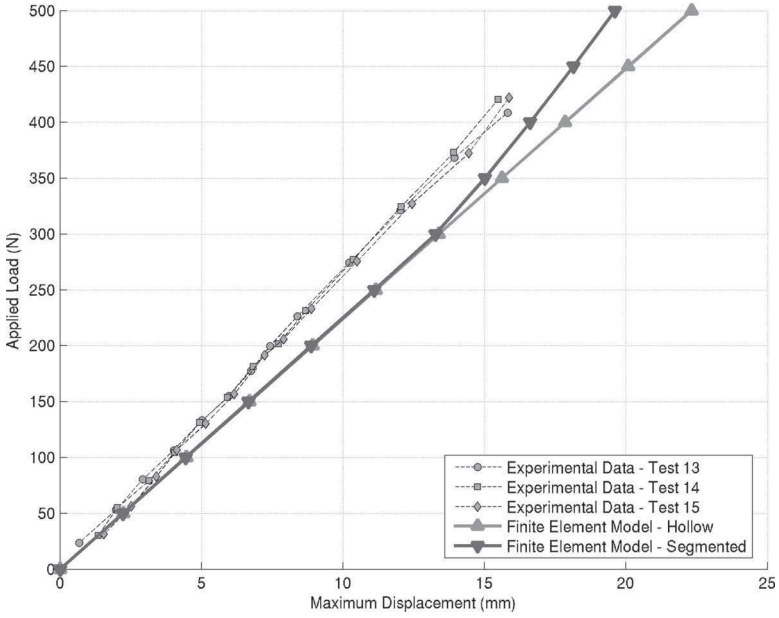


FIG. 13—Load LVDT displacement.

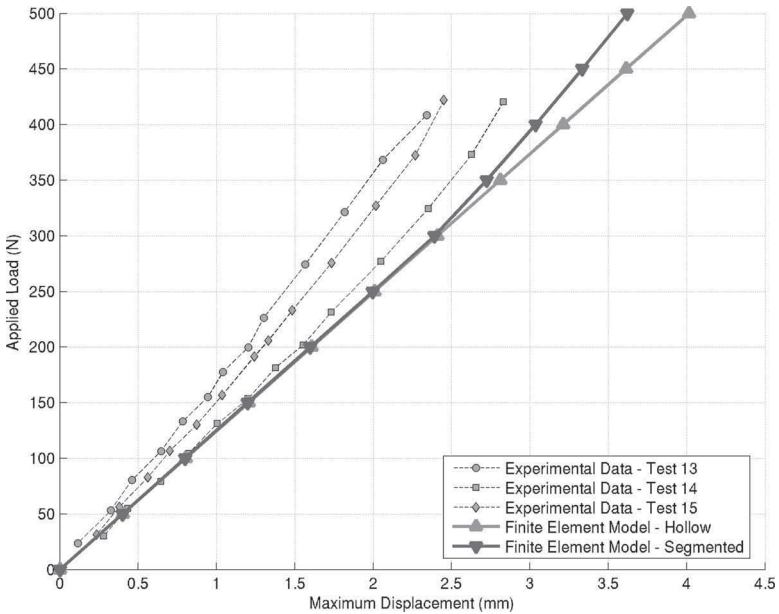


FIG. 14—Left element LVDT displacement.

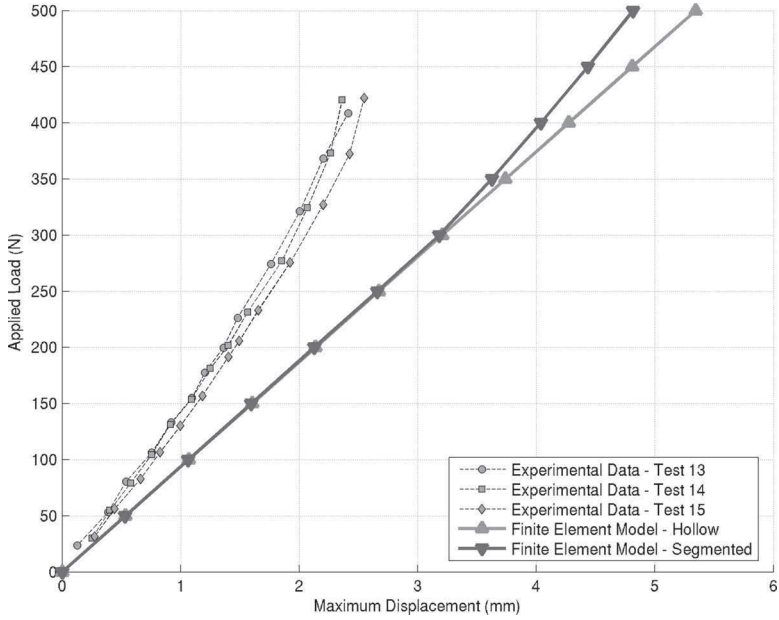


FIG. 15—Right element LVDT displacement.

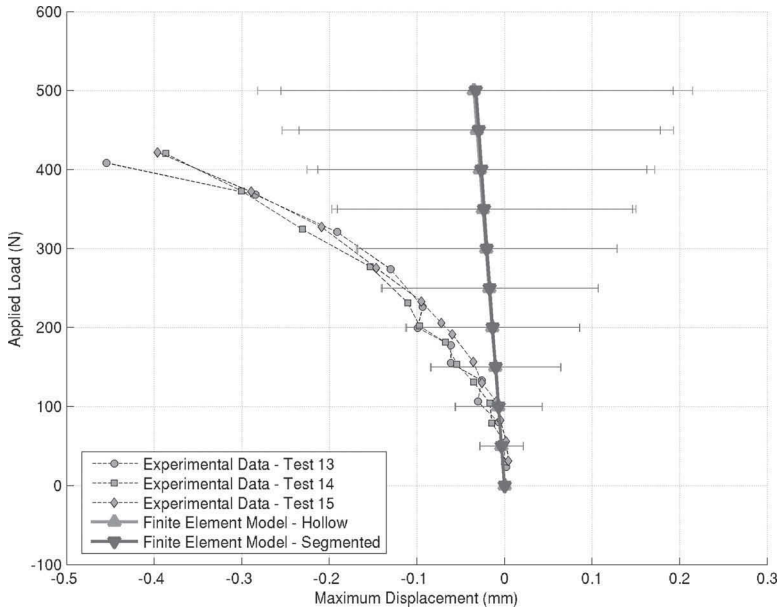


FIG. 16—Left endplate LVDT displacement.

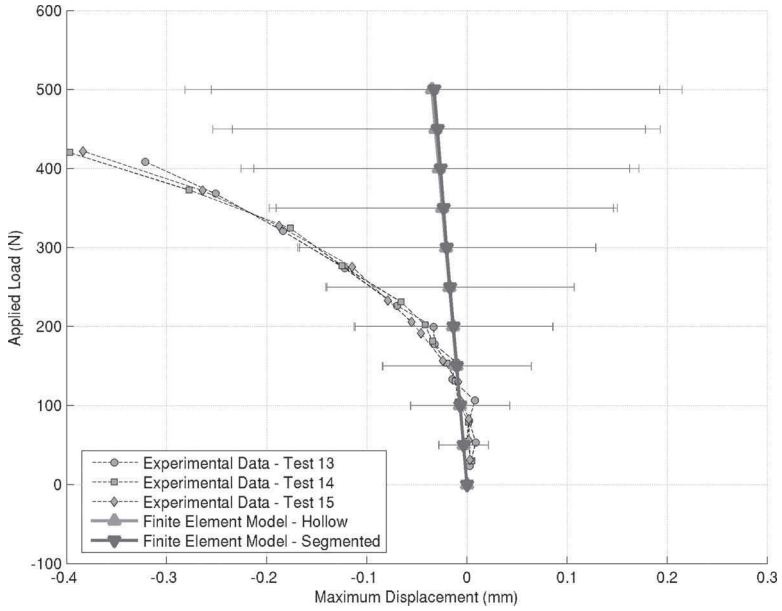


FIG. 17—Right endplate LVDT displacement.

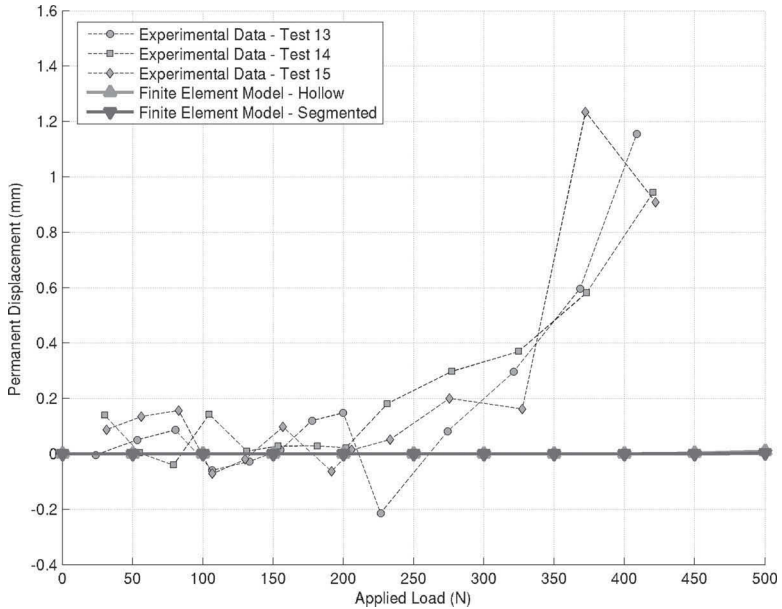


FIG. 18—Load LVDT plasticity.

range of loads up to 400 N applied to the bundle (Figs. 13–15), and this is also indicated by the plot of permanent displacements shown in Fig. 18. However, both the experimental results of Fig. 18 and the bundle behavior shown in Fig. 15 indicate that the bundle begins to behave plastically for loads greater than about 200 N.

The hollow model predicts a linear relationship between load and displacement for the whole range of loads tested consistent with linear elastic behavior. Similarly, the experimentally found displacement values at the center of the pulled element and towards the left endplate also behaved linearly, except for the displacements recorded near the right endplate. Since the experimental results are observed to be quite repeatable and provide consistent results, the observed bundle behavior cannot be readily explained as a result of experimental error. Rather, it would appear to indicate that the bundle characteristics have an inherent asymmetry. This asymmetric behavior could well be caused by material property dissimilarities at the endplate-to-endcap welds and should be more fully explored. Zircaloy-4 fabrication has changed over time and recent Zircaloy-4 material properties may have drifted from the MATPRO values. Given the differences in the onset of permanent deformation in the model and experiment, it is expected that the plastic material properties given in MATPRO are not reliable for mechanical modeling of the CANDU fuel bundle.

The segmented model that includes the pellets reduces the simulated bundle displacement towards the experimentally observed values but it does not quite explain the observed behavior either. It is observed that the segmented pellet model also provides a linear relationship between load and displacement consistent with linear elastic behavior. While addition of the pellets to the model does approach the general behavior of the observed displacements near the endplates, it fails to predict the behavior observed for displacements at the point of application of the load, even though the new predicted values from the simulation are closer to the observed values and reduce the variance between observed and predicted displacements at the mid-point of the pulled element to about 10 %.

At applied forces less than approximately 300 N, there is no observable difference between the hollow and segmented pellet models. However, as applied loads exceed 300 N, the pellets act to stiffen the element, which also appears to be observed in some of the experimental results, primarily the values from the right end LVDT (Fig. 15). In general, more displacement was seen along the element in the simulations than in the experiments. At applied loads less than 50 N the modeled and experimental results agree within the experimental uncertainty, but the slope of the lines up to the plastic region, between 200 N and 300 N applied force from the experimental data, suggests the modeled fuel elements are not sufficiently stiff.

The results for the modeled endplate LVDT data contain “error bars” associated with the values (Figs. 16 and 17). The plotted values are based on the displacements of the endplate at the element axis, but in the experiments the LVDT does not measure this displacement exactly. The error bars are plotted to indicate the range of possible displacements of the LVDT in the weld region.

Comparison of the endplate LVDT displacements shows that the modeled endplates are stiffer than the observed in the experiment. At low applied load,

the results may be the same given the large uncertainty of the measurement based on LVDT position, but at higher load the endplate behaves very differently between the model and the experiment.

The permanent displacement for the LVDT at the load point of application per load cycle is plotted against the experimental data in Fig. 18. Displacements at other locations of the bundle follow similar trends. From the experimental data, permanent deformation of the element is first observable in the range between 200 N to 300 N. However, the modeled results show no indication of significant plastic deformation.

As indicated earlier, forces applied to the bundles during storage or transportation are normally at the low end of the applied forces used in these tests, and unlikely to be greater than 100 N. In this range, the model at this time provides an adequate tool to predict stresses in the bundle relevant to its management. Further work, however, is being planned to elucidate the observed behavior and improve the model predictions. In particular, the impact that material variability and variability at the endplate-to-endcap welds could have on the developed models.

Conclusions and Recommendations

This paper has discussed the finite element bundle models created for the 28-element CANDU fuel bundle. The models are being developed to map out the stress levels and distributions in used fuel bundles during the dry storage period. After discharge from the reactors, the bundle elements are usually bowed and this permanent characteristic deformation of the elements has been accounted for in the models.

Predicted stresses and deformations from the ANSYS fuel bundle models were validated against experiments on unirradiated 28-element CANDU fuel bundles. In this instance, results from “pull element” mechanical tests are being reported and compared with predictions from the models. During all tests the applied force and deformation of the bundle at five locations were recorded. Simulations of the tests were run with the fuel bundle models using the ANSYS finite element package.

A comparison of the simulated results and the experimental results show that the models currently do not accurately predict the response of the bundle over the entire load range examined up to 400 N. The model overpredicts displacements for a given load when compared to the test results. However, the model predictions for bundle behavior during normal storage or transportation appear adequate. Also, at larger loads it generally appeared that the simulated endplates were stiffer than the actual bundle endplates.

The disagreement between the mechanical tests and the simulations is not fully understood. A major assumption in developing the model was to ignore the Zircaloy-4 material variability throughout the bundle. This was done since material properties for heat affected Zircaloy-4 are not known. Similarly, the Zr-4 is modeled with an isotropic elastic modulus, whereas the modulus of the sheath is anisotropic. The material property values used for the model could partially account for the different behavior of the simulated results along the

elements (over-prediction of deformation) compared with the endplate (under-prediction of deformation).

In creating the model geometry, nominal fuel bundle design values were used. The manufactured geometries are likely different than the design geometries within the allowed tolerances. It is possible that some parameters, such as radial gap between the fuel pellets and the fuel element sheath, have a large effect on the deformation of fuel elements. The model is fully parametric and can be used to further explore the parameters of greatest sensitivity to the response of the bundles. This analysis will be performed in the future to allow for a better understanding of how the bundle responds to applied loads and increase the accuracy of stress or strain predictions using the models.

Further work will be undertaken to investigate the impact that material variability, variability at the endplate/endcap welds, and evolution of specifications on bundle geometry might have on the observed discrepancies. Incorporation of irradiated fuel bundle properties and geometries will also be performed in the future.

Acknowledgments

The authors would like to thank Jay Snell of Stern Laboratories for performing the CANDU fuel bundle mechanical tests and providing the raw experimental data.

References

- [1] Hohorst, J. K., *SCDAP/RELAP5/MOD2 Code Manual, Volume 4: MATPRO—A Library of Materials Properties for Light-Water-Reactor Accident Analysis*, EG&G Idaho, Inc., Idaho Falls, 1990.

Author Index

A

Anandaraj, V., 195-208

B

Bolton, C. J., 93-113

C

Cho, H. S., 163-174

D

Dohi, K., 64-92, 128-151

F

Flewitt, P. E. J., 93-113
Freire-Canosa, J., 251-274

G

Gérard, R., 26-39
Garner, F. A., 237-250, 209-218
Ghoniem, N., 175-194
Gundermann, A., 40-63
Gusev, M. N., 237-250, 209-218

H

Hein, H., 40-63

I

Ishino, S., 64-92
Iwase, A., 152-162

K

Karthik, V., 195-208
Kasada, R., 163-174
Keim, E., 40-63
Kimura, A., 163-174

Kondo, K., 219-236

L

Lampman, T. J., 251-274
Lee, J. H., 163-174
Lucon, E., 26-39

M

Maksimkin, O. P., 237-250, 209-218
Matsuzawa, H., 128-151,
152-162
Miwa, Y., 219-236
Moskovic, R., 93-113
Muralidharan, N. G., 195-208

N

Nagasawa, K., 175-194
Nanstad, R. K., 1-25
Nishida, K., 64-92, 128-151
Nishinoiri, K., 219-236
Nishiyama, Y., 152-162
Nomoto, A., 64-92, 128-151

O

Onizawa, K., 152-162
Osipov, I. S., 209-218

P

Parameswaran, P., 195-208
Popescu, A., 251-274

R

Raj, B., 195-208
Rindelhardt, U., 114-127

S

Saroja, S., 195-208
Schnabel, H., 40-63
Schuhknecht, J., 114-127
Scibetta, M., 26-39
Seibert, T., 40-63
Server, W. L., 1-25
Sharafat, S., 175-194
Silniagina, N. S., 209-218
Soneda, N., 64-92, 128-151

T

Takahashi, A., 175-194
Toktogulova, D. A., 237-250
Tomimatsu, M., 128-151
Tsukada, T., 219-236

V

Venkiteswaran, C. N., 195-208
Venugopal, V., 195-208
Viehrig, H. W., 114-127
Vijayalakshmi, M., 195-208
Viswanathan, K. V. Kasi, 195-208

W

Weiss, F. P., 114-127
Wootton, M. R., 93-113

Y

Yamaguchi, M., 152-162
Yamashita, S., 219-236

Subject Index

I

12Cr18Ni10Ti stainless steel, 209-218

A

atom probe tomography, 128-151
austenitic stainless steel, 219-236

B

beltline welding seam, 114-127

C

CANDU fuel, 251-274
carbon segregation, 152-162
carbon-manganese steel, 93-113
Charpy impact, 1-25
copper, 1-25
Cr content, 163-174
crack arrest, 40-63

D

deformation wave, 209-218
dislocation cell, 219-236
dislocation channel, 219-236
dpa, 195-208
ductile-to-brittle transition region, 26-39
ductile-to-brittle transition temperature (DBTT), 152-162
ductility, 195-208

E

embrittlement, 152-162
embrittlement correlation, 64-92
energy balance, 237-250
excess heat, 237-250

F

finite element modeling, 251-274
fracture toughness, 26-39, 114-127, 1-25, 40-63

G

grain-boundary, 152-162

H

high damage dose, 209-218
high fluence, 128-151

I

integrity assessment, 114-127
intergranular fracture, 152-162
irradiation embrittlement, 163-174, 40-63
irradiation hardening, 163-174
irradiation temperature, 163-174

L

latent energy, 237-250

M

Magnox power station, 93-113
martensite, 209-218
master curve, 1-25, 40-63

Master Curve, 26-39, 114-127
 microstructural characterization, 64-92
 monitoring programme, 93-113
 Multi-Modal Master Curve, 26-39

N

neutron irradiation, 163-174, 93-113, 237-250, 219-236, 152-162, 40-63
 neutron irradiation embrittlement, 64-92, 128-151
 nickel, 1-25

O

oxide dispersion strengthened steel, 163-174

P

phosphorus segregation, 152-162
 plastic deformation, 219-236
 post-irradiation annealing, 237-250
 precipitates, 195-208
 PWR, 1-25

R

radiation embrittlement, 1-25
 reactor pressure vessel, 64-92, 128-151, 152-162
 reactor pressure vessel steel, 114-127, 40-63
 reactor pressure vessels, 1-25
 RT_{NDT} , 40-63
 RT_{T_0} , 40-63

Russian WWER-type reactor, 114-127

S

spent fuel storage, 251-274
 steel reactor pressure vessel, 93-113
 surveillance capsules, 26-39
 surveillance data, 64-92

T

transmission electron microscopy, 128-151, 195-208
 trepans, 114-127
 true stress–true strain relation, 219-236

U

ultimate tensile strength, 195-208

V

voids, 195-208

W

weld metal, 114-127
 work hardening rate, 219-236
 WWER, 1-25

Y

yield strength, 195-208



www.astm.org

ISBN: 978-0-8031-5523-7

Stock #: STP1513